

Development and Implementation of Advanced Soft Soil Models in Finite Elements

By

Nallathamby Sivasithamparam

A thesis submitted to the University of Strathclyde in partial
fulfillment of the requirements for the degree of Doctor of Philosophy
in the Faculty of Engineering

2012

The copyright of this thesis belongs to the author under the terms of the United Kingdom Copyright Acts as qualified by University of Strathclyde Regulation 3.50. Due acknowledgement must always be made of the use of any material contained in, or derived from, this thesis.

Signed:

Date:

This thesis is dedicated to my loving sister

Satkunaseelan Renuka

who passed away during the time I was writing this
thesis.

Acknowledgements

The research would not have been possible without the support of many people whom it is appropriate to acknowledge and thank. Firstly, I wish to express my profound gratitude and sincere appreciation to Prof. Minna Karstunen for her guidance, support, freedom and unfailing patience throughout my research. Her time spent on this research, numerous discussions and review of the research proposal and the final thesis is gratefully acknowledged. I am also deeply indebted to my second supervisor, Dr. Mike Kenny who helped me with writing thesis.

The work described in this thesis was founded by scholarships from both the University of Strathclyde and Overseas Research Students Awards Scheme (ORSAS). The work was also sponsored by the Marie Curie Research Training Network on Advanced Modelling of Ground Improvement on Soft Soils (AMGISS: MRTN-CT-2004-512120), Industry-Academia Partnerships and Pathways (IAPP) project on Modelling Installation Effects in Geotechnical Engineering (GEO-INSTALL: PIAG-GA-2009-230638) and International Research Staff Exchange Scheme (IRSES) project on Geo-Excel (PIRSES-GA-2008-230860). The funding of all parties is gratefully acknowledged.

I would also like to thank Dr. Paul Bonnier and Dr. Ronald Brinkgreve from PLAXIS BV for their endless efforts in helping me to implement user defined soil models to the PLAXIS finite element code during my stay in PLAXIS BV, Netherlands as secondee for 9 months.

Finally, but by no means least, I am sincerely grateful to my wife, Jasotha for her constant support, kindness, love and understanding which provided me with persevering courage and constant simulation. I am also obliged to my parents and sister for their support and love for such long time.

Abstract

Numerical algorithms to implement an advanced nonlinear constitutive model, S-CLAY1S, for natural soft clay into PLAXIS are studied in order to reduce the numerical instability. Simulations performed using several triaxial tests and a benchmark test indicate that the use of an automatic substepping modified Newton-Raphson (MNR) algorithm can eliminate or minimize the problem. Therefore, this algorithm is adopted to implement S-CLAY1S into PLAXIS as a user defined soil model. The modified S-CLAY1S model was proposed by incorporating Lode angle dependency failure criterion. This has improved the model predictions in failure condition especially in extension.

A hybrid implicit numerical algorithm for the Sekiguchi-Ohta (SO) inviscid/viscid models capable of robustly overcoming the vertex singularity is presented. The proposed hybrid algorithm consists of modified Newton-Raphson algorithm and Stolle's algorithm, used to implement the SO models into PLAXIS. Numerical simulations and benchmark test demonstrate the algorithm's accuracy and numerical stability even for large strains.

The main part of this thesis is the development and implementation into FE code of a new constitutive model to represent the cyclic behaviour of natural soft clays. The S-CLAY1S model has been extended to the bubble surface plasticity in which smooth transitions between elastic and plastic behaviour can be modelled. The model developed in this research is named 'B-SCLAY1S' and requires thirteen parameters. Numerical examples show that the implementation into PLAXIS of the present model is successful. Finally, applications of the B-SCLAY1S model are made in two levels. First, simulations and comparison with laboratory tests including kaolin, Swiss lacustrine clay and Bothkennar clay test data. Second, the finite element benchmark analysis of an embankment and a pile driving problem subjected to cyclic loading were presented. At both levels the B-SCLAY1S is shown to be superior to the S-CLAY1S models, mainly because it captures the small strain behaviour.

Contents

List of Figures	xvii
List of Tables	xviii
List of Algorithms	xix
List of Notations	xx
1 Introduction	1
1.1 Objectives	2
1.2 Secondment	3
1.3 Layout of Thesis	3
2 Constitutive Models	5
2.1 Simple soil models	5
2.1.1 Elastic models	5
2.1.2 Elasto-plastic models	6
2.1.2.1 Elastic-perfectly plastic models	6
2.1.2.2 Hardening elastic-plastic models	6
2.2 Critical State Theory	7
2.2.1 Original Cam-clay (CC) model	7
2.2.2 Modified Cam-clay (MCC) model	8
2.2.3 Sekiguchi-Ohta (SO) model	10
2.2.3.1 SO inviscid model	10

2.2.3.2	SO viscid model	11
2.2.4	Shortcomings of the original, modified Cam clay and Sekiguchi-Ohta models	12
2.3	Advanced critical state models	12
2.3.1	S-CLAY1 model	13
2.3.2	S-CLAY1S model	14
2.3.3	EVP-SCLAY1S model	15
2.3.4	Shortcomings of advanced critical state models	16
2.4	Cyclic loading models	18
2.4.1	Bounding surface model	19
2.4.2	MIT-E3 model	20
2.4.3	Subloading surface model	21
2.4.4	Bubble surface model	22
2.5	Other alternative approaches in soil models	26
2.5.1	Hyperplasticity model	26
2.5.2	Hypoplasticity model	26
2.5.3	Multilaminate model	27
2.5.4	Disturbed state concept model	28
2.6	Summary	29
3	Further improvement and implementation of S-CLAY1S model	31
3.1	Mathematical formulation in general stress space	31
3.1.1	Elastic behaviour	32
3.1.2	Yield function	32
3.1.3	Flow rule	34
3.1.4	Hardening rule	34
3.1.5	Hardening modulus	35
3.2	Numerical implementation	36
3.2.1	Euler forward (explicit) method	38

3.2.2	Euler backward (implicit) method	45
3.2.3	Modified Newton-Raphson (implicit) method	48
3.3	Performance comparison of different algorithms	54
3.3.1	Simulations of strain-controlled triaxial tests	54
3.3.2	Simulations of benchmark test	61
3.4	Lode angle dependency	65
3.4.1	Formulation of Lode angle dependency	66
3.4.2	Verification and validation of Lode angle dependency	67
3.4.3	Benchmark applications using Lode angle dependency	72
3.5	Summary	73
4	Implementation of Sekiguchi-Ohta (SO) models	74
4.1	Introduction	74
4.2	SO inviscid model	79
4.2.1	Mathematical formulation of the SO inviscid model	79
4.2.2	Singularity of the SO inviscid model	82
4.2.3	Implementation of the inviscid SO model into PLAXIS	84
4.2.3.1	Modified Newton-Raphson (MNR) method	84
4.2.3.2	Stolle's implicit method	87
4.2.4	Verification of the SO inviscid model	93
4.3	SO viscid model	96
4.3.1	Mathematical formulation of the SO viscid model	96
4.3.2	Singularity of the SO viscid model	100
4.3.3	Dry side of the SO viscid model	100
4.3.4	Verification of the SO viscid model	102
4.4	Application to a benchmark problem	105
4.5	Summary	111

5	B-SCLAY1S model formulation and its implementation	112
5.1	Introduction	112
5.2	Triaxial stress space	113
5.2.1	Elastic part of the model	113
5.2.2	Equation of surfaces	114
5.2.3	Flow rule	115
5.2.4	Hardening rules	115
5.2.5	Hardening modulus	118
5.3	General stress space	121
5.3.1	Preliminaries	122
5.3.2	Elastic part of the model	122
5.3.3	Yield and plastic potential surface	123
5.3.4	Equation of surface	123
5.3.5	Flow rule	124
5.3.6	Hardening rules	124
5.3.7	Hardening modulus	126
5.3.8	Centre of Bubble	128
5.3.9	Pore water pressure	130
5.4	Determination of model parameters	130
5.5	Numerical implementation into PLAXIS	132
5.6	Summary	142
 6	 Parametric study of B-SCLAY1S	 144
6.1	Introduction	144
6.2	Size of Bubble	145
6.3	Plastic modulus parameter	149
6.4	Standard parameters	152
6.5	Anisotropy parameters	160
6.6	Destructuration parameter	165

6.7	Small strain stiffness	170
6.8	Constant q slow cyclic triaxial simulations	172
6.9	Summary	176
7	Verification and application of the B-SCLAY1S model	177
7.1	Verification against <i>Al-Tabbaa (1987)</i> simulations	177
7.2	Comparison with <i>Messerklinger (2006)</i> triaxial test results	184
7.2.1	Compression test: S2T4 ($\Delta p' = \text{constant}$)	185
7.2.2	Compression test: S2cT1 ($\eta = 0.9$)	188
7.2.3	Isotropic compression test: S2T3 ($\Delta q = \text{constant}$)	190
7.2.4	Extension test: S2aT4 ($\Delta p' = \text{constant}$)	192
7.3	Comparison with <i>McGinty (2006)</i> triaxial results	195
7.4	Application to an embankment	201
7.5	Application to a pile driving problem	204
7.6	Summary	209
8	Conclusions and Recommendations	210
8.1	Summary and Conclusions	210
8.1.1	Numerical algorithms to implement into FE code	211
8.1.2	Lode angle dependency	211
8.1.3	Hybrid algorithm to implement the SO models	211
8.1.4	Bubble surface B-SCLAY1S model	212
8.2	Recommendations for future work	212
8.2.1	Modified S-CLAY1S model	212
8.2.2	Sekiguchi-Ohta models	213
8.2.3	B-SCLAY1S model	213
	References	214
A	Definitions in general stress space	226

B Derivatives of S-CLAY1S	229
C The SO model	234
D Determination of SO models parameters	236
D.0.4 SO inviscid model parameters	236
D.0.5 SO viscid model parameters	238
E Derivatives of B-SCLAY1S	240
F Determination of B-SCLAY1S model parameters	242
G Parametric study of B-SCLAY1S	247

List of Figures

2.1	The original Cam clay (CC) model yield surface	8
2.2	The modified Cam clay (MCC) model yield surface	9
2.3	The Sekiguchi-Ohta (SO) model yield surface	10
2.4	The S-CLAY1 yield surface in triaxial stress space	13
2.5	The S-CLAY1S yield surface in triaxial stress space	14
2.6	The EVP-SCLAY1S yield surface in triaxial stress space	16
2.7	The S-CLAY1S model response: (a) effective stress path, (b) stress-strain response and (c) pore pressure-strain response	17
2.8	Typical response: (a) effective stress path, (b) stress-strain response and (c) pore pressure-strain response (Muir Wood, 1990)	17
2.9	Characteristics stiffness-strain behaviour of soil with typical strain ranges (after Atkinson & Sallfors, 1991)	18
2.10	Sketch of bounding surface model in triaxial stress space	19
2.11	Sketch of MIT-E3 model in triaxial stress space	21
2.12	Subloading surface model in triaxial stress space	22
2.13	Bubble surface model in triaxial stress space (after Al-Tabbaa, 1987)	23
2.14	Bubble model for structured soil (Muir Wood, 1995)	25
2.15	Yield curve and failure criterion on a sampling plane (Schuller & Schweiger, 2002)	28
2.16	Schematic of relative intact and fully adjusted clusters in DSC (Desai & Toth, 1996)	29
2.17	Summary of constitutive models discussed in this chapter	30

LIST OF FIGURES

3.1	The S-CLAY1S yield surface in triaxial stress space	33
3.2	The Drucker-Prager failure surface in the π -plane	34
3.3	Explicit stress update with substepping (after Yu, 2006)	39
3.4	Sketch indicating yield surface drift (after Potts & Gens, 1985)	41
3.5	Undrained triaxial stress path	57
3.6	Isotropic straining stress path	57
3.7	Explicit Euler-forward: Undrained compression simulation	58
3.8	Implicit Euler-backward: Undrained compression simulation	58
3.9	Implicit MNR: Undrained compression simulation	58
3.10	Explicit Euler-forward: Undrained extension simulation	59
3.11	Implicit Euler-backward: Undrained extension simulation	59
3.12	Implicit MNR: Undrained extension simulation	59
3.13	Explicit Euler-forward: Isotropic straining simulation	60
3.14	Implicit Euler-backward: Isotropic straining simulation	60
3.15	Implicit MNR: Isotropic straining simulation	60
3.16	Finite element mesh of the geometry around the footing	61
3.17	Comparison of displacement at point A	63
3.18	Comparison of stress paths at point B & C	64
3.19	S-CLAY1S yield surface	66
3.20	Stress paths in π -plane during isochoric monotonic loading	68
3.21	Stress paths for undrained extension E400 and E150 tests of Hong Kong Marine clay (data from Zhou <i>et al.</i> , 2006)	70
3.22	Deviator stress against axial strain in undrained extension test (data from Zhou <i>et al.</i> , 2006)	70
3.23	Comparison of original and modified S-CLAY1 simulations with triaxial test data S2aT4 (Messerklinger, 2006)	72
3.24	Effect of the shape of footing on the deviatoric plane	73
4.1	Yield surfaces of Sekiguchi-Ohta model	76

LIST OF FIGURES

4.2	The original Cam-clay yield and the constraint functions in principal stress space (Pipatpongsa <i>et al.</i> , 2009a)	76
4.3	Constraint and yield surfaces of Sekiguchi-Ohta model	77
4.4	Numerical simulation of constraint surface	78
4.5	Sekiguchi-Ohta model yield surface in triaxial stress space	79
4.6	Sekiguchi-Ohta model yield surface in principal stress space	83
4.7	Stress hovering along K_0 line during 1D consolidation (after Iizuka & Tachiabna, 2009)	83
4.8	Hybrid algorithm for the SO model implementation	84
4.9	Random movement of the MNR algorithm	87
4.10	Schematic view of Stolle’s implicit algorithm	90
4.11	Undrained triaxial compression	94
4.12	Undrained triaxial extension	94
4.13	Triaxial simulation	95
4.14	Triaxial compression simulation along K_0 -line	96
4.15	Sekiguchi-Ohta viscid model dry/wet side in principal stress space . .	101
4.16	Undrained simulation at different OCR values (after Takeyama <i>et al.</i> , 2005)	101
4.17	Sekiguchi-Ohta model viscid model in wet side alone	102
4.18	Comparison of effect of strain rate with Sekiguchi & Ohta (1977) results	103
4.19	Triaxial simulation at varying directions	104
4.20	Triaxial simulations to verify the dry side cut off	104
4.21	The geometry and mesh of the benchmark embankment	106
4.22	Time settlement curves at point A predicted by SO inviscid/viscid models	109
4.23	Surface settlement at the end of analysis predicted by SO inviscid/viscid models	109
4.24	Final horizontal displacement at the embankment toe predicted by SO inviscid/viscid models	110

LIST OF FIGURES

4.25 Excess PWP with time at point B predicted by SO inviscid/viscid models	110
5.1 The B-SCLAY1S model yield surface in triaxial stress space	115
5.2 Relative translation of the bubble surface along the vector \mathcal{U}	117
5.3 Diagram showing the position of maximum value of ℓ , ℓ_{max}	121
5.4 Schematic illustration of drift correction of bubble surface	129
5.5 A multi-stage triaxial test (after Al-Tabbaa (1987))	132
5.6 Schematic illustration of drift correction of bubble surface	140
5.7 Bubble surface intersection: elastic to plastic transition	142
6.1 Influence of bubble size R of Test B2 (McGinty, 2006) simulation, where $\eta_1 = 0$ and $\eta_2 = 0.70$	147
6.2 Influence of bubble size R of Test B6 (McGinty, 2006) simulation, where $\eta_1 = 0$ and $\eta_2 = -0.70$	148
6.3 Influence of hardening parameter ψ of Test B2 (McGinty, 2006) simulation, where $\eta_1 = 0$ and $\eta_2 = 0.70$	150
6.4 Influence of hardening parameter ψ of Test B6 (McGinty, 2006) simulation, where $\eta_1 = 0$ and $\eta_2 = -0.70$	151
6.5 Influence of intrinsic compression index λ_i of Test B2 (McGinty, 2006) simulation, where $\eta_1 = 0$ and $\eta_2 = 0.70$	154
6.6 Influence of intrinsic compression index λ_i of Test B6 (McGinty, 2006) simulation, where $\eta_1 = 0$ and $\eta_2 = -0.70$	155
6.7 Influence of swelling index κ of Test B2 (McGinty, 2006) simulation, where $\eta_1 = 0$ and $\eta_2 = 0.70$	156
6.8 Influence of swelling index κ of Test B6 (McGinty, 2006) simulation, where $\eta_1 = 0$ and $\eta_2 = -0.70$	157
6.9 Influence of Poisson's ratio ν' of Test B2 (McGinty, 2006) simulation, where $\eta_1 = 0$ and $\eta_2 = 0.70$	158
6.10 Influence of Poisson's ratio ν' of Test B6 (McGinty, 2006) simulation, where $\eta_1 = 0$ and $\eta_2 = -0.70$	159

LIST OF FIGURES

6.11 Influence of anisotropy parameter μ of Test B2 (McGinty, 2006) simulation, where $\eta_1 = 0$ and $\eta_2 = 0.70$ 161

6.12 Influence of anisotropy parameter μ of Test B6 (McGinty, 2006) simulation, where $\eta_1 = 0$ and $\eta_2 = -0.70$ 162

6.13 Influence of anisotropy parameter β of Test B2 (McGinty, 2006) simulation, where $\eta_1 = 0$ and $\eta_2 = 0.70$ 163

6.14 Influence of anisotropy parameter β of Test B6 (McGinty, 2006) simulation, where $\eta_1 = 0$ and $\eta_2 = -0.70$ 164

6.15 Influence of initial bonding χ_0 of Test B2 (McGinty, 2006) simulation, where $\eta_1 = 0$ and $\eta_2 = 0.70$ 166

6.16 Influence of initial bonding χ_0 of Test B6 (McGinty, 2006) simulation, where $\eta_1 = 0$ and $\eta_2 = -0.70$ 167

6.17 Influence of destructurational parameter a and b of Test B2 (McGinty, 2006) simulation, where $\eta_1 = 0$ and $\eta_2 = 0.70$ 168

6.18 Influence of destructurational parameter a and b of Test B6 (McGinty, 2006) simulation, where $\eta_1 = 0$ and $\eta_2 = -0.70$ 169

6.19 Initial location and size of the bubbles and bounding surfaces 171

6.20 $G - \gamma$ curves 171

6.21 Influence of $\kappa = 0.02$ 173

6.22 Influence of $\kappa = 0.03$ 173

6.23 Influence of $\kappa = 0.04$ 173

6.24 Influence of $R = 0.10$ 174

6.25 Influence of $R = 0.15$ 174

6.26 Influence of $R = 0.20$ 174

6.27 Influence of $\psi = 1.0$ 175

6.28 Influence of $\psi = 1.5$ 175

6.29 Influence of $\psi = 2.0$ 175

7.1 Undrained stress paths after isotropic stress history 179

7.2 Undrained stress paths after a one-dimensional stress history 180

7.3 Slow cyclic isotropic constant q triaxial simulation: η against ϵ_s 181

LIST OF FIGURES

7.4	Slow cyclic isotropic constant q triaxial simulation: η against ϵ_v . . .	182
7.5	Undrained stress paths after a one-dimensional stress history	183
7.6	B-SCLAY1 and MCC yield surfaces compared with test data (data after Messerklinger, 2006)	185
7.7	Model simulation and test results for compression test: S2T4 (data after Messerklinger, 2006)	186
7.8	Model simulation and test results for compression test: S2T4. Shear versus volumetric strain increment (data after Messerklinger, 2006) .	187
7.9	Model simulation and test results for compression test: S2cT1 (data after Messerklinger, 2006)	189
7.10	Model simulation and test results for isotropic compression test: S2cT1. Shear versus volumetric strain increment (data after Messerklinger, 2006)	190
7.11	Model simulation and test results for isotropic compression test: S2T3 (data after Messerklinger, 2006)	191
7.12	Model simulation and test results for isotropic compression test: S2T3. Shear versus volumetric strain increment (data after Messerklinger, 2006)	192
7.13	Model simulation and test results for extension test: S2aT4 (data after Messerklinger, 2006)	194
7.14	Model simulation and test results for extension test: S2T4. Shear versus volumetric strain increment (data after Messerklinger, 2006) .	195
7.15	B-SCLAY1S and S-CLAY1S simulations of Test C2 where $\eta_1 = 1.10$ and $\eta_2 = -0.50$	198
7.16	B-SCLAY1S and S-CLAY1S simulations of Test C6 where $\eta_1 = 0.20$ and $\eta_2 = 1.04$	199
7.17	B-SCLAY1S and S-CLAY1S simulations of Test C7 where $\eta_1 = 0.42$ and $\eta_2 = -0.70$	200
7.18	Comparison of time settlement curve at point A	202
7.19	Comparison of horizontal displacement predictions at the embankment toe for B-SCLAY1S and S-CLAY1S	203
7.20	Comparison of surface settlement curves at the end of analyses	203

LIST OF FIGURES

7.21 Comparison of excess PWP at the centreline of the embankment for B-SCLAY1S and S-CLAY1S	204
7.22 Pulse load time curve	205
7.23 Geometry for pile driving problem	206
7.24 Mesh used for pile driving problem	206
7.25 Pile settlement with time comparison for B-SCLAY1S and S-CLAY1S	207
7.26 Excess PWP with time comparison for B-SCLAY1S and S-CLAY1S .	208
F.1 The compression index of remoulded and natural soil	244
G.1 Influence of bubble size R of Test B7 (McGinty, 2006) simulation, where $\eta_1 = 0$ and $\eta_2 = 0$	248
G.2 Influence of hardening parameter ψ of Test B7 (McGinty, 2006) simulation, where $\eta_1 = 0$ and $\eta_2 = 0$	249
G.3 Influence of intrinsic compression index λ_i of Test B7 (McGinty, 2006) simulation, where $\eta_1 = 0$ and $\eta_2 = 0$	250
G.4 Influence of swelling index κ of Test B7 (McGinty, 2006) simulation, where $\eta_1 = 0$ and $\eta_2 = 0$	251
G.5 Influence of Poisson's ratio ν' of Test B7 (McGinty, 2006) simulation, where $\eta_1 = 0$ and $\eta_2 = 0$	252
G.6 Influence of anisotropy parameter μ of Test B7 (McGinty, 2006) simulation, where $\eta_1 = 0$ and $\eta_2 = 0$	253
G.7 Influence of anisotropy parameter β of Test B7 (McGinty, 2006) simulation, where $\eta_1 = 0$ and $\eta_2 = 0$	254
G.8 Influence of initial bonding χ_0 of Test B7 (McGinty, 2006) simulation, where $\eta_1 = 0$ and $\eta_2 = 0$	255
G.9 Influence of destructurational parameter a and b of Test B7 (McGinty, 2006) simulation, where $\eta_1 = 0$ and $\eta_2 = 0$	256

List of Tables

3.1	Material parameters of Bothkennar clay for S-CLAY1S	55
3.2	Time taken by different numerical algorithms	65
3.3	Material parameters of Hong Kong Marine clay for S-CLAY1	69
3.4	Material parameters of lacustrine clay (after Messerklinger, 2006) . . .	71
4.1	Comparison of the MNR and Stolle's algorithm	93
4.2	Material parameters used for the SO inviscid model verification	93
4.3	Material parameters used for the SO viscid model verification (Sekiguchi & Ohta, 1977)	103
4.4	Soil parameters of sand and peat layer	105
4.5	Material parameters of soft clay for SO inviscid & viscid models	107
5.1	Hierarchical of the B-SCLAY1S model	131
6.1	Material parameters of Bothkennar clay for B-SCLAY1S	145
7.1	Material parameters used by Al-Tabbaa (1987) for speswhite kaolin . .	178
7.2	Material parameters of lacustrine clay (data after Messerklinger, 2006)	184
7.3	Summary of stress paths used in simulation from test series C	196
F.1	Parameters required for the B-SCLAY1S model	243

List of Algorithms

1	: Intersection algorithm	40
2	: Drift algorithm	42
3	: Explicit algorithm for S-CLAY1S	43
4	: Calculation of plastic multiplier for explicit algorithm	44
5	: Calculation of plastic strains	44
6	: Update state variables	45
7	: Euler backward implicit algorithm for S-CLAY1S	47
8	: Calculation of plastic multiplier for implicit algorithm	48
9	: An automatic substepping scheme for MNR algorithm of S-CLAY1S	51
10	: MNR algorithm of S-CLAY1S	52
11	: MNR iteration scheme	53
12	: Algorithm to find best p' value	91
13	: Stolle implicit algorithm of the SO inviscid model	92
14	: An automatic sub-stepping scheme for the explicit algorithm of B-SCLAY1S	136
15	: Subroutine to identify active yield surface	137
16	: Explicit algorithm for B-SCLAY1S	138
17	: Update state variables	139
18	: Drift correction and bubble centre update	139

List of Notations

The main notations used in this thesis are given in this section. The notations are described in the relevant section too.

Roman Letters

a	absolute effectiveness of destructuration
b	relative effectiveness of plastic deviatoric strains on destructuration
c'	soil effective cohesion
e	initial void ratio
e_0	void ratio
D	Dilatancy
$[D^e]$	elastic stress constitutive matrix
$[D^{ep}]$	elasto-plastic stress constitutive matrix
E	Young modulus
F	Flow function
f_b	bubble surface function
f_y	yield function
$FTOL$	tolerance value
G	shear modulus
$(J_2)_\alpha$	modified second invariant to α -line
$(J_3)_\alpha$	modified third invariant to α -line
\bar{J}_2	modified second invariant to K_0 -line
K'	elastic bulk modulus
K'_w	bulk modulus of water
K_0	coefficient of earth pressure at rest
K_0^{nc}	coefficient of earth pressure at rest for normally consolidated soil
k_x	permeability in x-direction

k_y	permeability in y-direction
M	slope of critical state line
M_c	value of M in triaxial compression
M_e	value of M in triaxial extension
N	strain rate coefficient
p'	mean effective stress
p'_a	mean effective stress of bubble centre
p'_m	size of yield curve in p:q-space
p'_{mi}	size of intrinsic yield curve in p:q-space
$p'_{m,0}$	initial size of yield curve in p:q-space
p_y	plastic potential function
q	deviatoric stress
q_a	deviatoric stress of bubble centre
\bar{q}	modified deviatoric stress to K_0 -line
R	ratio of size of the bubble to bounding surface
$RTOL$	tolerance value
S	scalar quantity
t	time
t_0	initial time
Δt	change of time
u	pore water pressure
v	specific volume
\dot{v}_o	initial volumetric strain rate

Greek Symbols

α	scalar rotation of yield function
α_0	initial α value
α_{xx}	x-component of deviatoric fabric tensor
α_{yy}	y-component of deviatoric fabric tensor
α_{zz}	zz-component of deviatoric fabric tensor
α_{xy}	xy-component of deviatoric fabric tensor
α_{yz}	yz-component of deviatoric fabric tensor
α_{zx}	zx-component of deviatoric fabric tensor
$\underline{\alpha}_d$	deviatoric fabric tensor

β	relative effectiveness of plastic deviatoric strains on rotational hardening
C_α	coefficient of secondary consolidation
$\Delta\epsilon_p^e$	volumetric strain increment
$\Delta\Lambda$	plastic multiplier
$\Delta\Lambda_L$	lower surface plastic multiplier in the SO model
$\Delta\Lambda_U$	upper surface plastic multiplier in the SO model
$\underline{\epsilon}^e$	elastic strain vector
$\underline{\epsilon}^p$	plastic strain vector
ϵ_v^p	plastic volumetric strain
ϵ_v^{vp}	visco-plastic volumetric strain
$\Delta\epsilon_q^e$	triaxial elastic deviatoric strain increment
$\Delta\epsilon_v^e$	triaxial elastic volumetric strain increment
$\Delta\epsilon_q^p$	triaxial plastic deviatoric strain increment
$\Delta\epsilon_v^p$	triaxial plastic volumetric strain increment
γ'	effective unit weight of soil
Γ	scalar quantity
\mathcal{H}	hardening modulus
\mathcal{H}_0	isotropic hardening modulus
\mathcal{H}_α	anisotropic hardening modulus
\mathcal{H}_χ	destruction modulus
κ	slope of the swelling line
κ^*	modified swelling index
λ	slope of the normal compression line
λ^*	modified compression index
λ_i	slope of the normal intrinsic compression line
ℓ	distance of bubble surface to the bounding surface
ℓ_{max}	maximum distance of bubble surface to the bounding surface
\mathcal{U}	a vector
$\underline{\sigma}'$	effective stress vector
$\Delta\underline{\sigma}'$	effective stress increment vector
σ'	effective stress state
ν'	Poisson's ratio
Ω	scalar quantity
ω	apparent viscosity coefficient
ψ	exponent in the hardening function
η	stress ratio

η_c	stress ratio at normally consolidated state
η_{K_0}	stress ratio at K_0 state
η_0	initial stress ratio
θ	value of Lode angle
Θ	scalar quantity
χ	degree of bonding
χ_0	initial degree of bonding

Abbreviations

<i>CC</i>	Cam-clay model
<i>CSL</i>	critical state line
<i>IPP</i>	integration point program
<i>MCC</i>	modified Cam-clay model
<i>OCR</i>	over consolidation ratio
<i>POP</i>	pre-overburden pressure
<i>SO</i>	Sekiguchi-Ohta
<i>UDSM</i>	user defined soil model

Chapter 1

Introduction

Due to the growth of population in the cities geotechnical engineers have to design and construct infrastructures on soft soils. Due to the complexity of soft soil behaviour, engineers are using computational modelling techniques, such as the finite element method to solve engineering problems in practice. The accuracy of finite element analyses is dependent on several factors, one of which is the ability of the material model used in the finite element code to predict the stress-strain behaviour of the material. This creates greater need for accurate constitutive models, which account for complex behavior of soft soil such as anisotropy, destructuration and time dependency resulting from the nature of deposition, geological history and any subsequent processes.

In addition to developing accurate constitutive models, the robustness and efficiency of a finite element code also depends on the integration procedures used to implement the constitutive equations into a finite element package. In finite element calculations, strain increments for a given loading step are input to the constitutive driver, and the corresponding stress increments with constitutive behavior of material are returned to the main finite element code. The efficiency and accuracy of a finite element code may suffer if stress increments cannot be correctly calculated for given set of strain increments. Therefore, the numerical algorithms to integrate constitutive equations is a key component of constitutive model development.

The soft soils in the vicinity of structures such as railway tracks, at the vicinity of windmill foundations and offshore foundations that are exposed to cyclic loading may experience significant permanent plastic deformation. Standard critical state models cannot adequately simulate permanent plastic deformation and/or other important features with respect to the cyclic response when the loading history

remains inside the yield surface. In order to predict the cyclic response of soft soil correctly, a suitable constitutive model has to be used in the finite element analysis.

The original part of this research is the development of a new constitutive model which is applicable for cyclic behavior of soft soils. In parallel, improvements of an existing constitutive model in terms of a numerical procedure to integrate constitutive equations are made and the implementation of constitutive models into the PLAXIS finite element code is discussed.

1.1 Objectives

The aim of this research is to develop, improve and implement constitutive models in the PLAXIS finite element code to account for complex soft soil behavior under both monotonic and cyclic loading.

The main objectives are:

- To explore numerical methodologies for implementing advanced constitutive models of soft soil in PLAXIS to minimize the numerical instability and improve the numerical efficiency.
- To study the existing S-CLAY1S model which accounts for anisotropy and destructuration of soft soil, to further improve the model and to implement these improvements in PLAXIS using robust numerical algorithms.
- To develop numerical algorithms to solve the singularity problem of the Sekiguchi-Ohta models in order to implement the models in PLAXIS.
- To develop a mathematical formulation for cyclic behaviour of soft soil and implement the model in PLAXIS. This model, developed by author, is known as B-SCLAY1S, and forms the major original part of this research project.
- To verify and validate the constitutive models implemented in PLAXIS, and to apply them to a number of benchmark problems representing typical geotechnical applications.

1.2 Secondment

The author was seconded to PLAXIS B.V. (The Netherlands) for 9 months from November 2008 to August 2009 as part of the EC-funded Geo-Install Industry-Academia Pathways and Partnership (PIAG-GA-2009-230638) project. During this period, the author was supervised by Dr. Ronald Brinkgreve and Dr. Paul Bonnier, and given a task to implement the Sekiguchi-Ohta models (inviscid/viscid) in the commercial finite element code PLAXIS as a user defined soil model (UDSM). This secondment led to a breakthrough: a new implicit hybrid algorithm used to implement the models in PLAXIS which overcomes singularity of the Sekiguchi-Ohta models. The work was done in collaboration with Dr. Paul Bonnier. The proposed new algorithm and implementation in PLAXIS are detailed in Chapter 4.

1.3 Layout of Thesis

This thesis is divided into eight chapters. The outline of the work presented in this thesis is given below:

Chapter 2 incorporates a literature review of constitutive models which covers conventional constitutive models, advanced non-linear constitutive models, constitutive models for cyclic loading and other alternative approaches in soil modelling. The S-CLAY1S model (Wheeler *et al.*, 2003 and Karstunen *et al.*, 2005), the Bubble model (Al-Tabbaa, 1987 and Al-Tabbaa & Wood, 1989) and several soil models thought to be the most relevant for this work are reviewed and the main differences between them are discussed.

In **Chapter 3**, the mathematical formulation of the S-CLAY1S model is presented in detail. A modification to the model to account for the Lode angle dependency is proposed and discussed. The implementation of the modified S-CLAY1S model incorporating these modifications in PLAXIS is explained, as are the numerical algorithms used for the implementation. The inclusion of Lode angle dependency into the S-CLAY1S model is validated with published experimental data on natural marine clay. The implementation of the modified S-CLAY1S model in PLAXIS is verified by simulating benchmark tests with PLAXIS.

In **Chapter 4**, the Sekiguchi-Ohta (SO) (Sekiguchi & Ohta, 1977) model is presented, in its original formulation in triaxial stress space and general stress space. Discontinuity at the vertex of the model and the numerical difficulties encountered

in the stress derivatives of the yield surface are discussed. A novel hybrid implicit numerical algorithm is introduced to overcome the singularity of the model, which is presented and discussed. The implementation of the general formulation of the model into the PLAXIS finite element code and the verification of the model is also given in this chapter.

In **Chapter 5**, the new B-SCLAY1S model is explained in detail. The mathematical formulation of the model in triaxial stress space and general stress space is presented and discussed. Parameters determination of the B-SCLAY1S model is covered. A number of strategies are explored in order to reduce the numerical instability which occurs when implementing the model into PLAXIS.

In **Chapter 6**, a parametric study of the B-SCLAY1S model is carried out to investigate the relative importance and the effective range of each parameter of the model.

In **Chapter 7**, verification and application of the B-SCLAY1S model for benchmark tests is presented. The verification of the model implementation is carried out for an isotropic B-SCLAY1S model with the MCC bubble model (Al-Tabbaa, 1987) predictions. The benchmark problems used include the analysis of an embankment for static loading conditions and pile driving for cyclic loading conditions.

Chapter 8 presents a summary of the main findings of the study including conclusions and discussions, and gives recommendations for further research.

Chapter 2

Constitutive Models

This chapter presents a review of existing conventional and advanced constitutive models for static and cyclic behavior of clay. The review covers elastic models, elasto-plastic models, the critical state theory and classical critical state models, advanced critical state models, cyclic loading models and other alternative approaches in modelling soil behavior. The main features of the existing models are discussed together with their limitations.

2.1 Simple soil models

2.1.1 Elastic models

The simplest type of modelling of soil is the elastic model; the behavior of an elastic soil is described by Hooke's law. The elastic model has a 'one to one' stress strain relationship. Hence the stress is uniquely determined by strain. The parameters, Young's modulus (E') and Poisson's ratio (ν'), are needed to describe the response of isotropic homogeneous soil to a change of stress states in elasticity theory. The simple elastic constitutive models ignore important features of real soil behavior, such as high nonlinearity with both strength and stiffness depending on stress and strain level. Nonlinear elastic models give a substantial improvement in representing the shape of the stress strain curve. Two of the most common non-linear elastic models are the $K - G$ model or Barron-Sandler model (Naylor *et al.*, 1981) and the hyperbolic model (Kondner, 1963). Both models have simple hypoelastic (nonlinear but reversible) formulations in the elastic moduli which are functions of stress state

and model parameters. Nonlinear elastic models have several shortcomings, including 1) stress history and path dependency are not taken into account 2) it is not possible to model irrecoverable plastic strain along an unload-reload path 3) dilatant response during shearing violates the principles of thermodynamics and cannot be simulated within the framework of elasticity.

2.1.2 Elasto-plastic models

In elasto-plastic models, the behavior of soil is characterized by the existence of reversible and irreversible deformations called elastic and plastic deformations, respectively. A yield surface is adopted for soils to define where the response of soil changes from elastic to plastic. Stress changes inside a chosen yield surface produce an elastic response. As soon as the stresses touch the yield surface, a combination of elastic and plastic responses occurs.

In general, there are two types of elasto-plastic models; elastic-perfectly plastic models and hardening elastic-plastic models.

2.1.2.1 Elastic-perfectly plastic models

Elastic-perfect plasticity implies that the yield surface is fixed in the stress space and there is no hardening/softening law required. There is no expansion or contraction of the yield surface. Examples of elastic-perfectly plastic models are: Tresca (1864), von Mises (1913), Mohr-Coulomb (see e.g. Potts & Zdravkovic, 1999), Drucker & Prager (1952), Lade & Duncan (1975) and Matsuoka & Nakai (1974, 1982). Deformation prior to yielding is assumed to be linear elastic governed by the elastic parameters (E') and (ν'). The elastic-perfectly plastic models behave purely elastic until the yield surface. This does not represent the real soil behaviour.

2.1.2.2 Hardening elastic-plastic models

With hardening models, soil behavior is characterized by the existence of reversible (elastic) and irreversible (plastic) deformations combined with hardening/softening. The mathematical theory of elastic-plasticity is well established and has been the foundation for the development of many soil models. Various permutations and combinations of the yield functions, plastic potentials and hardening rules give rise to different models.

One of the major developments of constitutive models in the last 50 years is the introduction of models based on the critical state soil mechanics. This was started by Roscoe and his co-workers at the University of Cambridge in the late 1950s (Roscoe *et al.*, 1958, Roscoe & Poorooshasb, 1963, Roscoe *et al.*, 1963b, Roscoe & Schofield, 1963, Roscoe & Burland, 1968 and Schofield & Wroth, 1968). A brief review of critical state soil mechanics is presented in the next section.

2.2 Critical State Theory

The theory of soil behavior known as ‘critical state soil mechanics’ was developed from the application of the theory of plasticity to soil mechanics. The first critical state models were the series of Cam-clay formulations developed at the University of Cambridge by Roscoe and his co-workers. The formulation of the original Cam-clay (CC) model as an elastic-plastic constitutive law was presented by Roscoe & Schofield (1963), Roscoe *et al.* (1963b) and Schofield & Wroth (1968). Afterwards, Roscoe & Burland (1968) proposed the Modified Cam-clay (MCC) model.

The critical state concept is based on the consideration that, when a soil sample is sheared, it will eventually reach an ultimate or critical state at which plastic shearing can continue indefinitely without changes in volume or effective stresses. When the critical state is reached, critical states for a given soil form a unique line in $q - p' - v$ space referred to as the Critical State Line (CSL) where p' is the mean effective stress, q is the deviatoric stress and v is specific volume.

2.2.1 Original Cam-clay (CC) model

The original Cam-clay model was developed by Roscoe & Schofield (1963) assuming Drucker-Prager failure criterion. The Cam-clay models (original and modified) are essentially based on the assumption that changes in the size of the current yield surface are related to permanent changes in volume. The models permit the compression and shearing of clays to be simply combined and leads to a class of models of what can be called volumetric hardening models. All other assumptions stated in Section 2.1.2 for an elastic-plastic model are retained in the original and modified Cam-clay models.

The yield surface of original Cam clay model in triaxial stress space is expressed as follows:

$$\frac{q}{p'} = M \ln \frac{p'_m}{p'} \quad (2.1)$$

where p'_m is the preconsolidation pressure at hydrostatic axes and M is the stress ratio q/p' at critical state. The yield surface is plotted in Fig. (2.1). In the original Cam-clay model, it is assumed that plastic flow obeys an associated flow rule. The yield surface is assumed to expand with constant shape, and the size of the yield surface is assumed to be related to the changes in volume as follows:

$$\Delta \epsilon_v^p = \frac{\lambda - \kappa}{v} \frac{\Delta p'_m}{p'} \quad (2.2)$$

where $\Delta \epsilon_v^p$ is plastic volumetric strain increment, λ is the slope of the normal compression line and κ is the slope of the swelling line.

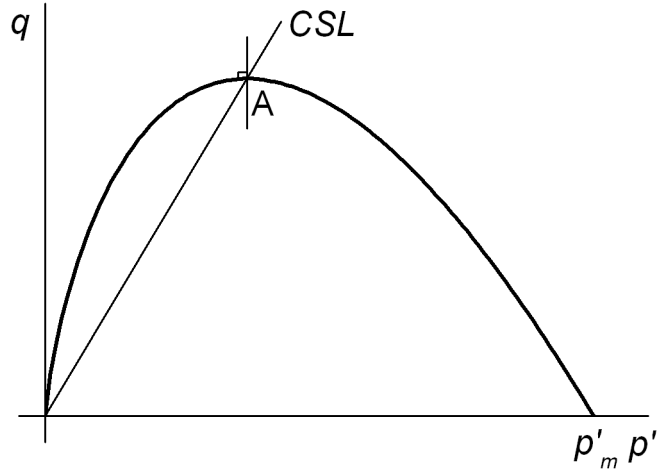


Figure 2.1: The original Cam clay (CC) model yield surface

2.2.2 Modified Cam-clay (MCC) model

The modified Cam-clay model was developed by Roscoe & Burland (1968) as a modification to the original Cam-clay model. This model successfully reproduces the major deformation characteristics of soft clay and is more widely used for numerical predictions than the original Cam-clay model. It has been used effectively in several

applications, and a summary of these applications can be found in Wroth & Houlsby (1985).

One of the main improvements of the modified Cam-clay model from the original Cam-clay model is the prediction of the coefficient of the earth pressure at rest $K_{0,nc}$ for one-dimensional normal compression. Furthermore, the discontinuity of the original Cam-clay yield surface at $q = 0$ causes difficulties because the associated flow rule will predict an infinite number of possible strain increment vectors for isotropic compression. This causes difficulty in finite element formulation. The modified Cam-clay model overcomes these problems by adopting an elliptical-shaped yield surface (see Fig. (2.2)) which has the following expression:

$$q^2 = M^2(p'p'_m - p'^2) \quad (2.3)$$

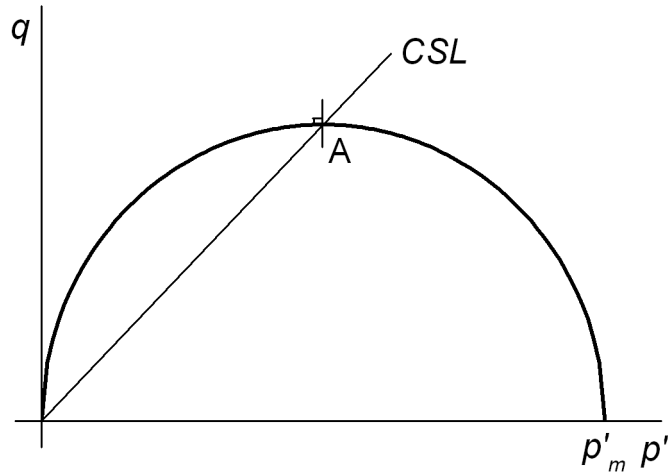


Figure 2.2: The modified Cam clay (MCC) model yield surface

The flow rule for modified Cam-clay model is assumed to be associated. The yield surface is assumed to expand with a constant shape and its size is controlled by the pressure (p'_m). The hardening relationship for modified Cam-clay is the same as the original Cam-clay model as follows:

$$\Delta \epsilon_p^p = \frac{\lambda - \kappa}{v} \frac{\Delta p'_m}{p'} \quad (2.4)$$

In both Cam-clay models, when the stress state reaches the crest of the yield surface (point A in Fig. (2.1) and (2.2)) unlimited plastic shear strains develop with

no plastic volumetric strain. At this point, shearing continues indefinitely without change in size of yield surface. This condition is known as a critical state.

2.2.3 Sekiguchi-Ohta (SO) model

The original Cam-clay model was developed based on isotropically consolidated samples. However, Sekiguchi & Ohta (1977) proposed a model for K_0 consolidated clays by changing a classical yield surface into another shape centered on the K_0 line. The new shape of the SO model accounts for the anisotropy developed during K_0 normally consolidation (i.e. consolidation under conditions of zero lateral strain), see Fig. (2.3). This model is called in the following chapters the SO inviscid (time-independent) model. Further to SO inviscid model, Sekiguchi & Ohta (1977) formulated a viscid formulation which describes consistently both anisotropy and time dependency. This model is called in the following chapters the SO viscid (time-dependent) model.

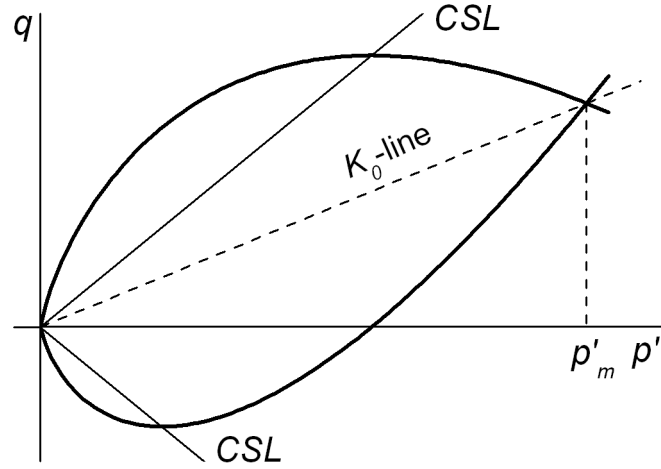


Figure 2.3: The Sekiguchi-Ohta (SO) model yield surface

2.2.3.1 SO inviscid model

Sekiguchi & Ohta (1977) introduced a new stress parameter, generalized stress ratio η^* . This is defined by:

$$\eta^* = \sqrt{\frac{3}{2}(\eta_{ij} - \eta_{ij0})(\eta_{ij} - \eta_{ij0})} \quad (2.5)$$

where

$$\eta_{ij} = \frac{s_{ij}}{p'}, \quad \eta_{ij0} = \frac{s_{ij0}}{p'_{m0}}$$

where s_{ij} is stress deviator and s_{ij0} is stress deviator at preconsolidation stress state.

The yield function of the SO inviscid model (see Fig. (4.5)) is expressed in the form:

$$f(\sigma', \epsilon_v^p) = MD \ln \frac{p'}{p'_{m,0}} + D\eta^* - \epsilon_v^p \quad (2.6)$$

where $p'_{m,0}$ is effective mean stress at the end of completion of anisotropic consolidation (typically K_0 consolidation), ϵ_v^p is volumetric plastic strain, M is slope of critical state line and D is a coefficient of dilatancy proposed by Shibata (1963), which can be defined as:

$$D = \frac{\lambda - \kappa}{M(1 + e_0)}$$

where e_0 is initial void ratio.

2.2.3.2 SO viscid model

The SO viscid model is a constitutive law formulation for anisotropically normally consolidated clay with volumetric creep. The flow equation of the viscid model is:

$$F = C_\alpha \ln \left\{ 1 + \frac{\dot{\epsilon}_0 t}{C_\alpha} \exp \left(\frac{f(\sigma')}{C_\alpha} \right) \right\} - \epsilon_v^{vp} \quad (2.7)$$

where C_α is the coefficient of secondary compression, t is the current time, $\dot{\epsilon}_0$ is the initial volumetric strain rate, ϵ_v^{vp} is the visco-plastic part of the volumetric strain and the $f(\sigma')$ is defined as:

$$f(\sigma') = MD \ln \frac{p'}{p'_m} + D\eta^*$$

where M is critical state parameter and D is a coefficient of dilatancy. A detailed description of the Sekiguchi-Ohta models is given in Chapter 4.

2.2.4 Shortcomings of the original, modified Cam clay and Sekiguchi-Ohta models

The above mentioned classical critical state soil models are known to be able to predict the behavior of normally and lightly overconsolidated clay reasonably well. However, there are several shortcomings which are summarized briefly below.

The original Cam-clay and Sekiguchi-Ohta models have a discontinuity in the yield surface which causes difficulties in numerical calculation for plastic strain increments. The flow rule will predict an infinite number of possible strain increments due to the vertex or singularity of the yield surface. However, this problem is eliminated with the modified Cam-clay model.

The original and modified Cam-clay models assume soils are isotropic but it is well known that soils are anisotropic due the mode of deposition. However, this problem is addressed with the Sekiguchi-Ohta model which assumes initial stress induced anisotropy.

The original and modified Cam clay models do not take into account the degradation of bonds during plastic straining of soil known as destructuration typical to natural clay and the time effects of soil known as creep. Though Sekiguchi-Ohta viscid model addresses the creep behavior of soil, it does not take into account destructuration of soil.

The modelling of soil under cyclic loading is another shortcoming of the above mentioned classical critical state soil models. The essential features of the models are that on primary loading large plastic strains occur but on subsequent unload reload cycles within the yield surface only purely elastic strains are produced. However in reality, all unload reload cycles result in the gradual accumulation of permanent strain and/or pore pressure generation and the occurrence of hysteretic behaviour.

2.3 Advanced critical state models

In order to achieve better agreement between predicted and observed soil behavior, a large number of modifications have been proposed to the classical critical state soil models. The following sections discuss the most important advanced critical state models in relation to this thesis, such as S-CLAY1, S-CLAY1S and EVP-SCLAY1S models.

2.3.1 S-CLAY1 model

The S-CLAY1 model was founded on ideas by Wheeler (1997) and was subsequently modified to its current form by Wheeler *et al.* (1999) and Wheeler *et al.* (2003). The model is an extension of conventional critical state models, with anisotropy of plastic behavior represented through an inclined yield surface and a rotational component of hardening to represent the development or erasure of fabric anisotropy during plastic straining. In generalised formulation of S-CLAY1, the use of stress invariants is no longer possible due to the evolution of anisotropy in the model.

For the simplified conditions of a triaxial stress space, the S-CLAY1 yield function (f_y) identical to that suggested by Dafalias (1986a) and Korhonen & Lojander (1987) can be expressed in terms of the mean effective stress p' and deviator q :

$$f_y = (q - \alpha p')^2 + (M^2 - \alpha^2) (p'_m - p')p' = 0 \quad (2.8)$$

where M is the slope of the critical state line, p'_m defines the size of the yield curve and α defines the orientation of the yield curve, see Fig. (2.4). The scalar parameter α is a measure of the degree of plastic anisotropy of the soil. With $\alpha = 0$ the soil behavior is isotropic and Eq. 2.8 corresponds to the yield curve in the conventional modified Cam-clay model.

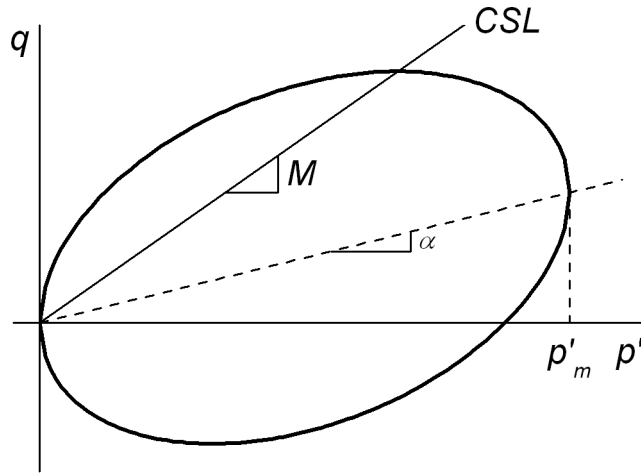


Figure 2.4: The S-CLAY1 yield surface in triaxial stress space

The rotational hardening law describes the changes in the orientation of the yield surface with plastic straining. In triaxial stress space, the hardening law takes

the following form:

$$d\alpha = \mu \left(\left[\frac{3\eta}{4} - \alpha \right] \langle d\epsilon_v^p \rangle + \beta \left[\frac{\eta}{3} - \alpha \right] |d\epsilon_d^p| \right) \quad (2.9)$$

where $d\epsilon_d^p$ is the increment of plastic deviatoric strain, and μ and β are two additional soil constants. The soil constant β controls the relative effectiveness of plastic shear strains and plastic volumetric strains in setting the overall instantaneous target value for α (which will lie between $\frac{3\eta}{4}$ and $\frac{\eta}{3}$), whereas the soil constant μ controls the absolute rate of rotation of the yield surface towards its current target value of α . $\langle \cdot \rangle$ are Macaulay brackets and $\langle \Delta\epsilon_v^p \rangle = \Delta\epsilon_v^p$ for $\Delta\epsilon_v^p > 0$ and $\langle \Delta\epsilon_v^p \rangle = 0$ for $\Delta\epsilon_v^p < 0$. $||$ is a norm (of deviatoric plastic strain).

2.3.2 S-CLAY1S model

The S-CLAY1S model, developed by Koskinen *et al.* (2002a,b) and Karstunen *et al.* (2005), is an extension of the S-CLAY1 model incorporating the influence of bonding and destructuration.

In triaxial stress space, the yield curve of the S-CLAY1S model can be expressed similarly to S-CLAY1 by Eq.2.8. The natural and intrinsic yield surface of the S-CLAY1S model is shown in Fig. (2.5).

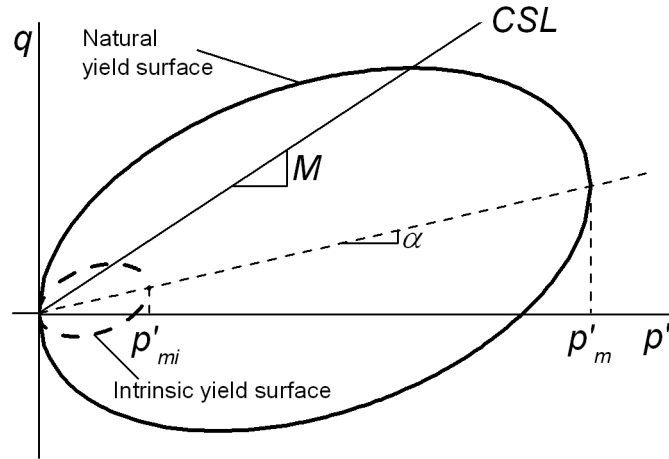


Figure 2.5: The S-CLAY1S yield surface in triaxial stress space

The effect of the bonding is introduced by the intrinsic and natural yield surfaces (Gens & Nova, 1993). The intrinsic yield surface is of smaller size but same

orientation as the yield curve of the natural soil. The size of the intrinsic yield surface is defined by the state variable p'_{mi} which is linked to the size of the natural yield by:

$$p'_m = (1 + \chi)p'_{mi} \quad (2.10)$$

where χ defines the amount of bonding. The degradation of bonding with plastic straining (the destructuration law) is given by Eq.2.11 with a and b are two additional soil constants controlling the the rate of degradation. A detailed description of the S-CLAY1S model is given in Chapter 3.

$$d\chi = -a\chi (|d\epsilon_v^p| + b|d\epsilon_d^p|) \quad (2.11)$$

2.3.3 EVP-SCLAY1S model

The EVP-SCLAY1S model is a new visco-plastic model developed by Karstunen & Yin (2010). The EVP-SCLAY1S model framework is developed based on the S-CLAY1S model (Karstunen *et al.*, 2005) and Perzyna's overstress theory (Perzyna, 1966a). The elastic behavior of the model is assumed to be isotropic and the visco-plastic strain rate, $\dot{\epsilon}^{vp}$, is defined by Eq.2.12 following the original proposal by Perzyna (1966a). The model obeys the associated flow rule with respect to the dynamic loading surface.

$$\dot{\epsilon}^{vp} = \omega \langle \Phi(F) \rangle \frac{\partial f_d}{\partial \sigma'_{ij}} \quad (2.12)$$

where ω is the apparent viscosity coefficient, $\Phi(F)$ is the overstress function representing the ratio of dynamic loading surface and static yield surface, see Fig. (2.6) and $\langle \rangle$ are Macaulay brackets and $\langle \Phi(F) \rangle = \Phi(F)$ for $\Phi(F) > 0$ and $\langle \Phi(F) \rangle = 0$ for $\Phi(F) < 0$. $\Phi(F)$ is defined as:

$$\Phi(F) = \exp \left[N \left(\frac{p_m^d}{p_m^s} - 1 \right) \right] - 1 \quad (2.13)$$

where N is strain-rate coefficient.

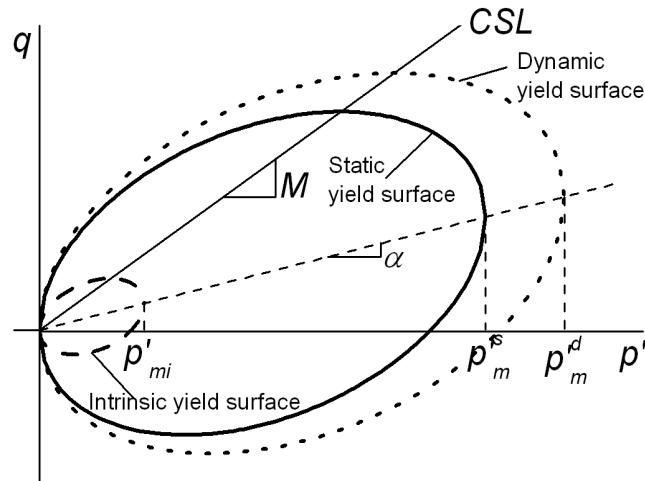


Figure 2.6: The EVP-SCLAY1S yield surface in triaxial stress space

2.3.4 Shortcomings of advanced critical state models

Though the advanced models such as S-CLAY1S (Karstunen *et al.*, 2005) and EVP-SCLAY1S (Karstunen & Yin, 2010) models capture the most important aspects of natural soil behaviour for normally consolidated and lightly over-consolidated soils, modelling of soil under cyclic loading is a shortcoming of the above mentioned advanced critical state soil models. The essential features of the models are that on primary loading large plastic strain occurs but on subsequent unload reload cycles within the yield surface only purely elastic strains are produced, see Fig. (2.7). However, typical response (Muir Wood, 1990) show that all unload reload cycles results in the gradual accumulation of permanent strain and/or pore pressure and hysteretic behavior occurs as shown in Fig. (2.8).

The critical state models were discussed so far assumes an approximately linear elastic behaviour for over-consolidated clays within the state boundary surface. However, pre-failure behaviour of over-consolidated clays is highly non-linear and inelastic from the very early stages of loading. Generally soil yielding occurs at very small strains i.e. less than 0.001% (Atkinson & Sallfors, 1991). Fig. 2.9 shows the typical strain ranges experienced under a variety of geotechnical structures; and with the increasing strains, soil stiffness decays non-linearly (Atkinson & Sallfors, 1991) where normalised shear modulus (G/G_0) is used to express the non-linear behaviour of strain-dependent modulus of soil. Experimental $G - \gamma$ curves have been presented

2.3 Advanced critical state models

by many researchers (e.g. Atkinson & Sallfors, 1991; Mair, 1993; Ishihara, 1996 and White *et al.*, 2001).

Various approaches suggested to account for cyclic behaviour and the non-linearity within the yield surface will be discussed in the following section.

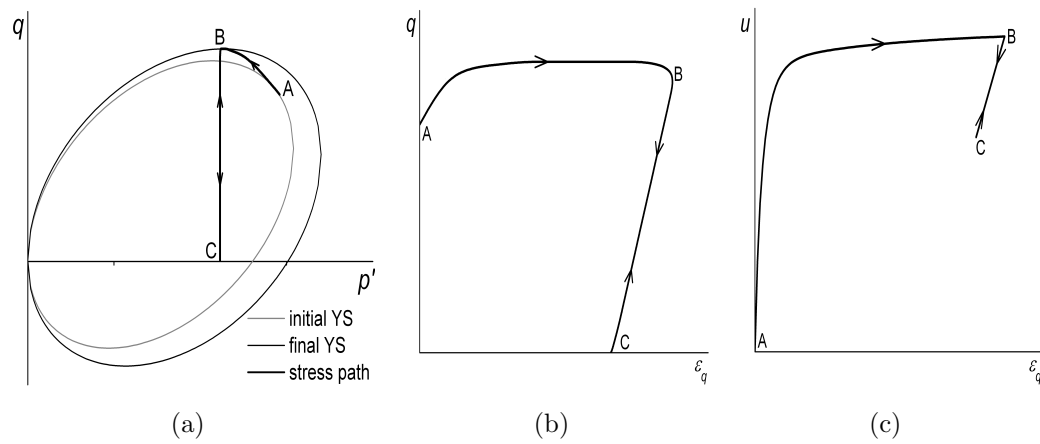


Figure 2.7: The S-CLAY1S model response: (a) effective stress path, (b) stress-strain response and (c) pore pressure-strain response

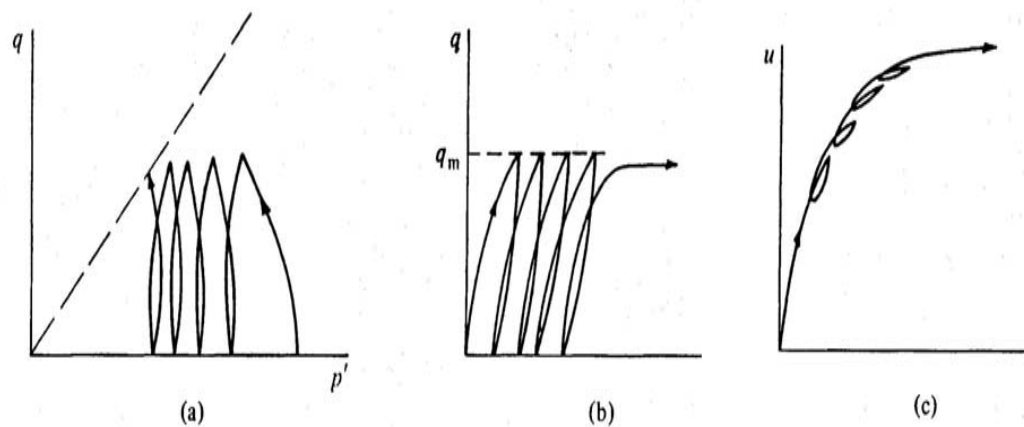


Figure 2.8: Typical response: (a) effective stress path, (b) stress-strain response and (c) pore pressure-strain response (Muir Wood, 1990)

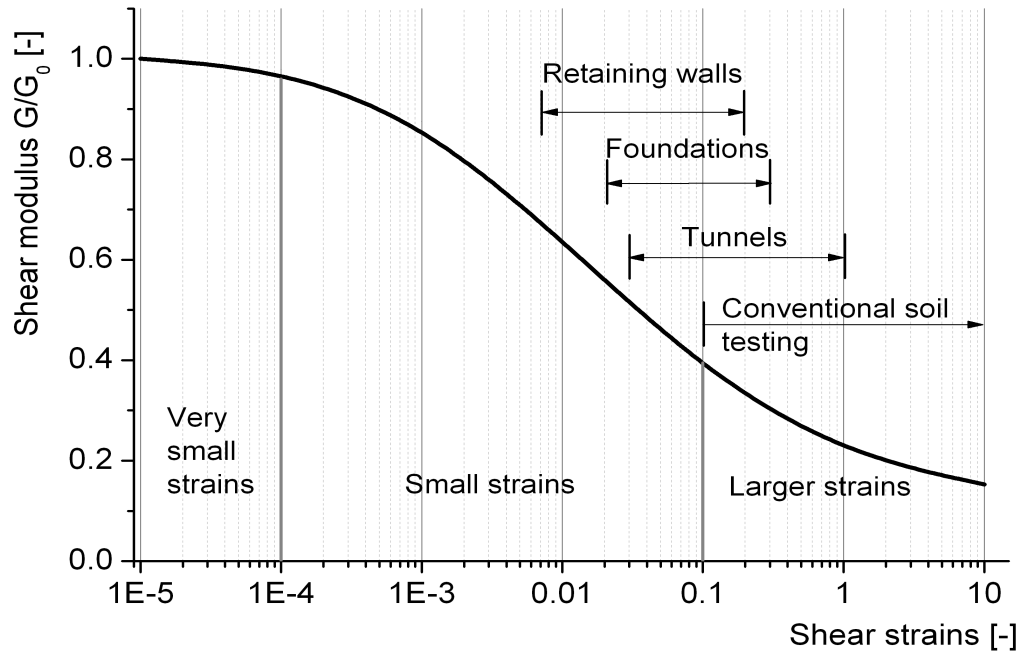


Figure 2.9: Characteristics stiffness-strain behaviour of soil with typical strain ranges (after Atkinson & Salfors, 1991)

2.4 Cyclic loading models

Various models have been developed for cyclic loading since Iwan (1967) and Mróz (1967) independently formulated the first kinematic hardening model for metals which was later applied to soils by Prévost (1977, 1978). Mróz *et al.* (1979) described a two-surface kinematic hardening model which has a kinematic yield surface inside the consolidation surface. Carter *et al.* (1982) developed a simple way of modeling cyclic loading behaviour using the critical state soil model by reducing the size of the yield surface in an isotropic manner on unloading. Pender (1982) proposed a cyclic loading model based on the Critical State Soil Mechanics framework. Ghaboussi & Momen (1982) proposed a cyclic model for sand using isotropic and kinematic hardening for the yield surface. Nova (1982) described a model, which is suitable for both granular material and clay.

The following subsections brief the most important cyclic loading models in relation to this research, such as the bounding surface model, the MIT-E3 model,

the subloading surface model and the bubble surface model, developed for improved predictions of cyclic behaviour of clay.

2.4.1 Bounding surface model

The concept of bounding surface was first proposed by Dafalias & Popov (1975) and Krieg (1975) independently for modeling cyclic behavior of metals. Since the introduction of bounding surface plasticity, a variety of plasticity constitutive models (Dafalias & Herrmann (1982); Aboim & Roth (1982); McVay & Taesiri (1985); Bardet (1986); Whittle (1993b) and Yu & Khong (1993)) have been developed. The key features of bounding surface plasticity models are that plastic deformation may occur when stress states lie inside the yield surface, and a smooth transition from high to low stiffness is achieved during plastic deformation.

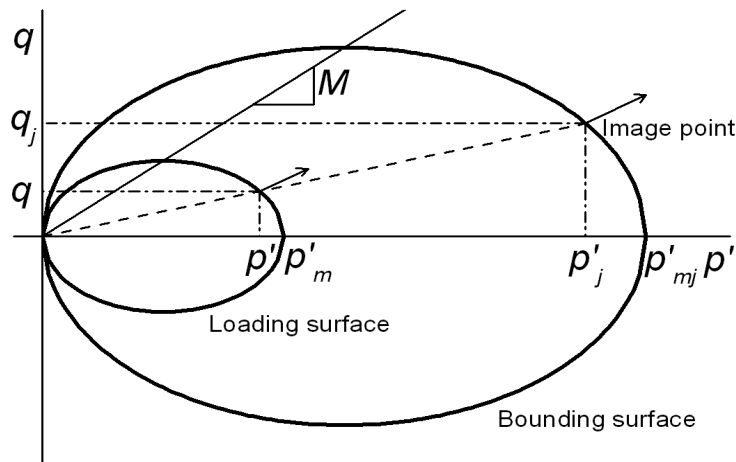


Figure 2.10: Sketch of bounding surface model in triaxial stress space

The sketch of a typical bounding surface and loading surface of bounding surface plasticity in triaxial stress space is shown in Fig. (2.10). The plastic modulus depends upon the distance between the current state of stress and a corresponding stress (image stress) on the bounding line. The stress state does not have to satisfy the consistency condition, which allows the generation of irreversible strain with simpler isotropic hardening. The disadvantage of this bounding surface type models is the unrealistic ratcheting behaviour for small unload-reload cycles.

2.4.2 MIT-E3 model

The MIT-E3 model has been developed at the Massachusetts Institute of Technology (MIT) (Whittle, 1993a and Whittle & Kavvadas, 1994). The model incorporates three key aspects of the behavior of clay:

- anisotropy and strain hardening/softening behavior,
- small strain non-linearity and hysteretic response in unloading and reloading,
- bounding surface plasticity for irrecoverable, anisotropic and path dependent behavior of moderately overconsolidated clays ($OCR < 8$).

The MIT-E3 model has an inclined yield function, which is an elliptical MCC yield surface (see Fig. (2.11)), written in the form:

$$f_y = (q - p'.b)^2 - M^2 p'(p'_m - p) = 0 \quad (2.14)$$

where b defines the inclination of yield surface and M is the ratio of the semi-axes of the ellipsoid, which is slightly different from the critical state definition. The failure criterion is defined by an anisotropic conical surface as follows:

$$h = (q - p'.\xi)^2 - k^2 p'^2 = 0 \quad (2.15)$$

where h describes the boundaries of the critical state cone in compression and extension. ξ defines the symmetry axis of cone and constant k is the half range of critical state cone, see Fig. (2.11).

The MIT-E3 model requires a large number of soil parameters (15 parameters), some of which are not easily obtainable using routine geotechnical testing (Potts & Zdravkovic, 1999). Because of this, to date, its use has been mainly limited to the research and development environment.

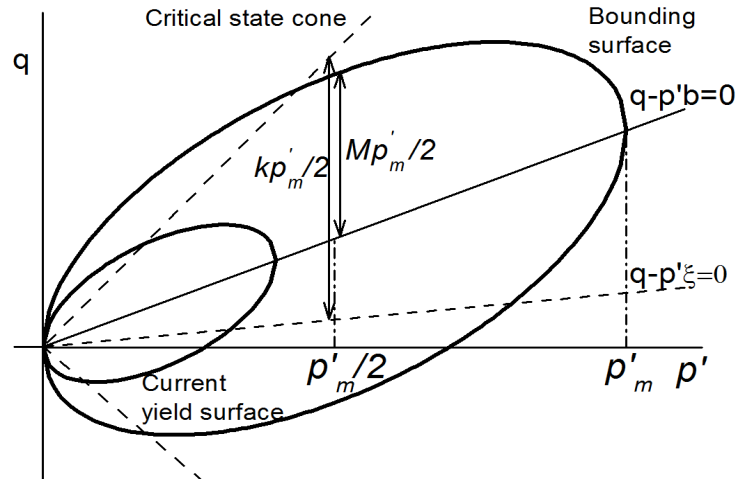


Figure 2.11: Sketch of MIT-E3 model in triaxial stress space

2.4.3 Subloading surface model

The subloading surface model (Hashiguchi, 1980, 1989) possesses the following features:

- interior of the yield surface is not purely elastic domain but plastic deformation is induced during loading/reloading;
- smooth transition between normally consolidated and over-consolidated states;
- strain hardening behaviour with positive dilatancy.

In subloading surface theory, the conventional yield surface is renamed as the normal-yield surface and the subloading surface which is similar to normal-yield surface, lies in a position of similarity and represents the same orientation, see Fig. (2.12). The subloading surface expands/contracts within the normal-yield surface passing through a current stress point during the loading and unloading process. The plastic strain rate depends on the ratio of the size of the subloading surface to that of the normal-yield surface, so that it is used to capture the cyclic loading behavior of clays. The limitation of the model when applied to cyclic loading is that elastic behavior is predicted during unloading until the stress state reaches the similarity-center, which does not corresponds to the real behavior of soils.

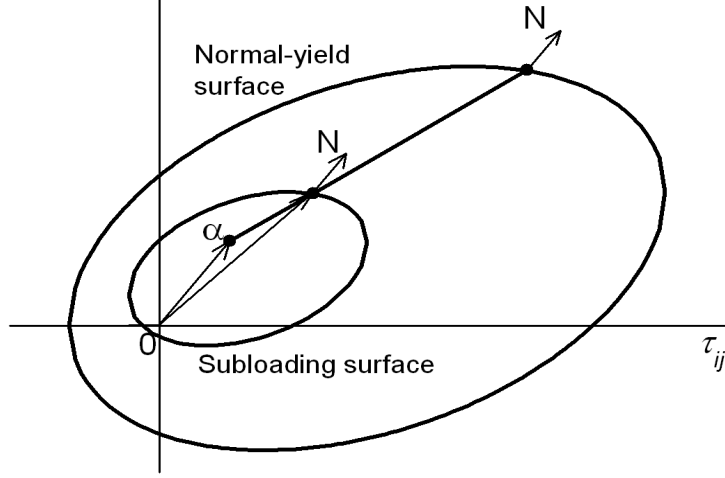


Figure 2.12: Subloading surface model in triaxial stress space

2.4.4 Bubble surface model

The original ‘bubble’ model was proposed and formulated in triaxial stress space under the framework of critical state soil mechanics by Al-Tabbaa (1987) and Al-Tabbaa & Wood (1989). The bubble model is similar to the two-surface model proposed by Mróz *et al.* (1979). The outer surface of the bubble model, called the bounding surface, is the same as the modified Cam-clay surface, which is centered on the p' axis and passes through the origin but does not intersect the q axis. The inner surface is called the ‘bubble’, which encloses the elastic region. The bubble surface has the same shape as the modified Cam-clay surface (bounding surface). The ratio of size between the bubble surface and the bounding surface is a constant expressed by the parameter ‘ R ’. The two surfaces are illustrated in Fig. (2.13).

The bounding f_y and bubble f_b surface functions in triaxial stress space are given as follows:

$$f_y = \frac{(q)^2}{M^2} + \left(p' - \frac{p'_m}{2}\right)^2 - \left(\frac{p'_m}{2}\right)^2 = 0 \quad (2.16)$$

$$f_b = \frac{[q - q_b]^2}{M^2} + (p' - p'_b)^2 - R^2 \left(\frac{p'_m}{2}\right)^2 = 0 \quad (2.17)$$

where p'_b and q_b are centre of bubble surface and R is the ratio of the size of the bubble surface to that of the bounding surface, see Fig. 2.13.

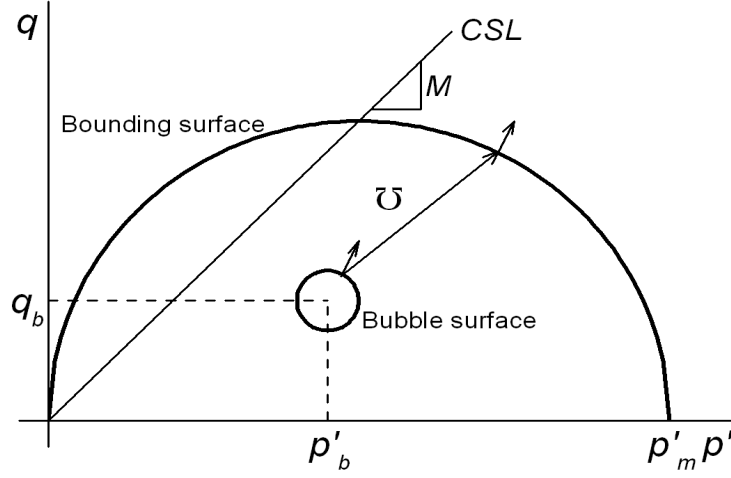


Figure 2.13: Bubble surface model in triaxial stress space (after Al-Tabbaa, 1987)

The kinematic hardening rule of the bubble is given:

$$\begin{Bmatrix} dp'_b \\ dq_b \end{Bmatrix} = \frac{dp'_m}{p'_m} \begin{Bmatrix} p'_b \\ q_b \end{Bmatrix} + S \begin{Bmatrix} \frac{p'-p'_b}{R} - (p' - p'_m) \\ \frac{q-q_b}{R} - q \end{Bmatrix} \quad (2.18)$$

where S is a scalar quantity.

The kinematic hardening rule is similar to the translation rule proposed by Hashiguchi (1985). The translation rule of the bubble has to guarantee that the bubble and the bounding surface can touch at a common normal, but must never intersect. A conjugate point on the bounding surface can be associated with the current stress point on the bubble in such a way that these two points have the same direction of outward normal. Translation of the bubble, which occurs when plastic strains are being generated, can be separated into two components. One part is associated with change in size of the surfaces (the first term of Eq. 2.18), the other part is associated with translation of the bubble along the vector \mathcal{U} (the second term of Eq. 2.18).

The hardening function is given by:

$$h = h_0 + H \quad (2.19)$$

where h_0 is the plastic modulus when the bubble and the bounding surface are in contact corresponding to the current stress point. H is a scalar quantity to ensure

a smooth fall of stiffness when the bubble approaches the bounding surface. h_0 and H are given by equations 2.20 and 2.21 respectively.

$$h_o = \frac{p' - p'_b}{\lambda^* - \kappa^*} \left[p'(p' - p'_b) + \frac{q(q - q_b)}{M^2} \right] \quad (2.20)$$

$$H = \frac{1}{\lambda^* - \kappa^*} \left(\frac{\ell}{\ell_{max}} \right)^\psi \left(\frac{p'_m}{2} \right)^3 \quad (2.21)$$

where ℓ and ℓ_{max} are given by:

$$\ell = \frac{1}{R \frac{p'_m}{2}} \left[(p' - p'_b) \left[\frac{p' - p'_b}{R} - \left(p' - \frac{p'_m}{2} \right) \right] + \frac{q - q_b}{M^2} \left(\frac{q - q_b}{R} - q \right) \right] \quad (2.22)$$

$$\ell_{max} = p'_m(1 - R) \quad \text{for } M \leq 1 \quad (2.23a)$$

$$\ell_{max} = p'_m M(1 - R) \quad \text{for } M > 1 \quad (2.23b)$$

It should be noted that in Eq. 2.22, ℓ_{max} only depends on the size of the surfaces. A modification was made by Muir Wood (1995) so that ℓ_{max} also depends on the current stress state. In fact many other functions of H can be chosen as long as they can ensure a smooth reduction of stiffness. Al-Tabbaa & Wood (1989) reported that the transition of stiffness as the effective stress path leaves the elastic region on reaching the edge of the bubble is too abrupt, but this can be improved by altering the hardening function H .

The original bubble model was enhanced for structured soil by Muir Wood (1995) and Muir Wood & Rouainia (2000). The process of destructuration is modelled by introducing another surface called the ‘reference’ surface (basically it is an intrinsic surface) and the bounding surface is renamed the ‘structure’ surface, see Fig. (2.14). The bubble surface has the same shape as the reference and structure surfaces, and their sizes are represented by Rp'_m , p'_m and rp'_m respectively. r represents the size of the structure surface determined by exponential destructuration law in the following form:

$$r = 1 + (r_0 - 1) \exp \left(\frac{-k\epsilon_{ds}}{\lambda - \kappa} \right) \quad (2.24)$$

where r_0 describes the initial size of the structure surface (not less than 1); k is a parameter controlling the rate of destructuration with strain. ϵ_{ds} is the destructuration strain and rate of destructuration strain can be given as follows.

$$\delta r = \frac{-k}{\lambda - \kappa} (r - 1) \delta \epsilon_{ds} \quad (2.25)$$

where $\delta \epsilon_{ds}$ can be calculated from:

$$\delta \epsilon_{ds} = \sqrt{(1 - A)(\delta \epsilon_p^p)^2 + A(\delta \epsilon_q^p)^2} \quad (2.26)$$

where A is a parameter controlling contribution of volumetric and distortional strains to destructuration ranging from 0 to 1.

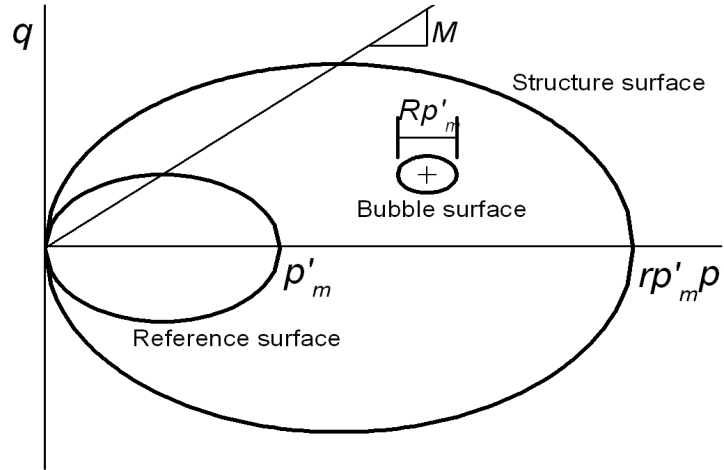


Figure 2.14: Bubble model for structured soil (Muir Wood, 1995)

Some of the advances/limitations of the bubble model are:

- The bubble model can simulate small-strain behaviour of soils; non-linearity starts from the early stage of loading.
- Depending on the position of bubble surface relative to the bounding surface, the bubble model predicts anisotropic yielding and stiffness but isotropic strength.
- The bubble model predicts hysteretic behaviour and accumulation of plastic strains during cyclic loading and unloading. This is important for the modelling of cyclic behaviour of soils.

- The bubble model cannot simulate inherent anisotropy and the evolution of anisotropy of natural soil behaviour.

2.5 Other alternative approaches in soil models

In order to achieve better agreement between the predicted and observed soil behavior, a large number of approaches have been proposed as an alternative to traditional elasto-plasticity theory. A brief summary of some of the most important approaches such as hyperplasticity, hypoplasticity, multilaminate and disturbed state concept are discussed below.

2.5.1 Hyperplasticity model

As an alternative to conventional plasticity theory, which may violate the law of thermodynamics, Collins & Housby (1997) proposed an approach to model soil behavior called 'hyperplasticity' theory based on Ziegler's concept (Ziegler, 1983). A constitutive model in hyperplasticity theory is completely defined by two scalar potential functions: (i) an energy function and (ii) a dissipation function (yield function) (Housby & Puzrin, 1999 and Housby & Puzrin, 2006). The hyperplasticity model has been further developed into a rate-dependant model (Housby & Puzrin, 2002) from two scalar potential functions; instead of a dissipation potential function, force potential and flow potential functions are used to model rate-dependant plasticity.

Although hyperplasticity theory obeys the laws of thermodynamics, for simple models this approach may not offer significant advantages over conventional plasticity (Housby, 1981). Because of this, hyperplasticity models are not generally used.

2.5.2 Hypoplasticity model

Hypoplastic models were first developed by Kolymbas (1987, 1988) and Chambon & Desrues (1985) independently for granular materials. Gudehus (1996) and von Wolffersdorff (1996) include the critical state concept into modelling hypoplasticity. Further, granular hypoplastic models were extended to clays by Gudehus (2004) and Herle & Kolymbas (2004) for rate-dependent and rate-independent behaviour,

2.5 Other alternative approaches in soil models

respectively. Recently, Mašin (2005, 2007) proposed a hypoplastic model suitable for description of clay behaviour, which is combined with the critical state soil mechanics.

Hypoplastic models are incrementally non-linear constitutive models. The hypoplastic constitutive model is more complex than the classical plasticity model, but is primarily applicable to granular materials. In classical plasticity, the plastic strain rate depends only on the stress state whereas in hypoplasticity it depends on the stress state and on the stress rate direction (Dafalias, 1986b). It is worth noting hypoplasticity has no thermodynamics basis and fundamentally it ignores the law of thermodynamics. The disadvantage of hypoplasticity models is that many parameters are required and they are not easily determined by laboratory tests.

2.5.3 Multilaminate model

The basic feature of the multilaminate framework is to consider various integration planes to formulate the stress strain relationship, see Fig. (2.15). In contrast to the classical plasticity theory, flow and hardening rules are formulated on the planes rather than in three dimensional stress space. The multilaminate framework was presented for rocks by Zienkiewicz & Pande (1977) and extended to soils by Pande & Sharma (1983) and Pietruszczak & Pande (1987). Schuller (2000) introduced within the multilaminate framework a strain-softening formulation to capture the post peak behavior of soil. More recently, the multilaminate model was further developed within the framework of induced and inherent anisotropy of soils (Schweiger *et al.*, 2009). The disadvantages of the multilaminate modelling are:

- difficulties in defining inherent anisotropy.
- expensive computational effort require to store all possible state parameters for each individual sampling plane.
- there is no global equivalent to the yield function and the definition in the plane is rather arbitrary.

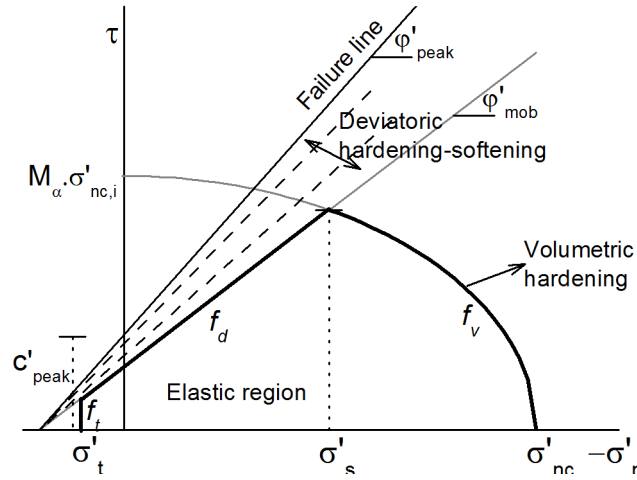


Figure 2.15: Yield curve and failure criterion on a sampling plane (Schuller & Schweiger, 2002)

2.5.4 Disturbed state concept model

The initial idea of disturbed state concept (DSC) was proposed by Desai (1974). The disturbed state concept (DSC) for deforming material is assumed to be a mixture of two constituent parts, the relative intact (RI) and fully adjusted (FA) states, see Fig. (2.16). The DSC based constitutive modelling includes elastic, plastic and creep deformations, microcracking, damage and softening, stiffening and cyclic fatigue under thermomechanical loading (Desai & Zhang, 1998). According to DSC, external excitation from mechanical, environmental and thermal forces causes the transformation of the microstructure of the materials from the RI state to the FA state at randomly disturbed locations. Microstructural transformation causes particle reorientation and relative motions. This disturbance can be expressed as a combination of individual contributions from RI and FA parts by using disturbance (D) as a coupling mechanism. The advantages of the DSC are:

- free from mesh dependence due to the coupling mechanism within its framework (Desai, 2001).
- the DSC models are “significantly simplified, involve fewer parameters and easier to implement in computer procedures”, Carter *et al.* (2000).
- the DSC can be applied to modelling geomaterials, interfaces and joints (Carter *et al.*, 2000)

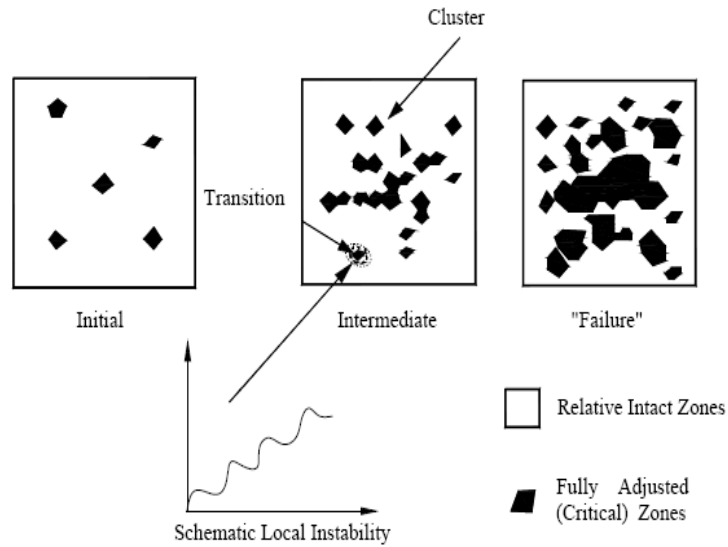


Figure 2.16: Schematic of relative intact and fully adjusted clusters in DSC (Desai & Toth, 1996)

2.6 Summary

In this chapter, the constitutive models in relation to this thesis were described. The chapter started with introducing the simple elasto-plastic models and critical state theory including Cam-clay models and Sekiguchi-Ohta models. Then the advanced constitutive models such as S-CLAY1S and cyclic loading models such as the bubble surface model are presented. Finally some alternative approaches in constitutive modelling have been introduced. Summary of constitutive models discussed in this chapter is given in Fig. 2.17. **Chapters 3, 4 and 5** discuss in more detail the constitutive models S-CLAY1S, Sekiguchi-Ohta and the bubble surface model, respectively.

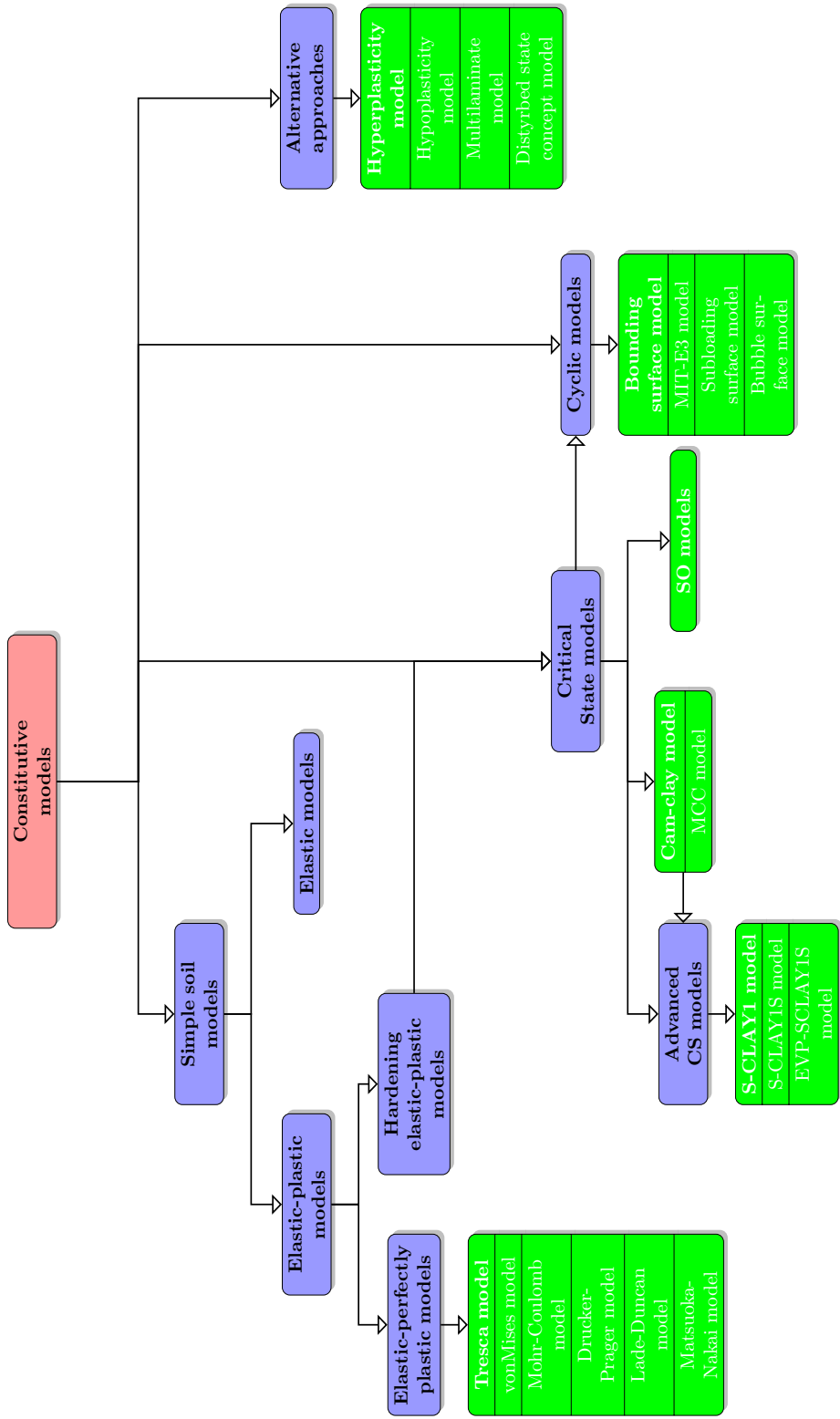


Figure 2.17: Summary of constitutive models discussed in this chapter

Chapter 3

Further improvement and implementation of S-CLAY1S model

This chapter discusses further development and implementation of the S-CLAY1S model as a user defined soil model (UDSM) into the PLAXIS finite element program. It summarizes the mathematical formulation of S-CLAY1S model in general stress space. The implementation of the S-CLAY1S model incorporating these modifications in PLAXIS is explained, as are the numerical algorithms used for the implementation. Modification to the model in relation to Lode angle dependency is proposed and discussed. The inclusion of Lode angle dependency into the S-CLAY1S model is validated with published experimental data on natural marine clay. The implementation of the modified S-CLAY1S model in PLAXIS is verified through benchmark tests in PLAXIS.

3.1 Mathematical formulation in general stress space

The S-CLAY1S model, which was developed by Karstunen *et al.* (2005), is an extension to the earlier model S-CLAY1 (Wheeler *et al.*, 2003) incorporating the influence of bonding and destructuration. This section describes the mathematical formulation of the S-CLAY1S model in general stress space which is necessary in order to

3.1 Mathematical formulation in general stress space

implement the model into the PLAXIS finite element program. The generalization of the model was given by Wiltafsky (2003).

3.1.1 Elastic behaviour

The elastic behavior of the S-CLAY1S model is the same as in the critical state Cam-clay type models. The elastic bulk modulus, K' , and the elastic shear modulus, G , are defined by the following expressions (see e.g. Potts & Zdravkovic, 1999 and Muir Wood, 2004):

$$K' = \frac{1+e}{\kappa} p' \quad (3.1)$$

$$G = \frac{3(1-2\nu')}{2(1+\nu')} \frac{1+e}{\kappa} p' \quad (3.2)$$

where κ is the slope of swelling line, p' is mean effective stress, e is the current void ratio and ν' is the Poisson's ratio. The elastic stiffness matrix, $[D^e]$, can be expressed in terms of the elastic shear modulus (G) as follows (see e.g. Potts & Zdravkovic, 1999 and Muir Wood, 2004):

$$[D^e] = \begin{bmatrix} 2G \frac{1-\nu'}{1-2\nu'} & 2G \frac{\nu'}{1-2\nu'} & 2G \frac{\nu'}{1-2\nu'} & 0 & 0 & 0 \\ 2G \frac{\nu'}{1-2\nu'} & 2G \frac{1-\nu'}{1-2\nu'} & 2G \frac{\nu'}{1-2\nu'} & 0 & 0 & 0 \\ 2G \frac{\nu'}{1-2\nu'} & 2G \frac{\nu'}{1-2\nu'} & 2G \frac{1-\nu'}{1-2\nu'} & 0 & 0 & 0 \\ 0 & 0 & 0 & G & 0 & 0 \\ 0 & 0 & 0 & 0 & G & 0 \\ 0 & 0 & 0 & 0 & 0 & G \end{bmatrix} \quad (3.3)$$

3.1.2 Yield function

The yield surface of the S-CLAY1S model can be expressed in the general stress space as follows:

$$f_y = \frac{3}{2} \frac{\{\underline{\sigma}'_d - \alpha_d p'\}^T \{\underline{\sigma}'_d - \alpha_d p'\}}{M^2 - \alpha^2} + \left(p' - \frac{p'_m}{2}\right)^2 - \left(\frac{p'_m}{2}\right)^2 = 0 \quad (3.4)$$

3.1 Mathematical formulation in general stress space

In the above equation $\underline{\sigma}'_d$ and $\underline{\alpha}_d$ are the deviatoric stress vector and the deviatoric fabric vector respectively (see Appendix A for definitions). $\{\}$ represents vector. M is the value of the stress ratio $\eta = q/p'$ at critical states, p'_m defines the size of the yield surface and α defines the orientation of yield surface, see Fig. (3.1). The scalar parameter α is a measure of the degree of anisotropy of the soils, with $\alpha = 0$, the soil behavior is isotropic and the yield surface corresponds to the modified Cam-clay model. For simplicity it can be written as $\underline{s} = \underline{\sigma}'_d - \underline{\alpha}_d p'$ and yield surface becomes:

$$f_y = \frac{3}{2} \frac{\{\underline{s}\}^T \{\underline{s}\}}{M^2 - \alpha^2} + \left(p' - \frac{p'_m}{2}\right)^2 - \left(\frac{p'_m}{2}\right)^2 = 0 \quad (3.5)$$

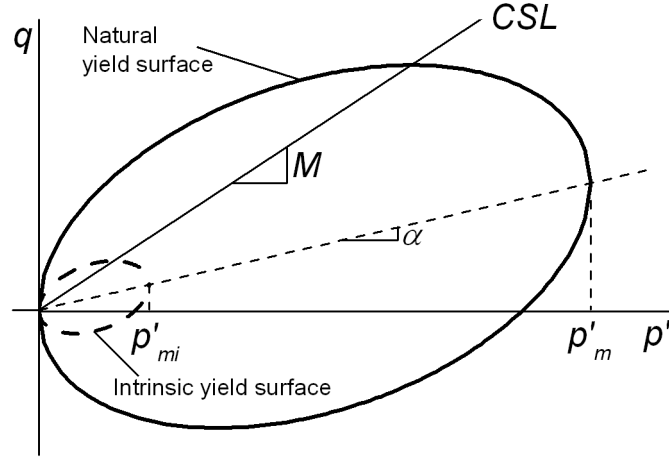


Figure 3.1: The S-CLAY1S yield surface in triaxial stress space

The intrinsic yield surface (Gens & Nova, 1993) has the same shape and orientation as the yield surface of the natural (bonded) soil but is smaller in size, and represents the yielding behaviour of an equivalent unbonded soil. The size of the intrinsic yield surface is described by p'_{mi} , and this is related to the size of the yield surface for the bonded soil by a parameter χ which determines the current degree of bonding as follows:

$$p'_m = (1 + \chi)p'_{mi} \quad (3.6)$$

The S-CLAY1S model incorporates a Drucker-Prager failure criterion, which was one of the earliest proposed failure criteria. The Drucker-Prager failure criterion assumes circular shape in the π -plane as shown in Fig. (3.2). The π -plane is

3.1 Mathematical formulation in general stress space

a plane perpendicular to the p' -axis ($\sigma'_1 = \sigma'_2 = \sigma'_3$). In the context of S-CLAY1S, due to the effect of anisotropy, the axis of symmetry of the failure surface does not coincide with the hydrostatic axis.

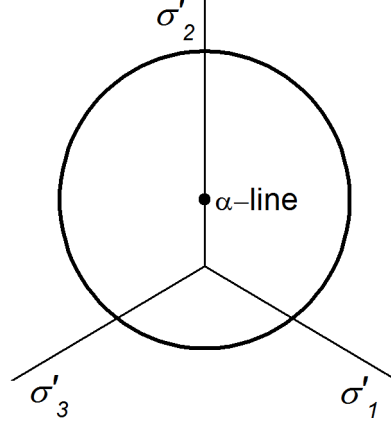


Figure 3.2: The Drucker-Prager failure surface in the π -plane

3.1.3 Flow rule

The assumption of an associated flow rule is a reasonable approximation of a natural clay when combined with an inclined yield surface (Wheeler *et al.*, 2003, Karstunen & Koskinen, 2008). Therefore, the S-CLAY1S model assumes an associated flow rule so that the yield surface given in Eq. 3.5 serves as a plastic potential function as follows:

$$p_y = \frac{3}{2} \frac{\{\underline{s}\}^T \{\underline{s}\}}{M^2 - \alpha^2} + \left(p' - \frac{p'_m}{2}\right)^2 - \left(\frac{p'_m}{2}\right)^2 = 0 \quad (3.7)$$

The increment of plastic strain is determined using the plastic multiplier $\Delta\Lambda$ as:

$$\Delta \underline{\epsilon}^p = \Delta\Lambda \frac{\partial p_y}{\partial \underline{\sigma}'} \quad (3.8)$$

3.1.4 Hardening rule

The S-CLAY1S model incorporates three hardening laws. The first of the hardening laws relates to the change in size of the intrinsic yield surface, which is assumed

3.1 Mathematical formulation in general stress space

to be related solely to plastic volumetric strain ($d\epsilon_v^p$) (Karstunen *et al.*, 2005) as follows:

$$\Delta p'_{mi} = \frac{(1+e)p'_{mi}}{\lambda_i - \kappa} \Delta \epsilon_v^p \quad (3.9)$$

where λ_i is the slope of the intrinsic normal compression line for a reconstituted soil and κ is the slope of the elastic (pre-yield) swelling line in the $v : \ln p'$ plane (specific volume : $v = 1 + e$). It is worth noting that when the parameter χ relates to Eq. 3.6 is set to zero and the S-CLAY1S model becomes the S-CLAY1 model (without destructuration), and the first hardening law relates to the yield surface as in the modified Cam-clay model as follows:

$$\Delta p'_m = \frac{(1+e)p'_m}{\lambda - \kappa} \Delta \epsilon_v^p \quad (3.10)$$

where λ is the slope of the post-yield compression line in the $v : \ln p'$ plane.

The second hardening law is called the ‘rotational hardening law’ (Wheeler *et al.*, 2003) and describes the change of the orientation of the yield surface with plastic straining. The rotational hardening law in general stress space is:

$$\Delta \underline{\alpha}_d = \mu \left(\left[\frac{3\underline{\sigma}'_d}{4p'} - \underline{\alpha}_d \right] \langle \Delta \epsilon_v^p \rangle + \beta \left[\frac{\underline{\sigma}'_d}{3p'} - \underline{\alpha}_d \right] \Delta \epsilon_d^p \right) \quad (3.11)$$

where μ and β are soil constants: where μ governs the absolute rate at which $\underline{\alpha}_d$ changes with plastic straining and β governs the relative effectiveness of volumetric and deviatoric strains in the rotation of yield surface. $\langle \rangle$ are Macaulay brackets and $\langle \Delta \epsilon_v^p \rangle = \Delta \epsilon_v^p$ for $\Delta \epsilon_v^p > 0$ and $\langle \Delta \epsilon_v^p \rangle = 0$ for $\Delta \epsilon_v^p < 0$.

The third hardening law (Karstunen *et al.*, 2005) relates the degradation of bonding with plastic straining is given as:

$$\Delta \chi = -a\chi \left[|\Delta \epsilon_v^p| + b |\Delta \epsilon_d^p| \right] \quad (3.12)$$

where a and b are soil constants controlling the rate of degradation.

3.1.5 Hardening modulus

The hardening modulus is formulated by incorporating three hardening moduli which include anisotropy and destructuration. The first hardening modulus (stan-

standard modulus), \mathcal{H}_0 , relates to isotropic hardening similar to the modified Cam-clay (MCC) hardening modulus. The second hardening modulus (anisotropic modulus), \mathcal{H}_α , relates to the rotation of the inclined yield surface. The third hardening modulus (destruction modulus), \mathcal{H}_χ , relates to the degradation of bonding. The hardening modulus of the S-CLAY1S model can be expressed as:

$$\mathcal{H} = \mathcal{H}_0 + \mathcal{H}_\alpha + \mathcal{H}_\chi \quad (3.13)$$

The standard hardening modulus (\mathcal{H}_0) is as follows:

$$\mathcal{H}_0 = -p'(1 + \chi)p'_{mi} \frac{1 + e}{\lambda_i - \kappa} \frac{\partial p_y}{\partial p'} \quad (3.14)$$

The anisotropic hardening modulus (\mathcal{H}_α) as follows:

$$\mathcal{H}_\alpha = \left\{ \frac{\partial f_y}{\partial \alpha_d} \right\}^T \left[\left\{ \frac{\partial \alpha_d}{\partial \epsilon_v^p} \right\} \left\langle \frac{\partial p_y}{\partial p'} \right\rangle + \left\{ \frac{\partial \alpha_d}{\partial \epsilon_d^p} \right\} \sqrt{\frac{3}{2} \left\{ \frac{\partial p_y}{\partial \sigma'_d} \right\}^T \left\{ \frac{\partial p_y}{\partial \sigma'_d} \right\}} \right] \quad (3.15)$$

The destruction hardening modulus (\mathcal{H}_χ) as follows:

$$\mathcal{H}_\chi = \frac{\partial f_y}{\partial \chi} \left[\frac{\partial \chi}{\partial \epsilon_v^p} \left| \frac{\partial p_y}{\partial p'} \right| + \frac{\partial \chi}{\partial \epsilon_d^p} \sqrt{\frac{3}{2} \left\{ \frac{\partial p_y}{\partial \sigma'_d} \right\}^T \left\{ \frac{\partial p_y}{\partial \sigma'_d} \right\}} \right] \quad (3.16)$$

The derivatives of each components in the above equations are given in Appendix B.

3.2 Numerical implementation

To carry out a non-linear finite element analysis using the S-CLAY1S model, it is necessary to compute the elastic-plastic matrix, $[D^{ep}]$ relating an increment of strain to an increment of stress:

$$\{\Delta \underline{\sigma}'\} = [D^{ep}] \{\Delta \underline{\epsilon}\} \quad (3.17)$$

where $\{\Delta \underline{\epsilon}\}$ is defined in Appendix A.

The definition of the yield surface places some restrictions on the stresses, i.e. stresses can lie within the yield surface (elasticity) or on the surface itself. Stresses

cannot, however, exist outside the surface. This is described mathematically as the consistency condition (\dot{f}_y) and is given for the S-CLAY1S yield surface as follows:

$$\dot{f}_y = \frac{\partial f_y}{\partial \underline{\sigma}'} \Delta \underline{\sigma}' + \frac{\partial f_y}{\partial p'_m} \Delta p'_m + \frac{\partial f_y}{\partial \underline{\alpha}} \Delta \underline{\alpha} + \frac{\partial f_y}{\partial \chi} \Delta \chi = 0 \quad (3.18)$$

By using standard manipulation, the expression for the elastic-plastic matrix, $[D^{ep}]$, can be obtained as:

$$[D^{ep}] = [D^e] - \frac{[D^e] \begin{bmatrix} \frac{\partial p_y}{\partial \underline{\sigma}'} \end{bmatrix} \begin{bmatrix} \frac{\partial f_y}{\partial \underline{\sigma}'} \end{bmatrix}^T [D^e]}{\begin{bmatrix} \frac{\partial f_y}{\partial \underline{\sigma}'} \end{bmatrix}^T [D^e] \begin{bmatrix} \frac{\partial p_y}{\partial \underline{\sigma}'} \end{bmatrix} + \mathcal{H}_0 + \mathcal{H}_\alpha + \mathcal{H}_\chi} \quad (3.19)$$

where $[D^e]$ is the elastic stiffness matrix and \mathcal{H}_0 , \mathcal{H}_α and \mathcal{H}_χ are hardening moduli.

Combining Equations 3.17 and 3.19 results in the expression for the change of stress relating to an increment of strain which is given as:

$$\{\Delta \underline{\sigma}'\} = \left[[D^e] - \frac{[D^e] \begin{bmatrix} \frac{\partial p_y}{\partial \underline{\sigma}'} \end{bmatrix} \begin{bmatrix} \frac{\partial f_y}{\partial \underline{\sigma}'} \end{bmatrix}^T [D^e]}{\begin{bmatrix} \frac{\partial f_y}{\partial \underline{\sigma}'} \end{bmatrix}^T [D^e] \begin{bmatrix} \frac{\partial p_y}{\partial \underline{\sigma}'} \end{bmatrix} + \mathcal{H}_0 + \mathcal{H}_\alpha + \mathcal{H}_\chi} \right] \{\Delta \underline{\epsilon}\} \quad (3.20)$$

The above equation can be further written as follows

$$\{\Delta \underline{\sigma}'\} = \{\Delta \underline{\sigma}'\}^e - \Delta \Lambda [D^e] \frac{\partial p_y}{\partial \underline{\sigma}'} \quad (3.21)$$

where the plastic multiplier $\Delta \Lambda$ is given by

$$\Delta \Lambda = \left[\frac{\begin{bmatrix} \frac{\partial f_y}{\partial \underline{\sigma}'} \end{bmatrix}^T [D^e] \{\Delta \underline{\epsilon}\}}{\begin{bmatrix} \frac{\partial f_y}{\partial \underline{\sigma}'} \end{bmatrix}^T [D^e] \begin{bmatrix} \frac{\partial p_y}{\partial \underline{\sigma}'} \end{bmatrix} + \mathcal{H}_0 + \mathcal{H}_\alpha + \mathcal{H}_\chi} \right] \quad (3.22)$$

The terms $\partial f_y / \partial \underline{\sigma}'$ and $\partial p_y / \partial \underline{\sigma}'$ needed for the calculation of plastic multiplier $\Delta \Lambda$ in Eq. 3.22 can be obtained from the following equations:

$$\frac{\partial f_y}{\partial \underline{\sigma}'} = \frac{\partial f_y}{\partial p'} \frac{\partial p'}{\partial \underline{\sigma}'} + \frac{\partial f_y}{\partial \underline{s}} \frac{\partial \underline{s}}{\partial \underline{\sigma}'} \quad (3.23)$$

$$\frac{\partial p_y}{\partial \underline{\sigma}'} = \frac{\partial p_y}{\partial p'} \frac{\partial p'}{\partial \underline{\sigma}'} + \frac{\partial p_y}{\partial \underline{s}} \frac{\partial \underline{s}}{\partial \underline{\sigma}'} \quad (3.24)$$

When a strain increment produces an elastic stress state outside the yield surface, a plastic flow occurs. The plastic flow requires stress integration of Eq. 3.21. Numerical integration techniques such as the forward (explicit) and backward (implicit) Euler method and the modified Newton-Raphson (implicit) method provide approximations for these integrations. Since the integration is an approximation, it is very important to choose the correct numerical integration techniques to minimize resulting integration error.

3.2.1 Euler forward (explicit) method

Constitutive equations are most straightforward to formulate in classical explicit (Euler forward) integration schemes, but their accuracy depends significantly on the given step size. The stress update which employs the Forward Euler method is performed stepwise by using the previous elasto-plastic stiffness matrix as shown in Eq. 3.19. If the calculation steps are set relatively large, the computational error is accumulated on the result. Therefore the stress may not be on the yield surface in the elasto-plastic state at the current time. In order to minimize this problem, a sub-stepping explicit numerical algorithm, yield intersection from elastic to plastic algorithm and correction of yield drift algorithm are used. Before discussing the sub-stepping explicit algorithm, it is important to briefly discuss the yield surface intersection algorithm and the correction for drift algorithm.

If plasticity is associated with a given strain increment, the incremental stress-strain constitutive relationship is written as:

$$\{\underline{\sigma}'_{n+1}\} = \{\underline{\sigma}'_n\} + [D_n^{ep}] \{\Delta \underline{\epsilon}\} \quad (3.25)$$

It is necessary to locate the yield surface intersection when an elastic trial stress goes from the purely elastic state, $f_y(\underline{\sigma}'_0, \mathcal{H}) < 0$, to elastic-plastic state, $f_y(\underline{\sigma}'_0 + \Delta \underline{\sigma}'^e, \mathcal{H}) > 0$, during a load increment (see Fig. 3.3), where $\underline{\sigma}'_0$ is an initial stress vector and $\Delta \underline{\sigma}'^e$ is an elastic trial stress increment vector. Therefore, the proportion of the strain increment (scalar quantity Ω) that only causes elastic behaviour can be found by solving the following nonlinear equation:

$$f_y(\underline{\sigma}'_0 + \Omega \Delta \underline{\sigma}'^e, \mathcal{H}) = f_y(\underline{\sigma}'_{int}, \mathcal{H}) = 0 \quad (3.26)$$

where $\underline{\sigma}'_{int} = \underline{\sigma}'_0 + \Omega \Delta \underline{\sigma}'^e$.

The above equation can be solved by using the Pegasus intersection scheme (Sloan *et al.*, 2001). Once the scalar quantity Ω ($0 \leq \Omega \leq 1$) is determined, the portion of the strain increment which causes plastic deformation can be found. The exact yield condition $f_y(\underline{\sigma}'_{int}, \mathcal{H}_0) = 0$ is replaced by the approximation $f_y(\underline{\sigma}'_{int}, \mathcal{H}_0) \leq FTOL$, where $FTOL$ is the tolerance value and is a small positive value. A suitable value for tolerance $FTOL$ is typically in the range of 10^{-6} to 10^{-9} (Sloan *et al.*, 2001). In the S-CLAY1S model numerical implementation, $FTOL$ is assumed to be 10^{-7} . The advantage of the Pegasus algorithm over the Newton-Raphson and Scant algorithm that it is unconditionally convergent and does not require the use of derivatives (see Sloan *et al.*, 2001 for details). A summary of the intersection algorithm using the Pegasus scheme is given in Algorithm 1.

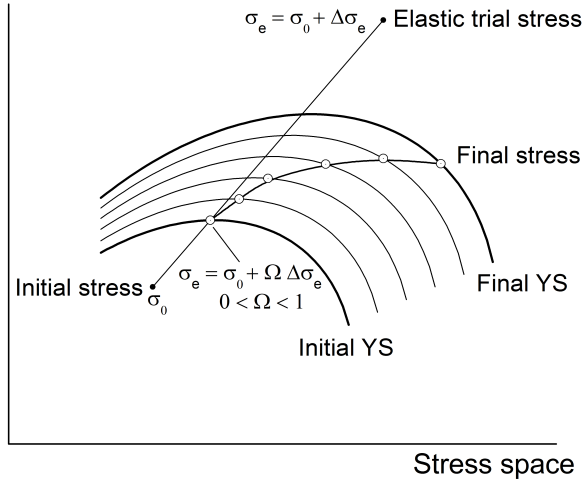


Figure 3.3: Explicit stress update with substepping (after Yu, 2006)

In the explicit integration scheme, the stresses may diverge from the yield surface at the end of each sub-increment. This is commonly known as yield surface ‘drift’ and depends on the accuracy of the integration scheme and the non-linearity of the constitutive equations. Potts & Gens (1985) examined five methods to account for this drift. These involve correcting the stresses by projecting back along the plastic flow, the total strain increment, reducing second variant and constant p' and the accumulated effective stress direction. In addition, a method called ‘correct method’, which accounts for changes in elastic strains that accompany any stress correction is considered. Potts & Gens (1985) concluded from this investigation that projecting back along the plastic flow direction gives sufficiently accurate predictions. The stresses are, however, projected back to the yield surface $f_y(\underline{\sigma}'_c, \mathcal{H}_B)$ as shown

Algorithm 1 : Intersection algorithm

```

if  $f_y(\underline{\sigma}', \mathcal{H}_0) * f_y(\underline{\sigma}' + \Delta\underline{\sigma}'^e, \mathcal{H}_0) < 0$  then

    REQUIRE: Initial values of  $\Omega_0$  and  $\Omega_1$ 

    SET:  $f_y^0 = f_y(\underline{\sigma}' + \Omega_0 \Delta\underline{\sigma}'^e, \mathcal{H}_0)$  and  $f_y^1 = f_y(\underline{\sigma}' + \Omega_1 \Delta\underline{\sigma}'^e, \mathcal{H}_0)$ 

    for ( Iteration = 1, MaxIts ) do
         $\Omega = \Omega_1 - f_y^1 * \frac{\Omega_1 - \Omega_0}{f_y^1 - f_y^0}$ 

        Calculate new yield function
         $f_y^{new} = f_y(\underline{\sigma}' + \Omega \Delta\underline{\sigma}'^e, \mathcal{H}_0)$ 

        if  $f_y^{new} < FTOL$  then
            return  $\Omega$ 
        end if

        if  $f_y^{new} * f_y^0 < 0$  then
            SET:  $\Omega_1 = \Omega$  and  $f_y^1 = f_y^{new}$ 
        else
            SET:  $f_y^1 = \frac{f_y^1 f_y^0}{f_y^0 + f_y^{new}}$ 
            SET:  $\Omega_0 = \Omega$  and  $f_y^0 = f_y^{new}$ 
        end if
    end for

    return  $\Omega$ 
end if

```

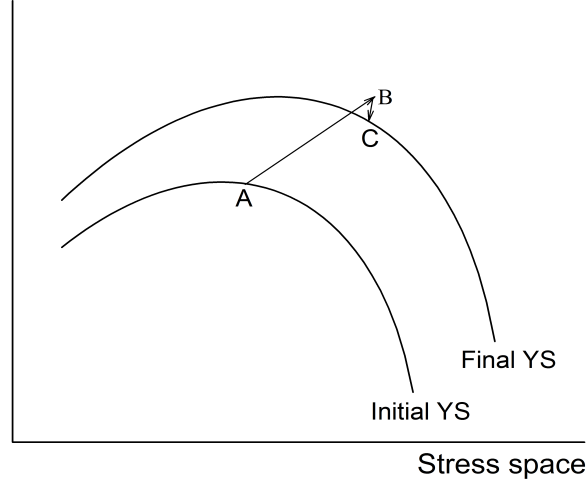


Figure 3.4: Sketch indicating yield surface drift (after Potts & Gens, 1985)

in Fig.3.4 along the plastic flow direction and \mathcal{H}_C set is equal to \mathcal{H}_B . The corrected stresses can be written as follows:

$$\underline{\sigma}'_C = \underline{\sigma}'_B - \Theta \frac{\partial p_y}{\partial \underline{\sigma}'} \quad (3.27)$$

The corrected stresses must satisfy the yield condition:

$$f_y(\underline{\sigma}'_C, \mathcal{H}_C) = f_y\left(\underline{\sigma}'_B - \Theta \frac{\partial p_y}{\partial \underline{\sigma}'}, \mathcal{H}_B\right) \quad (3.28)$$

where scalar value Θ can be found from Taylor series as follows:

$$\Theta = \frac{f_y(\underline{\sigma}'_C, \mathcal{H}_C)}{\left\{ \frac{\partial p_y}{\partial \underline{\sigma}'} \right\}^T \left\{ \frac{\partial f_y}{\partial \underline{\sigma}'} \right\}} \quad (3.29)$$

The iterative procedure to find the Θ value for correction of the drift from yield surface is summarized in Algorithm 2. Initial substitution of values of $\left\{ \frac{\partial p_y}{\partial \underline{\sigma}'} \right\}$ and $\left\{ \frac{\partial f_y}{\partial \underline{\sigma}'} \right\}$ are evaluated at point 'A', i.e., at the beginning of the step.

Algorithm 2 : Drift algorithm

```

if  $Abs\left(f_y(\underline{\sigma}'_B, \mathcal{H}_B)\right) > FTOL$  then

    REQUIRE: Initial values of  $\left(\frac{\partial p_y}{\partial \sigma'}\right)$  and  $\left(\frac{\partial f_y}{\partial \sigma'}\right)$ 

    for ( Iteration = 1, MaxIts ) do

        
$$\Theta = \frac{f_y(\underline{\sigma}'_C, \mathcal{H}_C)}{\left(\frac{\partial p_y}{\partial \sigma'}\right)\left(\frac{\partial f_y}{\partial \sigma'}\right)}$$

        
$$\underline{\sigma}'_C = \underline{\sigma}'_B - \Theta \frac{\partial p_y}{\partial \sigma'}$$


        Calculate  $f_y(\underline{\sigma}'_C, \mathcal{H}_C)$ 

        if  $f_y(\underline{\sigma}'_C, \mathcal{H}_C) < FTOL$  then
            return  $\underline{\sigma}'_C$ 
        end if
    end for

    return
end if

```

The S-CLAY1S model is implemented in PLAXIS using the substepping with error control explicit numerical scheme (Sloan, 1987 and Sloan *et al.*, 2001) which starts with the known strain increment $\{\Delta \underline{\epsilon}\}$, initial stresses $\{\Delta \underline{\sigma}'_0\}$, initial hardening parameter \mathcal{H}_0 and an initial pseudo time step ΔT_1 . For a given strain increment, $\{\Delta \underline{\epsilon}\}$, the constitutive relations to be integrated at each Gauss point are described in Equations 3.21 and 3.25. The explicit algorithm for the S-CLAY1S model is shown in Algorithm 3.

Algorithm 3 : Explicit algorithm for S-CLAY1S

DECIDE: n_sub by $StepSize$: (n_sub = number of substepping)

GET: $\{\underline{\sigma}'_0\}$, $\{\Delta\underline{\epsilon}\}$, \mathcal{H}_0 and $FTOL$

for (Iteration = 1 to n_sub) **do**

Calculate: $\{\Delta\underline{\sigma}'\}^e = [D^e] \{\Delta\underline{\epsilon}\}$ and $\{\underline{\sigma}'\}^e = \{\underline{\sigma}'_0\} + \{\Delta\underline{\sigma}'\}^e$

Calculate: $f_y(\{\underline{\sigma}'\}^e, \mathcal{H}_0)$ and $f_y(\{\underline{\sigma}'_0\}, \mathcal{H}_0)$! for checking yield criterion

if $f_y(\{\underline{\sigma}'\}^e, \mathcal{H}_0) \leq FTOL$ **then**

Purely elastic behavior

return

end if

! Start plastic correction

if $f_y(\{\underline{\sigma}'\}^e, \mathcal{H}_0) \geq FTOL$ **then**

if $f_y(\{\underline{\sigma}'_0\}, \mathcal{H}_0) \leq FTOL$ and $f_y(\{\underline{\sigma}'\}^e, \mathcal{H}_0) \geq FTOL$ **then**

Follow intersection Algorithm 1

Update corresponding strains:

$\{\Delta\underline{\epsilon}\} \leftarrow (1 - \Omega) \{\Delta\underline{\epsilon}\}$

end if

Calculate plastic multiplier $\Delta\Lambda$: Go to Algorithm 4

Calculate plastic strains : Go to Algorithm 5

Update state variables : Go to Algorithm 6

Update stresses: $\{\underline{\sigma}'\} = \{\underline{\sigma}'_0\} + [D^e] \{\Delta\underline{\epsilon}^p\}$

Calculate $f_y^f = f_y(\{\underline{\sigma}'\}, \mathcal{H})$! check for drift correction

if $f_y^f > FTOL$ **then**

follow drift correction Algorithm 2

end if

end if

return

end for

Algorithm 4 : Calculation of plastic multiplier for explicit algorithm

Calculate derivatives of yield & potential surfaces:

$$\frac{\partial f_y}{\partial \sigma'} = \frac{\partial f_y(\{\sigma'\}, \mathcal{H}_0)}{\partial \sigma'} : \text{from Appendix B}$$

$$\frac{\partial p_y}{\partial \sigma'} = \frac{\partial p_y(\{\sigma'\}, \mathcal{H}_0)}{\partial \sigma'} : \text{from Appendix B}$$

Calculate Hardening modulus:

$$\mathcal{H} = \mathcal{H}_0 + \mathcal{H}_\alpha + \mathcal{H}_X$$

\mathcal{H}_0 : from Eq. 3.14

\mathcal{H}_α : from Eq. 3.15

\mathcal{H}_X : from Eq. 3.16

Calculate:

$$\left[\frac{\partial f_y}{\partial \sigma'} \right]^T [D^e] \left[\frac{\partial p_y}{\partial \sigma'} \right]$$

Calculate $\Delta\Lambda$: from Eq. 3.22

return $\Delta\Lambda$

Algorithm 5 : Calculation of plastic strains

Calculate plastic strain increment

$$\{\Delta \underline{\epsilon}^p\} = \Delta\Lambda \frac{\partial p_y}{\partial \sigma'}$$

$$\Delta \epsilon_v^p = \Delta \epsilon_x^p + \Delta \epsilon_y^p + \Delta \epsilon_z^p$$

Calculate:

$\{\Delta \underline{\epsilon}_d^p\}$: from Appendix A

$$\Delta \epsilon_d^p = \sqrt{\frac{3}{2} \{\Delta \underline{\epsilon}_d^p\}^T \{\Delta \underline{\epsilon}_d^p\}}$$

return $\{\Delta \underline{\epsilon}^p\}$, $\Delta \epsilon_v^p$ and $\Delta \epsilon_d^p$

Algorithm 6 : Update state variables

Calculate:

$$\Delta p'_{mi} = \frac{(1+e)p'_{mi}}{\lambda_i - \kappa} \Delta \epsilon_v^p$$

$$\Delta \underline{\alpha}_d = \mu \left(\left[\frac{3\sigma'_d}{4p'} - \underline{\alpha}_d \right] \langle d\epsilon_v^p \rangle + \beta \left[\frac{\sigma'_d}{3p'} - \underline{\alpha}_d \right] \Delta \epsilon_d^p \right)$$

$$\Delta \chi = -a\chi \left[|\Delta \epsilon_v^p| + b |\Delta \epsilon_d^p| \right]$$

Update state variables:

$$\{\underline{\alpha}\}_{1,2,3} \leftarrow \underline{\alpha} + \Delta \underline{\alpha}_d + 1$$

$$\{\underline{\alpha}\}_{4,5,6} \leftarrow (\underline{\alpha} + \Delta \underline{\alpha}_d) / \sqrt{2}$$

$$\alpha \leftarrow \sqrt{\frac{3}{2} \{\underline{\alpha} + \Delta \underline{\alpha}_d\} \{\underline{\alpha} + \Delta \underline{\alpha}_d\}^T}$$

$$p'_{mi} \leftarrow p'_{mi} + \Delta p'_{mi}$$

$$\chi \leftarrow \chi + \Delta \chi$$

$$p'_m \leftarrow (p'_{mi} + \Delta p'_{mi}) * (1 + (\chi + \Delta \chi))$$

return $\{\underline{\alpha}\}$, α , p'_{mi} , χ and p'_m

3.2.2 Euler backward (implicit) method

Using the Euler backward implicit integration scheme, the trial stress is modified under consideration of the occurring plastic strains as long as convergence is reached. The convergence criterion is fulfilled when the iterative stress state returns to the yield surface. If plasticity is associated with a given strain increment, it is essential to solve the following system of equations:

$$\{\underline{\sigma}'_{n+1}\} = \{\underline{\sigma}'_n\} + [D_{n+1}^{ep}] \{\Delta \underline{\epsilon}\} \quad (3.30)$$

To derive the backward Euler scheme, the yield surface f_y can be expanded about $\underline{\sigma}'_0$ and \mathcal{H} using Taylor series. Ignoring second order terms and above, this gives the following expansion:

$$f_y = f_y^0 + \frac{\partial f_y}{\partial \underline{\sigma}'} \{\Delta \underline{\sigma}'\} + \frac{\partial f_y}{\partial \mathcal{H}} \Delta \mathcal{H} \quad (3.31)$$

Based on Eq. 3.21, it is possible to calculate the elastic predictor as:

$$\{\Delta \underline{\sigma}'\} = -\Delta \Lambda [D^e] \frac{\partial f_y}{\partial \underline{\sigma}'} \quad (3.32)$$

The rate of hardening parameter $\Delta \mathcal{H}$ can be derived (see for details Sloan *et al.*, 2001) from the following equation:

$$\Delta \mathcal{H} = -\Delta \Lambda \frac{\mathcal{H}}{\partial f_y / \partial \mathcal{H}} \quad (3.33)$$

By setting $f_y = 0$ in Eq. 3.31 and combining Eq. 3.32 and Eq. 3.33, the plastic multiplier is given as:

$$\Delta \Lambda = \left[\frac{f_y^0}{[\partial f_y / \partial \underline{\sigma}']^T [D^e] [\partial p_y / \partial \underline{\sigma}'] + \mathcal{H}} \right] \quad (3.34)$$

Wiltafsky (2003) implemented first the S-CLAY1S model in PLAXIS using the Euler backward scheme. In this implementation, one input parameter *Stepsize* has been added to provide a possibility to control the size of the loading increment within the subroutine. Details of the implementation is given by Wiltafsky (2003). This implicit algorithm has a similar limitation to the explicit algorithm that if the *Stepsize* is set relatively large, the computational error is accumulated on the result. It may be concluded that in order to obtain accurate solutions for non-linear problems, sufficiently small *Stepsize* is required. The implementation of S-CLAY1S using a single step Euler backward scheme is summarized in Algorithm 7.

Algorithm 7 : Euler backward implicit algorithm for S-CLAY1S

DECIDE: n_sub by $StepSize$: (n_sub = number of substepping)

FIND: $\{\Delta\epsilon\} \leftarrow \{\Delta\epsilon\} / n_sub$

GET: $\{\sigma'_0\}$, \mathcal{H}_0 and $FTOL$

for (Iteration = 1 to n_sub) **do**

$\{\Delta\epsilon\}^t = \{\Delta\epsilon\}$

$\{\Delta\epsilon\}^p = 0$

while (until convergence is reached) **do**

$\{\Delta\epsilon\}^t = \{\Delta\epsilon\}^t - \{\Delta\epsilon\}^p$

$\{\Delta\epsilon\}^p = 0$

Calculate: $\{\Delta\sigma'\}^e = [D^e] \{\Delta\epsilon\}^t$ and $\{\sigma'\}^e = \{\sigma'_0\} + \{d\sigma'\}^e$

Calculate: $f_y(\{\sigma'\}^e, \mathcal{H}_0)$! Check yield criterion

if $f_y(\{\sigma'\}^e, \mathcal{H}_0) \leq FTOL$ **then**

Purely elastic behaviour

return

end if

! Start plastic correction

if $f_y(\{\sigma'\}^e, \mathcal{H}_0) \geq FTOL$ **then**

Calculate plastic multiplier $\Delta\Lambda$: Go to Algorithm 8

Calculate plastic strains : Go to Algorithm 5

Update state variables : Go to Algorithm 6

end if

end while

end for

Algorithm 8 : Calculation of plastic multiplier for implicit algorithm

Calculate F_y

Calculate derivatives of yield & potential surfaces:

$$\frac{\partial f_y}{\partial \sigma'} = \frac{\partial f_y(\{\sigma'_0\}, \mathcal{H}_0)}{\partial \sigma'} : \text{from Appendix B}$$

$$\frac{\partial p_y}{\partial \sigma'} = \frac{\partial p_y(\{\sigma'_0\}, \mathcal{H}_0)}{\partial \sigma'} : \text{from Appendix B}$$

Calculate Hardening modulus:

$$\mathcal{H} = \mathcal{H}_0 + \mathcal{H}_\alpha + \mathcal{H}_X$$

\mathcal{H}_0 : from Eq. 3.14

\mathcal{H}_α : from Eq. 3.15

\mathcal{H}_X : from Eq. 3.16

Calculate:

$$\left[\frac{\partial f_y}{\partial \sigma'} \right]^T [D^e] \left[\frac{\partial G_y}{\partial \sigma'} \right]$$

Calculate $\Delta\Lambda$: from Eq. 3.34

return $\Delta\Lambda$

3.2.3 Modified Newton-Raphson (implicit) method

The discussion on Euler forward (explicit) and backward (implicit) schemes has highlighted that errors can occur when large increment steps are used. The modified Newton-Raphson (MNR) scheme with automatic substepping described in this section rectifies this problem by eliminating residual errors in the system of equations. The MNR scheme uses an iterative technique to solve the system of non-linear constitutive equations of the S-CLAY1S model. The proposed MNR scheme is generally very robust, but it is relatively expensive, as for each estimate for the strain the inverse of a iterative scheme matrix needs to be calculated. The MNR scheme may also not converge when the behaviour is strongly non-linear. To avoid this problem, the proposed MNR scheme includes an automatic substepping routine to stabilize the scheme.

The basic elasto-plastic assumption is that strain rate consists of two parts, i.e. elastic and plastic strain rates as follows:

$$\underline{\Delta\epsilon} = \underline{\Delta\epsilon}^e + \underline{\Delta\epsilon}^p \quad (3.35)$$

By using Eq. 3.8, it can be written as:

$$\underline{\Delta\epsilon} = \underline{\Delta\epsilon}^e + \Delta\Lambda \frac{\partial p_y}{\partial \underline{\sigma}'} \quad (3.36)$$

When there is plasticity, it should satisfy (due to associated flow rule) the following conditions:

$$\underline{\Delta\epsilon} - \underline{\Delta\epsilon}^e - \Delta\Lambda \frac{\partial f_y}{\partial \underline{\sigma}'} = 0 \quad (3.37)$$

$$f_y(\underline{\sigma}', \mathcal{H}) = 0 \quad (3.38)$$

In total, there are seven equations, comprising six strain conditions and one yield condition to be solved using MNR iteration. Further, the six strain conditions can be written for iteration as follows:

$$\underline{\Delta\epsilon}_n - \underline{\Delta\epsilon}_n^e - \delta \underline{\Delta\epsilon}_{n+1}^e - (\Delta\Lambda_n + \delta \Delta\Lambda_{n+1}) \left(\frac{\partial f_y}{\partial \underline{\sigma}'_n} + \frac{\partial^2 f_y}{\partial^2 \underline{\sigma}'_{n+1}} \delta \underline{\sigma}'_{n+1} \right) = 0 \quad (3.39)$$

The higher order term of above equation expansion is neglected giving:

$$\underline{\Delta\epsilon}_n - \underline{\Delta\epsilon}_n^e - \delta \underline{\Delta\epsilon}_{n+1}^e - \Delta\Lambda_n \frac{\partial f_y}{\partial \underline{\sigma}'_n} - \Delta\Lambda_n \frac{\partial^2 f_y}{\partial^2 \underline{\sigma}'_{n+1}} \delta \underline{\sigma}'_{n+1} - \delta \Delta\Lambda_{n+1} \frac{\partial f_y}{\partial \underline{\sigma}'_n} = 0 \quad (3.40)$$

The above equation can be restructured as follows:

$$\left(\mathbf{I} + \Delta\Lambda_n \frac{\partial^2 f_y}{\partial^2 \underline{\sigma}'_{n+1}} [D^e]_{n+1} \right) \delta \underline{\Delta\epsilon}_{n+1}^e + \frac{\partial f_y'}{\partial \underline{\sigma}_n} \delta \Delta\Lambda_{n+1} = \underline{\Delta\epsilon}_n - \underline{\Delta\epsilon}_n^e - \Delta\Lambda_n \frac{\partial f_y}{\partial \underline{\sigma}'_n} \quad (3.41)$$

The yield surface equation can be formulated as:

$$\frac{\partial f_y}{\partial \underline{\sigma}'_n} [D]_{n+1} \delta \underline{\epsilon}_{n+1}^e = -f_{y,n} \quad (3.42)$$

Total system of equations to be solved by the MNR iteration scheme can be derived from Eq. 3.21 and Eq. 3.22 as follows:

$$\begin{bmatrix} \mathbf{I} + \Delta\Lambda_n \frac{\partial^2 f_y}{\partial \sigma_n^2} [D^e]_{n+1} & \frac{\partial f_y}{\partial \sigma_n'} \\ \frac{\partial f_y}{\partial \sigma_n'} [D^e]_{n+1} & 0 \end{bmatrix} \begin{Bmatrix} \delta\Delta\epsilon_{n+1}^e \\ \delta\Delta\Lambda_{n+1} \end{Bmatrix} = \begin{Bmatrix} \Delta\epsilon_n - \Delta\epsilon_n^e - \Delta\Lambda_n \frac{\partial f_y}{\partial \sigma_n'} \\ -f_{y,n} \end{Bmatrix} \quad (3.43)$$

where \mathbf{I} is the identity matrix.

From the above system of equations, the changes of elastic strain increment and the plastic multiplier can be calculated using MNR iteration. In each iteration, the state variables are updated. MNR algorithm's k^{th} local iteration is in the form:

$$\left[\Xi_{n+1}^{(k)} \right] \left\{ \delta\Delta v_{n+1}^{(k)} \right\} = \left\{ \underline{R}^{(k)} \right\} \quad (3.44)$$

where the components of $\left[\Xi_{n+1}^{(k)} \right]$, $\left\{ \delta\Delta v_{n+1}^{(k)} \right\}$ and $\left\{ \underline{R}^{(k)} \right\}$ are in Eq. 3.43 and their partial derivatives are given in Appendix B. The iterative process can be completed when changes are very small ($|\delta\Delta\Lambda_{k+1}| \ll |\Delta\Lambda_{k+1}|$ and $\|f_y\| \ll \|f_y^0\|$). The first iteration can start from the following system of equations:

$$\begin{bmatrix} \mathbf{I} & \frac{\partial f}{\partial \sigma_1'} \\ \frac{\partial f_y}{\partial \sigma_n'} [D^e]_1 & 0 \end{bmatrix} \begin{Bmatrix} \Delta\epsilon_1^e \\ \Delta\Lambda_1 \end{Bmatrix} = \begin{Bmatrix} 0 \\ -f_y^0 \end{Bmatrix} \quad (3.45)$$

The implementation of S-CLAY1S using an automatic substepping modified Newton-Raphson scheme is summarized in Algorithm 9.

Algorithm 9 : An automatic substepping scheme for MNR algorithm of S-CLAY1S

GET: $\{\sigma'_0\}$, \mathcal{H}_0 , $\{\Delta\epsilon\}$ and $FTOL$

ASSUME: $T_0 = 0$ and $dT = 1$

FIND: $\{\Delta\epsilon\}^t = dT * \{\Delta\epsilon\}$

99 Continue

NewStep = 1

CALL: S-CLAY1S subroutine Algorithm 10

if ($NewStep < 0.9999$) **then**

$dT = NewStep * dT$

$\{\Delta\epsilon\}^t = dT * \{\Delta\epsilon\}$

if ($dT > 0.0001$) **then**

 GO TO 99

else

 CALL: S-CLAY1S subroutine Algorithm 10

 Abort " Too small step size"

end if

end if

$T_0 = T_0 + dT$

if ($T_0 < 0.9999$) **then**

$dT = 1 - T_0$

$\{\Delta\epsilon\}^t = dT * \{\Delta\epsilon\}$

 GO TO 99

end if

return

Algorithm 10 : MNR algorithm of S-CLAY1S

GET: $\{\underline{\sigma}'_0\}$, \mathcal{H}_0 , $\{\Delta\underline{\epsilon}\}$, $RTOL$ and $FTOL$
Calculate: $\{\Delta\underline{\sigma}'\}^e = [D^e] \{\Delta\underline{\epsilon}\}$ and $\{\underline{\sigma}'\}^e = \{\underline{\sigma}'_0\} + \{\Delta\underline{\sigma}'\}^e$
Calculate: $f_y(\{\underline{\sigma}'\}^e, \mathcal{H}_0)$! Check yield criterion

if $(f_y(\{\underline{\sigma}'\}^e, \mathcal{H}_0) \leq FTOL)$ **then**

 Purely elastic behaviour

return

end if

if $f_y(\{\underline{\sigma}'\}^e, \mathcal{H}_0) \geq FTOL$ **then**

 SET: $f_y^t = f_y$ and $\{\Delta\underline{\epsilon}\}^e = \{\Delta\underline{\epsilon}\}$

 Calculate plastic multiplier $\Delta\Lambda$: Go to Algorithm 8

 Calculate plastic strains : Go to Algorithm 5

 Update state variables : Go to Algorithm 6

 Update strain: $\{\Delta\underline{\epsilon}\}^e = \{\Delta\underline{\epsilon}\}^e - \{\Delta\underline{\epsilon}\}^p$

 Update stresses: $\{\underline{\sigma}'\} = \{\underline{\sigma}'_0\} + [D^e] \{\Delta\underline{\epsilon}\}^p$

 Calculate: $f_y = f_y(\{\underline{\sigma}'\}, \mathcal{H})$ and $\left\{\frac{\partial f_y}{\partial \underline{\sigma}'}\right\}$

 Estimate residual error: $\{\underline{R}\} = \{\Delta\underline{\epsilon}\} - \{\Delta\underline{\epsilon}\}^t - \Delta\Lambda \frac{\partial F_y}{\partial \underline{\sigma}'}$

 Calculate: $R_n = \sqrt{\{\underline{R}\}^T \{\underline{R}\}}$

 SET: $iConv = 0$

if $(Abs(F_y) < FTOL \text{ AND } R_n < RTOL)$ **then**

$iConv = 1$

return

else

 CALL MNR iteration scheme Algorithm 11

end if

if $(iConv = 0)$ **then**

 NewStep = 0.25 ! divergence

return

end if

end if

return

Algorithm 11 : MNR iteration scheme

```

GET: MaxIt
 $f_y^e = f_y$ 
for (Iteration = 1, MaxIt) do
  Calculate  $\frac{\partial f_y}{\partial \underline{\sigma}'}$  and  $\frac{\partial^2 f_y}{\partial \underline{\sigma}'^2}$  from Appendix B
  Estimate residual error
   $\{R\} = \{\Delta \underline{\epsilon}\} - \{\Delta \underline{\epsilon}\}^t - \Delta \Lambda \frac{\partial f_y}{\partial \underline{\sigma}'}$ 
   $R_n = \sqrt{\{R\}^T \{R\}}$ 
  ASSEMBLE:  $[\Xi_{n+1}^{(k)}]$  from Eq. 3.43

  FIND:  $[\Xi_{n+1}^{(k)}]^{-1}$ 
  if ( $[\Xi_{n+1}^{(k)}]$  is singular) then
    NewStep = 0.25
    return
  end if
  Calculate:  $\Delta \Lambda = \Delta \Lambda + \delta \Delta \Lambda$ 
  Calculate:  $\{\Delta \underline{\epsilon}\}^e = \{\Delta \underline{\epsilon}\}^e + \delta \{\Delta \underline{\epsilon}\}^e$ 
  Calculate:  $\{\Delta \underline{\epsilon}\}^p = \{\Delta \underline{\epsilon}\} - \{\Delta \underline{\epsilon}\}^e$ 
  Update stresses:  $\{\underline{\sigma}'\}_{n+1}^{(k)} = \{\underline{\sigma}'\}_n + [D^e]_n \{\Delta \underline{\epsilon}^p\}_{n+1}^{(k)}$ 
  Update state variables : Go to Algorithm 6
  Calculate  $f_y = f_y(\underline{\sigma}'_{n+1}^{(k)}, \mathcal{H}_{n+1}^{(k)})$ 

  if ( $f_y^e/f_y > 1000$ ) then
    NewStep = 0.25 ! divergence
    return
  end if

  if ( $f_y < FTOL$  AND  $R_n < STOL$ ) then
     $iConv = 1$ 
    return
  end if

end for
return

```

3.3 Performance comparison of different algorithms

The performance of the numerical algorithms used to implement the advanced kinematic hardening S-CLAY1S model can be studied by analyzing their relative accuracy, stability and efficiency. The relative accuracy can be defined as the degree of closeness of a numerical solution to the exact result. The relative accuracy can be studied by comparing numerical results from an algorithm with an algorithm that converges to the exact solution for very small steps. A step size independent algorithm which produces an accurate solution for large strain increments is desirable. The stability can be described as the ability to achieve convergence without varying randomly, hovering and oscillating. Here, the efficiency is defined as the computing cost of an algorithm to produce results.

The performance analysis is carried out using the integration point program (IPP) and the finite element program PLAXIS. The IPP of S-CLAY1S is a standalone program directly used to input strain-controlled loading paths without connecting to the finite element program. A big advantage of the IPP is that better control of the program is achieved and it is easier to debug. The algorithms have been tested inside the finite element program PLAXIS for the solution of a relatively simple boundary value problem.

The material parameters for soft Bothkennar clay used for all analyses are summarized in Table 3.1. Bothkennar clay has been extensively studied and sufficient laboratory data is available to derive material parameters for the S-CLAY1S model (e.g. Géotechnique Symposium in Print, 1992; McGinty, 2006; McGinty *et al.*, 2008).

3.3.1 Simulations of strain-controlled triaxial tests

Verification of the S-CLAY1S model implementation using different algorithms is performed by using IPP without involving the finite element software PLAXIS. The S-CLAY1S model is strain-driven, i.e. known increments in strain are input to the model and the corresponding stresses are output. Thus by specifying strain increments, and the material parameters, the corresponding stress output can be used for model verification without the need for the finite element code PLAXIS.

Undrained compression, extension and isotropic compression were chosen to cover many important stress strain conditions in triaxial tests. Strain controlled IPP was used to simulate these tests. Volume is conserved for undrained tests

3.3 Performance comparison of different algorithms

Table 3.1: Material parameters of Bothkennar clay for S-CLAY1S

Soil constants					
κ	ν'	λ	M	γ (kN/m^3)	$k_x = k_y$ (m/day)
0.02	0.2	0.3	1.5	16.5	2.5 E-4
State variables					
e_0	K_0	α_0	χ_0	OCR	
2.0	0.5	0.59	8.0	1.5	
Additional parameters for anisotropy					
β	μ				
1.0	50.0				
Additional parameters for destructuration					
λ_i	a	b			
0.18	9.0	0.2			

on saturated clay; therefore, undrained tests can be simulated by applying $d\epsilon_1 = -2d\epsilon_2 = -2d\epsilon_3$. The isotropic compression test was simulated by applying a strain increment $d\epsilon_2 = d\epsilon_1 = d\epsilon_3$.

Three triaxial simulations which represent typical stress paths in the triaxial stress space are simulated. Stress paths and the initial and final yield surfaces of S-CLAY1S in undrained triaxial compression and extension simulations are shown side by side in Fig. (3.5). For isotropic straining, Fig. (3.6) shows the stress path and the initial and final yield surface of S-CLAY1S in $p' - q$ space. Figs. (3.7), (3.8) and (3.9) show undrained compression simulations for the Euler forward, the Euler backward and the MNR respectively. The undrained extension simulations are shown in Figs. (3.10), (3.11) and (3.12) and the isotropic compression simulations are presented in Figs. (3.13), (3.14) and (3.15).

The undrained test simulations assumed that the sample is normally consolidated and undrained shearing starts from $p' = 12kPa$ and $q = 12kPa$; the maximum vertical strain applied to the sample is 6%. Fig. (3.7) and Fig. (3.10) show comparison of the undrained compression and extension simulations using the substepping explicit numerical algorithm at the strain increments 0.01%, 0.06% and 0.6%.

3.3 Performance comparison of different algorithms

Further larger increments were not simulated because the allowed maximum strain increment in the algorithm is 0.1%. If larger increments are used, they (increments) will be subdivided due to the substepping explicit algorithm e.g for 0.6%. It was clearly observed from the stress-strain simulation, that the results are sensitive to the increment size. However, by reducing the maximum allowed increment size, the explicit algorithm can produce small errors for a large strain increment size at the larger computational cost. In finite element analysis, a maximum strain increment applied is 0.01% to avoid divergence of the solution and/or minimize the numerical errors.

The undrained compression and extension simulations from the Euler-backward implicit algorithm are compared for the strain increments 0.01%, 0.06%, 0.6% and 1.2% in Fig. (3.8) and Fig. (3.11). In addition, Euler-forward explicit results are also presented. The results show that stress paths and stress-strain curves are sensitive to the size of increment and give very large errors for the larger increment size. The simulation with the size of strain increment 0.6% and 1.2% gave larger errors in the p' and q values.

Fig. (3.9) and Fig. (3.12) show comparison of undrained compression and extension simulation using the automatic substepping modified Newton-Raphson (MNR) for given strain increments 0.01%, 0.06%, 0.6% and 1.2%. The simulations are not very sensitive to the size of strain increment and well with the same magnitude. The accuracy of the MNR algorithm depends on the substepping tolerance.

Fig. (3.13), Fig. (3.14) and Fig. (3.15) compare the isotropic compression stress paths and stress-strain curves for the explicit method, implicit Euler-backward and implicit (MNR) algorithms respectively. Inspection of Fig. (3.14) indicates clearly that the Euler-backward implicit algorithm is sensitive to the size of increment. However, substepping explicit and MNR algorithm are relatively insensitive to the increment size and are of similar magnitude.

3.3 Performance comparison of different algorithms

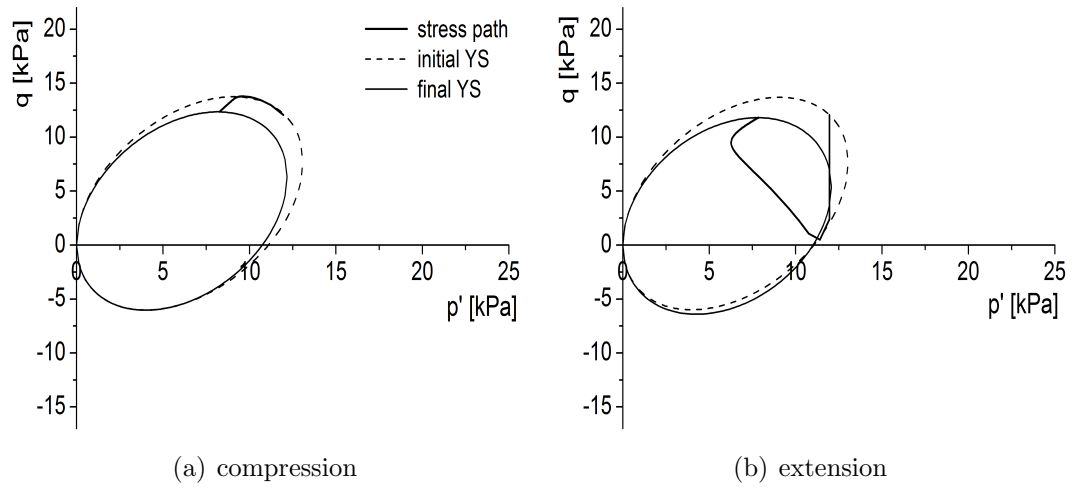


Figure 3.5: Undrained triaxial stress path

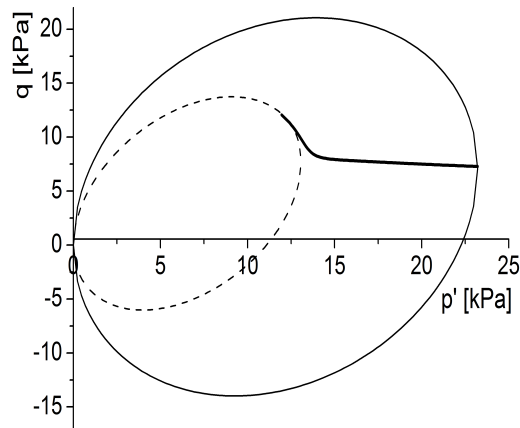


Figure 3.6: Isotropic straining stress path

3.3 Performance comparison of different algorithms

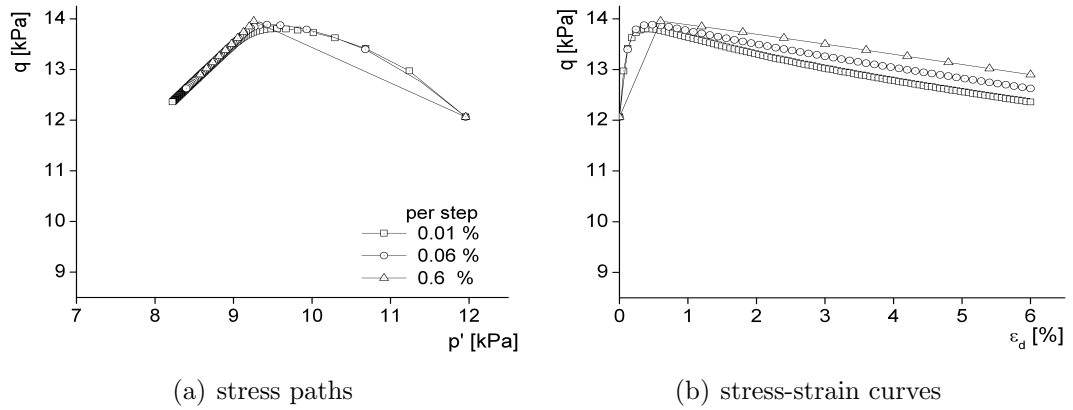


Figure 3.7: Explicit Euler-forward: Undrained compression simulation

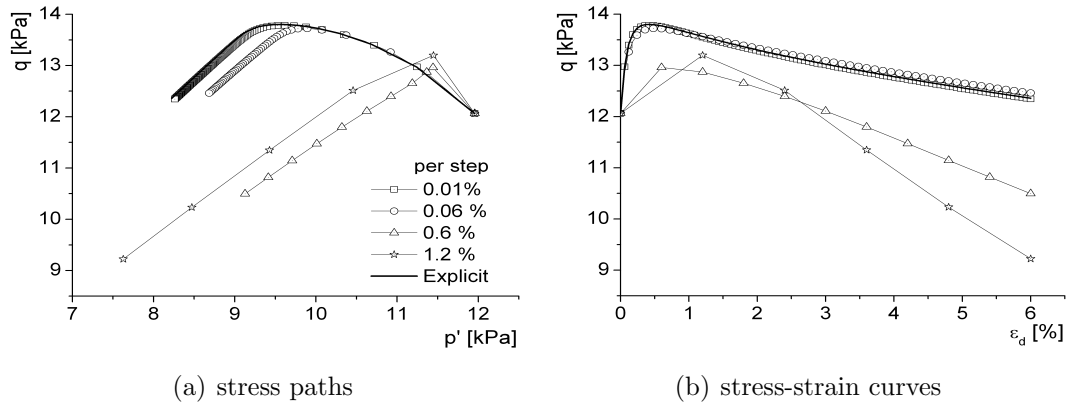


Figure 3.8: Implicit Euler-backward: Undrained compression simulation

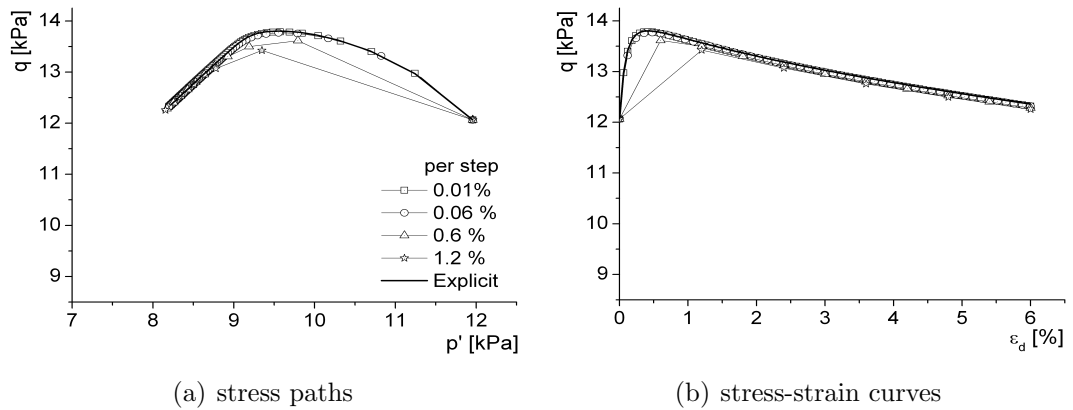


Figure 3.9: Implicit MNR: Undrained compression simulation

3.3 Performance comparison of different algorithms

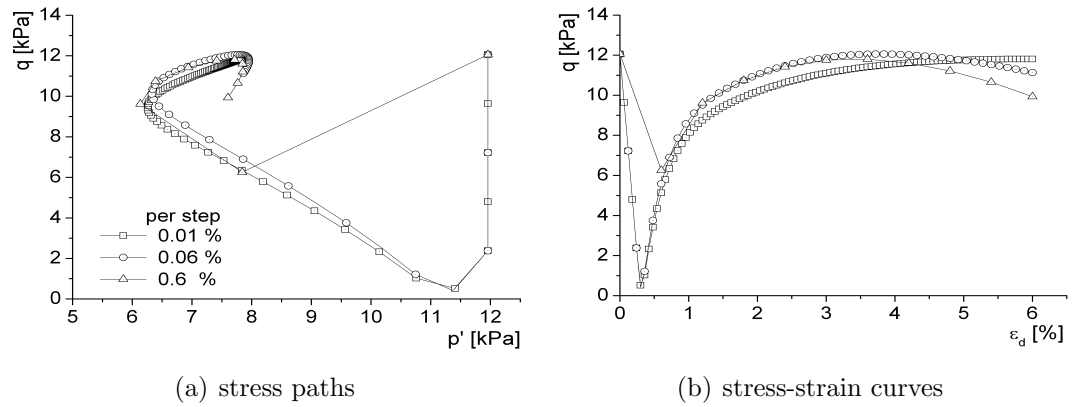


Figure 3.10: Explicit Euler-forward: Undrained extension simulation

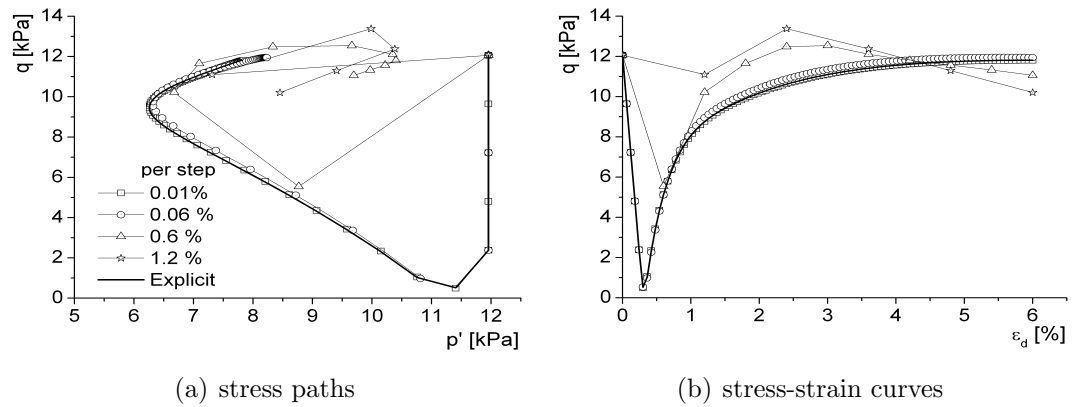


Figure 3.11: Implicit Euler-backward: Undrained extension simulation

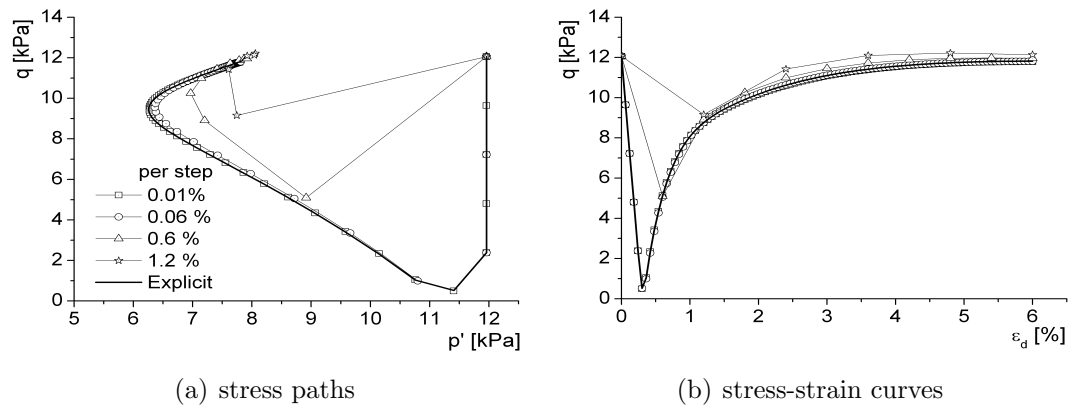


Figure 3.12: Implicit MNR: Undrained extension simulation

3.3 Performance comparison of different algorithms

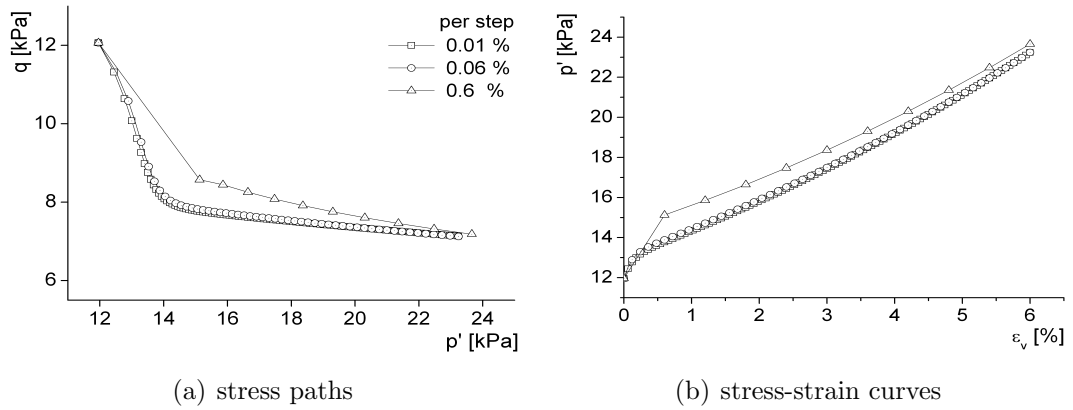


Figure 3.13: Explicit Euler-forward: Isotropic straining simulation

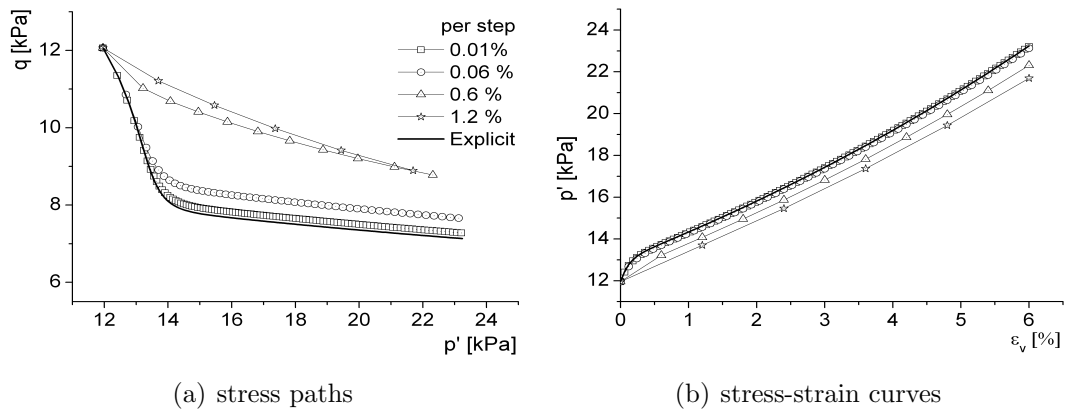


Figure 3.14: Implicit Euler-backward: Isotropic straining simulation

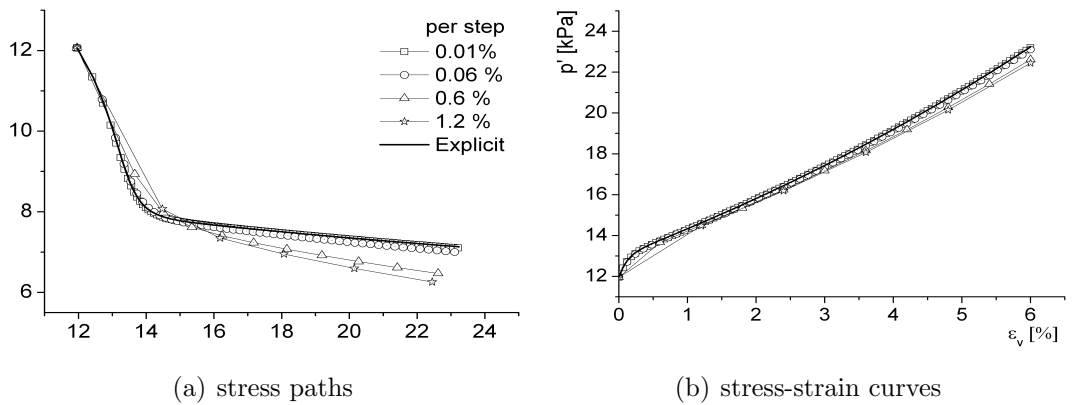


Figure 3.15: Implicit MNR: Isotropic straining simulation

3.3.2 Simulations of benchmark test

The S-CLAY1S model has been implemented into the PLAXIS finite element program using all the algorithms described above. In this section, simulations of a surface strip footing are presented using the same properties for Bothkennar clay used in earlier triaxial simulations (see Table. 3.1 for model parameters). A displacement controlled strip footing was analyzed under drained conditions. The model is 4m in height and 4m in width; 228 triangular 8 noded elements are utilized as shown in Fig. (3.16). The length of the footing is 1m. The initial stress condition was computed by assuming normally consolidated clay with in-situ $K_0 = 0.5$. The footing was given a maximum vertical displacement of 0.2m. The water table is assumed to be 1m below the surface.

Fig. (3.17) shows the comparison of footing load F_y versus displacement at nodal point A for the explicit Euler-backward, implicit Euler-backward and implicit MNR methods, respectively. Since the explicit method has a maximum increment limit of 0.01%, there is no difference in the results for increment sizes 0.01% and 0.1% as shown in Fig. (3.17(a)), but the displacement shows little difference from increment size 0.001%.

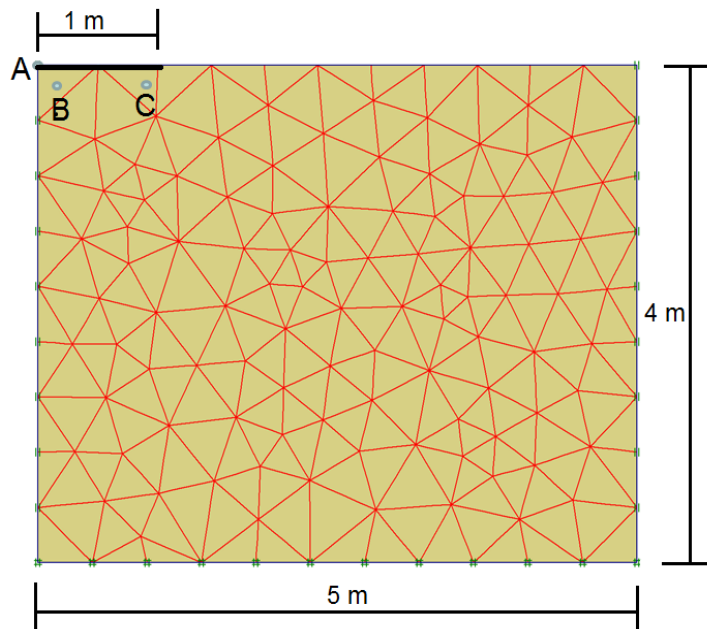


Figure 3.16: Finite element mesh of the geometry around the footing

3.3 Performance comparison of different algorithms

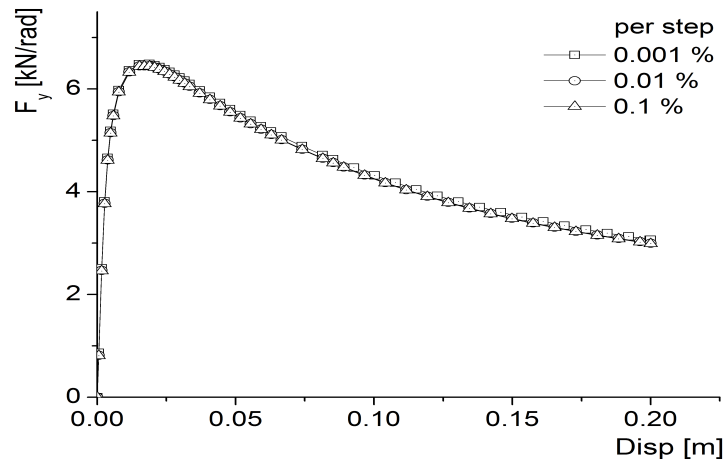
The maximum size of strain increment means that any strain increment applied which is higher than the allowed maximum value is subdivided into several sub increments to the limit strain increment. The explicit algorithm stress paths for the Gauss points B and C is shown in Fig. (3.18(a)). Results of stress paths shows that there is no difference for increment sizes 0.01% and 0.1% and little deviation from the stress path of increment size 0.001%. The implicit (Euler-backward) algorithm displacement of nodal point A and stress paths of gauss points B and C are shown in Fig. (3.17(b)) and Fig. (3.18(b)). The results show very clearly that when the strain increment size increases the difference in the results also increases. The stress paths and displacement curve for strain increment size 1.0% shows clear deviation from the proper results represented by increment size 0.001%. Using the Euler-backward implicit algorithm to analyse a practical engineering problem, a geotechnical engineer should be aware about the value of stepsize in the input program.

Fig. (3.17(c)) and Fig. (3.18(c)) show the displacement curve at nodal point A and the stress paths at Gauss point B and C for the modified Newton-Raphson implicit method. Since there is no limitation for the strain increment size in the implicit MNR algorithm, only one displacement curve and stress path are shown. The implicit MNR algorithm does not require a stepsize as a input value, giving an advantage over the other algorithms for practicing engineers and researchers.

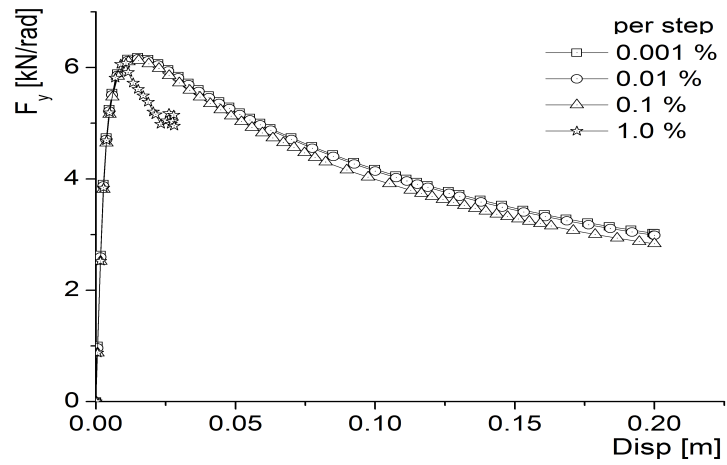
Table. 3.2 shows the time taken by different algorithms to complete the above mentioned benchmark problem, which measures the efficiency. Even though the Euler forward and backward algorithms appear to be relatively faster than the MNR algorithm when larger increment sizes used (e.g. 0.01% for the Euler forward and 0.1% for the Euler backward), the increments are not sufficiently small for real geotechnical problems. In practice, geotechnical engineers choose small increment sizes to avoid numerical convergence issues. Because of this conservative assumption, it can be less efficient in terms of computational time (e.g. 0.001% for the Euler forward and 0.01% for the Euler backward) to use the Euler forward or backward algorithm than the MNR algorithm.

Based on the efficiency, displacement curves and stress paths, it can be concluded that the modified Newton-Raphson algorithm is the best algorithm to integrate constitutive equations of the S-CLAY1S model. These findings agree with the findings of Potts *et al.* (2002) who showed that the modified Newton-Raphson algorithm is more accurate and less dependent on increment size than the other algorithms.

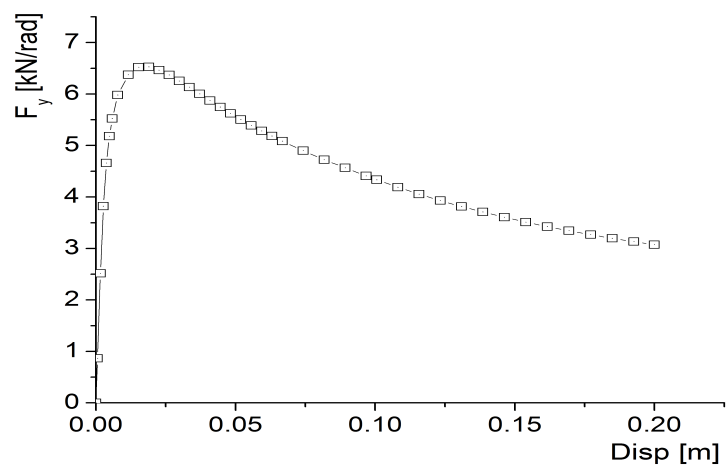
3.3 Performance comparison of different algorithms



(a) Explicit Euler-forward



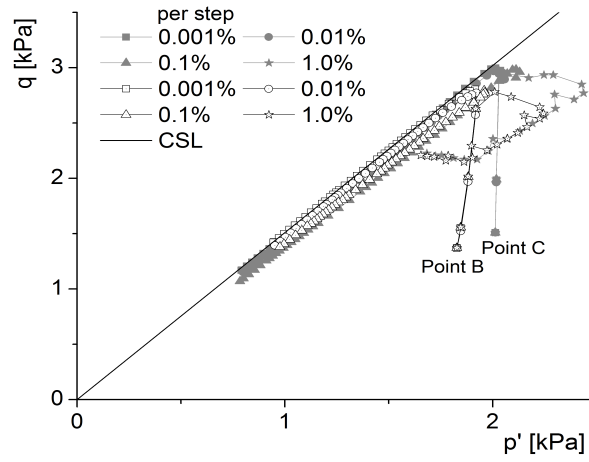
(b) Implicit Euler-backward



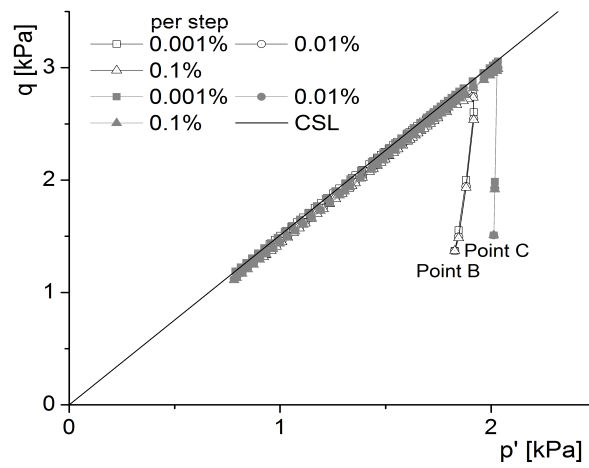
(c) Implicit MNR

Figure 3.17: Comparison of displacement at point A

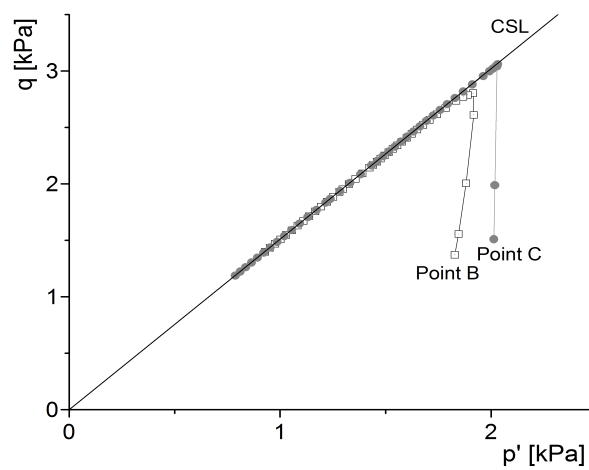
3.3 Performance comparison of different algorithms



(a) Explicit Euler-forward



(b) Implicit Euler-backward



(c) Implicit MNR

Figure 3.18: Comparison of stress paths at point B & C

Table 3.2: Time taken by different numerical algorithms

Explicit (Euler-forward)	
<i>size of increment</i> [%]	<i>time</i> [s]
0.1	48
0.01	47
0.001	256
Implicit (Euler-backward)	
<i>size of increment</i> [%]	<i>time</i> [s]
1.0	48
0.1	33
0.01	125
0.001	820
Implicit (MNR)	
<i>size of increment</i> [%]	<i>time</i> [s]
–	107

3.4 Lode angle dependency

The stress ratio at critical state M is assumed to be constant for the original S-CLAY1S model i.e. the Drucker-Prager failure criterion is adopted ($M_c = M_e$). However, the experimental results by McGinty (2006) on Bothkennar clay showed that the value of critical state in triaxial compression (M_c) was greater than in triaxial extension (M_e). Further, Potts & Zdravkovic (1999) suggest that the Mohr-Coulomb criterion is more appropriate to failure conditions especially in extension. Therefore the critical state constant M should be a function of Lode angle in stress space. In the proposed modified S-CLAY1S model, critical state constant M has been made a function of Lode angle, according to the expression proposed by Sheng *et al.* (2000). This formulation incorporates a smooth failure yield surface as an alternative to the Mohr-Coulomb failure surface. The Sheng *et al.* (2000) failure surface gains an advantage from a numerical point of view over the Mohr-Coulomb failure surface by avoiding corners in the failure surface. Fig. (3.19) shows the yield surfaces of the original and proposed S-CLAY1S models in the $p' - q$ plane and the failure surface in the π plane.

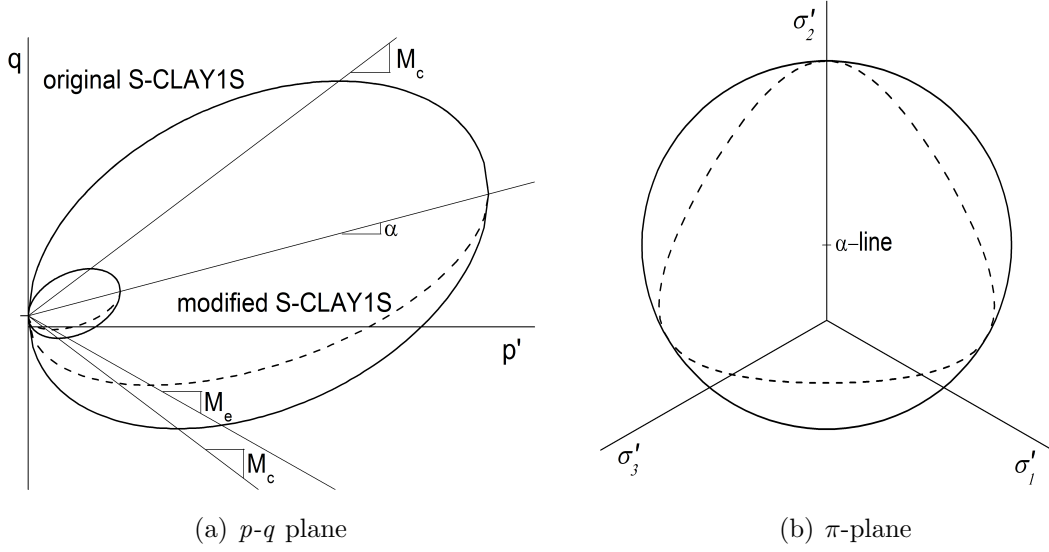


Figure 3.19: S-CLAY1S yield surface

3.4.1 Formulation of Lode angle dependency

The Lode angle dependent yield surface of S-CLAY1S is formulated in general space as follows:

$$f_y = \frac{3}{2} \frac{(\sigma'_d - \alpha_d p') : (\sigma'_d - \alpha_d p')}{M^2(\theta) - \alpha^2} + \left(p' - \frac{p'_m}{2}\right)^2 - \left(\frac{p'_m}{2}\right)^2 = 0 \quad (3.46)$$

The function $M(\theta)$ defines the shape of the failure surface in the deviatoric plane of the S-CLAY1S yield surface, and θ is the value of Lode angle. The magnitude of θ defines the orientation of the stress state within the deviatoric plane. The general version of function $M(\theta)$ is defined for an isotropic model:

$$M(\theta) = M_c \left(\frac{2m^n}{1 + m^n + (1 - m^n) \sin 3\theta} \right)^{\frac{1}{n}} \quad (3.47)$$

According to Sheng *et al.* (2000), a possible form for the variation of $M(\theta)$ for an isotropic model is given as:

$$M(\theta) = M_c \left(\frac{2m^4}{1 + m^4 + (1 - m^4) \sin 3\theta} \right)^{\frac{1}{4}} \quad (3.48)$$

where m :

$$m = \frac{M_e}{M_c} \quad (3.49)$$

where M_c is the value of M in triaxial compression with $\theta = -30^\circ$, and M_e is the value of M in triaxial extension with $\theta = 30^\circ$.

For the anisotropic S-CLAY1S model, the size of the yield curve p'_m is defined on the α -line ($\underline{\sigma}'_d - \underline{\alpha}_d p' = 0$) rather than on the isotropic axis ($\underline{\sigma}'_d = 0$). Therefore, for consistency, Lode angle dependency should be incorporated by making the parameter $M(\theta)$ in the yield surface equation a function of the modified Lode angle θ_α , which corresponds to the stress state to the α - line and can be defined as:

$$\sin 3\theta_\alpha = - \left[\frac{3\sqrt{3} (J_3)_\alpha}{2 (J_2)_\alpha^{\frac{3}{2}}} \right] \quad (3.50)$$

where $(J_2)_\alpha$ and $J(J_3)_\alpha$ are the second and third invariants of the modified stress deviator $\underline{\sigma}'_d - \underline{\alpha}_d p'$ which compares the stress state with the α - line. Definitions of $(J_2)_\alpha$ and $(J_3)_\alpha$ can be found in Appendix A.

A possible form for variation of $M(\theta)$ for S-CLAY1S with modified Lode angle θ_α is given as:

$$M(\theta) = M_c \left(\frac{2m^4}{1 + m^4 + (1 - m^4)\sin 3\theta_\alpha} \right)^{\frac{1}{4}} \quad (3.51)$$

All necessary terms of derivatives for modified Lode angle dependency are given in Appendix B.

3.4.2 Verification and validation of Lode angle dependency

The Lode angle dependent S-CLAY1S model implementation is verified for the following cases;

- *Case 1* The original S-CLAY1S model in which it is assumed that both the shape of the plastic potential and yield surface in the deviatoric plane are circular with the value of constant M

- *Case 2* The modified S-CLAY1S model in which it is assumed that both the shape of plastic potential and yield surface in the deviatoric plane are of the Sheng *et al.* (2000) shape in Fig. (3.19), and $\partial M/\partial\sigma_{ij}$ is allowed to vary according to Eq. 3.48 for both yield surface and plastic potential.

Isochoric monotonic loads were applied in radial direction for verification of the modified S-CLAY1S model implementation. Fig. (3.20) shows the S-CLAY1S model mobilization of stress path in the π -plane for *Case 1*, and *Case 2* respectively. As shown in Fig. (3.20(b)), the modified S-CLAY1S model shows good agreement with the Sheng *et al.* (2000) failure surface. However, the stress mobilization in the π -plane produces a shape which is not exactly the same as the Sheng *et al.* (2000) failure surface due to the rotational hardening of S-CLAY1S.

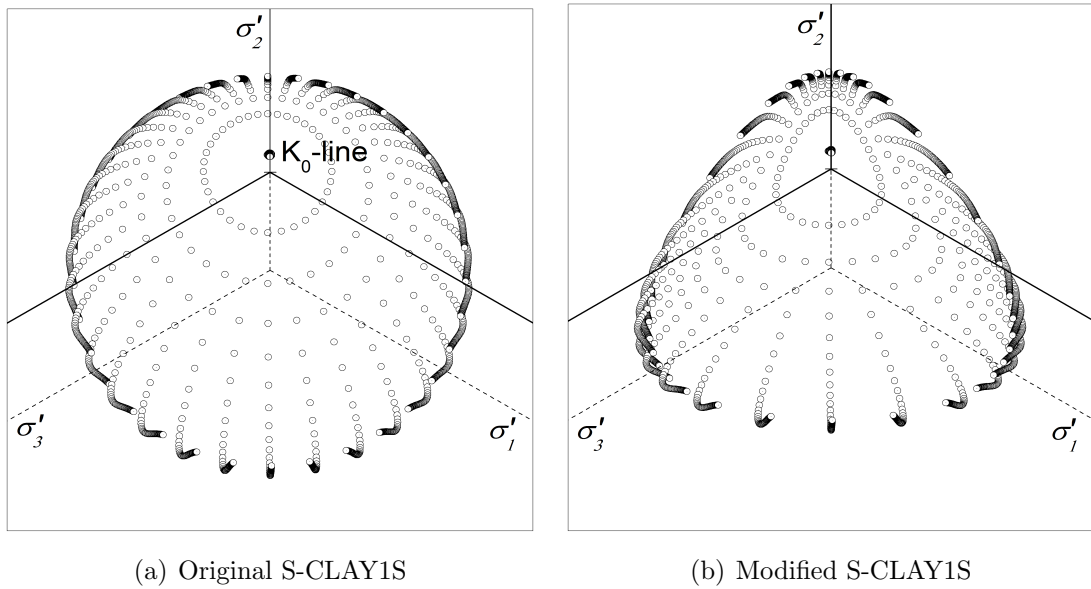


Figure 3.20: Stress paths in π -plane during isochoric monotonic loading

The ability of the modified S-CLAY1s model to simulate real soil behaviour was assessed by simulating laboratory data from a triaxial extension test. Hong Kong Marine clay lab data by Zhou *et al.* (2006) was used for the comparison with the original and modified S-CLAY1S models. Model parameters for the S-CLAY1S model were obtained from Leoni *et al.* (2008). The anisotropy of Hong Kong Marine clay was taken into account for simulation and the destructuration is switched off in the S-CLAY1S model simulations. Hence the S-CLAY1S model becomes the S-CLAY1 model. In this simulation, the two set of tests considered are E150 and E400

Table 3.3: Material parameters of Hong Kong Marine clay for S-CLAY1

Soil constants				
κ	ν'	λ	M_c	M_e
0.0564	0.25	0.238	1.243	0.879
State variables				
e_0	α_0	OCR		
2.0	0.474	1.0		
Additional parameters for anisotropy				
β	μ			
0.807	43.15			

as originally labeled by Zhou *et al.* (2006). Table 3.3 shows the full data set used in this simulation. The soil sample was first consolidated following the K_0^{NC} line and then sheared in undrained extension.

In Fig. (3.21), the comparisons between the predicted and experimental stress paths are plotted for Hong Kong Marine clay (Zhou *et al.*, 2006). The modified S-CLAY1S model with Lode angle dependency shows good agreement with the laboratory data, even though the final deviatoric stress is higher than the laboratory value. This is due to the fact that the M_e value has been calculated assuming Mohr-Coulomb in extension given no triaxial extension tests were made. By contrast, the original S-CLAY1S model shows a much higher deviatoric stress value than the experimental value and clearly deviates from the experimental data. For comparison, the MCC model simulation also plotted.

The stress strain plots are shown in Fig. (3.22(a)) and Fig. (3.22(b)) for laboratory data E400 and E150 respectively. Both the original and modified S-CLAY1S numerical simulations do not match exactly the experimental data but modified S-CLAY1S model deviates less from the experimental data. This difference would be expected due to the creep behaviour of Hong Kong marine clay. Both S-CLAY1S models could be improved by applying small-strain stiffness in the constitutive modelling. By changing the failure criterion from the Drucker-Prager to the Sheng *et al.* (2000) formulation, the model has been substantially improved, especially in extension simulations.

3.4 Lode angle dependency

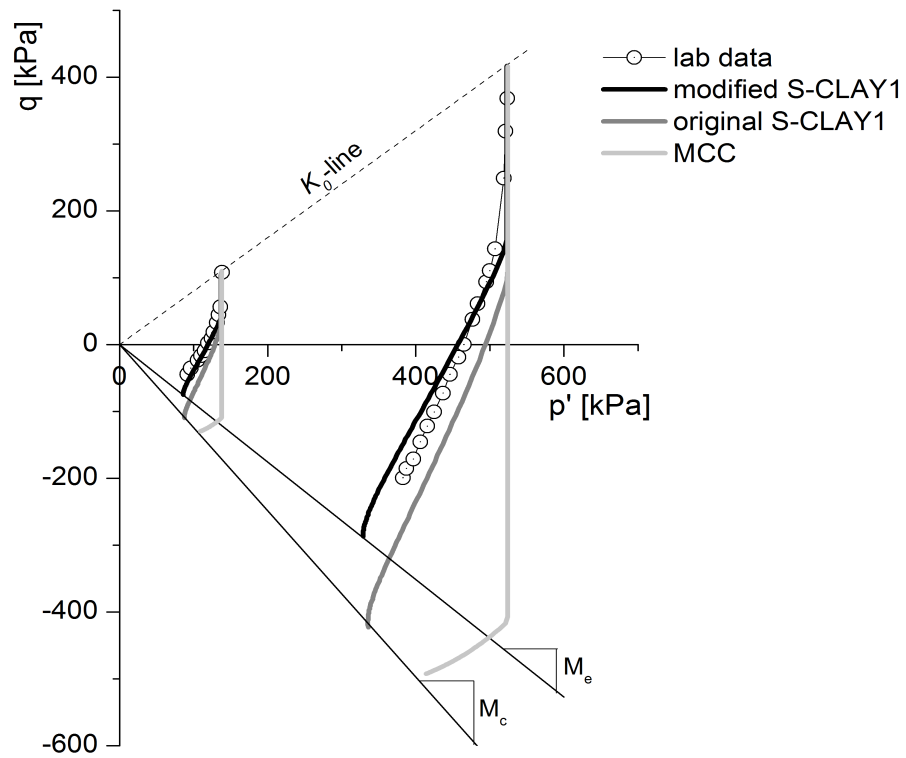


Figure 3.21: Stress paths for undrained extension E400 and E150 tests of Hong Kong Marine clay (data from Zhou *et al.*, 2006)

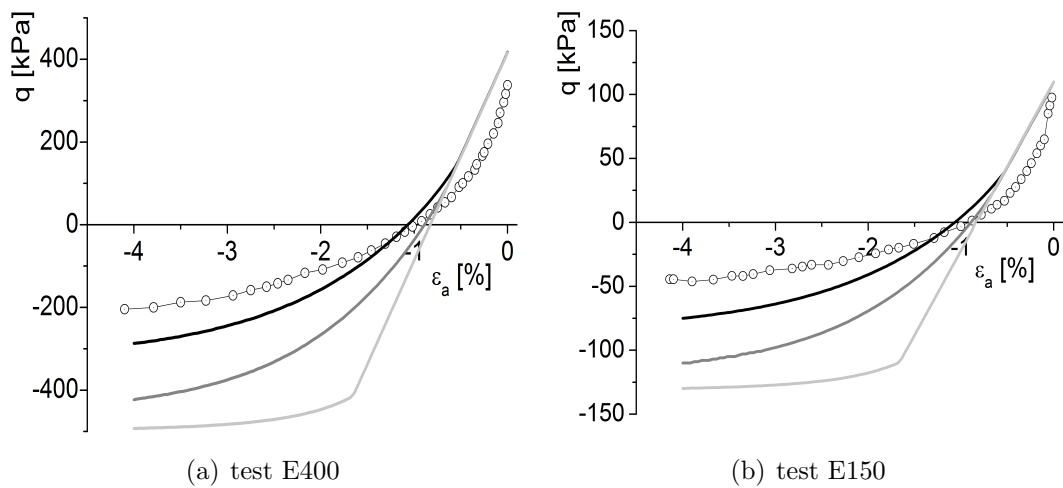


Figure 3.22: Deviator stress against axial strain in undrained extension test (data from Zhou *et al.*, 2006)

3.4 Lode angle dependency

The modified and original S-CLAY1 model (without destructuration) is compared for Swiss lacustrine clay triaxial test data in extension (S2aT4) provided by Messerklinger (2006).

The natural test sample was first reconsolidated in the triaxial apparatus to a stress state of $p' = 300 \text{ kPa}$ and $q = 225 \text{ kPa}$ beyond the in-situ preconsolidation stress along the stress ratio $\eta_{K0} = 0.75$, unloaded to a stress state of $p' = 150 \text{ kPa}$ and $q = 112.5 \text{ kPa}$ using drained swelling along the stress ratio $\eta_{K0} = 0.75$. Then the probing extension stress path was simulated using stress increment ratio $\eta = -7.1$ and $\delta\sigma'_1/\delta\sigma'_3 = -1.1$. Table 3.4 summarizes the model parameters which were obtained from Messerklinger (2006).

Table 3.4: Material parameters of lacustrine clay (after Messerklinger, 2006)

Soil constants				
κ	ν'	λ	M_c	M_e
0.01	0.1	0.053	1.25	0.88
State variables				
e_0	α_0	OCR		
0.693	0.42	1.0		
Additional parameters for anisotropy				
β	μ			
1.31	5			

Comparison of the original and modified S-CLAY1 models simulation results to the triaxial test data S2aT4 are presented in Fig. (3.23). Both models do not predicts very well plastic volumetric straining, the original S-CLAY1 model overpredicts whereas the modified S-CLAY1 underpredicts (Fig. 3.23(a)). The shear strain predictions (Fig. 3.23(b)) show that the modified S-CLAY1 model simulates the lab data more accurately than the original S-CLAY1 model. The results of simulation after incorporating Lode angle dependency are more close to the experimental results in extension than with the Drucker-Prager failure criterion.

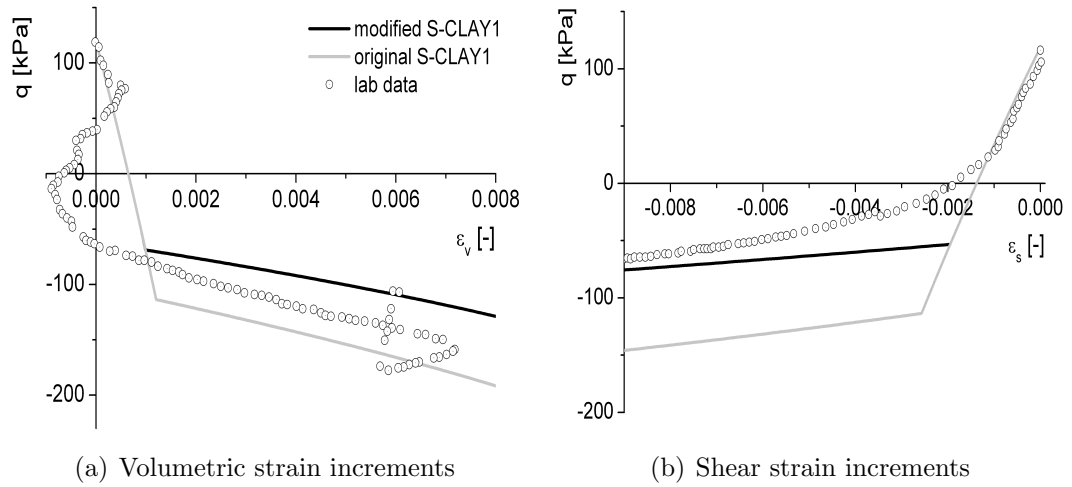


Figure 3.23: Comparison of original and modified S-CLAY1 simulations with triaxial test data S2aT4 (Messerklinger, 2006)

3.4.3 Benchmark applications using Lode angle dependency

To further investigate the importance of the Lode angle dependency, a finite element benchmark test carried out for an axis-symmetric and plane strain footing on Bothkennar clay (assumed $M_c = 1.5$ and $M_e = 1.1$) described Section 3.3.2 was simulated. The results of the investigation are presented in Fig. (3.24) where the applied vertical load F_y is plotted against displacement at point A (see Fig. 3.16). For the axis-symmetric (circular) footing, the effect of Lode angle dependency is found to be not significant (see Fig. 3.24(a)) as would be expected. This is due the fact that the M value calculated using Eq. 3.51 for the Lode angle dependent S-CLAY1S model is similar to the the value of M_c used in Lode angle independent S-CLAY1S model under triaxial compression. However, for the plane strain (strip) footing, the Lode angle dependency has an effect on the load-displacement behaviour (see Fig. 3.24(b)).

Furthermore, the Lode angle dependency is even more significant in 3-dimensional finite element analysis than in 2-dimensional analysis. Modified S-CLAY1S model requires further validation in the 3D finite element applications.

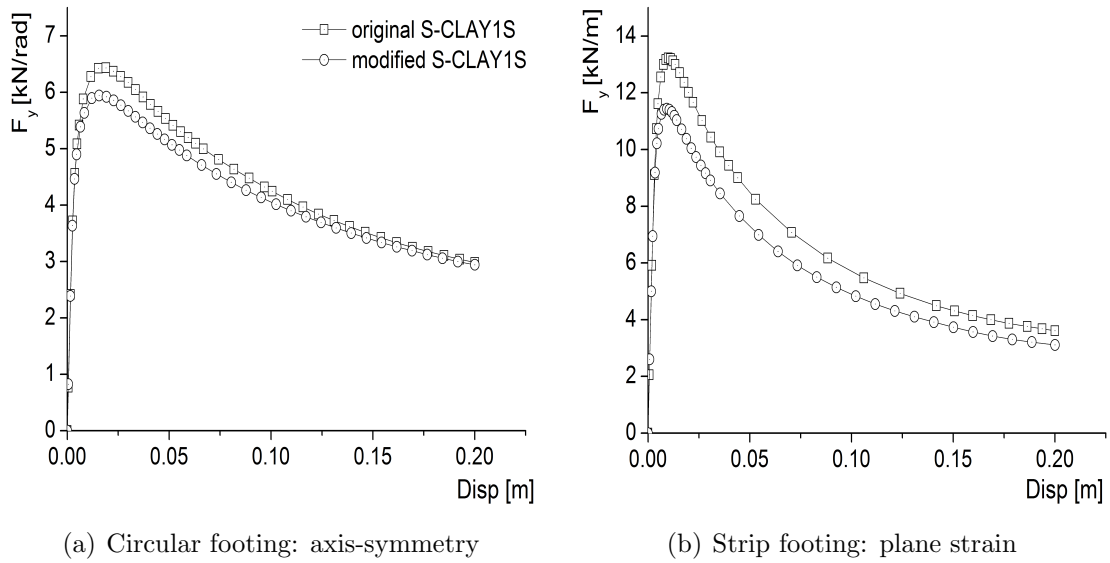


Figure 3.24: Effect of the shape of footing on the deviatoric plane

3.5 Summary

The S-CLAY1S model is implemented into the finite element code PLAXIS using an automatic substepping modified Newton-Raphson algorithm (MNR). The MNR algorithm performance was compared with explicit Euler-forward and implicit Euler-backward algorithms. The comparison showed that the MNR algorithm is very robust, but it is relatively expensive, as for each strain increment, the inverse of a iterative scheme matrix needs to be calculated.

The modified S-CLAY1S model is an extension of the original S-CLAY1S model which includes Lode angle dependency. The purpose was to incorporate Lode angle dependency to improve the model predictions in failure conditions especially in the axial extension. The model simulations comparison to the experimental data highlights the importance of Lode angle dependency. The modified S-CLAY1S model numerical implementation is verified using benchmark tests too.

Chapter 4

Implementation of Sekiguchi-Ohta (SO) models

In this chapter, the Sekiguchi-Ohta (SO) inviscid/viscid models are presented in their original formulation in triaxial stress space and general stress space. Discontinuity at the vertex of the models and numerical difficulties encountered in the stress derivatives of the yield surface are discussed. A novel hybrid implicit numerical algorithm is introduced to overcome the singularity of the models. The implementation of the general formulation of the model into the PLAXIS finite element code and the verification of the models are also given in this chapter.

4.1 Introduction

This chapter discusses implementation of Sekiguchi-Ohta (SO) inviscid model and viscid (time-dependent) model, which both account for initial stress-induced anisotropy proposed by Sekiguchi & Ohta (1977). These models have been widely used in geotechnical engineering practice in Japan. Because of this, there is a demand for the SO models to be implemented into the finite element codes.

The yield surface of the SO model falls into the category of non-smooth yield surface (see Fig. 4.1(a)) due to the corner along the K_0 -line. However, overcoming the singularity of the model at the corner of the yield surface at which the gradient is not defined has been a great challenge. This singularity problem is clearly seen for cases such as K_0 consolidation, self-weight consolidation, K_0 creep and ageing, as well as site responses when the level of the water table is changed (Pipatpongsa *et al.*,

2002a). Similar difficulty in implementation of original Cam-clay model (Roscoe *et al.*, 1963a) was also found due to the non-smooth yield surface. However, because of the position of the corner, this is a major issue with the SO models, as the stress paths are often close to K_0 region in many geotechnical applications such as foundation loading.

Since the SO models (Sekiguchi & Ohta, 1977) were developed, numerous papers have been published in relation to the numerical implementation of the models for engineering practice (Iizuka & Tachiabna, 2009; Pipatpongsa *et al.*, 2009b; Takeyama *et al.*, 2005; Pipatpongsa & Tachibana, 2005; Yuttapongtada *et al.*, 2003; Pipatpongsa *et al.*, 2002a; Pipatpongsa *et al.*, 2002b; Pipatpongsa *et al.*, 2001; Pipatpongsa & Ohta, 2000). Most of the papers adapt an algorithm to evaluate plastic flow at the corner of the yield surface proposed by Simo *et al.* (1988) using an intersecting multi-surface by employing Koiter's associated flow rule (Koiter, 1953). Based on this idea, when the stress comes to the corner of the SO yield surface, two activated yield loci referred to upper and lower yield surfaces intersecting each other as shown in Fig. 4.1(b) are used to calculate plastic flow using Koiter's rule as follows:

$$d\epsilon^p = \Delta\Lambda_L \frac{\partial f_L}{\partial \sigma'} + \Delta\Lambda_U \frac{\partial f_U}{\partial \sigma'} \quad (4.1)$$

where $\Delta\Lambda_L$ and $\Delta\Lambda_U$ are lower and upper yield surface plastic multipliers respectively.

The above mentioned algorithm has two problems when used in finite element analysis. The first problem is to identify the upper and lower yield surface in general stress space because the SO yield surface is a single yield surface with a vertex. The other problem associated with this algorithm is that when loading goes from one surface to the other surface (upper to lower or lower to upper), it is not possible to switch the yield surface to continue the calculation. This problem can produce a large error in finite element analysis.

In the case of the original Cam-clay model, to avoid this numerical uncertainty, recently Pipatpongsa & Ohta (2008) and Pipatpongsa *et al.* (2009a) proposed an alternative method using Koiter's flow rule to determine plastic flow at the vertex of the original Cam-clay model by additionally considering a constraint plane (see Fig. 4.2). However, there is no equivalent implementation proposed to the SO models by the above authors.

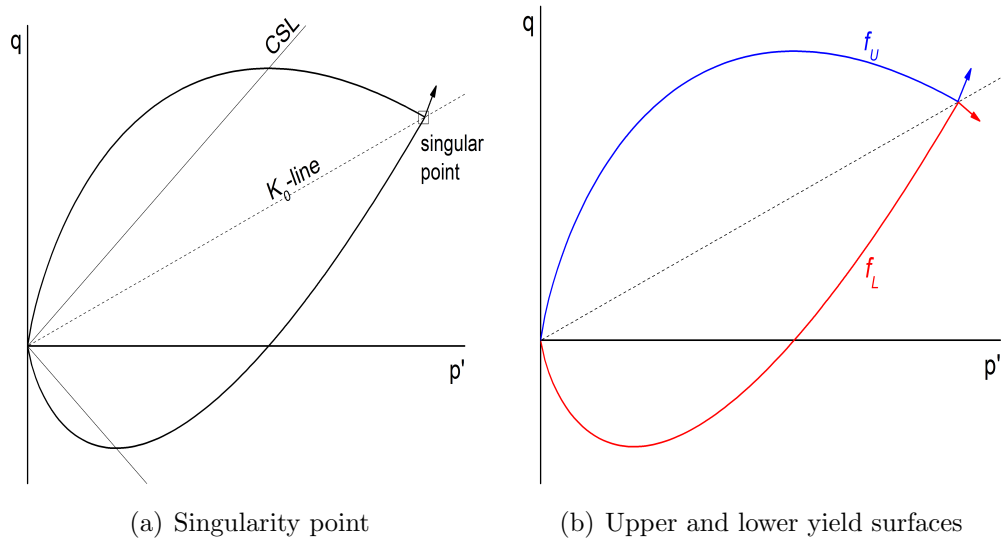


Figure 4.1: Yield surfaces of Sekiguchi-Ohta model

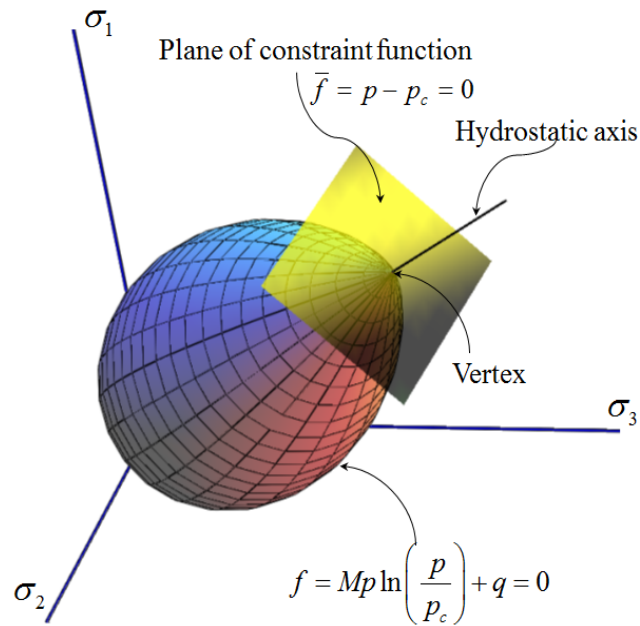


Figure 4.2: The original Cam-clay yield and the constraint functions in principal stress space (Pipatpongsa *et al.*, 2009a)

In this study, a constraint surface is applied to the SO inviscid model using single step backward implicit algorithm in the vertical direction and perpendicular to the K_0 line as shown in Fig. 4.3. This approach has not previously been applied to the SO models.

To verify the numerical implementation of the constraint yield surface added to the SO inviscid model, an integration point program (IPP) is used to simulate triaxial K_0 consolidation. The following initial stress and strain are applied; $p' = 71.5$ kPa, $q = 42.5$ kPa and 10% strain. In Fig. 4.4, the simulation of the SO inviscid model along the K_0 line with and without the constraint surface is presented. Fig. 4.4(a) shows stress along the the K_0 line without constraint surface. Due to the singularity at the corner, and that there is no special treatment for the singularity, stresses hover along the K_0 line. When additional constraint surface is placed exactly on the corner, it shows huge numerical error as shown in Fig. 4.4(b). In contrast to the other cases, it produces 3 times higher values for predicted stresses. The constraint surface is placed exactly at the yield surface vertex, the algorithm tries to evaluate the gradient at the vertex. This numerical error comes from the non-determination of derivative at the corner.

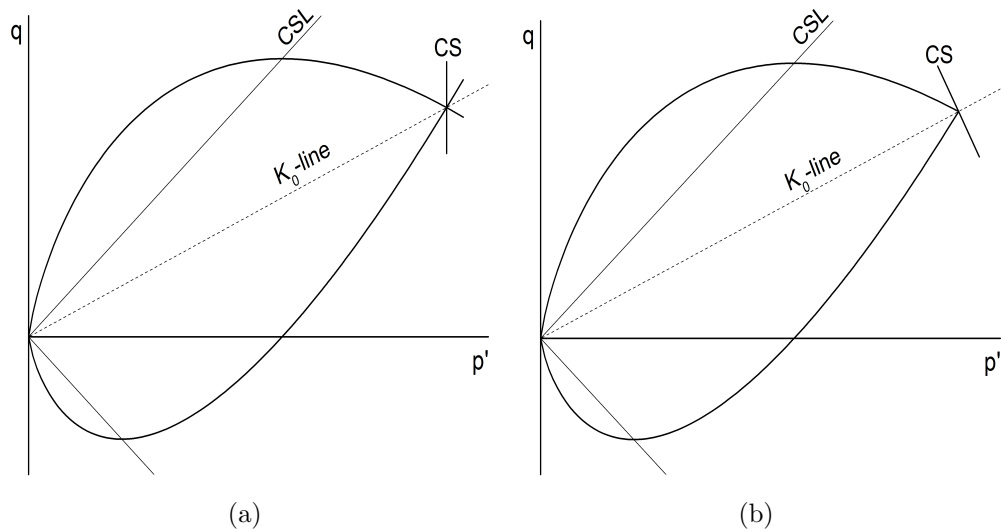


Figure 4.3: Constraint and yield surfaces of Sekiguchi-Ohta model

To avoid this non-determination, the constraint surface is placed 1% and 5% off from the corner of the value of p' at vertex. Fig. 4.4(c) and Fig. 4.4(d) show the simulation when the constraint surface is placed at 1% and 5% off from the corner respectively. The predicted stresses deviate slightly from the K_0 line but there is no numerical instability. It can be clearly seen that when the constraint surface is placed further away from the corner, the predicted results also deviate further from the K_0 line.

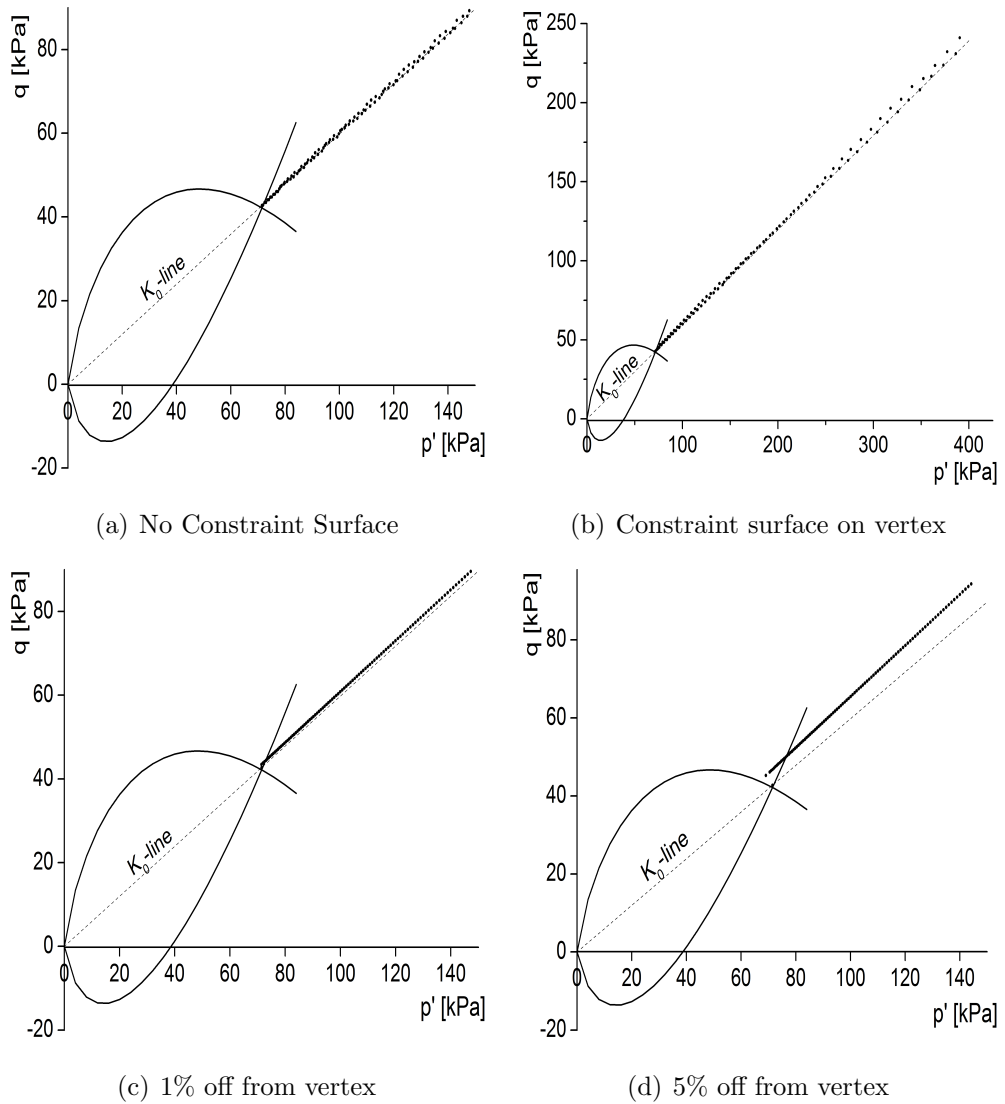


Figure 4.4: Numerical simulation of constraint surface

The following sections present a new hybrid implicit algorithm proposed and used to implement the SO models into the PLAXIS finite element code. Furthermore, the numerical implementation is validated at integration point program (IPP) level and subsequently a benchmark boundary value problem is described.

4.2 SO inviscid model

4.2.1 Mathematical formulation of the SO inviscid model

The yield function (f_y) of the SO inviscid model (see Fig. 4.5) is originally expressed by Sekiguchi & Ohta (1977) in the following equation where M is the critical state frictional parameter, p' is the mean stress, $p'_{m,0}$ is the effective mean stress at the end of K_0 consolidation, \bar{q} is the modified deviatoric stress to K_0 -line, ϵ_v^p is the volumetric plastic strain and D is the coefficient of dilatancy.

$$f_y = MD \ln\left(\frac{p'}{p'_{m,0}}\right) + D \frac{\bar{q}}{p'} - \epsilon_v^p \quad (4.2)$$

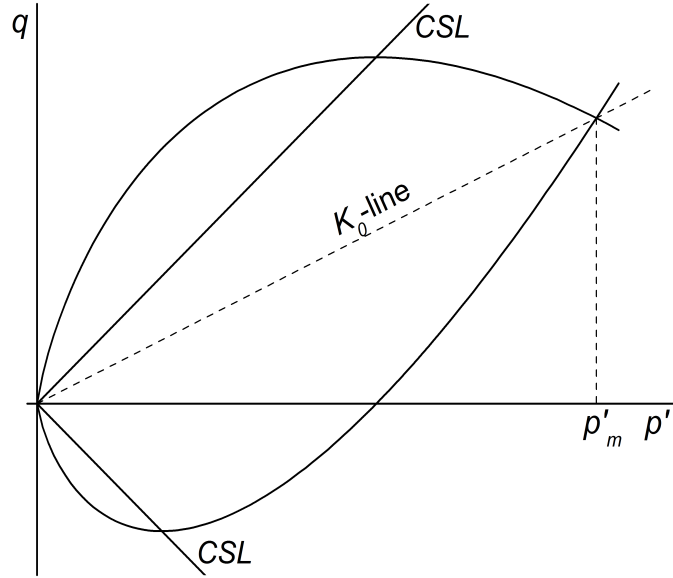


Figure 4.5: Sekiguchi-Ohta model yield surface in triaxial stress space

where $\bar{q} = \sqrt{3\bar{J}_2}$ and the modified second invariant \bar{J}_2 to the K_0 -line can be found as:

$$\bar{J}_2 = \frac{1}{2} \left(\bar{s}_{xx}^2 + \bar{s}_{yy}^2 + \bar{s}_{zz}^2 \right) + \bar{s}_{xy}^2 + \bar{s}_{yz}^2 + \bar{s}_{zx}^2 \quad (4.3)$$

where the vector \bar{s} can be derived as:

$$\bar{s} = s - p'\eta \quad (4.4)$$

where the vectors s and η are described as following (note that this definition is different from that used in Appendix A):

$$s = \begin{bmatrix} \sigma'_{xx} - p' \\ \sigma'_{yy} - p' \\ \sigma'_{zz} - p' \\ \sigma'_{xy} \\ \sigma'_{yz} \\ \sigma'_{zx} \end{bmatrix} \quad (4.5)$$

The value of η can be calculated by assuming initially normally consolidated situation:

$$\eta^T = \left(-\frac{1 - K_0^{nc}}{2 + 2K_0^{nc}} \quad 2\frac{1 - K_0^{nc}}{2 + 2K_0^{nc}} \quad -\frac{1 - K_0^{nc}}{2 + 2K_0^{nc}} \quad 0 \quad 0 \quad 0 \right) \quad (4.6)$$

From Eq.(4.3) and Eq.(4.4), \bar{s} is found:

$$\bar{s} = \begin{bmatrix} \sigma'_{xx} - p' - p'\eta_{xx} \\ \sigma'_{yy} - p' - p'\eta_{yy} \\ \sigma'_{zz} - p' - p'\eta_{zz} \\ \sigma'_{xy} - p'\eta_{xy} \\ \sigma'_{yz} - p'\eta_{yz} \\ \sigma'_{zx} - p'\eta_{zx} \end{bmatrix} \quad (4.7)$$

The hardening/softening of the materials induced by the plastic volumetric strain is given by the following equation:

$$p'_m = p'_{m,o} e^{\frac{(\epsilon_v^p - \epsilon_{v0}^p)}{(MD)}} \quad (4.8)$$

where D is defined as:

$$D = \frac{\lambda^* - \kappa^*}{M} \quad (4.9)$$

where λ^* and κ^* are the modified compression and swelling indices.

Using Eq.(4.2) and Eq.(4.8), the yield function of the SO model can be derived in an alternative form as follows:

$$f_y = MD \ln\left(\frac{p'}{p'_m}\right) + D\frac{\bar{q}}{p'} \quad (4.10)$$

The consistency condition (\dot{f}_y) of the yield function of the SO inviscid model is written as following:

$$\dot{f}_y = \frac{\partial f_y}{\partial \underline{\sigma}'} \Delta \underline{\sigma}' + \frac{\partial f}{\partial p'_m} \Delta p'_m = 0 \quad (4.11)$$

where $\Delta p'_m$ is derived from Eq.(4.8) is given as:

$$\Delta p'_m = \frac{p'_m}{MD} d\epsilon_v^p \quad (4.12)$$

Also from the incremental stress strain constitutive relationship; the change of stress is written as:

$$\Delta \underline{\sigma}' = [D^e] (\Delta \underline{\epsilon} - \Delta \underline{\epsilon}^p) \quad (4.13)$$

The SO inviscid model incorporates the associated plastic flow rule using the plastic multiplier $\Delta \Lambda$ which can be found as follows:

$$\Delta \underline{\epsilon}^p = \Delta \Lambda \frac{\partial f_y}{\partial \underline{\sigma}'} \quad (4.14)$$

$$\Delta \epsilon_v^p = \Delta \Lambda \frac{\partial f_y}{\partial p'} \quad (4.15)$$

By substituting Eq.(4.12) and Eq.(4.13) into Eq.(4.11), the following equation can be derived:

$$\dot{f}_y = \frac{\partial f_y}{\partial \underline{\sigma}'} : [D^e] (\Delta \underline{\epsilon} - \Delta \underline{\epsilon}^p) + \frac{\partial f}{\partial p'_m} \frac{p'_m}{MD} d\epsilon_v^p = 0 \quad (4.16)$$

By further substituting Eq.(4.14) and Eq.(4.15) into Eq.(4.16) the plastic multiplier $\Delta \Lambda$ can be derived as follows:

$$\Delta \Lambda = \frac{\frac{\partial f_y}{\partial \underline{\sigma}'} : [D^e] : \Delta \underline{\epsilon}}{\frac{\partial f_y}{\partial \underline{\sigma}'} [D^e] \frac{\partial f_y}{\partial \underline{\sigma}'} - \frac{\partial f}{\partial p'_m} \frac{p_m}{MD} \frac{\partial f}{\partial p'}} \quad (4.17)$$

4.2.2 Singularity of the SO inviscid model

The partial derivatives with respect to stress of the SO inviscid yield function can be written as follows:

$$\frac{\partial f_y}{\partial \sigma'} = \frac{\partial f_y}{\partial p'} \frac{\partial p'}{\partial \sigma'} + \frac{\partial f_y}{\partial \bar{q}} \frac{\partial \bar{q}}{\partial \sigma'} \quad (4.18)$$

where $\frac{\partial f_y}{\partial p'}$ and $\frac{\partial p'}{\partial \sigma'}$ can be derived as:

$$\frac{\partial f_y}{\partial p'} = \frac{MD}{p} - D \frac{\bar{s}}{p^2} \quad (4.19)$$

$$\frac{\partial p'}{\partial \sigma'} = \frac{1}{3} m \quad (4.20)$$

where $\underline{m}^T = (1 \ 1 \ 1 \ 0 \ 0 \ 0)$

And similarly the partial derivatives of $\frac{\partial f_y}{\partial \bar{q}}$ and $\frac{\partial \bar{s}}{\partial \sigma'}$ can be found as follows:

$$\frac{\partial f_y}{\partial \bar{s}} = \frac{D}{p'} \quad (4.21)$$

$$\frac{\partial \bar{q}}{\partial \sigma'} = \frac{3}{2\bar{q}} \frac{\partial \bar{J}_2}{\partial \sigma'} \quad (4.22)$$

The details of above derivation is given in Appendix C.

By substituting Eq.(4.19), Eq.(4.20), Eq.(4.21) and Eq.(4.22) into Eq. (4.18), the partial derivatives of yield function w.r.t stress can be derived as:

$$\frac{\partial f_y}{\partial \sigma'} = \left(\frac{MD}{p} - D \frac{\bar{s}}{p^2} \right) \left(\frac{1}{3} m \right) + \left(\frac{D}{p} \right) \left(\frac{3}{2\bar{q}} \frac{\partial \bar{J}_2}{\partial \sigma'} \right) \quad (4.23)$$

In the above formulation, when the stress comes to the corner on the yield surface moving along the K_0 consolidation line where $s = p'\eta$, the derivatives cannot be determined (see the corner in Fig. 4.6). In this case:

$$\bar{q} = 0 \quad \text{when} \quad s = p'\eta \quad (4.24)$$

The derivative of yield surface goes to infinity (singularity) when \bar{q} becomes zero.

$$\frac{\partial f_y}{\partial \sigma'} \rightarrow \infty \quad (4.25)$$

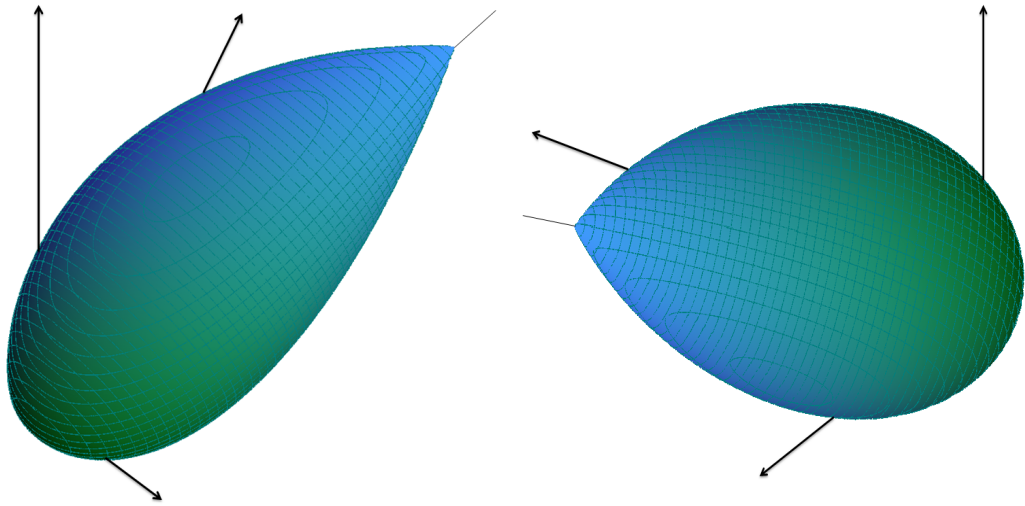
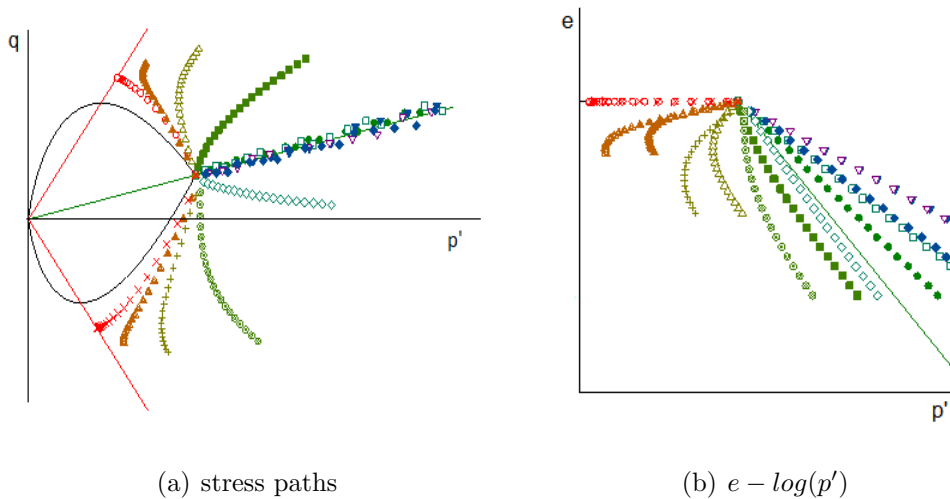


Figure 4.6: Sekiguchi-Ohta model yield surface in principal stress space



(a) stress paths

(b) $e - \log(p')$

Figure 4.7: Stress hovering along K_0 line during 1D consolidation (after Iizuka & Tachiabna, 2009)

Due to the singularity on the corner of the SO model yield surface, the plastic flow at a point of preconsolidated stress from the K_0 consolidation cannot be eval-

uated correctly. Previous work by Iizuka & Tachiabna (2009) has shown that the stresses hover along the K_0 line, see Fig. 4.7.

4.2.3 Implementation of the inviscid SO model into PLAXIS

As discussed earlier in this chapter, the difficulty of implementing the SO models into PLAXIS comes from the singularity at the yield surface. A novel hybrid implicit algorithm consisting of a modified Newton-Raphson (MNR) and Stolle's implicit algorithm (Stolle *et al.*, 1997) is introduced to overcome the singularity of the SO model. The MNR and Stolle's algorithms have their own limitations when integrating the SO model constitutive equations as discussed later. However, the aim of this study is to combine both algorithms as shown in Fig. 4.8 in such a way as to produce a robust algorithm which will enable the SO model to be implemented in PLAXIS.

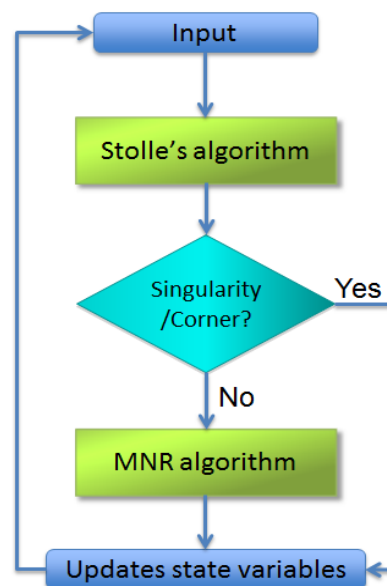


Figure 4.8: Hybrid algorithm for the SO model implementation

4.2.3.1 Modified Newton-Raphson (MNR) method

The MNR algorithm is discussed in detail in Chapter 3 for the S-CLAY1S model implementation in PLAXIS. However, this section covers the mathematical formu-

lation for MNR algorithm but not the algorithm in detail. Following equations are used to formulate an iterative procedure of MNR algorithm:

$$\Delta \underline{\epsilon} = \Delta \underline{\epsilon}^e + \Delta \underline{\epsilon}^p = \Delta \underline{\epsilon}^e + \Delta \Lambda \frac{\partial f_y}{\partial \underline{\sigma}'} \quad (4.26)$$

$$f_y = f_y(\underline{\sigma}', p'_m) \quad (4.27)$$

When there is a plasticity, the following conditions should be satisfied:

$$\Delta \underline{\epsilon} - \Delta \underline{\epsilon}^e - \Delta \Lambda \frac{\partial f_y}{\partial \underline{\sigma}'} = 0 \quad (4.28)$$

$$f(\underline{\sigma}', p'_m) = 0 \quad (4.29)$$

In total, there are 7 equations, 6 associated with strains and one related to the yield function. The 6 strain components can be written for the iteration procedure as follows;

$$\Delta \underline{\epsilon} - \Delta \underline{\epsilon}_k^e - \delta \Delta \underline{\epsilon}_{k+1}^e - (\Delta \Lambda_k + \delta \Delta \Lambda_{k+1}) \left(\frac{\partial f_y}{\partial \underline{\sigma}'_k} + \frac{\partial^2 f_y}{\partial^2 \underline{\sigma}'_{k+1}} \delta \underline{\sigma}'_{k+1} \right) = 0 \quad (4.30)$$

By neglecting higher order terms and restructuring the above system of equations, the following system of equations for modified Newton-Raphson iterative process can be derived.

$$\left(\mathbf{I} + \Delta \Lambda_k \frac{\partial^2 f_u}{\partial^2 \underline{\sigma}'_{k+1}} [D^e] \right) \delta \Delta \underline{\epsilon}_{k+1}^e + \frac{\partial f_y}{\partial \underline{\sigma}'_k} \delta \Delta \Lambda_{k+1} = \Delta \underline{\epsilon} - \Delta \underline{\epsilon}_k^e - \delta \Delta \underline{\epsilon}_{k+1}^e \quad (4.31)$$

The yield surface equation f_y is reformulated as following;

$$f_{y,k+1} = MD \ln \frac{p'}{p'_{m,k}} + D \frac{\bar{q}}{p'} - (\Delta \epsilon_{v,k+1}^p - \Delta \epsilon_{v,k}^p) \quad (4.32)$$

This can be further simplified in the form of iteration as follows;

$$f_{y,k+1} = f_{y,k} + \frac{\partial f_y}{\partial \underline{\sigma}'_k} [D^e] \delta \underline{\epsilon}_{k+1}^e - \delta \Delta \epsilon_{v,k+1}^p \quad (4.33)$$

For very small change of strain $\delta\Delta\epsilon_{v,k+1}^p = -\delta\Delta\epsilon_{v,k+1}^e$. Hence it is written as;

$$f_{y,k+1} = f_{y,k} + \frac{\partial f_y}{\partial \underline{\sigma}'_k} [D^e] \delta \underline{\epsilon}_{k+1}^e + \delta \Delta \epsilon_{v,k+1}^e \quad (4.34)$$

Since $f_{y,k+1} = 0$, the above equation is written in the following form:

$$\left(\underline{m} + \frac{\partial f_y}{\partial \underline{\sigma}'_k} [D^e] \right) \delta \underline{\epsilon}_{k+1}^e = -f_k \quad (4.35)$$

By combining Eq.(4.31) and Eq.(4.35), the system of non-linear equations can be written as a matrix form as follows:

$$\begin{bmatrix} \mathbf{I} + \Delta \Lambda_k \frac{\partial^2 f_y}{\partial^2 \underline{\sigma}'_k} [D^e] & \frac{\partial f_y}{\partial \underline{\sigma}'_k} \\ \underline{m} + \frac{\partial f_y}{\partial \underline{\sigma}'_k} [D^e] & 0 \end{bmatrix} \begin{Bmatrix} \delta \Delta \underline{\epsilon}_{k+1}^e \\ \delta \Delta \Lambda_{k+1} \end{Bmatrix} = \begin{Bmatrix} \Delta \underline{\epsilon} - \Delta \underline{\epsilon}_k^e - \Delta \Lambda_k \frac{\partial f_y}{\partial \underline{\sigma}'_k} \\ -f_{y,k} \end{Bmatrix} \quad (4.36)$$

From Eq.(4.36), elastic strain increments and plastic multiplier can be calculated and updated for the iteration as follows;

$$\Delta \epsilon_{k+1}^e = \Delta \epsilon_k^e + \delta \Delta \epsilon_{k+1}^e \quad (4.37a)$$

$$\Delta \underline{\epsilon}^p = \Delta \underline{\epsilon} - \Delta \underline{\epsilon}_{k+1}^e \quad (4.37b)$$

$$p_{m,k+1} = p_{m,0} \exp \frac{\Delta \epsilon_v^p}{\lambda * -\kappa * } \quad (4.37c)$$

$$\underline{\sigma}'_{k+1} = \underline{\sigma}'_0 + [D^e] \Delta \underline{\epsilon}^e \quad (4.37d)$$

The iteration can be stopped when changes are very small. The above system of non-linear equations of the SO inviscid model is implemented in a similar way as for the MNR method in Chapter 3.

Limitation of the MNR method

When \bar{q} becomes negative during the iteration process as shown in Fig.4.9, the modified Newton-Raphson algorithm shows random movement around the $p' - q$ plane. In Fig.4.9(a), it converges to a solution after 4 iterations whereas in Fig.4.9(b) it took 13 iterations to start real convergence. This is a major drawback of the MNR method.

Another drawback of this algorithm is that it cannot solve the singularity of the SO model when stress comes to the vertex of the SO model.

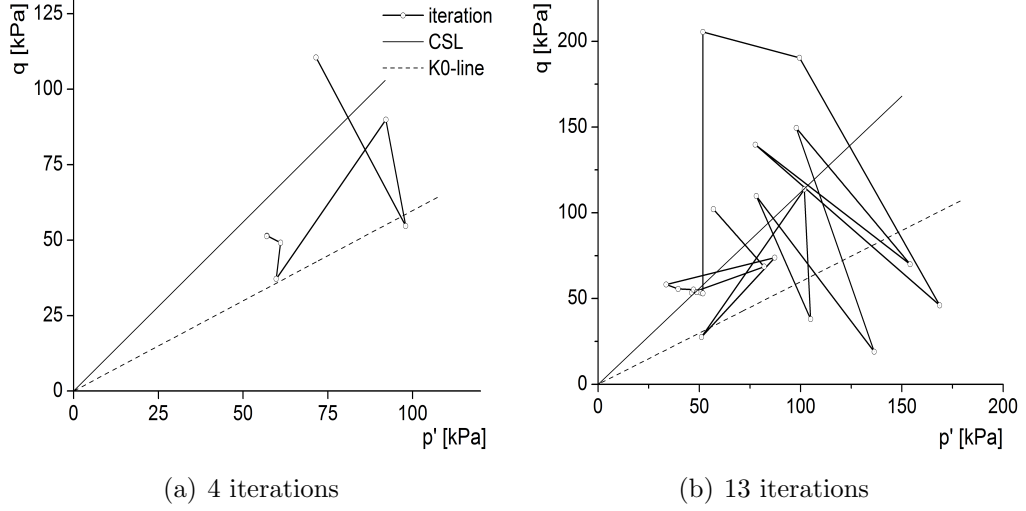


Figure 4.9: Random movement of the MNR algorithm

4.2.3.2 Stolle's implicit method

This implicit algorithm was first proposed by Stolle *et al.* (1997) to integrate the Soft Soil Creep (SSC) model to overcome the limitation of size of admissible time step of the semi implicit procedure developed by Stolle (1991). Stolle's algorithm is an efficient numerical algorithm, which solves the non-linear equation of the SO inviscid model using a stress update, which is first performed in the (p', q) space using radial return before the general stress space components are updated. A schematic view of the Stolle's algorithm is shown in Fig. 4.10. For a given elastic trial stress (p'^e, q^e) , a correct yield surface as shown in thick line in Fig. 4.10(a) should be found by varying p' value and corresponding q value. This procedure is detailed below.

The general stress components of the SO inviscid model can be written as a combination of p' and q as follows:

$$\bar{s} = s - p'\eta = \begin{bmatrix} \sigma'_{xx} - p' - p'\eta_{xx} \\ \sigma'_{yy} - p' - p'\eta_{yy} \\ \sigma'_{zz} - p' - p'\eta_{zz} \\ \sigma'_{xy} - p'\eta_{xy} \\ \sigma'_{yz} - p'\eta_{yz} \\ \sigma'_{zx} - p'\eta_{zx} \end{bmatrix} \quad (4.38)$$

When the value of p' and/or \bar{q} changes, the general stress components can be back-calculated using the elastic stress component as follows;

$$\underline{\sigma}'(p', \bar{q}) = \underline{m}p' + p'\eta + \frac{\bar{q}}{\bar{q}^e} \left\{ \begin{array}{l} \sigma_{xx}^{le} - p'^e - p'^e\eta_{xx} \\ \sigma_{yy}^{le} - p'^e - p'^e\eta_{yy} \\ \sigma_{zz}^{le} - p'^e - p'^e\eta_{zz} \\ \sigma_{xy}^{le} - p'^e\eta_{xy} \\ \sigma_{yz}^{le} - p'^e\eta_{yz} \\ \sigma_{zx}^{le} - p'^e\eta_{zx} \end{array} \right\} \quad (4.39)$$

$$\underline{\sigma}'(p', \bar{q}) = \underline{m}p' + p'\eta + \frac{\bar{q}}{\bar{q}^e} \bar{s}^e \quad (4.40)$$

Supposing the calculation starts assuming a value of p' , and the p' is on the yield surface, the elastic volumetric strain can be derived as follows;

$$\Delta\epsilon_v^e = \frac{p' - p'_0}{K} \quad (4.41)$$

where p'_0 is initial p' value and K is bulk modulus. Since the given total strain increment is known, the plastic volumetric strain can be calculated as follows;

$$\Delta\epsilon_v^p = \Delta\epsilon_v - \Delta\epsilon_v^e \quad (4.42)$$

From the hardening function, preconsolidation pressure p'_m can be calculated as follows:

$$p_m = p_{m,0} \exp \frac{\Delta\epsilon_v^p}{MD} \quad (4.43)$$

The value for \bar{q} can be calculated from the assumption previously made that the stress is on the yield surface as follows:

$$\bar{q} = -Mp' \ln \frac{p'}{p'_m} \quad (4.44)$$

By using the Eq.(4.39), 6 general stress components can be calculated. The elastic strain increments can be calculated using following form:

$$\Delta\epsilon^e = [D^e]^{-1} \left(\underline{\sigma}'(p', \bar{q}) - \underline{\sigma}'_0 \right) \quad (4.45)$$

Once the stresses and plastic strains are calculated, the plastic multiplier $\Delta\Lambda$ can be found using the following equations:

$$\Delta\Lambda = \frac{\Delta\epsilon_v^p}{\partial f_y / \partial p'} \quad (4.46)$$

The plastic multiplier $\Delta\Lambda$ and plastic strain increments are calculated for the updated stress, and the stress can be updated from the plastic strain increment $\Delta\epsilon^p$ is found as follows:

$$\Delta\epsilon^p = \Delta\Lambda \frac{\partial f}{\partial \sigma} \quad (4.47)$$

Using above plastic strain increment, plastic stress increment can be calculated.

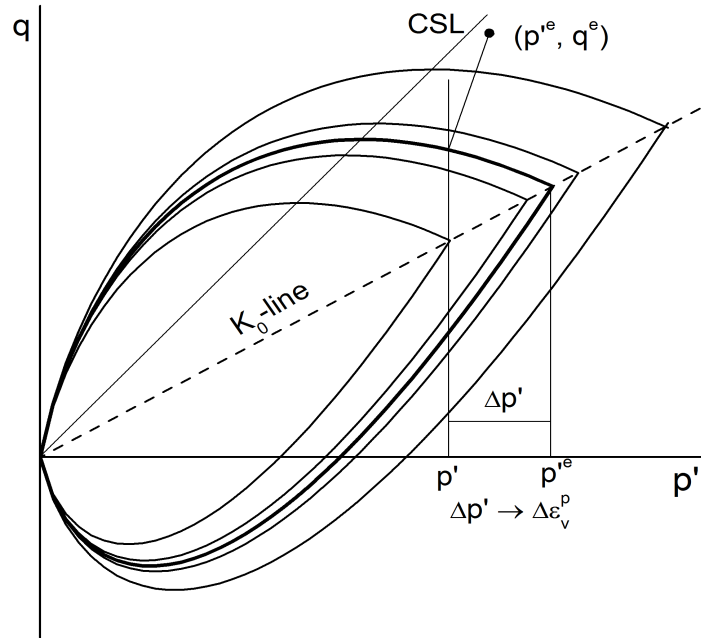
$$\Delta\sigma^p = [D^e] \Delta\epsilon^p \quad (4.48)$$

From above stress, the final temporary stress can be found as;

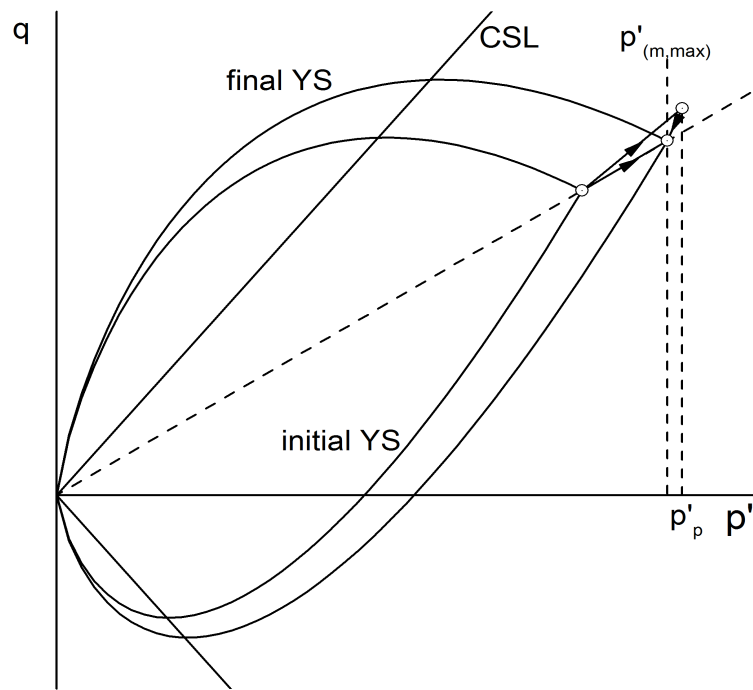
$$\sigma^{et} = \sigma + \Delta\sigma^p \quad (4.49)$$

If there is no difference between σ^e and σ^{et} , iteration can be stopped; otherwise a new p' is chosen and calculation is repeated from Eq.4.41. When the stress come to the vertex of the model, stress is updated as shown in Fig.4.10(b).

Assumed p' should be modified until $\bar{q}^e - \bar{q}_t^e \approx 0$ have a small difference. The Stolle implicit algorithm to implement the SO inviscid model is summarized in Algorithms 12 and 13.



(a) Find a correct yield surface



(b) Stress update at the vertex

Figure 4.10: Schematic view of Stolle's implicit algorithm

Algorithm 12 : Algorithm to find best p' value

GET: $\{\underline{\sigma}'_0\}$, \mathcal{H}_0 , $\{\Delta\epsilon\}$, δ , $RTOL$ and $FTOL$

Calculate: $p'_0 = 1/3tr[\underline{\sigma}'_0]$ and $\Delta\epsilon_v$

Calculate: $\{\Delta\underline{\sigma}'\}^e = [D^e]\{\Delta\epsilon\}$ and $\{\underline{\sigma}'\}^e = \{\underline{\sigma}'_0\} + \{d\underline{\sigma}'\}^e$

Calculate: p'_e and $\bar{q}^e = \sqrt{3\bar{J}_2}$ and \bar{J}_2 from Eq.4.3

if $(F_y(\{\underline{\sigma}'\}^e, \mathcal{H}_0) \leq FTOL)$ **return** ! purely elasticity

! Calculate maximum value of p'_m

1 Continue

Calculate: $\Gamma = p'_e - K * \Delta\epsilon_v^p - p'_{m0} * \exp(\frac{\Delta\epsilon_v^p}{MD})$

Calculate: $d\Gamma = -K * -p'_{m0} * \exp(\frac{\Delta\epsilon_v^p}{MD})/MD$

$$\delta\epsilon_v^p = -\frac{\Gamma}{d\Gamma}$$

$$\Delta\epsilon_v^p = \Delta\epsilon_v^p + \delta\epsilon_v^p$$

if $(\Gamma > FTOL)$ **then**

GO TO 1

end if

Calculate: $p'_m = p'_{m0} * \exp(\frac{\Delta\epsilon_v^p}{MD})$

$$p'_{m,max} = p'_m$$

! Do iteration to calculate stresses & strains

CALL Algorithm 13

!Update stresses

$$p' = p'_-$$

$$\text{Calculate: } \Delta\epsilon_v^e = \frac{p' - p'_0}{K}$$

Update: p'_m

Calculate: \bar{q} from Eq. 4.44

Calculate: $\underline{\sigma}'^t$ from Eq. 4.39

return

Algorithm 13 : Stolle implicit algorithm of the SO inviscid model

GET: p'_{max} ASSUME: $p' = (1 - 10^{-6})p'_{max}$ **5 Continue** $it = it + 1$ **while** $k = 0, 1$ **do** **if** $(k = 1) \Rightarrow p' = p' + \delta$ Calculate: $\Delta\epsilon_v^e = \frac{p' - p'_0}{K}$ and $\Delta\epsilon_v^p = \Delta\epsilon_v - \Delta\epsilon_v^e$ Update: p'_{mi} from Eq. 4.43 Calculate: \bar{q} from Eq. 4.44 Calculate: $\underline{\sigma}'^t$ from Eq. 4.39 Calculate: $\partial f_y / \partial \underline{\sigma}'^t$ and $\Delta\Lambda = \frac{\Delta\epsilon_v^p}{\partial f_y / \partial p'^t}$ Calculate: $\Delta\epsilon^p = \Delta\Lambda \frac{\partial f_y}{\partial \underline{\sigma}'^t}$ and $\underline{\sigma}'^{e,t} = \underline{\sigma}'^t + [D^e]\Delta\epsilon^p$ Calculate: $p'^{e,t}$ and $\bar{q}^{e,t}$ **if** $(k=0)$ **then** Calculate: $dq_a = \bar{q}^{e,t} - \bar{q}^e$ **else** Calculate: $dq_b = \bar{q}^{e,t} - \bar{q}^e$ and $dq = (dq_b - dq_a) / \delta$ Calculate: $p'_- = p' - dq_b / dq$ **end if****end while****if** $(p'_- > p'_{max})$ **then** $p' = p'_{max}$ $dq_a = 0$ **return****end if****if** $(Abs(dq_a) > RTOL)$ **then** **GO TO 5****end if****return**

Limitation of Stolle's implicit method

This algorithm has a problem that when there is shear component given into the input, it produces a slight error. This slight error is caused by the back calculation of general stress components using p' and \bar{q} in Eq.(4.39). Table.4.1 shows the comparison of the MNR and alternative algorithm when a shear component is given during undrained shearing test.

Table 4.1: Comparison of the MNR and Stolle's algorithm

	Initial stress	the MNR final stress	Stolle's method final stress
σ_{xx}	57.24886	56.52565	56.47672
σ_{yy}	100.0000	95.98568	96.05137
σ_{zz}	57.24886	56.52565	56.47672
σ_{xy}	1.000000	0.545683	0.704445

4.2.4 Verification of the SO inviscid model

In order to test the performance of the numerical implementation of the SO inviscid model, three different tests were carried out using an integration point program (IPP). The verification and the performance of the implementation were done through the simulation of an undrained triaxial test, radial strain controlled triaxial test and triaxial compression along K_0 line. An arbitrary set of soil parameters to represent clay were used for the verification of the model, the parameters are given in Table. 4.2.

Table 4.2: Material parameters used for the SO inviscid model verification

M	κ^*	λ^*	D	e_0	K_0^{nc}	ν
1.12	0.02368	0.1368	0.101	1.5	0.5725	0.364

Undrained Triaxial test

The initial state variables were generated from an initial vertical stress of $\sigma_y = 100kPa$ and an OCR of 1.0. In order to compare accuracy of the integration method, undrained compression and extension tests were repeated with 1, 5, 10 and 50 steps for an applied strain of 10%. Fig.4.11 and 4.12 shows undrained compression and

extension simulations respectively. It can be seen that the influence of the step size is relatively insignificant, and therefore the simulations results are satisfactory.

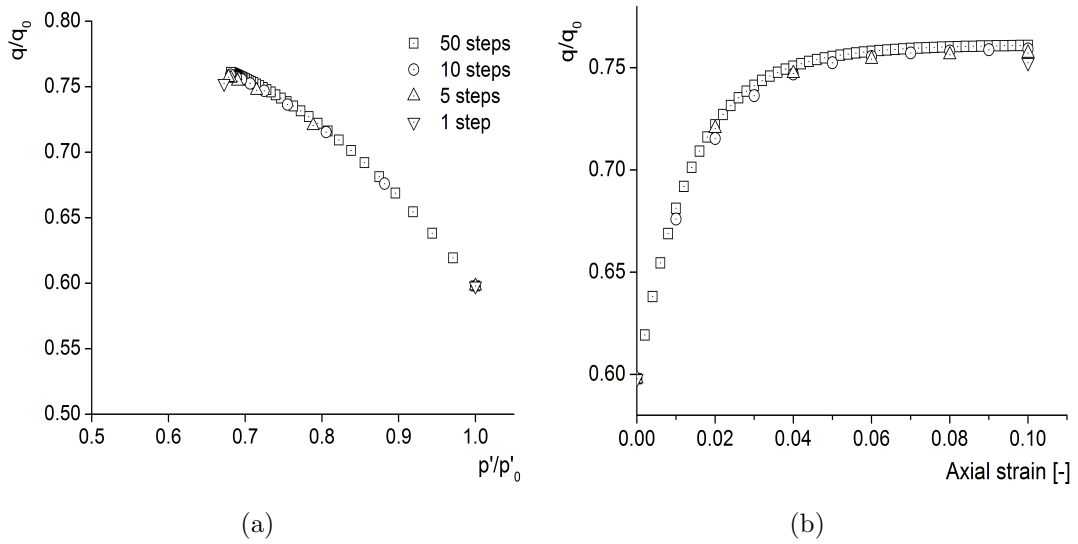


Figure 4.11: Undrained triaxial compression

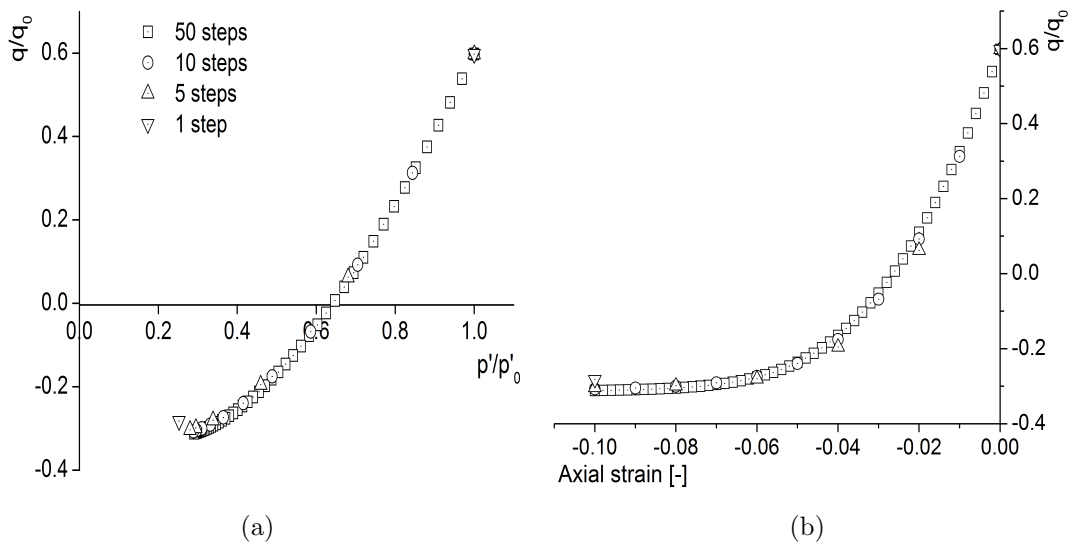


Figure 4.12: Undrained triaxial extension

Triaxial compression and extension

The initial state variables were generated from an initial vertical stress of $\sigma_y = 100kPa$ and an OCR of 1.0. The radial strain increment was simulated as β varies from -0.5 to -0.26 using a step size of 0.01 applied in 10 steps and given strain $\epsilon_a = 1\%$ as $\epsilon^T = \{\beta\epsilon_a, \epsilon_a, \beta\epsilon_a, 0, 0, 0\}$. Fig.4.13(a) shows the simulation of compression in the $p' - q$ space. Another triaxial test was simulated as β varies from -0.5 to 0.5 in step size of 0.01 applied in 10 steps and given strain $\epsilon_a = -1\%$ as $\epsilon^T = \{\beta\epsilon_a, \epsilon_a, \beta\epsilon_a, 0, 0, 0\}$. The results of the simulation is plotted in $p' - q$ space as shown in Fig.4.13(b), clearly show that there are no apparent numerical errors.

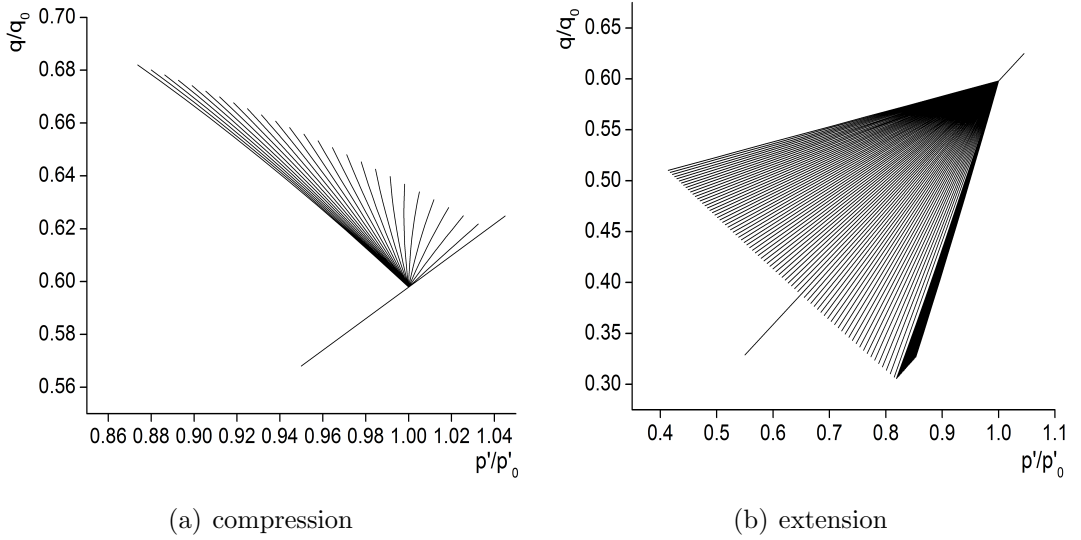
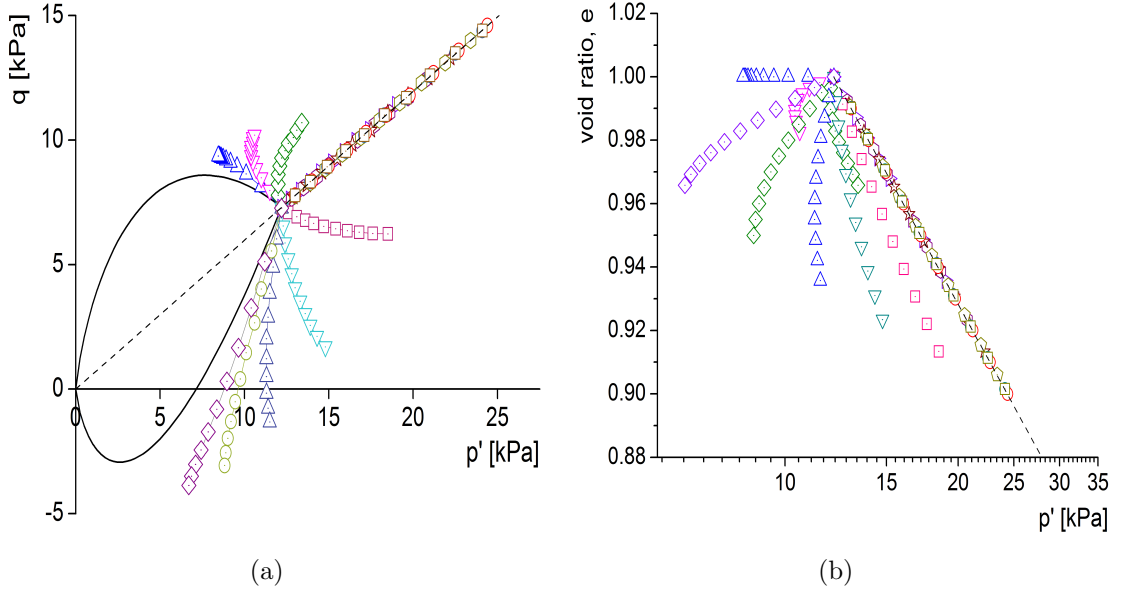


Figure 4.13: Triaxial simulation

Triaxial compression along K_0 line

Fig. 4.14 shows the performance of the hybrid algorithm to overcome the singularity of the SO inviscid model. The initial values of p' and q are 12.2 kPa and 7.27 kPa respectively. It can be seen that stress points lie along the K_0 line with no hovering and no stress points lie above the λ line as it is shown in Fig. 4.7.


 Figure 4.14: Triaxial compression simulation along K_0 -line

4.3 SO viscid model

4.3.1 Mathematical formulation of the SO viscid model

Sekiguchi & Ohta (1977) proposed an elasto-viscoplastic plastic constitutive model, which accounts for creep or relaxation, called the SO viscid model. In this section, the SO viscid model is formulated so that it can be implemented in PLAXIS. In the SO viscid model, the volume change due to creep (secondary consolidation) is linearly related to time expressed in a logarithmic scale (Takeyama *et al.* (2007)). An important distinction from the overstress theory (Perzyna, 1966b) is that the current stress state can not be outside the yield surface therefore the consistency condition is applicable. In Perzyna theory, the stress state is allowed to be outside the yield surface and directly define the plastic relaxation equations in stress space.

The flow function F of viscid model is written as follows:

$$F = C_\alpha \ln \left(1 + \frac{\dot{\epsilon}_o t}{C_\alpha} \exp \left(\frac{f(\sigma')}{C_\alpha} \right) \right) - \epsilon_v^{vp} = 0 \quad (4.50)$$

where C_α is coefficient of secondary consolidation, t is the real time, $\dot{\epsilon}_o$ is the initial volumetric strain rate and ϵ_v^{vp} is viscoplastic volumetric strain. The scalar function

$f(\sigma')$ can be defined as follows:

$$f(\sigma') = MD \ln \frac{p'}{p'_0} + D \frac{\bar{q}}{p'} \quad (4.51)$$

The flow function F can be transformed to a scalar function and hardening parameter as follows:

$$g(\sigma', h) = f(\sigma') - h(\epsilon_v^{vp}, t) = 0 \quad (4.52)$$

where the hardening parameter $h(\epsilon_v^{vp}, t)$ is defined as follows:

$$h(\epsilon_v^{vp}, t) = C_\alpha \ln \left\{ \frac{c_\alpha}{\dot{\nu}_o t} \left[\exp \left(\frac{\epsilon_v^{vp}}{c_\alpha} \right) - 1 \right] \right\} \quad (4.53)$$

The initial time to calculate the hardening parameter should not be zero ($t \neq 0$) because it is not determined hence it is assumed that $t = 1E-7$. Another assumption made for a starting condition is that the hardening parameter h is equal to zero, $h = 0$, hence the initial visco-plastic volumetric strain is calculated as follows:

$$C_\alpha \ln \left\{ \frac{c_\alpha}{\dot{\nu}_o t} \left[\exp \left(\frac{\epsilon_v^{vp}}{c_\alpha} \right) - 1 \right] \right\} = 0 \quad (4.54)$$

$$\epsilon_{vo}^{vp} = C_\alpha \ln \left\{ \frac{\dot{\nu}_o t}{c_\alpha} + 1 \right\} = 0 \quad (4.55)$$

The consistency condition of flow function for the SO viscid model can be written as follows:

$$\dot{F} = \frac{dF}{dt} = 0 \quad (4.56)$$

$$\dot{F} = \frac{\partial F}{\partial \sigma'} \dot{\sigma}' + \frac{\partial F}{\partial \epsilon_v^{vp}} \dot{\epsilon}_v^{vp} + \frac{\partial F}{\partial t} \quad (4.57)$$

The SO viscid model assumes the associated flow rule and viscoplastic strains can be derived as follows:

$$\dot{\epsilon}^{vp} = \Delta \Lambda' \frac{\partial F}{\partial \sigma'} \quad (4.58)$$

$$\dot{\epsilon}_v^{vp} = \Delta\Lambda' \frac{\partial F}{\partial p'} \quad (4.59)$$

where $\Delta\Lambda'$ is rate of visco-plastic multiplier. The increment of stress can be written as;

$$\dot{\sigma}' = [D^e](\dot{\epsilon} - \dot{\epsilon}^{vp}) \quad (4.60)$$

$$\dot{\sigma}' = [D^e](\dot{\epsilon} - \Delta\Lambda' \frac{\partial F}{\partial \sigma'}) \quad (4.61)$$

By combining Eq.(4.57), Eq.(4.59) and Eq.(4.61);

$$\dot{F} = \frac{\partial F}{\partial \sigma'} [D^e](\dot{\epsilon} - \Delta\Lambda' \frac{\partial F}{\partial \sigma'}) + \frac{\partial F}{\partial \epsilon_v^{vp}} \Delta\Lambda' \frac{\partial F}{\partial p'} + \frac{\partial F}{\partial t} = 0 \quad (4.62)$$

From the above equation, the plastic multiplier can be derived as;

$$\Delta\Lambda' = \frac{\frac{\partial F}{\partial \sigma'} [D^e] \dot{\epsilon} + \frac{\partial F}{\partial t}}{\frac{\partial F}{\partial \sigma'} [D^e] \frac{\partial F}{\partial \sigma'} - \frac{\partial F}{\partial \epsilon_v^{vp}} \frac{\partial F}{\partial p'}} \quad (4.63)$$

where the derivatives can be found from the following equations:

$$\frac{\partial F}{\partial \sigma'} = \frac{\partial f(\sigma')}{\partial \sigma'} \quad (4.64a)$$

$$\frac{\partial F}{\partial p'} = \frac{\partial f(\sigma')}{\partial p'} \quad (4.64b)$$

$$\frac{\partial F}{\partial \epsilon_v^{vp}} = -1 \quad (4.64c)$$

By combining Eq.(4.63) and Eq.(4.64), the plastic multiplier $\Delta\Lambda'$ can be derived as follows:

$$\Delta\Lambda' = \frac{\frac{\partial f(\sigma')}{\partial \sigma'} [D^e] \dot{\epsilon} + \frac{\partial F}{\partial t}}{\frac{\partial f(\sigma')}{\partial \sigma'} [D^e] \frac{\partial f(\sigma')}{\partial \sigma'} + \frac{\partial f(\sigma')}{\partial p'}} \quad (4.65)$$

From Eq.(4.61) and Eq.(4.65), we can derive the stress increment as follows;

$$\dot{\sigma}' = [D^e]\dot{\epsilon} - [D^e] \left[\frac{\frac{\partial f(\sigma')}{\partial \sigma'} [D^e] \dot{\epsilon} + \frac{\partial F}{\partial t}}{\frac{\partial f(\sigma')}{\partial \sigma'} [D^e] \frac{\partial f(\sigma')}{\partial \sigma'} + \frac{\partial f(\sigma')}{\partial p'}} \right] \frac{\partial f(\sigma')}{\partial \sigma'} \quad (4.66)$$

Change of stress can be written in the following incremental form:

$$d\sigma' = \Delta t \dot{\sigma}' \quad (4.67)$$

By substituting Eq.(4.67) into Eq.(4.66):

$$d\sigma' = [D^e]\dot{\epsilon}\Delta t - [D^e] \left[\frac{\frac{\partial f(\sigma')}{\partial \sigma'} [D^e] \dot{\epsilon}\Delta t + \frac{\partial F}{\partial t}\Delta t}{\frac{\partial f(\sigma')}{\partial \sigma'} [D^e] \frac{\partial f(\sigma')}{\partial \sigma'} + \frac{\partial f(\sigma')}{\partial p'}} \right] \frac{\partial f(\sigma')}{\partial \sigma'} \quad (4.68)$$

Stress and strain can be written in the following incremental form:

$$d\sigma' = [D^e]d\epsilon - [D^e] \left[\frac{\frac{\partial f(\sigma')}{\partial \sigma'} [D^e]d\epsilon + \frac{\partial F}{\partial t}\Delta t}{\frac{\partial f(\sigma')}{\partial \sigma'} [D^e] \frac{\partial f(\sigma')}{\partial \sigma'} + \frac{\partial f(\sigma')}{\partial p'}} \right] \frac{\partial f(\sigma')}{\partial \sigma'} \quad (4.69)$$

Similarly the plastic multiplier can also be written in the incremental form as follows:

$$\Delta\Lambda = \Delta\Lambda' \Delta t \quad (4.70)$$

$$\Delta\Lambda = \frac{\frac{\partial f(\sigma')}{\partial \sigma'} [D^e]d\epsilon + \frac{\partial F}{\partial t}\Delta t}{\frac{\partial f(\sigma')}{\partial \sigma'} [D^e] \frac{\partial f(\sigma')}{\partial \sigma'} + \frac{\partial f(\sigma')}{\partial p'}} \quad (4.71)$$

where $\frac{\partial f}{\partial \sigma'}$ is same as in Sekiguchi-Ohta inviscid model; see Section 2 for details of derivatives. Derivative of $\frac{\partial F}{\partial t}$ can be derived as follows:

$$\frac{\partial F}{\partial t} = \left[i_0 \exp\left(\frac{f(\sigma') - \epsilon_v^{vp}}{C_\alpha}\right) \right] \quad (4.72)$$

$\Delta t \frac{\partial F}{\partial t}$ in Eq.(4.71) is written as follows:

$$\Delta t \frac{\partial F}{\partial t} = \Delta t \dot{v}_0 \exp\left(\frac{f(\sigma') - \epsilon_v^{vp}}{C_\alpha}\right) \quad (4.73)$$

Takeyama *et al.* (2005) reported that $\Delta t \frac{\partial F}{\partial t}$ is not stable as written above. By using Maclaurin expansion, reformulation is done as follows;

$$\Delta t \dot{v}_0 \exp\left(\frac{f(\sigma) - \epsilon_v^{vp}}{C_\alpha}\right) \approx C_\alpha \ln \left\{ 1 + \frac{\Delta t}{C_\alpha} \dot{v}_0 \exp\left(\frac{f(\sigma) - \epsilon_v^{vp}}{C_\alpha}\right) \right\} \quad (4.74)$$

4.3.2 Singularity of the SO viscid model

As mentioned above, the stress derivatives $\frac{\partial f}{\partial \sigma'}$ of viscid model is the same as inviscid yield function. The derivative of $\frac{\partial f}{\partial \sigma'}$ goes to infinity (singularity) when stress comes to the corner of flow function ($\bar{q} = 0$).

$$\frac{\partial f(\sigma')}{\partial \underline{\sigma'}} \rightarrow \infty \quad (4.75)$$

To overcome the singularity of the SO viscid model, the hybrid algorithm discussed earlier is also used for this model.

4.3.3 Dry side of the SO viscid model

In Fig. 4.15, the point A represents the point of the yield curve with horizontal slope. If a soil element yields at a point to the right of A, it is said to be on the wet side, and to the left of A is on the dry side. Takeyama *et al.* (2005) reported first that when soil element yielding takes place in the dry side of the SO viscid model, the model experiences a problem in convergence. A triaxial undrained simulation was carried out by Takeyama *et al.* (2005) with different OCR values, and when the stress comes to the dry side it shows numerical instability as shown in Fig. 4.16.

To avoid this divergence problem on the dry side of the model and to improve the overall convergence of the model implementation, the SO viscid model is implemented in such a way that the model does not include the dry side, see Fig. 4.17.

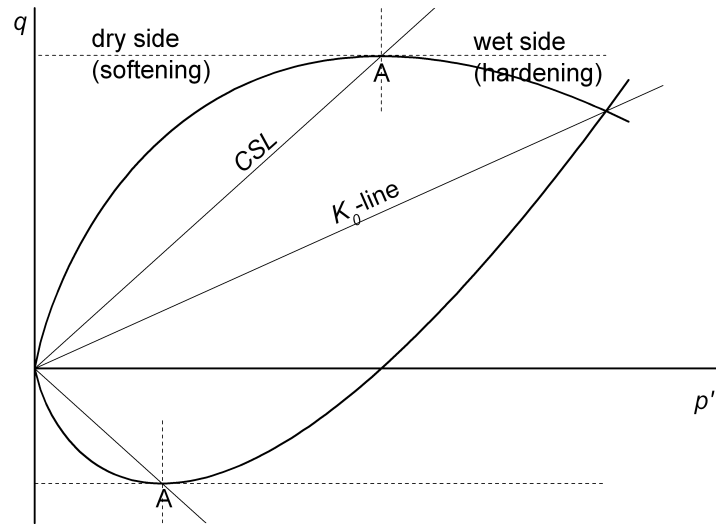


Figure 4.15: Sekiguchi-Ohta viscid model dry/wet side in principal stress space

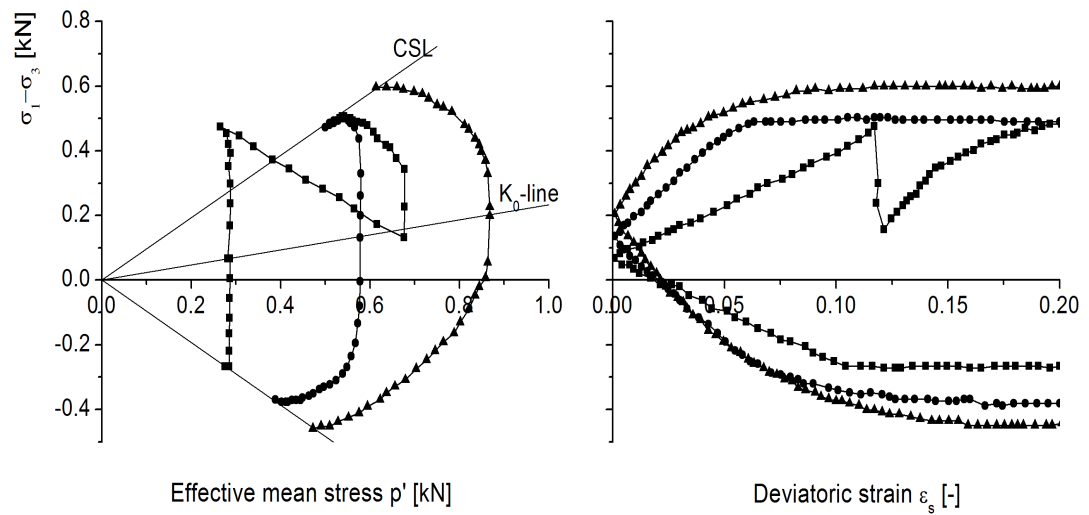


Figure 4.16: Undrained simulation at different OCR values (after Takeyama *et al.*, 2005)

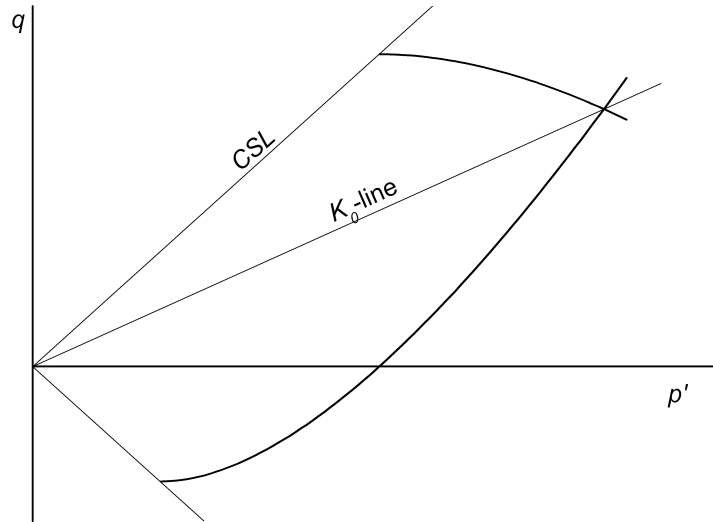


Figure 4.17: Sekiguchi-Ohta model viscid model in wet side alone

4.3.4 Verification of the SO viscid model

The verification of the SO viscid model was carried out in integration point program (IPP) by simulating triaxial laboratory tests. The model was validated against the simulation produced by Sekiguchi & Ohta (1977). Undrained stress-strain response was presented under conventional K_0 consolidation triaxial conditions to demonstrate the effect of strain rate. Table 4.3 shows the material parameters used in this simulation. Fig.4.18 shows the simulated triaxial undrained paths, on both compression and extension. The dots are from the original simulation of Sekiguchi & Ohta (1977) and the continuous line shows the implicit implementation in PLAXIS. These can be observed to be in close agreement.

Fig. 4.19 verifies the performance of the hybrid algorithm to overcome the singularity of the SO viscid model. The initial values of p' and q are 71.2 kPa and 47.27 kPa respectively. The simulation shows no hovering along the K_0 line. It can be concluded that the hybrid algorithm works robustly to handle the vertex of the model.

Fig.4.20(a) and 4.20(b) shows triaxial undrained simulations at different OCR values and unloading triaxial simulations in compression and extension respectively. In order to verify the dry side cut off from the SO inviscid model, undrained compression and extension tests were repeated with OCR values of 1, 1.5, 2, 4 and 10 for applied 10% of strain. The results appear to be stable.

Table 4.3: Material parameters used for the SO viscid model verification (Sekiguchi & Ohta, 1977)

Soil constants						
M	κ^*	λ^*	D	e_0	K_0^{nc}	ν'
0.96	0.0199	0.0921	0.053	2.0	0.50	0.394
Additional viscosity parameters						
c_α	$\dot{\nu}_o$					
0.0029	1.0 E-5					

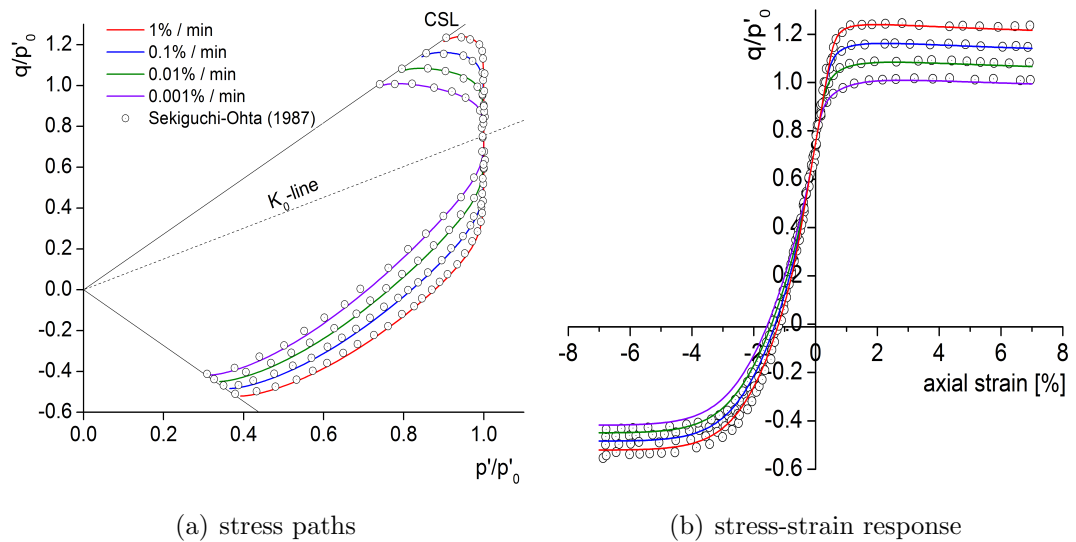


Figure 4.18: Comparison of effect of strain rate with Sekiguchi & Ohta (1977) results

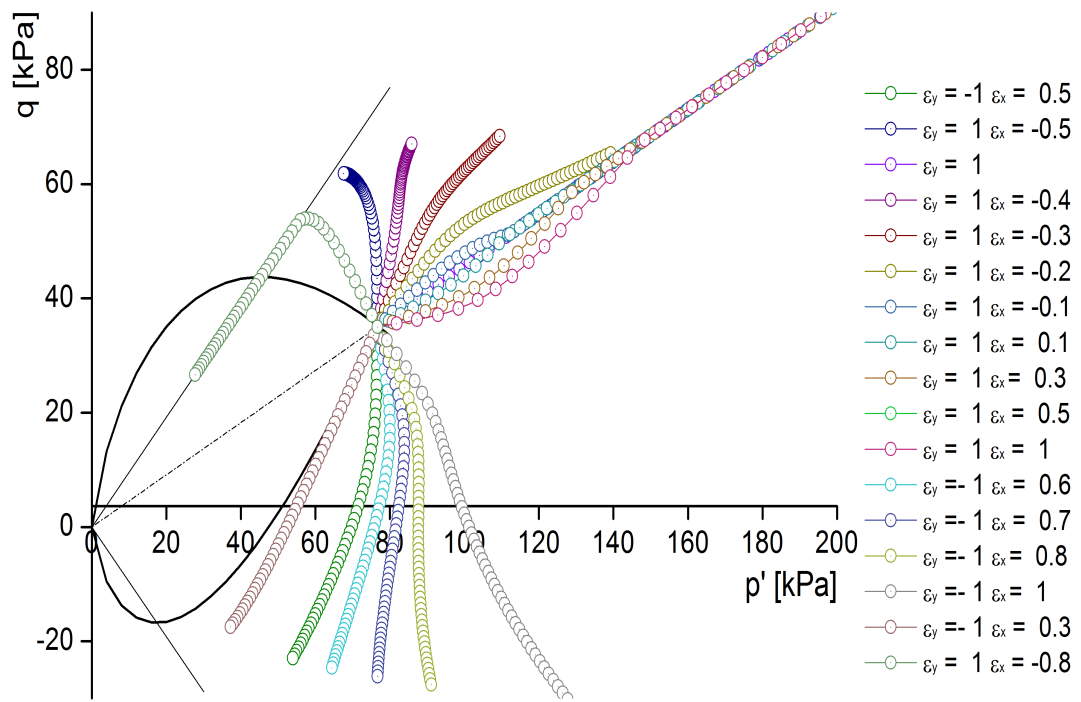
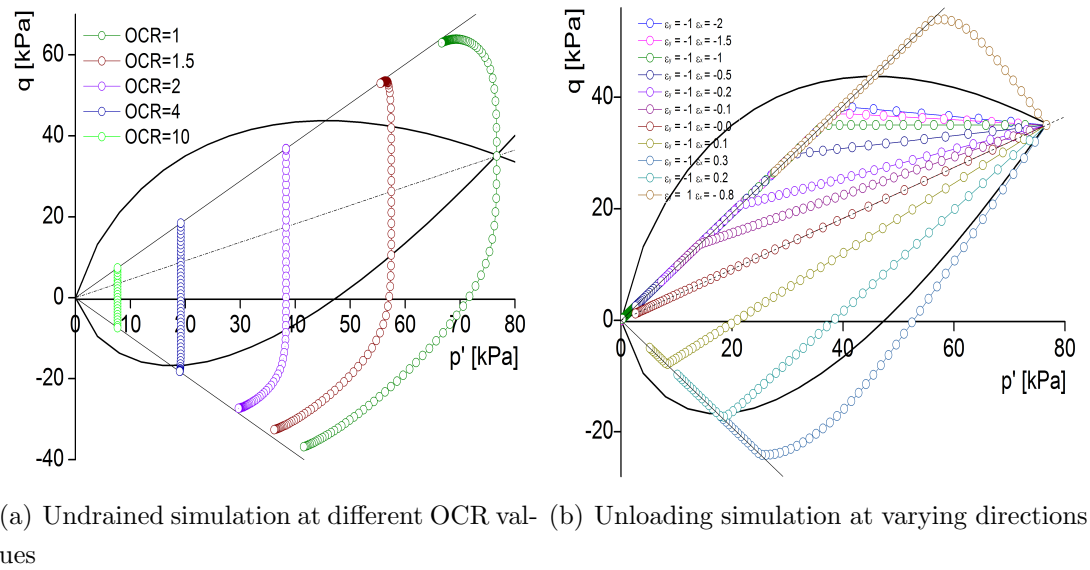


Figure 4.19: Triaxial simulation at varying directions



(a) Undrained simulation at different OCR values (b) Unloading simulation at varying directions

Figure 4.20: Triaxial simulations to verify the dry side cut off

4.4 Application to a benchmark problem

The performance of the hybrid numerical algorithm used to implement SO inviscid/viscid models is tested in finite element benchmark problems using PLAXIS and their results are compared in this section. This benchmark problem is to explore and verify the implementation of the SO models into PLAXIS. A benchmark embankment problem is selected to represent a typical geotechnical engineering problem where anisotropy and creep might play a role. Finite element calculations are performed with PLAXIS 2D using the SO models which have been implemented as a user defined soil model (UDSM).

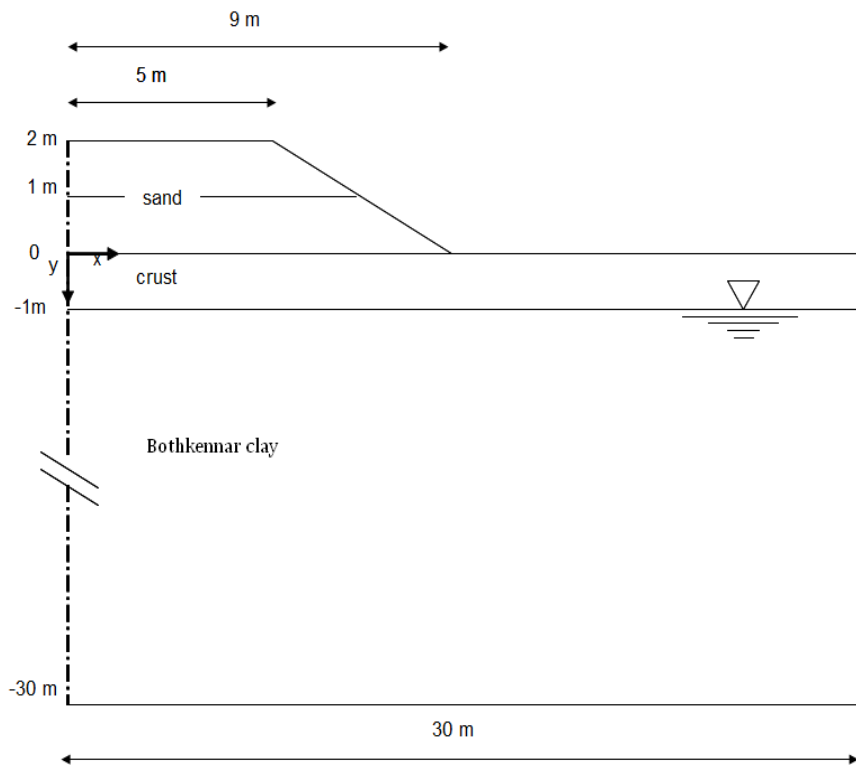
An embankment constructed on soft soil is assumed to be 2 m high, with a width at the top of 10 m and the side slopes with a gradient of 1:2. The soft soil is assumed to have the properties of soft Bothkennar clay which extends to a depth of 30m. At the surface there is a 1m depth over-consolidated dry crust. The geometry of the embankment is shown in Fig. 4.21(a). The groundwater table assumed to be located at 1 m below the ground surface. The finite element mesh used in this benchmark embankment is shown in Fig. 4.21(b).

The embankment, assumed to be made of granular material, was modelled with a simple Mohr Coulomb model; see Table 4.4 for material parameters. The crust layer is also modelled with the Mohr-Coulomb model (see Table 4.4 for material parameters). This embankment problem is hence expected to be dominated by the soft soil response and is not sensitive to the embankment and crust parameters.

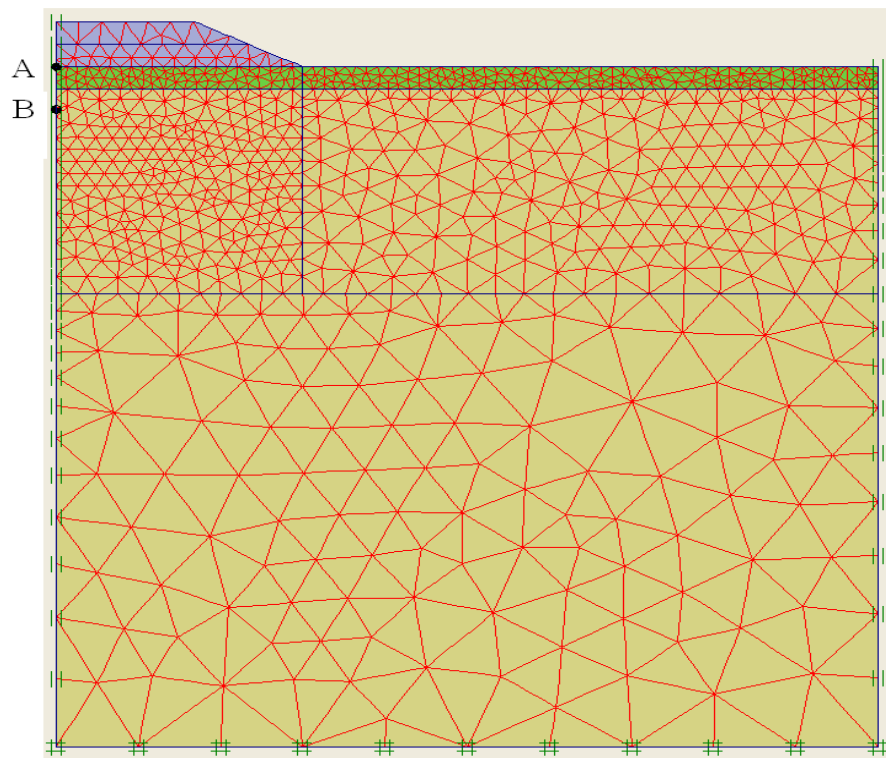
Table 4.4: Soil parameters of sand and peat layer

Dry crust						
E' (<i>kPa</i>)	ν'	C'	φ'	ψ'	γ (<i>kN/m³</i>)	$k_x = k_y$ (<i>m/day</i>)
3000.0	0.2	2.0	37.1	0.0	19.0	$1.0 \cdot 10^{-3}$
Sand						
E' (<i>kPa</i>)	ν'	C'	φ'	ψ'	γ (<i>kN/m³</i>)	k_x/k_y (<i>m/day</i>)
40000.0	0.35	2.0	40.0	0.0	20.0	$8.64 \cdot 10^{-5}$

4.4 Application to a benchmark problem



(a) Geometry and assumed soil profiles



(b) Mesh

Figure 4.21: The geometry and mesh of the benchmark embankment

4.4 Application to a benchmark problem

Bothkennar clay material has been extensively studied and a consistent set of laboratory data is available to derive material parameters for the SO inviscid model (e.g., Géotechnique Symposium in Print (1992), McGinty (2006), McGinty *et al.* (2008)) in a consistent manner. Based on the κ and λ values, and the initial void ratio, κ^* and λ^* can be calculated for the SO models. The permeability k is assumed to be the same in the vertical and horizontal direction for the sake of simplicity.

The ratio of secondary compression $C_{\alpha,e}$ for SO viscid model, expressed in terms of changes in vertical strain with log time and compression index C_c , is fairly constant for Bothkennar clay at about 0.06 – 0.11 (Nash *et al.*, 1992b, Hight *et al.*, 1992). Similar values were found by Mesri & Godlewski (1977) for wide range of clays. In this analysis, $C_{\alpha,e}/C_c$ value is assumed 0.05 ($\lambda = 0.434C_c$).

The physical meaning of initial volumetric strain rate \dot{v}_0 for SO viscid model is obvious (Sekiguchi, 1984), but it is rather difficult to estimate from the laboratory test data. However, Iizuka & Ohta (1987) proposed a procedure to estimate \dot{v}_0 using coefficient of consolidation C_v . This procedure is summarized in Appendix D. The C_v value is not a unique and is reduced when the stresses exceeded the yield stress (Nash *et al.*, 1992a). The field test values of C_v are substantially greater than those measured in the laboratory too (Nash *et al.*, 1992a). In this analysis, the C_v value 20 $m^2/year$ is assumed to be constant with depth from Nash *et al.* (1992a) laboratory test data. Table 4.5 gives the material parameters for Bothkennar clay used to simulate the SO inviscid&viscid models.

Table 4.5: Material parameters of soft clay for SO inviscid & viscid models

Soil constants							
κ^*	ν'	λ^*	M	D	K_0^{nc}	γ (kN/m^3)	$k_x = k_y$ (m/day)
0.00667	0.2	0.1	1.51	7.1	0.397	16.5	$2.5 \cdot 10^{-4}$
State variables							
e_0	OCR						
2.0	1.50						
Creep parameters							
C_α	\dot{v}_o						
0.0115	$3.5 \cdot 10^{-6}$						

4.4 Application to a benchmark problem

The analysis was performed using a small deformation assumption to compare the two models at boundary value level. The construction of the embankment was simulated by two undrained phases of 5 days each. In all analyses, drained conditions and zero initial pore pressures have been assumed above the clay layer. For the initial condition, the in-situ K_0 value was assumed to be 0.5 due to overconsolidation of Bothkennar clay. The first construction phase, in which the first layer of the embankment was built, was followed by a 30 day consolidation stage. After the completion of the second layer of embankment, the final consolidation was simulated until the maximum excess pore pressure had reduced to 1 kPa (i.e. practically full dissipation of excess pore pressures).

The settlement predictions versus time at the ground surface under the centreline of the embankment (point A in Fig. 4.21(b)) are shown in Fig. 4.22. The SO viscid model predicted significantly higher vertical displacements and longer time for full consolidation than the inviscid model. The creep behaviour of the SO viscid model is delayed the consolidation, by developing additional excess pore water pressure during consolidation and really effect the magnitude of settlement and consolidation time. The predicted settlement troughs at the end of the analyses are shown in Fig. 4.23 and the SO viscid model vertical deformation prediction of about 1.5 m is unrealistic.

Horizontal displacement predictions at the centreline line of the embankment are shown in Fig. 4.24 at the end of analyses. Again, considerable differences are observed between SO viscid and inviscid predictions. The SO viscid model predicts noticeably larger horizontal deformation than the SO inviscid model.

Fig. 4.25 compares the excess pore water pressure with time underneath (at 2m depth) the centreline of the embankment (point B in Fig. 4.21(b)). The SO viscid model predicts considerable excess pore water pressure in comparison to the SO inviscid model. Effect of creep results in significant consolidation time and from the stability point of view the embankment is modelled by the SO viscid model is less safe than the SO inviscid model.

4.4 Application to a benchmark problem

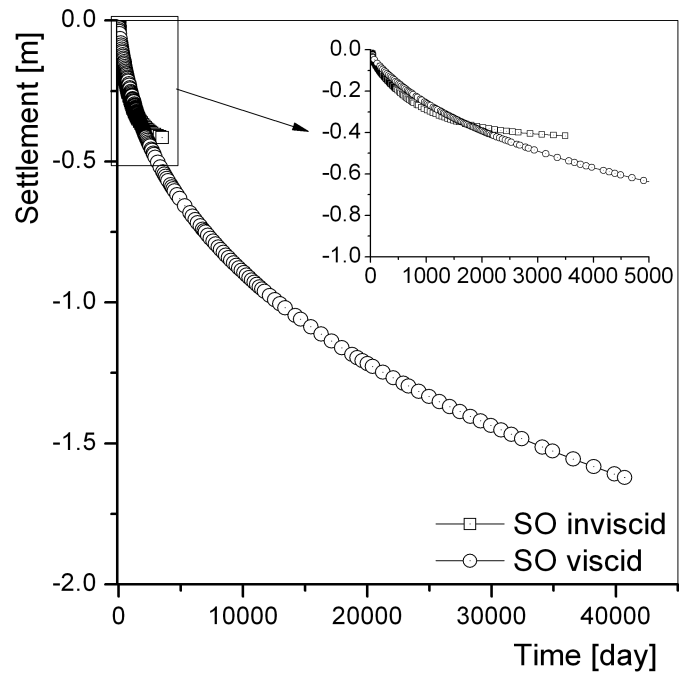


Figure 4.22: Time settlement curves at point A predicted by SO inviscid/viscid models

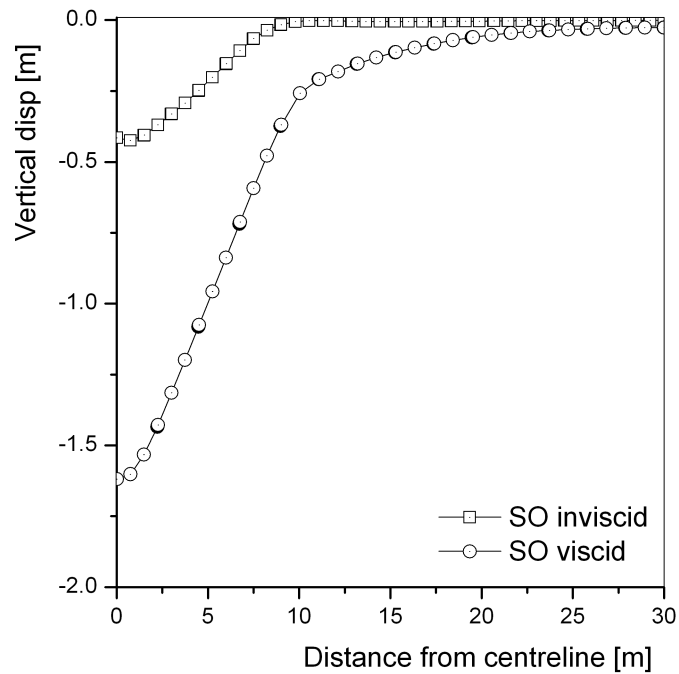


Figure 4.23: Surface settlement at the end of analysis predicted by SO inviscid/viscid models

4.4 Application to a benchmark problem

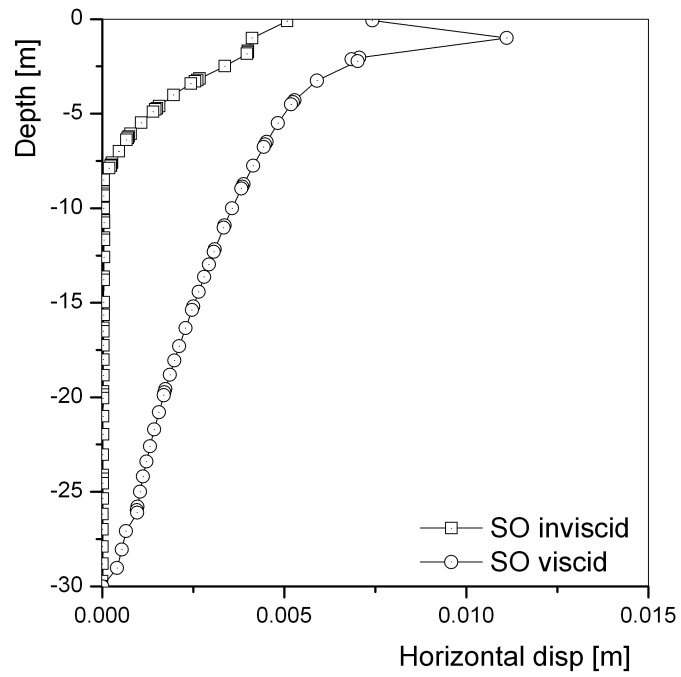


Figure 4.24: Final horizontal displacement at the embankment toe predicted by SO inviscid/viscid models

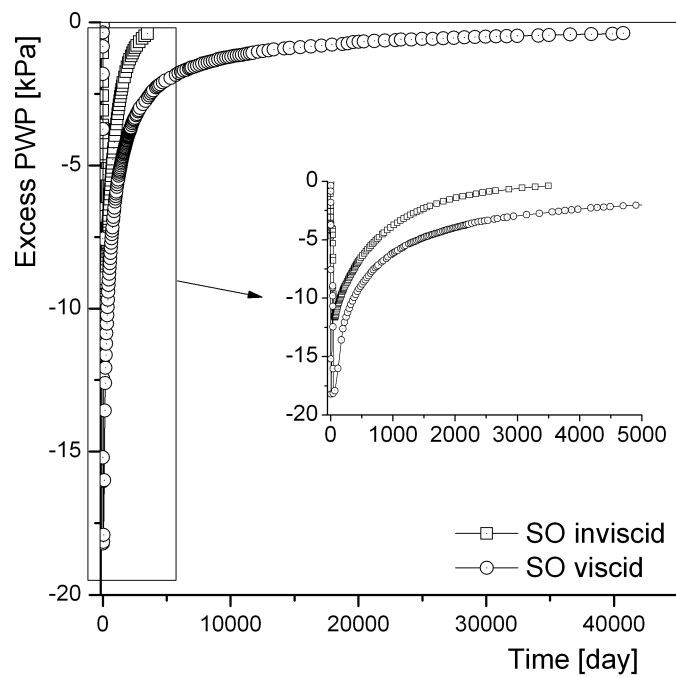


Figure 4.25: Excess PWP with time at point B predicted by SO inviscid/viscid models

4.5 Summary

The Sekiguchi-Ohta (SO) inviscid/viscid models were presented in general stress space. A new hybrid implicit algorithm to integrate the SO constitutive models was proposed. The hybrid algorithm that consists of modified Newton-Raphson (MNR) and Stolle's algorithm is described in this chapter. The hybrid algorithm described here has computational advantage to overcome the vertex singularity of the SO models. A series of strain controlled triaxial simulations were performed to verify the accuracy and stability of the hybrid algorithm. Furthermore, the models were implemented into the FE code PLAXIS and a benchmark test was done to verify the robustness of the numerical algorithm.

Chapter 5

B-SCLAY1S model formulation and its implementation

In this chapter, the formulation of the B-SCLAY1S model developed in this thesis is explained in detail. The mathematical formulation of the model in triaxial stress space and general stress space is presented. Parameter determination for the B-SCLAY1S model is discussed. A number of strategies are explored in order to reduce the numerical instability which occurs when implementing the model into PLAXIS.

5.1 Introduction

The original bubble model first proposed by Al-Tabbaa (1987) is based on the modified Cam-clay (MCC) (Roscoe & Burland, 1968) model, named as B-MCC by the author. The B-MCC model was formulated in triaxial stress space and validated against the slow cyclic response of speswhite kaolin. The model was shown to simulate many of the important aspects of observed response for speswhite kaolin, like hysteresis, accumulation of permanent strains and loading-unloading cycles. The model is capable of predicting both non-linearity and plasticity from the early stages of loading. Grammatikopoulou (2004) states “from the kinematic hardening model review, the simplest and most theoretically attractive is the two surface model developed by Al-Tabbaa (1987).” The review of the original bubble constitutive model (B-MCC) is given in **Chapter 2**. The B-MCC model mathematical formulations in general stress space and numerical implementation into a finite element program (ICFEP) were given by Grammatikopoulou (2004).

The proposed B-SCLAY1S model is a hierarchical extension of the S-CLAY1S model (Koskinen *et al.*, 2002a,b; Karstunen *et al.*, 2005; Karstunen & Koskinen, 2008) using the principles of the original bubble model to capture non-linearity and plasticity from the early stages of loading. The B-SCLAY1S model is developed within the framework of critical state theory and bounding surface plasticity. In B-SCLAY1S model, S-CLAY1S kinematic yield surface is treated as bounding surface and a kinematic bubble surface introduced within the bounding surface. The kinematic bubble surface, which is the same shape as the bounding surface but smaller in size and encloses truly elastic region. An intrinsic yield surface is introduced into B-SCLAY1S to simulate the destructuration of soil. The intrinsic surface is same as in S-CLAY1S model and formulated as it is in S-CLAY1S.

In the following sections, the B-SCLAY1S model is discussed in triaxial stress space and general stress space followed by determination of parameters and numerical implementation into PLAXIS.

5.2 Triaxial stress space

In triaxial stress space, the B-SCLAY1S model mathematical formulation is presented. The development of B-SCLAY1S model was based on axial symmetry in triaxial stress space. Stress quantities $p' = (\sigma_a + 2\sigma_r)/3$ and $q = (\sigma_a - \sigma_r)$ and strain quantities $\epsilon_v = \epsilon_a + 2\epsilon_r$ and $\epsilon_q = 2(\epsilon_a - \epsilon_r)/3$ are used where subscripts a and r denote the axial and the radial directions, respectively, of a triaxial stress space.

5.2.1 Elastic part of the model

When the stresses lie within the bubble surface, the predicted behaviour is elastic. The elastic bulk modulus, K' is the same as in the case of the S-CLAY1 model:

$$K' = \frac{(1 + e)p'}{\kappa} \quad (5.1)$$

For the calculation of elastic shear strains, a constant Poisson's ratio, ν' , was assumed. The elastic shear modulus, G is defined as:

$$G = \frac{3(1 + e)p'}{2\kappa} \frac{1 - 2\nu'}{1 + \nu'} \quad (5.2)$$

Therefore the elastic strain increments are given as:

$$\begin{Bmatrix} d\epsilon_v^e \\ d\epsilon_s^e \end{Bmatrix} = \begin{bmatrix} \frac{1}{K'} & 0 \\ 0 & \frac{1}{3G} \end{bmatrix} \begin{Bmatrix} dp' \\ dq \end{Bmatrix} \quad (5.3)$$

where the elastic bulk and shear moduli, K' and G , are given by Eq.5.1 and 5.2 respectively.

5.2.2 Equation of surfaces

The bounding surface of the model in triaxial stress space is the same as the S-CLAY1S model yield surface, given as follows:

$$f_y = \frac{(q - \alpha p')^2}{M^2 - \alpha^2} + \left(p' - \frac{p'_m}{2}\right)^2 - \left(\frac{p'_m}{2}\right)^2 = 0 \quad (5.4)$$

where M is the slope of the critical state line, p'_m defines the size of the yield curve and α defines the orientation of the yield curve, see Fig. 5.1. The scalar parameter α is a measure of the degree of plastic anisotropy of the soil.

The intrinsic yield surface is linked to the size of the bounding surface as follows:

$$p'_m = (1 + \chi)p'_{mi} \quad (5.5)$$

where p'_{mi} defines the size of the intrinsic yield surface and χ defines the amount of bonding.

The kinematic bubble surface, enclosing the truly elastic region, has a similar shape to the bounding surface, but is smaller in size. In triaxial stress space it is formulated as follows:

$$f_b = \frac{[(q - p'\alpha) - (q_b - p'_b\alpha)]^2}{M^2 - \alpha^2} + (p' - p'_b)^2 - R^2 \left(\frac{p'_m}{2}\right)^2 = 0 \quad (5.6)$$

where p'_b and q_b are centre of bubble surface and R is the ratio of the size of the kinematic bubble surface to that of the bounding surface, see Fig. 5.1.

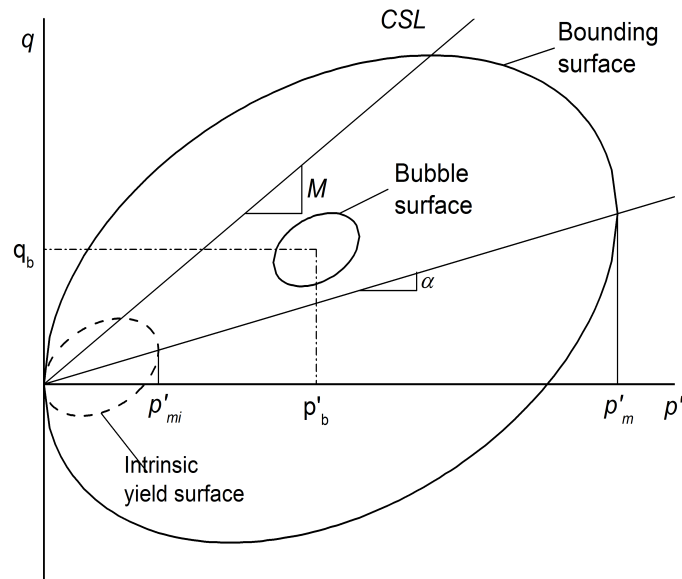


Figure 5.1: The B-SCLAY1S model yield surface in triaxial stress space

5.2.3 Flow rule

Experimental evidence suggests that the assumption of an associated flow is a good approximation of natural clays when combined with an inclined yield surface (Wheeler *et al.*, 2003). Therefore, plastic strains increment is assumed to be normal to the kinematic bubble surface at the current stress state. Hence, the flow rule of the model is the associated flow rule and the plastic potential is given by Eq. 5.2.

5.2.4 Hardening rules

The evolution of the bounding surface incorporates three hardening rules. The first of the hardening laws relates to the change in size of the intrinsic yield surface; the second hardening law called the 'rotational hardening law' (Wheeler *et al.*, 2003) describes the change of orientation of the inclined yield surface with plastic straining; the third hardening law (Karstunen *et al.*, 2005) relates the degradation of bonding with plastic straining, see Chapter 3 for details. The evolution of the bubble surface is described by a combination of the above mentioned three laws, and in addition the surface translates in the stress space following the current stress point. The combination of hardening rules forms the translation rule of the bubble surface.

Isotropic hardening rule

The model adopts the volumetric hardening rule, which is the same formulation of the S-CLAY1S model as given below.

$$dp'_{mi} = \frac{(1+e)}{\lambda_i - \kappa} p'_{mi} d\epsilon_v^p \quad (5.7)$$

In the equation above the change in size of the bounding surface is controlled by the plastic volumetric strain increment. λ and κ are slopes of the normal compression line and swelling line in the $e - \ln p'$ space, where e is void ratio.

Rotational hardening rule

The model incorporates rotational hardening to control the rotation of the bubble surface due to the anisotropy, in the same way as S-CLAY1S. The rotation of the bubble surface is defined as follows:

$$d\alpha = \mu \left[\left(\frac{3}{4} \frac{q}{p'} - \alpha \right) \langle d\epsilon_v^p \rangle + \beta \left(\frac{1}{3} \frac{q}{p'} - \alpha \right) d\epsilon_d^p \right] \quad (5.8)$$

where $d\epsilon_v^p$ is the plastic volumetric strain increment and $d\epsilon_d^p$ is plastic deviatoric strain increment. Parameter β controls the relative influence of the $d\epsilon_d^p$ and μ the absolute rate of the plastic strain increments on the rotation of the bubble surface.

Destructuration rule

The effect of the bonding is introduced by using the concept of an intrinsic yield surface is given by Eq. 5.5. The destructuration law describes the degradation of bonding with plastic straining where the plastic volumetric strains and plastic deviatoric strains tend to reduce the bonding parameter χ towards a target value of zero as follows:

$$d\chi = -a\chi (|d\epsilon_v^p| + b |d\epsilon_d^p|) \quad (5.9)$$

where a and b are two additional soil constants; parameter a controls the absolute rate of destructuration and parameter b controls the relative effectiveness of plastic deviatoric strains and plastic volumetric strains in destroying the bonding.

Translation rule

The translation rules of the bubble surface in B-SCLAY1S are formulated based on Al-Tabbaa (1987) translation rules. Two different translation rules are adopted, one for when bubble surface moves inside the bounding surface and one for when two surfaces are in contact.

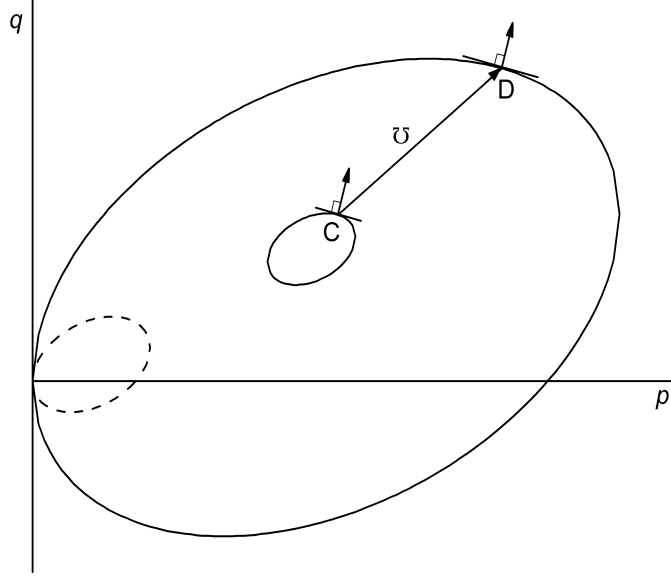


Figure 5.2: Relative translation of the bubble surface along the vector \mathcal{U}

The first translation rule describes the bubble surface movement within the bounding surface in such a way the bubble surface and bounding surface can come in contact at common normal but never intersect. Fig. 5.2 shows that the center of bubble surface moves along a vector, \mathcal{U} , which joins the current stress state to its conjugate stress point on the bounding surface. The vector \mathcal{U} is defined as follows:

$$\mathcal{U} = \left\{ \begin{array}{l} \frac{p' - p'_b}{R} - (p' - p'_m) \\ \frac{(q - p'\alpha) - (q_b - p'_b\alpha)}{R} - (q - p'\alpha) \end{array} \right\} \quad (5.10)$$

The translation rule contains two components, one is associated with the change of the bubble surface due to expansion or contraction of the bounding surface, the other one is associated with the movement of bubble surface along the vector \mathcal{U} .

The translation of the bubble is defined when the bubble moves within the bounding surface as follows:

$$\begin{Bmatrix} dp'_b \\ dq_b \end{Bmatrix} = \frac{dp'_m}{p'_m} \begin{Bmatrix} p'_b \\ q_b \end{Bmatrix} + S \begin{Bmatrix} \frac{p' - p'_b}{R} - (p' - p'_m) \\ \frac{(q - p'\alpha) - (q_b - p'_b\alpha)}{R} - (q - p'\alpha) \end{Bmatrix} \quad (5.11)$$

The S scalar quantity can be derived from the consistency condition of the bubble surface as follows (details given in Appendix):

$$S = \frac{\frac{\partial f_b}{\partial p'}(dp' - \frac{dp'_m}{p'_m}p'_b) + \frac{\partial f_b}{\partial q}(dq - \frac{dp'_m}{p'_m}q_b) + \frac{\partial f_b}{\partial p'_m}dp'_m}{\frac{\partial f_b}{\partial p'}\left(\frac{p' - p'_b}{R} - (p' - p'_m)\right) + \frac{\partial f_b}{\partial q}\left(\frac{(q - p'\alpha) - (q_b - p'_b\alpha)}{R} - (q - p'\alpha)\right)} \quad (5.12)$$

where partial derivatives are defined as follows:

$$\frac{\partial f_b}{\partial p'} = 2(p' - p'_b) - 2\left(\frac{(q - p'\alpha) - (q_b - p'_b\alpha)}{M^2 - \alpha^2}\right)(\alpha) \quad (5.13)$$

$$\frac{\partial f_b}{\partial q} = 2\left(\frac{(q - p'\alpha) - (q_b - p'_b\alpha)}{M^2 - \alpha^2}\right) \quad (5.14)$$

The second translation rule describes the movement of bubble when two surfaces are in contact at the current stress state, the vector \mathcal{U} becomes zero and the translation rule is reduced to:

$$\begin{Bmatrix} dp'_b \\ dq_b \end{Bmatrix} = \frac{dp'_m}{p'_m} \begin{Bmatrix} p'_b \\ q_b \end{Bmatrix} \quad (5.15)$$

5.2.5 Hardening modulus

The hardening modulus is defined in such a way that, when the two surfaces touch and experience continuous yielding, the model predicts the same behaviour as the S-CLAY1S model. It is initially formulated for the special case when two surfaces are in contact and then modified for other case when two surfaces are not in contact and the stress state is within the bounding surface.

The consistency condition is applied to the bounding surface to derive the plastic multiplier $\Delta\Lambda$. The consistency condition is a mathematical expression of the requirement that the stress state to stay on the bounding surface as long as loading continues, even though the bounding surface itself will be moving and changing shape due to hardening. Thus, the consistency condition is written as follows:

$$\dot{f}_y = \frac{\partial f_y}{\partial p'} dp' + \frac{\partial f_y}{\partial q} dq + \frac{\partial f_y}{\partial p'_{mi}} dp'_{mi} + \frac{\partial f_y}{\partial \alpha} d\alpha + \frac{\partial f_y}{\partial \chi} d\chi = 0 \quad (5.16)$$

By using above consistency condition, the plastic multiplier $\Delta\Lambda$ is derived and written in simplified form as follows:

$$\Delta\Lambda = \frac{\frac{\partial f_b}{\partial p'^e} dp'^e + \frac{\partial f_b}{\partial q} dq^e}{A + \mathcal{H}_0 + \mathcal{H}_\alpha + \mathcal{H}_\chi} \quad (5.17)$$

where \mathcal{H}_0 relates to isotropic hardening similar to modified Cam-clay (MCC) hardening modulus, \mathcal{H}_α relates to the rotation of inclined yield surface and \mathcal{H}_χ , relates to the degradation of bonding are defined as follows:

$$A = \frac{\partial f_b}{\partial p'} K' \frac{\partial f_b}{\partial p'} + \frac{\partial f_b}{\partial q} G \frac{\partial f_b}{\partial q} \quad (5.18)$$

$$\mathcal{H}_0 = -p'(1 + \chi) p'_{mi} \frac{1 + e}{\lambda_i - \kappa} \frac{\partial f_b}{\partial p'} \quad (5.19)$$

$$\mathcal{H}_\alpha = \left\{ \frac{\partial f_b}{\partial \alpha} \right\} \left[\left\{ \frac{\partial \alpha}{\partial \epsilon_v^p} \right\} \left\langle \frac{\partial f_b}{\partial p'} \right\rangle + \left\{ \frac{\partial \alpha}{\partial \epsilon_d^p} \right\} \frac{\partial f_b}{\partial q} \right] \quad (5.20)$$

$$\mathcal{H}_\chi = \frac{\partial f_b}{\partial \chi} \left[\frac{\partial \chi}{\partial \epsilon_v^p} \left| \frac{\partial f_b}{\partial p'} \right| + \frac{\partial \chi}{\partial \epsilon_d^p} \frac{\partial f_y}{\partial q} \right] \quad (5.21)$$

Kinematic hardening function \mathcal{H}_0 from Eq. 5.19 can be further derived using Eq. 5.5 and Eq. 5.13 as follows:

$$\mathcal{H}_0 = \frac{4(1 + e)}{\lambda_i - \kappa} \left[\left(p' - \frac{p'_m}{2} \right) - \frac{(q - \alpha p')}{M^2 - \alpha^2} (\alpha) \right] \left[p' \frac{p'_m}{2} \right] \quad (5.22)$$

The above hardening function is further extended using the yield function of S-CLAY1S model as follows:

$$\mathcal{H}_0 = \frac{4(1+e)}{\lambda_i - \kappa} \left[\left(p' - \frac{p'_m}{2} \right) - \frac{(q - \alpha p')}{M^2 - \alpha^2} (\alpha) \right] \left[\frac{(q - \alpha p')^2}{M^2 - \alpha^2} + \left(p' - \frac{p'_m}{2} \right) p' \right] \quad (5.23)$$

When the bubble lies inside the bounding surface, hardening modulus is defined based on Al-Tabbaa (1987) description, and \mathcal{H}_0 is replaced with a more general expression as follows:

$$\mathcal{H}_0 = \mathcal{H}_{0b} + \mathcal{H}_b \quad (5.24)$$

\mathcal{H}_{0b} is defined similarly the formulation for S-CLAY1S given in Eq. 5.23 as follows:

$$\mathcal{H}_{0b} = \frac{4(1+e)}{\lambda_i - \kappa} \left[\left(p' - p'_b \right) - \frac{(q - \alpha p') - (q_b - \alpha p'_b)}{M^2 - \alpha^2} (\alpha) \right] \left[p' (p' - p'_b) + \frac{(q - \alpha p') ((q - \alpha p') - (q_b - \alpha p'_b))}{M^2 - \alpha^2} \right] \quad (5.25)$$

where \mathcal{H}_b is a scalar quantity which is a function of the stress state. The hardening function \mathcal{H}_b was assumed to be of the form by Al-Tabbaa (1987) description is defined as follows:

$$\mathcal{H}_b = \frac{4(1+e)}{\lambda_i - \kappa} \left(\frac{\ell}{\ell_{max}} \right)^\psi \left(\frac{p'_m}{2} \right)^3 \quad (5.26)$$

ℓ_{max} is shown in Fig. 5.3 defined as follows:

$$\ell_{max} = p'_m \sqrt{1 + \alpha^2} (1 - R) \quad (5.27)$$

ℓ is the proximity of bubble surface to the bounding surface defined as follows:

$$\ell = \frac{1}{R \sqrt{1 + \alpha^2 \frac{p'_m}{2}}} \left[\left(p' - p'_b - \alpha \frac{(q - p'\alpha) - (q_b - p'_b\alpha)}{M^2 - \alpha^2} \right) \left(\frac{p' - p'_b}{R} - \left[p' - \frac{p'_m}{2} \right] \right) + \left(\frac{(q - p'\alpha) - (q_b - p'_b\alpha)}{M^2 - \alpha^2} \right) \left(\frac{(q - p'\alpha) - (q_b - p'_b\alpha)}{R} - (q - p'\alpha) \right) \right] \quad (5.28)$$

The resulting hardening \mathcal{H}_0 is given as follows:

$$\mathcal{H}_0 = \frac{4(1+e)}{\lambda_i - \kappa} \left[\left[(p' - p'_b) - \frac{(q - \alpha p') - (q_b - \alpha p'_b)}{M^2 - \alpha^2} (\alpha) \right] \left[p'(p' - p'_b) + \frac{(q - \alpha p')((q - \alpha p') - (q_b - \alpha p'_b))}{M^2 - \alpha^2} \right] + \left(\frac{\ell}{\ell_{max}} \right)^\psi \left(\frac{p'_m}{2} \right)^3 \right] \quad (5.29)$$

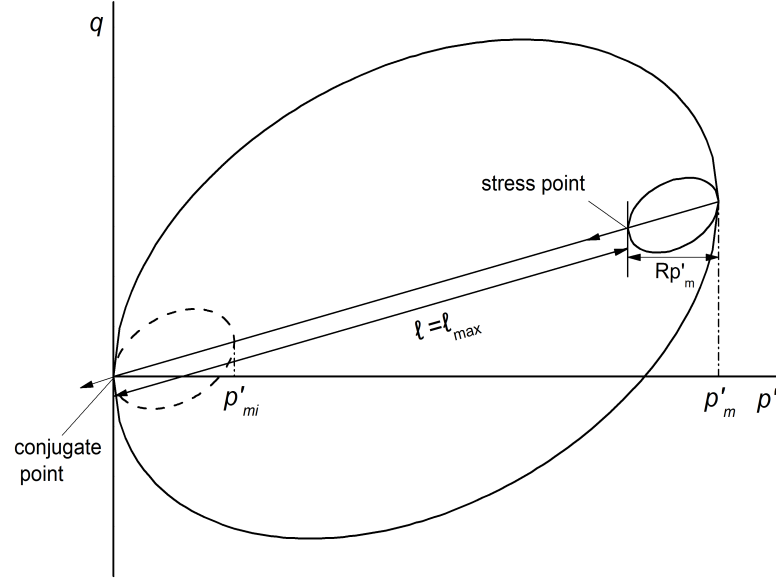


Figure 5.3: Diagram showing the position of maximum value of ℓ , ℓ_{max}

5.3 General stress space

This section describes the extension of the B-SCLAY1S model from triaxial stress space to general stress space, which is important in order to implement the model into the PLAXIS finite element program. Before the formulation of the model in general stress space two issues will be discussed; the generalization of stress, strain and fabric tensor in general 3D stress space and the shape of the yield and plastic potential surfaces assumed in the deviatoric plane.

5.3.1 Preliminaries

The generalization of the bubble surface can be performed in 3D stress space by using the following definitions:

The centre of bubble surface σ'_{bij} is defined as:

$$\underline{\sigma}'_b = \begin{pmatrix} \sigma'_{bxx} \\ \sigma'_{byy} \\ \sigma'_{bzz} \\ \sigma'_{bxy} \\ \sigma'_{byz} \\ \sigma'_{bzx} \end{pmatrix} \quad (5.30)$$

Mean effective stress of bubble centre, p'_b , is defined as:

$$p'_b = \frac{1}{3} (\sigma'_{bxx} + \sigma'_{byy} + \sigma'_{bzz}) \quad (5.31)$$

Deviator stress vector of bubble center σ'_{bd} defined as:

$$\underline{\sigma}'_{bd} = \begin{pmatrix} \sigma'_{bxx} - p'_b \\ \sigma'_{byy} - p'_b \\ \sigma'_{bzz} - p'_b \\ \sqrt{2}\sigma'_{bxy} \\ \sqrt{2}\sigma'_{byz} \\ \sqrt{2}\sigma'_{bzx} \end{pmatrix} \quad (5.32)$$

5.3.2 Elastic part of the model

If the stress path remains within the bubble surface, the predicted behaviour is isotropic elastic. The elastic bulk modulus, K' and elastic shear modulus G , is the same as in the case of the S-CLAY1S model:

$$K' = \frac{(1 + e)p'}{\kappa} \quad (5.33)$$

$$E' = 3(1 - 2\nu')K' \quad (5.34)$$

$$G = \frac{1}{2} \frac{E'}{1 + \nu'} \quad (5.35)$$

5.3.3 Yield and plastic potential surface

The extension of the model in general stress space requires some assumption of the shape of the yield and plastic potential surfaces in the deviatoric plane. The modified Cam-clay and the S-CLAY1S models assumed a circular shape of the yield and plastic potential surfaces in deviatoric plane. A circular shape in deviatoric plane implies that the model is independent of the Lode angle. B-SCLAY1S also assumes a circular shape because of the simplicity of the model. However, bubble models proposed by Muir Wood (1995); Muir Wood & Rouainia (2000) and Grammatikopoulou (2004) assume Lode angle dependent failure criterion, i.e., the critical state constant M is a function of Lode angle.

5.3.4 Equation of surface

The equation of bounding surface and intrinsic surface in general stress space are formulated as follows:

$$f_y = \frac{3}{2} \frac{\{\underline{s}\}^T \{\underline{s}\}}{M^2 - \alpha^2} + \left(p' - \frac{p'_m}{2}\right)^2 - \left(\frac{p'_m}{2}\right)^2 = 0 \quad (5.36)$$

$$p'_m = (1 + \chi)p'_{mi} \quad (5.37)$$

where \bar{s} is defined as follows:

$$\underline{s} = \underline{\sigma}'_d - \underline{\alpha}_d p' \quad (5.38)$$

The equation of the bubble surface in general stress space is given as follows:

$$f_b = \frac{3}{2} \frac{\{\underline{s} - \underline{s}_b\}^T \{\underline{s} - \underline{s}_b\}}{M^2 - \alpha^2} + (p' - p'_b)^2 - R^2 \left(\frac{p'_m}{2}\right)^2 = 0 \quad (5.39)$$

where \underline{s}_b is defined as follows:

$$\underline{s}_b = \underline{\sigma}'_{bd} - \underline{\alpha}_d p'_b \quad (5.40)$$

5.3.5 Flow rule

The model assumes associated flow rule. The bounding plastic potential surface, p_y , and the bubble plastic potential surface, p_b , are same as the bounding surface and the bubble surface respectively. So the flow rule is defined as follows:

$$\Delta \epsilon_{ij}^p = \Delta \Phi \frac{\partial p_b}{\partial \sigma_{ij}} = \Delta \Phi \frac{\partial f_b}{\partial \sigma_{ij}} \quad (5.41)$$

5.3.6 Hardening rules

The formulation of the hardening rules in general stress space is a combination of following rules:

Isotropic hardening rule

The first of the hardening laws relates to the change in size of the intrinsic yield surface, which is assumed to be related solely to plastic volumetric strain ($d\epsilon_v^p$) (Karstunen *et al.*, 2005) as follows:

$$\Delta p'_{mi} = \frac{(1+e)p'_{mi}}{\lambda_i - \kappa} \Delta \epsilon_v^p \quad (5.42)$$

where λ_i is the slope of the intrinsic normal compression line for a reconstituted soil and κ is the slope of the elastic (pre-yield) swelling line in the $v : \ln p'$ plane (specific volume : $v = 1 + e$). It is worth to note that when the B-SCLAY1S model becomes the B-SCLAY1 model (without destructuration), the first of the hardening laws relates to the yield surface as in the modified Cam-clay model follows:

$$\Delta p'_m = \frac{(1+e)p'_m}{\lambda - \kappa} \Delta \epsilon_v^p \quad (5.43)$$

Rotational hardening rule

The second hardening law called the 'rotational hardening law' (Wheeler *et al.*, 2003) describes the change of orientation of the inclined bubble surface with plastic straining. The rotational hardening law in general space is given as follows:

$$\Delta \alpha_d = \mu \left(\left[\frac{3\sigma'_d}{4p'} - \alpha_d \right] \langle \Delta \epsilon_v^p \rangle + \beta \left[\frac{\sigma'_d}{3p'} - \alpha_d \right] \Delta \epsilon_d^p \right) \quad (5.44)$$

where μ and β are two soil parameters, where μ governs the absolute rate at which α changes with plastic straining and β governs the relative effectiveness of volumetric and deviatoric strains in the rotation of yield surface. $\langle \rangle$ are Macaulay brackets and $\langle \Delta \epsilon_v^p \rangle = \Delta \epsilon_v^p$ for $\Delta \epsilon_v^p > 0$ and $\langle \Delta \epsilon_v^p \rangle = 0$ for $\Delta \epsilon_v^p < 0$.

Destructuration rule

The third hardening law (Karstunen *et al.*, 2005) called destructuration rule relates the degradation of bonding with plastic straining is given as follows:

$$\Delta \chi = -a \chi \left[|\Delta \epsilon_v^p| + b |\Delta \epsilon_d^p| \right] \quad (5.45)$$

where a and b being soil constants controlling the rate of degradation.

Translation rule

Two different translation rules adopted, one for the special case when bubble surface and bounding surface are in contact and one for the case when bubble surface moves within the bounding surface. Following sections explain in details.

Translation rule for two surfaces are in contact

With the bounding surface and the bubble surface are in contact, Grammatikopoulou (2004) used a translation rule in accordance with Stallebrass (1990) formulation to implement the MCC model based bubble surface model into ICFEP. The same concept, which ensures that the two surfaces remain tangential to each other for further loading, is applied. Changes of center of the bubble is given as follows:

$$\Delta \underline{\sigma}_b = (1 - R) \Delta \underline{\sigma}' + R \frac{\Delta \underline{\sigma}'_m}{2} \quad (5.46)$$

In terms of the isotropic and deviatoric components of the stress tensor of above equation can be rewritten as follows:

$$\Delta p'_b = (1 - R) \Delta p' + R \frac{\Delta p'_m}{2} \quad (5.47)$$

$$\Delta \underline{s}_b = (1 - R) \Delta \underline{s} \quad (5.48)$$

Translation rule for bubble surface moves within bounding surface

In this case, the translation rule formulated in general stress space is based on the rule proposed by Al-Tabbaa (1987) as follows:

$$\Delta\sigma_b = \frac{\Delta p'_m}{p'_m} \sigma'_b + S \left[\frac{\sigma' - \sigma'_b}{R} - \left(\sigma' - \frac{\sigma'_m}{2} \right) \right] \quad (5.49)$$

The above Eq.5.49 can be written in terms of the isotropic and deviatoric components of the stress tensor as follows:

$$\Delta p'_b = \frac{\Delta p'_m}{p'_m} p'_b + S \left[\frac{p' - p'_b}{R} - \left(p' - \frac{p'_m}{2} \right) \right] \quad (5.50)$$

$$\Delta \underline{s}_b = \frac{\Delta p'_m}{p'_m} \underline{s}_b + S \left[\frac{\underline{s} - \underline{s}_b}{R} - \underline{s} \right] \quad (5.51)$$

The scalar quantity S can be obtained as before by substituting Eq.5.50 and Eq.5.51 into the consistency condition for the bubble yield surface (Eq.5.39). The consistency condition for the bubble surface can be written as:

$$\dot{f}_b = \frac{\partial f_b}{\partial p'} \Delta p' + \frac{\partial f_b}{\partial p'_b} \Delta p'_b + \frac{\partial f_b}{\partial \underline{s}} \Delta \underline{s} + \frac{\partial f_b}{\partial \underline{s}_b} \Delta \underline{s}_b + \frac{\partial f_b}{\partial p'_{mi}} \Delta p'_{mi} + \frac{\partial f_b}{\partial \alpha_d} \Delta \alpha_d + \frac{\partial f_b}{\partial \chi} \Delta \chi = 0 \quad (5.52)$$

The scalar quantity S can be derived by substituting Eq. 5.50 and Eq. 5.51 into Eq. 5.52 as follows:

$$S = - \frac{\frac{\partial f_b}{\partial p'} (\Delta p' - \frac{\Delta p'_m}{p'_m} p'_b) + \frac{\partial f_b}{\partial \underline{s}} : (\Delta \underline{s} - \frac{\Delta p'_m}{p'_m} \underline{s}_b) + \frac{\partial f_b}{\partial p'_{mi}} \Delta p'_{mi} + \frac{\partial f_b}{\partial \alpha_d} \Delta \alpha_d + \frac{\partial f_b}{\partial \chi} \Delta \chi}{\frac{\partial f_b}{\partial p'} \left(\frac{p' - p'_b}{R} - \left(p' - \frac{p'_m}{2} \right) \right) + \frac{\partial f_b}{\partial \underline{s}} : \left(\frac{\underline{s} - \underline{s}_b}{R} - \underline{s} \right)} \quad (5.53)$$

The partial derivatives of the bubble yield surface required in Eq.5.53 will be given in the following sections.

5.3.7 Hardening modulus

The hardening modulus is formulated for the two different cases; the first one when the kinematic bubble surface moves within the bounding surface and the second one

when two surfaces are in contact. In the first case the kinematic bubble surface is active yield surface and formulation of hardening modulus follows the one proposed by Al-Tabbaa (1987). In the second case the active yield surface is the bounding surface and the hardening modulus reduces to the S-CLAYS hardening modulus. The hardening modulus of S-CLAY1S is given in Chapter 3, see for details.

Bubble surface moves within bounding surface

The hardening modulus, \mathcal{H} , formulated in general stress space comprises 4 different moduli:

$$\mathcal{H} = \mathcal{H}_{0b} + \mathcal{H}_b + \mathcal{H}_\alpha + \mathcal{H}_\chi \quad (5.54)$$

where \mathcal{H}_{0b} , \mathcal{H}_α , \mathcal{H}_χ and \mathcal{H}_b are given as follows:

$$\mathcal{H}_{0b} = \frac{4(1+e)}{\lambda_i - \kappa} \left[\frac{1}{2} \frac{\partial f_b}{\partial p'} \right] \left[\frac{1}{2} \frac{\partial f_b}{\partial \underline{s}} : \underline{s}_b + p'_b(p' - p'_b) + R^2 \left(\frac{p'_m}{2} \right)^2 \right] \quad (5.55a)$$

$$\mathcal{H}_b = \frac{4(1+e)}{\lambda_i - \kappa} \left(\frac{\ell}{\ell_{max}} \right)^\psi \left(\frac{p'_m}{2} \right)^3 \quad (5.55b)$$

$$\mathcal{H}_\alpha = \left\{ \frac{\partial f_b}{\partial \underline{\alpha}_d} \right\}^T \left[\left\{ \frac{\partial \underline{\alpha}_d}{\partial \epsilon_v^p} \right\} \left\langle \frac{\partial f_b}{\partial p'} \right\rangle + \left\{ \frac{\partial \underline{\alpha}_d}{\partial \epsilon_d^p} \right\} \sqrt{\frac{3}{2} \left\{ \frac{\partial f_b}{\partial \underline{\sigma}'_d} \right\}^T \left\{ \frac{\partial f_b}{\partial \underline{\sigma}'_d} \right\}} \right] \quad (5.55c)$$

$$\mathcal{H}_\chi = \frac{\partial f_b}{\partial \chi} \left[\frac{\partial X}{\partial \epsilon_v^p} \left| \frac{\partial f_b}{\partial p'} \right| + \frac{\partial \chi}{\partial \epsilon_d^p} \sqrt{\frac{3}{2} \left\{ \frac{\partial f_b}{\partial \underline{\sigma}'_d} \right\}^T \left\{ \frac{\partial f_b}{\partial \underline{\sigma}'_d} \right\}} \right] \quad (5.55d)$$

where ℓ is defined from Al-Tabbaa (1987) as follows:

$$\ell = \frac{1}{R\sqrt{1 + \alpha^2 \frac{p'_m}{2}}} \left[\frac{1}{2} \frac{\partial F_b}{\partial p'} \left[\frac{p' - p'_b}{R} - \left(p' - \frac{p'_m}{2} \right) \right] + \frac{1}{2} \frac{\partial F_b}{\partial \underline{s}} : \left\{ \frac{\underline{s} - \underline{s}_b}{R} - \underline{s} \right\} \right] \quad (5.56)$$

where ℓ_{max} is defined from Al-Tabbaa (1987) as follows:

$$\ell_{max} = p'_m \sqrt{1 + \alpha^2} (1 - R) \quad \text{for } M \leq 1 \quad (5.57a)$$

$$\ell_{max} = p'_m M \sqrt{1 + \alpha^2} (1 - R) \quad \text{for } M > 1 \quad (5.57b)$$

Two surfaces are in contact

When the two surfaces are in contact, the bounding surface is active yield surface and the hardening modulus, \mathcal{H} , reduces to the hardening modulus of S-CLAY1S model:

$$\mathcal{H} = \mathcal{H}_0 + \mathcal{H}_\alpha + \mathcal{H}_X \quad (5.58)$$

$$\mathcal{H}_0 = \frac{4(1+e)}{\lambda_i - \kappa} \left[\frac{1}{2} \frac{\partial f_y}{\partial p'} \right] \left[\frac{(q - \alpha p')^2}{M^2 - \alpha^2} + p'(p' - \frac{p'_m}{2}) \right] \quad (5.59)$$

$$\mathcal{H}_\alpha = \left\{ \frac{\partial f_y}{\partial \alpha_d} \right\}^T \left[\left\{ \frac{\partial \alpha_d}{\partial \epsilon_v^p} \right\} \left\langle \frac{\partial f_y}{\partial p'} \right\rangle + \left\{ \frac{\partial \alpha_d}{\partial \epsilon_d^p} \right\} \sqrt{\frac{3}{2}} \left\{ \frac{\partial f_y}{\partial \sigma'_d} \right\}^T \left\{ \frac{\partial f_y}{\partial \sigma'_d} \right\} \right] \quad (5.60)$$

$$\mathcal{H}_X = \frac{\partial f_y}{\partial \chi} \left[\frac{\partial \chi}{\partial \epsilon_v^p} \left| \frac{\partial f_y}{\partial p'} \right| + \frac{\partial \chi}{\partial \epsilon_d^p} \sqrt{\frac{3}{2}} \left\{ \frac{\partial f_y}{\partial \sigma'_d} \right\}^T \left\{ \frac{\partial f_y}{\partial \sigma'_d} \right\} \right] \quad (5.61)$$

5.3.8 Centre of Bubble

The initial centre of bubble is assumed to coincide with the initial stress state and given as follows:

$$\underline{\sigma}'_{b,0} = \underline{\sigma}'_0 \quad (5.62)$$

If the initial bubble centre $\underline{\sigma}'_{b,0}$ lies in between dotted surface and the bounding surface as shown in Fig. 5.4, the initial bubble centre must be corrected back to the dotted surface along the radial direction to satisfy the non-intersection translation rule. The dotted surface is defined in $p' - q$ space as follows:

$$f_L = \frac{(q - p'\alpha)^2}{M^2 - \alpha^2} + (p' - \frac{p'_m}{2})^2 - (1 - R)^2 \left(\frac{p'_m}{2} \right)^2 = 0 \quad (5.63)$$

The corrected bubble centre can be found using f_L . When stress state lies on

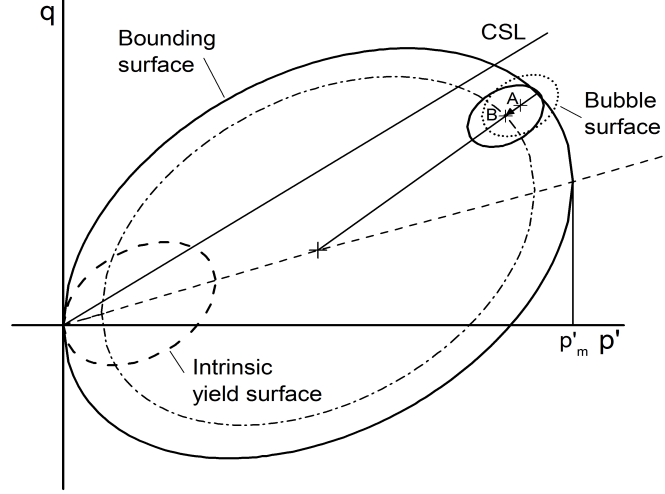


Figure 5.4: Schematic illustration of drift correction of bubble surface

the dotted surface (e.g. point B), the p' at point B can be derived as follows:

$$p'_B = \frac{p'_m}{2} + \sqrt{\frac{(1-R)^2 \left(\frac{p'_m}{2}\right)^2}{\frac{1}{M^2 - \alpha^2} \left(\frac{q_B - p'_B \alpha}{p'_B - p'_m/2}\right)^2 + 1}} \quad (5.64)$$

The slope of stress states at point A and B are the same about the centre of bounding surface. Hence

$$\frac{q_B - p'_B \alpha}{p'_B - p'_m/2} = \frac{q_A - p'_A \alpha}{p'_A - p'_m/2} \quad (5.65)$$

By using Eq. 5.64 and Eq. 5.65, the corrected bubble centre (p'_B , q_B) is derived as follows:

$$p'_B = \frac{p'_m}{2} + \sqrt{\frac{(1-R)^2 \left(\frac{p'_m}{2}\right)^2}{\frac{1}{M^2 - \alpha^2} \left(\frac{q_A - p'_A \alpha}{p'_A - p'_m/2}\right)^2 + 1}} \quad (5.66)$$

$$q_B = p'_B \alpha + \frac{q_A - p'_A \alpha}{p'_A - p'_m/2} (p'_B - p'_m/2) \quad (5.67)$$

The translation of the bubble surface is defined when bubble surface lies within the bounding surface as follows:

$$\Delta \sigma'_b = \frac{\Delta p'_m}{p'_m} [s_b + p'_b] + S \left[\frac{s - s_b}{R} - s + \frac{p' - p'_b}{R} - \left(p' - \frac{p'_m}{2} \right) \right] \quad (5.68)$$

The translation of the bubble surface is defined when the bubble surface and bounding surface are in contact at the current stress state, the above translation equation is reduced to:

$$\Delta \sigma'_b = \frac{\Delta p'_m}{p'_m} [s_b + p'_b] \quad (5.69)$$

5.3.9 Pore water pressure

An assumption is made that water and soil particles are incompressible under undrained condition for fully saturated soils. Therefore, the following equation is applicable:

$$\Delta \epsilon_v^p + \Delta \epsilon_v^e = 0 \quad (5.70)$$

where ϵ_v^p and ϵ_v^e are plastic and elastic volumetric strain change, respectively.

The pore water pressure is calculated when plastic deformation take place as follows:

$$u = -K'_w \Delta \epsilon_v^p = K'_w \Delta \epsilon_v^e \quad (5.71)$$

where K'_w is the bulk modulus of water.

5.4 Determination of model parameters

The proposed B-SCLAY1S model has a feature that it is a hierarchical extension of S-CLAY1S. By giving a value 1 for R , the model converges to the S-CLAY1S model. Similarly by setting the initial value of χ_0 to zero, and using apparent value of λ

5.4 Determination of model parameters

instead of intrinsic value λ_i , the proposed model accounts for small strain behaviour and anisotropy only, denoted as B-SCLAY1. Likewise model can be reduced to the elasto-plastic modified Cam-clay model (Roscoe & Burland, 1968) by setting $R = 1$ and destructuration and anisotropy parameters to zero. Table 5.1 summarizes all possible hierarchical models in B-SCLAY1S.

Table 5.1: Hierarchical of the B-SCLAY1S model

Model	Parameters
B-SCLAY1S	: All 13 model parameters required
B-SCLAY1	: $\chi_0 \rightarrow 0$ and $\lambda_i \rightarrow \lambda$
B-MCC	: $\chi_0 \rightarrow 0$, $\lambda_i \rightarrow \lambda$ and α_0 & $\mu \rightarrow 0$
S-CLAY1S	: $R \rightarrow 1$
S-CLAY1	: $R \rightarrow 1$, $\chi_0 \rightarrow 0$ and $\lambda_i \rightarrow \lambda$
MCC	: $R \rightarrow 1$, $\chi_0 \rightarrow 0$, $\lambda_i \rightarrow \lambda$ and α_0 & $\mu \rightarrow 0$

Thirteen model parameters are required to define the B-SCLAY1S model (see Appendix F). In this section, most relevant parameters to the bubble surface (κ , R and ψ) are discussed. The determination of other parameters is detailed in Appendix F.

Swelling index κ

The initial part of the swelling curve can be used to derive value of κ as shown in Fig. 5.5 (Al-Tabbaa, 1987).

Ratio of the size of the bubble surface R

Al-Tabbaa (1987) noted that model parameters accounting for isotropic modelling can be obtained from a multi-stage triaxial test. Fig. 5.5 shows an example of such a test. The test starts with an isotropic compression and isotropic swelling follows. The initial part of the swelling can be used to derive the value of R as shown in Fig. 5.5.

Exponent in the hardening function ψ

The parameter ψ cannot be measured directly from a test data and has to be determined by varying a value in a series of simulations (Al-Tabbaa, 1987).

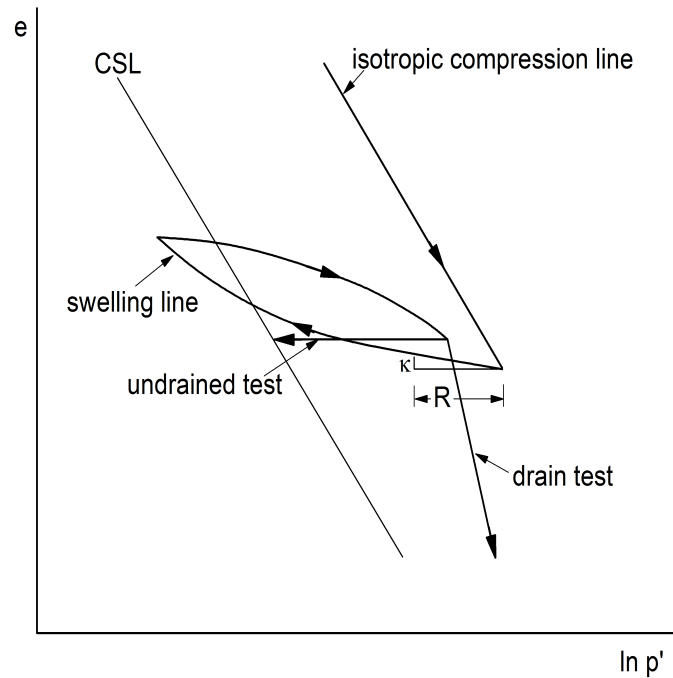


Figure 5.5: A multi-stage triaxial test (after Al-Tabbaa (1987))

5.5 Numerical implementation into PLAXIS

The proposed B-SCLAY1S constitutive model can be implemented into PLAXIS using so called *user defined soil model* (UDSM) option. Basically a developer has to write subroutines in FORTRAN (or any other) programming language for a constitutive model which will be linked to the main program using Dynamic Link Library (DLL) to the PLAXIS finite element program. Details of how to write a program for a user defined soil model are given in Brinkgreve *et al.* (2008). The B-SCLAY1S model is implemented into PLAXIS using a sub-stepping explicit scheme. Details of the implementation into PLAXIS is given in this section for only the ‘bubble’ (two surfaces are not in contact) and not for when two surfaces are in contact i.e., the model becomes S-CLAY1S (see for details **Chapter 3**).

In the explicit schemes, the stresses are computed directly from the consistency condition, the plastic potential and the hardening rule at previously known point. Accuracy and efficiency of the explicit algorithm is improved by combining with a sub-stepping algorithm, bubble surface intersection algorithm and surface drift algorithm.

The application of the explicit integration schemes for conventional plasticity

model has been demonstrated by Sloan (1987); Sloan *et al.* (2001). An explicit integration scheme with automatic sub-stepping and error control to integrate multiple yield surfaces and kinematic hardening rules were presented by Zhao *et al.* (2005). According to Zhao *et al.* (2005) and Luccioni *et al.* (2001), explicit stress integration schemes are preferable to implicit schemes when the constitutive equations become more complex and non-linear. Moreover, an implicit algorithm may not converge to the non-linear system of equations, and it is very difficult to derive the second-order derivative of the plastic potential for complex constitutive equations.

Explicit rather than implicit integration algorithms are preferred to implement the B-SCLAY1S model into PLAXIS as they are advantageous in regards to efficiency, robustness and accuracy for complex constitutive equations. Accuracy and efficiency of the implementation is enhanced further using an automatic sub-stepping and error control algorithms (Sloan, 1987; Sloan *et al.*, 2001). This integration scheme is adopted in this implementation by modifying it to suit the formulation of the B-SCLAY1S model for natural soils.

Recalling the incremental general stress- strain relationship to perform the non-linear finite element analysis as follows:

$$\{\Delta\sigma'\} = [D^{ep}] \{\Delta\epsilon\} \quad (5.72)$$

where $\{\Delta\epsilon\}$ is the imposed incremental strain. There is a standard method to obtain the expression for the elasto-plastic matrix, $[D^{ep}]$, which can be derived from the following standard formula:

$$[D^{ep}] = [D^e] - \frac{[D^e] \begin{Bmatrix} \partial p_b \\ \partial \sigma' \end{Bmatrix} \begin{Bmatrix} \partial f_b \\ \partial \sigma' \end{Bmatrix}^T [D^e]}{\begin{Bmatrix} \partial f_b \\ \partial \sigma' \end{Bmatrix}^T [D^e] \begin{Bmatrix} \partial p_b \\ \partial \sigma' \end{Bmatrix} + \mathcal{H}} \quad (5.73)$$

$[D^e]$ is the elastic matrix and \mathcal{H} is the hardening modulus. Since the B-SCLAY1S model assumes the associated flow rule, the yield surface and plastic potential are same $p_b = f_b$. The hardening modulus for the B-SCLAY1S model is given as follows:

$$\mathcal{H} = \mathcal{H}_{0b} + \mathcal{H}_b + \mathcal{H}_\alpha + \mathcal{H}_\chi \quad (5.74)$$

5.5 Numerical implementation into PLAXIS

The details of the hardening moduli are given in Section 1.3. The rest of this section presents explicit integration scheme for computing stresses from the incremental stress-strain relationship derived in Eq. 5.73

In explicit (Euler's forward) algorithm, the constitutive equations are integrated directly using the elasto-plastic matrix computed at the previously known stress point. It is also known as the tangential stiffness method. The stress at the next increment, $\{\underline{\sigma}'_{n+1}\}$ is calculated as follows:

$$\{\underline{\sigma}'_{n+1}\} = \{\underline{\sigma}'_n\} + \{\Delta\underline{\sigma}'\} \quad (5.75)$$

where $\{\underline{\sigma}'_n\}$ is the current stress and $\{\Delta\underline{\sigma}'\}$ is computed using Eq. 5.72. The corresponding plastic strains $\{\Delta\underline{\epsilon}\}^p$ is obtained using the following formula:

$$\{\Delta\underline{\epsilon}\}^p = \Delta\Lambda \left\{ \begin{array}{c} \frac{\partial p_b}{\partial \underline{\sigma}'} \end{array} \right\} \quad (5.76)$$

with

$$\Delta\Lambda = \frac{\left\{ \begin{array}{c} \frac{\partial f_b}{\partial \underline{\sigma}'} \end{array} \right\}^T [D^e] \{\Delta\underline{\epsilon}\}}{\left\{ \begin{array}{c} \frac{\partial f_b}{\partial \underline{\sigma}'} \end{array} \right\}^T [D^e] \left\{ \begin{array}{c} \frac{\partial p_b}{\partial \underline{\sigma}'} \end{array} \right\} + \mathcal{H}} \quad (5.77)$$

In order to achieve acceptable accuracy and guarantee the consistency condition at the end of each increment, the explicit algorithm requires small increment size.

The following state variables were used to program UDSM:

<i>StVar</i> (1)	:	α_x
<i>StVar</i> (2)	:	α_y
<i>StVar</i> (3)	:	α_z
<i>StVar</i> (4)	:	α_{xy}
<i>StVar</i> (5)	:	α_{yz}
<i>StVar</i> (6)	:	α_{zx}
<i>StVar</i> (7)	:	α
<i>StVar</i> (8)	:	p'_{mi}
<i>StVar</i> (9)	:	χ
<i>StVar</i> (10)	:	p'_m
<i>StVar</i> (11)	:	e_0
<i>StVar</i> (12)	:	σ'_{bxx}
<i>StVar</i> (13)	:	σ'_{byy}
<i>StVar</i> (14)	:	σ'_{bzz}
<i>StVar</i> (15)	:	σ'_{bxy}
<i>StVar</i> (16)	:	σ'_{byz}
<i>StVar</i> (17)	:	σ'_{bzx}
<i>StVar</i> (18)	:	123.

The procedures to program B-SCLAY1S model using the sub-stepping explicit scheme is summarized in Algorithm 14, 15, 16, 17 and 18. Furthermore, the bubble surface intersection algorithm and drift algorithm are discussed following the explicit algorithms of B-SCLAY1S.

5.5 Numerical implementation into PLAXIS

Algorithm 14 : An automatic sub-stepping scheme for the explicit algorithm of B-SCLAY1S

```
READ: material parameters
READ: state variables
GET:  $\{\sigma'_0\}$ ,  $\mathcal{H}_0$ ,  $\{\Delta\epsilon\}$  and  $FTOL$ 
ASSUME:  $T_0 = 0$  and  $dT = 1$ 
FIND:  $\{\Delta\epsilon\}^t = dT * \{\Delta\epsilon\}$ 

99 Continue

NewStep = 1
CALL: B-SCLAY1S subroutine from Algorithm 15

if ( $NewStep < 0.9999$ ) then
   $dT = NewStep * dT$ 
   $\{\Delta\epsilon\}^t = dT * \{\Delta\epsilon\}$ 

  if ( $dT > 0.0001$ ) then
    GO TO 99
  else
    CALL: B-SCLAY1S subroutine from Algorithm 15
    Abort " Too small step size"
  end if

end if

 $T_0 = T_0 + dT$ 
if ( $T_0 < 0.9999$ ) then
   $dT = 1 - T_0$ 
   $\{\Delta\epsilon\}^t = dT * \{\Delta\epsilon\}$ 
  GO TO 99
end if

return
```

Algorithm 15 : Subroutine to identify active yield surface

DECIDE: n_sub (maximum allowable strain increment)

for (Iteration = 1 to n_sub) **do**

Calculate: $\{\Delta\sigma'\}^e = [D^e] \{\Delta\epsilon\}$ and $\{\sigma'\}^e = \{\sigma'_0\} + \{\Delta\sigma'\}^e$ and $\{\sigma'\}^e = \{\sigma'_0\} + \{\Delta\sigma'\}^e$

Calculate: p', p'_b

Calculate \mathcal{U} from Eq. 5.10

if ($\mathcal{U} \leq 0$) **then**

B-SCLAY1S becomes S-CLAY1S

CALL: S-CLAY1S subroutine (given in Chapter 3)

else

Calculate: $f_b^e = f_b(\{\sigma'\}^e, \{\sigma'_b\}, \mathcal{H}_0)$ and $f_b^0 = f_b(\{\sigma'_0\}, \{\sigma'_b\}, \mathcal{H}_0)$ from Eq. 5.39

! Check yield condition

if ($f_b^e \leq \text{FTOL} \ \& \ f_b^0 \leq \text{FTOL}$) **then**

return ! Purely elastic behaviour

else

if ($f_b^e \geq \text{FTOL} \ \& \ f_b^0 \leq \text{FTOL}$) **then**

CALL: intersection subroutine

$\{\Delta\epsilon\} \leftarrow (1 - \Omega) \{\Delta\epsilon\}$

end if

CALL: B-SCLAY1S subroutine from Algorithm 16

end if

end if

end for

Calculate: new global stress state

Calculate: $\Delta\epsilon_v^e$

UPDATE: $e_0 = \Delta\epsilon_v * (1 + e_0) + e_0$! current void ratio

if Undrained **then**

$du = K'_w d\epsilon_v^e$

$u = u + du$! update pore water pressure

else

$u = u$

end if

return

Algorithm 16 : Explicit algorithm for B-SCLAY1S

Calculate: $\{\underline{\sigma}'_d\}$ and $\{\underline{\sigma}'_{bd}\}$
 Calculate: $\frac{\partial f_b}{\partial Q}$, $\frac{\partial f_b}{\partial p'}$, $\frac{\partial \bar{Q}}{\partial p'}$, $\left\{\frac{\partial \bar{Q}}{\partial \underline{\sigma}'}\right\}$ and $\left\{\frac{\partial f_b}{\partial \underline{\sigma}'}\right\}$ from Appendix E

Assume: $\left\{\frac{\partial p_b}{\partial \underline{\sigma}'}\right\} = \left\{\frac{\partial f_b}{\partial \underline{\sigma}'}\right\}^T$ from the associated flow rule

Calculate: $dd = \left\{\frac{\partial f_b}{\partial \underline{\sigma}'}\right\} [D^e] \left\{\frac{\partial p_b}{\partial \underline{\sigma}'}\right\}$

Calculate: $\left\{\frac{\partial \bar{Q}}{\partial \alpha_d}\right\}$ and $\left\{\frac{\partial p_b}{\partial \alpha_d}\right\}$ from Appendix E

Calculate: $\frac{\partial f_b}{\partial \chi}$ from Appendix E

Calculate: $\frac{\partial p'_{mi}}{\partial \epsilon_v}$ from Appendix E

Calculate: $\left\{\frac{\partial \alpha_d}{\partial \epsilon'_v}\right\}$ and $\left\{\frac{\partial \alpha_d}{\partial \epsilon'_d}\right\}$ from Appendix E

Calculate: $\frac{\partial \chi}{\partial \epsilon'_v}$ and $\frac{\partial \chi}{\partial \epsilon'_d}$

Calculate: $\left\{\frac{\partial f_y}{\partial \underline{\sigma}'_d}\right\}$

Calculate: b from Eq. 5.56

Calculate: b_{max} from Eq. 5.57

Calculate: $\mathcal{H} = \mathcal{H}_{0b} + \mathcal{H}_b + \mathcal{H}_\alpha + \mathcal{H}_X$ from Eq. 5.55

Calculate: $[D^{ep}]$ from Eq. 5.73

Calculate: $\Delta\Lambda$ from Eq. 5.77

Calculate: $\{\Delta \underline{\epsilon}^p\} = \Delta\Lambda \left\{\frac{\partial p_y}{\partial \underline{\sigma}'}\right\}$

Calculate: $\{\Delta \underline{\epsilon}'_d\}$ using Eq. A.10

Calculate: $\{\Delta \underline{\sigma}'\}$ from Eq. 5.72

UPDATE: stresses $\{\underline{\sigma}'\} = \{\underline{\sigma}'_0\} + \{\Delta \underline{\sigma}'\}$

UPDATE: state variables $StVar(1 : 10)$ CALL: subroutine Algorithm 17

Calculate: S from Eq. 5.53

UPDATE: bubble centre $\{\underline{\sigma}'_b\}$ from Eq. 5.68

CALL: Algorithm 17 ! Bubble drift correction

UPDATE: bubble centre $\{\underline{\sigma}'_b\}$

return

Algorithm 17 : Update state variables

Calculate:

$$\Delta p'_{mi} = \frac{(1+e)p'_{mi}}{\lambda_i - \kappa} \Delta \epsilon_v^p$$

$$\Delta \underline{\alpha}_d = \mu \left(\left[\frac{3\sigma'_d}{4p'} - \underline{\alpha}_d \right] \langle d\epsilon_v^p \rangle + \beta \left[\frac{\sigma'_d}{3p'} - \underline{\alpha}_d \right] \Delta \epsilon_d^p \right)$$

$$\Delta \chi = -a\chi \left[|\Delta \epsilon_v^p| + b |\Delta \epsilon_d^p| \right]$$

Update state variables:

$$\{\underline{\alpha}\}_{1,2,3} \leftarrow \underline{\alpha} + \Delta \underline{\alpha}_d + 1$$

$$\{\underline{\alpha}\}_{4,5,6} \leftarrow (\underline{\alpha} + \Delta \underline{\alpha}_d) / \sqrt{2}$$

$$\alpha \leftarrow \sqrt{\frac{3}{2} \{\underline{\alpha} + \Delta \underline{\alpha}_d\} \{\underline{\alpha} + \Delta \underline{\alpha}_d\}^T}$$

$$p'_{mi} \leftarrow p'_{mi} + \Delta p'_{mi}$$

$$\chi \leftarrow \chi + \Delta \chi$$

$$p'_m \leftarrow (p'_{mi} + \Delta p'_{mi}) * (1 + (\chi + \Delta \chi))$$

return

Algorithm 18 : Drift correction and bubble centre update

Calculate: $f_b = f_b(\{\underline{\sigma}'\}, \{\underline{\sigma}'_b\}, \mathcal{H})$

if ($Abs(f_b) \geq FTOL$) **then**

for (Iteration = 1, MaxIt) **do**

 ! Correct centre of bubble

$$\text{Calculate: } \Gamma = f_b / \begin{Bmatrix} \frac{\partial f_b}{\partial \underline{\sigma}'} \\ \frac{\partial f_b}{\partial \underline{\sigma}'} \end{Bmatrix}_T \begin{Bmatrix} \frac{\partial p_b}{\partial \underline{\sigma}'} \\ \frac{\partial p_b}{\partial \underline{\sigma}'} \end{Bmatrix}$$

$$\text{Calculate: } \{\underline{\sigma}'^t\} = \Gamma \begin{Bmatrix} \frac{\partial f_b}{\partial \underline{\sigma}'} \\ \frac{\partial f_b}{\partial \underline{\sigma}'} \end{Bmatrix}$$

$$\text{Update: } \{\underline{\sigma}'\} = \{\underline{\sigma}'\} - \{\underline{\sigma}'^t\}$$

 Calculate: $f_b = f_b(\{\underline{\sigma}'\}, \mathcal{H})$

if ($Abs(f_b) \leq FTOL$) **then**

return

end if

end for

end if

return

Correction of bubble surface drift

A correction of the bubble surface drift is required where the computed stresses fail to satisfy the yield condition on the updated bubble surface. The predicted stress state at the end of an increment may not lie on the current bubble surface due to the assumption of constant elasto-plastic matrix over the imposed strain increment. To avoid cumulative effect on subsequent computations, stresses are always corrected back to the current yield surface at the end of each increment (Potts & Gens, 1985). Fig. 5.6 shows the schematic illustration of the bubble drift correction.

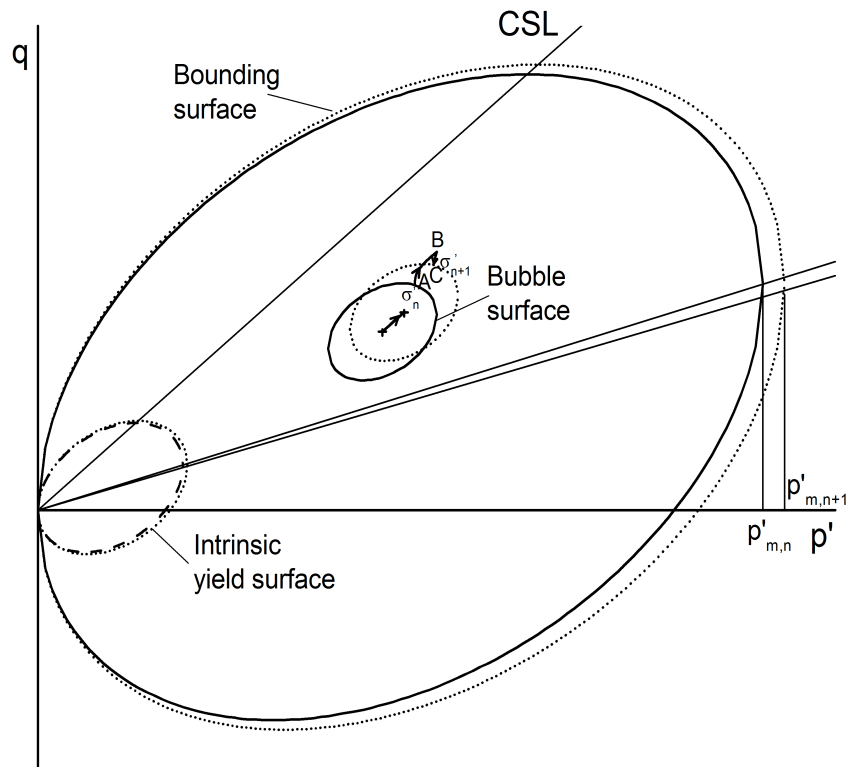


Figure 5.6: Schematic illustration of drift correction of bubble surface

In conventional plasticity, various methods of drift correction were used to restore the stress back to the yield surface. Potts & Gens (1985) proposed correction schemes which involve correcting stresses along the direction of the plastic flow, the total strain increment, the accumulated effective stress, normal to the yield surface and the consistency condition. Typically a systematic method is necessary to find a direction for correcting the stresses by projecting back to the yield surface. Based

on this considerations, a scheme is proposed to correct the stresses along the plastic flow direction to preserve the consistency condition.

The corrected stresses can be written as follows:

$$\underline{\sigma}'_C = \underline{\sigma}'_B - \delta \underline{\sigma}' \quad (5.78)$$

where $\delta \underline{\sigma}'_b$ can be found as follows:

$$\delta \underline{\sigma}'_b = \Gamma \left\{ \frac{\partial f_b}{\partial \underline{\sigma}'} \right\} \quad (5.79)$$

The corrected centre of bubble must satisfy the condition on the bubble surface as follows:

$$f_y(\underline{\sigma}'_C, \underline{\sigma}'_{b,C}, \mathcal{H}) = 0 \quad (5.80)$$

The above equation can be re-written by substituting Eq. 5.78 and Eq. 5.79 as follows:

$$f_y(\underline{\sigma}'_B - \delta \underline{\sigma}', \underline{\sigma}'_{b,C}, \mathcal{H}) = 0 \quad (5.81)$$

where Θ can be found using Taylor series expansion as follows:

$$\Gamma = \frac{f_y(\underline{\sigma}'_B, \underline{\sigma}'_{b,C}, \mathcal{H})}{\left\{ \frac{\partial f_b}{\partial \underline{\sigma}'} \right\}^T \left\{ \frac{\partial f_b}{\partial \underline{\sigma}'} \right\}} \quad (5.82)$$

In this procedure the stresses are updated to the bubble surface.

Bubble surface intersection

The bubble surface intersection algorithm is implemented to minimize the error in explicit algorithm when an elastic trial stress goes from the purely elastic state, $f_b(\underline{\sigma}'_n, \mathcal{H}) < 0$, to elastic-plastic state, $f_b(\underline{\sigma}'_{n+1} + d\underline{\sigma}'^e, \mathcal{H}) > 0$, during the load increment (see Fig. 5.7). The portion of the strain increment (scalar quantity Ω)

that only causes elastic behaviour can be found by solving the following nonlinear equation:

$$f_b(\underline{\sigma}'_n + \Omega \Delta \underline{\sigma}'^e, \mathcal{H}) = f_y(\underline{\sigma}'_{int}, \mathcal{H}) = 0 \quad (5.83)$$

The above equation can be solved by using the Pegasus intersection scheme (Sloan *et al.*, 2001). Once the scalar quantity Ω ($0 \leq \Omega \leq 1$) is determined, the portion of the strain increment which causes plastic deformation can be found. In Chapter 3, a summary of algorithm used to implement the S-CLAY1S is given and the same algorithm used to in the implementation of B-SCLAY1S.

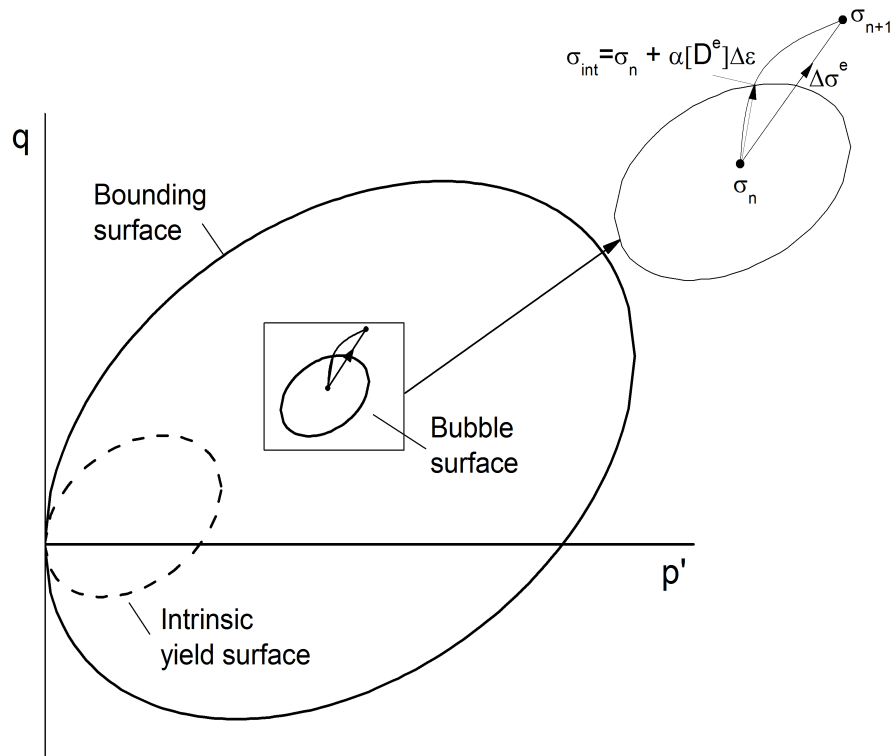


Figure 5.7: Bubble surface intersection: elastic to plastic transition

5.6 Summary

The S-CLAY1S model was developed by Karstunen *et al.* (2005) for simple monotonic loading conditions especially for normally consolidated or lightly over-consolidated

natural clays. However, some very important aspects of soil behaviour mainly in relation to the cyclic response cannot be adequately described by S-CLAY1S. The principal reason is that the classical concept of a yield surface provides a purely elastic stress range within the yield surface.

A new bubble B-SCLAY1S constitutive model, an extension of the S-CLAY1S model (Karstunen *et al.*, 2005) using the bubble surface concept (Al-Tabbaa, 1987) was introduced in this chapter. Two new parameters, ratio of the size of the bubble surface (R) and exponent in the hardening function (ψ) are introduced in the new model compared with S-CLAY1S. The salient feature of the introduced bubble surface is that plastic deformation may occur for stress state within the S-CLAY1S yield surface. The B-SCLAY1S model should be more realistic than S-CLAY1S in terms of predicting behaviour of over-consolidated clays and cyclic behaviour. The new model has been detailed in triaxial stress space first then generalized into the three-dimensional stress space and successfully implemented into PLAXIS.

A parametric study and application to some typical boundary value problems in geotechnical engineering are presented in detail in Chapter 6 and 7, respectively.

Chapter 6

Parametric study of B-SCLAY1S

This chapter presents a parametric study to examine the influences of the model parameters on behaviour of the bubble B-SCLAY1S model. The parametric study was carried out using B-SCLAY1S integration point program (IPP). The first part of parametric study is carried out by utilizing a set of parameters and triaxial experimental data provided by McGinty (2006) for Bothkennar clay. Secondly, the influence of bubble surface parameters on small-strain stiffness was investigated. Finally, the performance of the B-SCLAY1S model was analysed using simple constant q slow cyclic triaxial simulations. Results obtained from this chapter provide general guidance in choosing parameters for application of the B-SCLAY1S model in the following chapter.

6.1 Introduction

The B-SCLAY1S model explained in **Chapter 5** was used to perform the parametric study. The typical set of parameters were used from McGinty (2006) except the intrinsic λ_i value and the additional parameters for the bubble. McGinty (2006) suggested $\lambda_i = 0.18$ but $\lambda_i = 0.21$ was selected to well define the slope of the post yield compression in the simulation. The additional parameters to represent the bubble surface are assumed as $R = 0.15$ and $\psi = 1.5$. Typical values of parameters are given in Table 6.1, which are utilized as reference parameters for the parametric study.

The B-SCLAY1S model simulations of triaxial tests on vertical samples (McGinty, 2006) of Bothkennar clay were used in test Series B, named Test B2, B6 and B7. The

Table 6.1: Material parameters of Bothkennar clay for B-SCLAY1S

Soil constants					
κ	ν'	λ	M	γ (kN/m^3)	$k_x = k_y$ (m/day)
0.02	0.2	0.48	1.40	16.5	2.5 E-4
State variables					
e_0	K_0	α_0	χ_0	p'_{m0}	
2.0	0.5	0.31	10.0	84 kPa	
Additional parameters for anisotropy					
β	μ				
0.94	30				
Additional parameters for destructuration					
λ_i	a	b			
0.21	9.0	0.4			
Additional parameters for the bubble					
R	ψ				
0.15	1.5				

values of stress ratio η in the first and second loading stages were $\eta_1 = 0$ & $\eta_2 = 0.70$, $\eta_1 = 0$ & $\eta_2 = -0.70$ and $\eta_1 = 0$ & $\eta_2 = 0$ for Test B2, Test B6 and Test B7, respectively. Simulations of Test B7 are given in Appendix G.

The above mentioned tests were first loaded isotropically from mean effective stress of $p' = 16$ kPa to $p' = 210$ kPa. The first load takes the sample to a stress level approximately three times the initial yield stress. The Test B2 was isotropically unloaded to mean effective stress of $p' = 9.9$ kPa and again reloaded at stress ratio $\eta = 0.70$ to effective stress of $p' = 550$ kPa and $q = 388$ kPa. The Test B6 was isotropically unloaded to mean effective stress of $p' = 10$ kPa and again reloaded at stress ratio $\eta = -0.70$ to effective stress of $p' = 326$ kPa and $q = -229$ kPa.

6.2 Size of Bubble

The size of the bubble R controls the non-linear behaviour at small strain. The simulations of the model are compared with experimental data for Series B, Test

B2 and Test B6 in Figs. 6.1 and 6.2 respectively using varying R values of 0.1, 0.15, 0.20 and 0.25. In each figure the stress strain behaviour presented in terms of volumetric strain ϵ_v versus logarithm of mean effective stress $\ln p'$, deviator stress q versus deviatoric strain ϵ_d , axial stress σ_a versus axial strain ϵ_a and deviatoric strain ϵ_d versus volumetric strain ϵ_v .

The model predicts the experimental data very well for all the R values for the 1st loading of isotropic compression and is generally a good match with the experimental data (see Figs, 6.1 and 6.2). In particularly $\ln p'$ vs ϵ_v plots in Figs. 6.1(a) and 6.2(a), the model predicts generally good match to the experimental data before unloading starts for the all R values. The R value 0.10 predicts slightly lower volumetric strain before the bubble reaching the bounding surface compared to the experimental results. During unloading and reloading after each of the first loading stages, the R value has a greater influence in the prediction.

In the axial stress-strain plots in Figs. 6.1(b) and 6.2(b), the model is in good agreement with the experimental data. In terms of axial strain, higher value of R predicts results which are closer to the experimental data than the lower value of R .

In plots of deviatoric stress-strain response in Figs. 6.1(c) and 6.2(c), a small amount of negative shear strain is observed in the experimental data and this behaviour is well predicted by the model for all R values. The B-SCLAY1S model simulation underestimates the deviatoric strain during the reloading stage. A higher value of R predicts more closely to the experimental deviatoric strain than a lower value of R .

Strain paths plots are shown in Figs. 6.1(d) and 6.2(d) for Test B2 and B6 respectively. Simulations show the influence of R in the behaviour of the deviatoric and volumetric strain. The model prediction generally match well with the experimental data. A higher value of R predicts more closely to the experimental deviatoric strain than a lower value of R .

The test data is well modelled by the B-SCLAY1S model in general for the R value of 0.15.

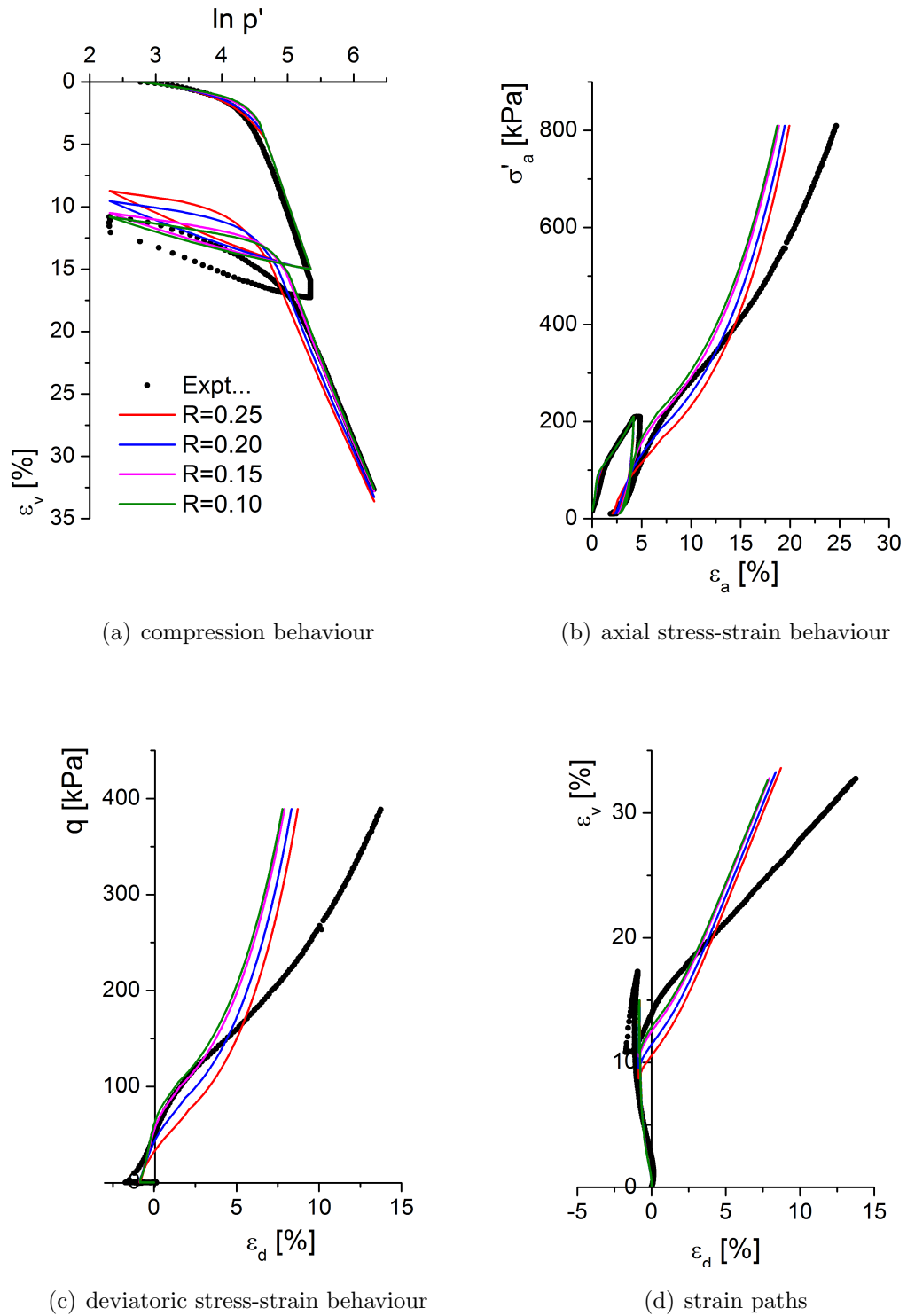


Figure 6.1: Influence of bubble size R of Test B2 (McGinty, 2006) simulation, where $\eta_1 = 0$ and $\eta_2 = 0.70$

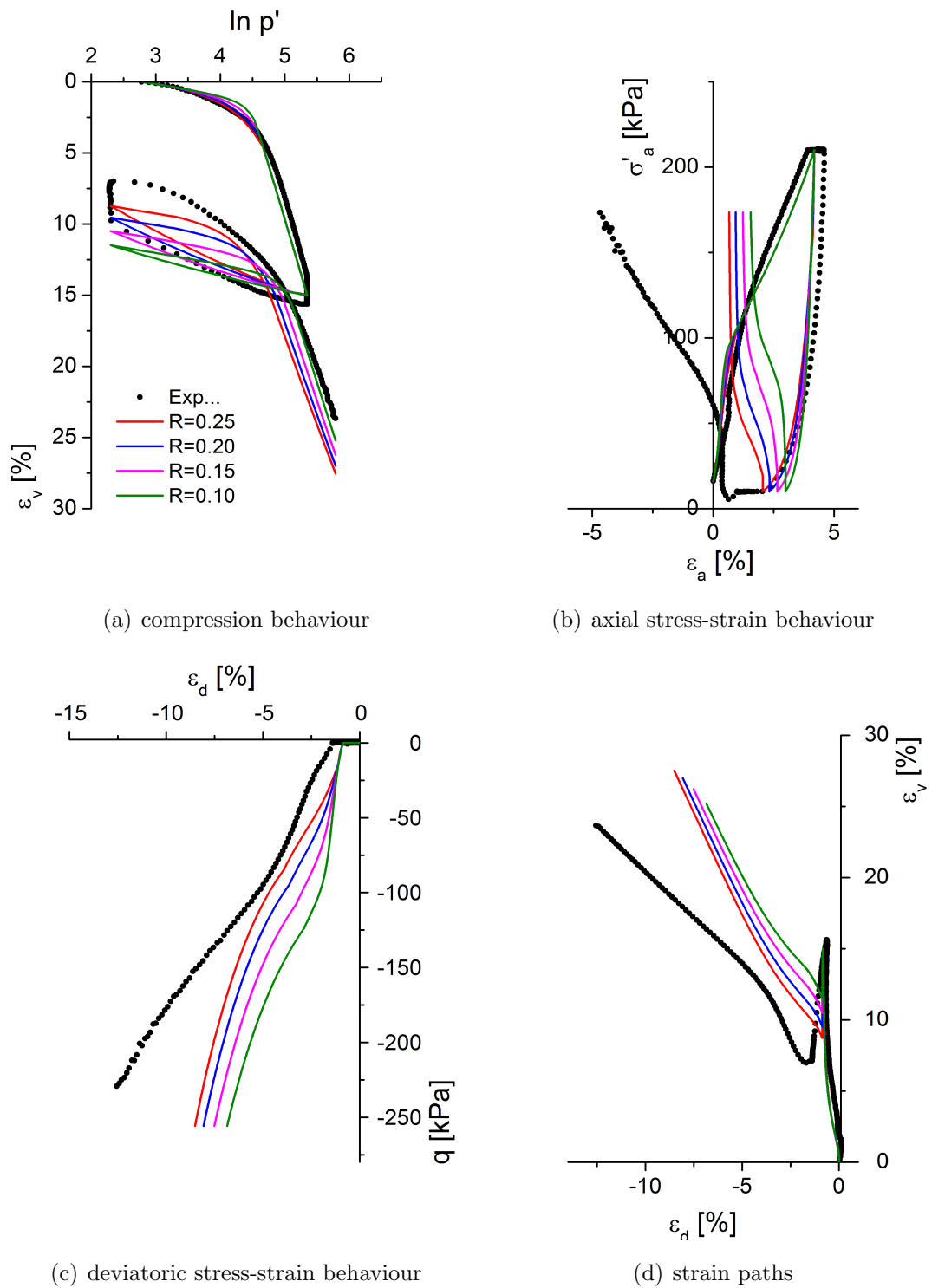


Figure 6.2: Influence of bubble size R of Test B6 (McGinty, 2006) simulation, where $\eta_1 = 0$ and $\eta_2 = -0.70$

6.3 Plastic modulus parameter

Plastic modulus parameter ψ controls the degradation of stiffness when plastic deformation occurs. The simulations of the model are compared with experimental data for tests in Series B (Test B2 and Test B6) in Figs. 6.3 and 6.4 respectively, using varying ψ values of 2.5, 2.0, 1.5 and 1.0. In each figure the stress strain behaviour presented in terms of volumetric strain ϵ_v versus logarithm of mean effective stress $\ln p'$, deviator stress q versus deviatoric strain ϵ_d , axial stress σ_a versus axial strain ϵ_a and deviatoric strain ϵ_d versus volumetric strain ϵ_v .

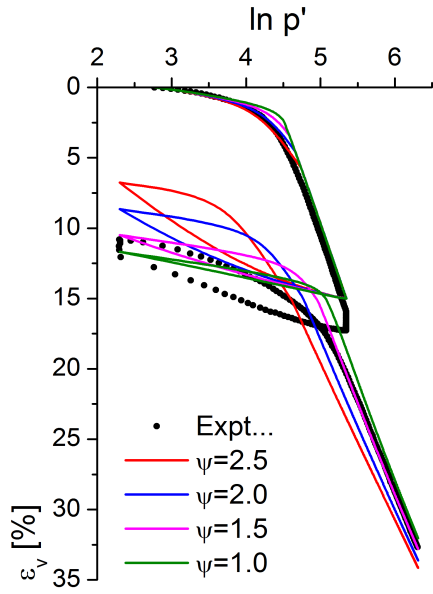
The model predicts almost similar behaviour for all the values of ψ for the 1st loading of isotropic compression and is generally a good match with the experimental data (see Figs. 6.1 and 6.2). In particularly $\ln p'$ vs ϵ_v plots in Figs. 6.3(a) and 6.4(a), the model predicts generally good match against experimental data before unloading starts for the all ψ values. The ψ value 1.0 predicts slightly lower volumetric strain before the bubble reaches the bounding surface compared to the experimental data. During unloading and reloading after each of the first loading stages, the ψ has a greater influence in the prediction.

In the axial stress-strain plots in Figs. 6.1(b) and 6.2(b), the model shows a good agreement with the experimental data. In simulation of Test B6, the model underestimates the axial strain. In terms of axial strain a higher value of ψ predicts more closely to the experimental data than a lower value of ψ .

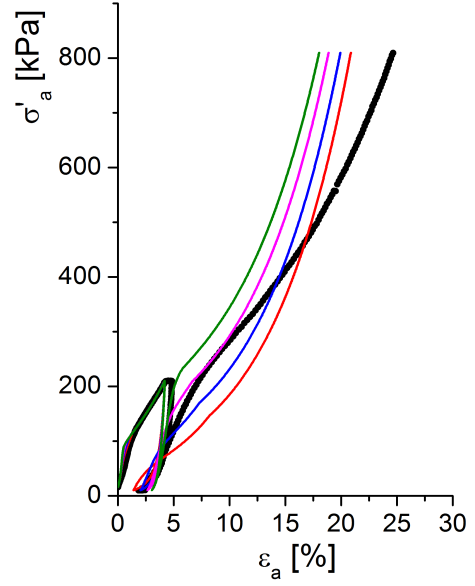
In plots of deviatoric stress-strain in Figs. 6.3(c) and 6.4(c), a small amount of negative shear strain is observed in the experimental data and this behaviour is well predicted by the model for all the ψ values used. The B-SCLAY1S model simulation underestimates the deviatoric strain during the reloading stage. A higher value of ψ predicts more closely to the experimental deviatoric strain than a lower value of ψ .

Strain paths plots are shown in Figs. 6.3(d) and 6.4(d) for Test B2 and B6, respectively. In Test B2 and B6 simulations show the influence of ψ in the behaviour of the deviatoric and volumetric strain. A higher value of ψ predicts a better match with the experimental deviatoric strain than a lower value of ψ .

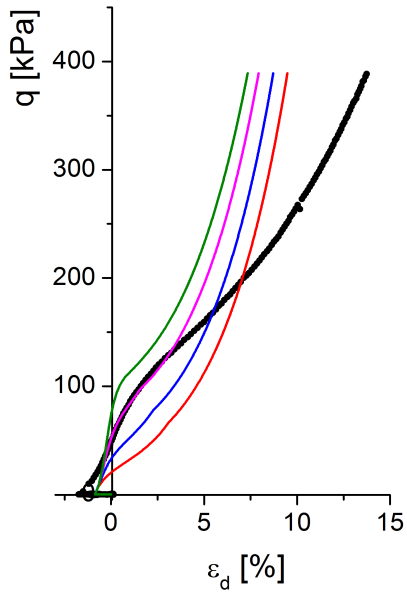
The plastic modulus parameter $\psi = 1.5$ of B-SCLAY1S gives a good match to the experimental data.



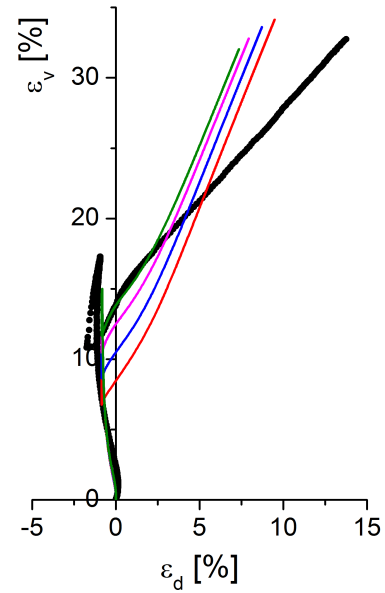
(a) compression behaviour



(b) axial stress-strain behaviour



(c) deviatoric stress-strain behaviour



(d) strain paths

Figure 6.3: Influence of hardening parameter ψ of Test B2 (McGinty, 2006) simulation, where $\eta_1 = 0$ and $\eta_2 = 0.70$

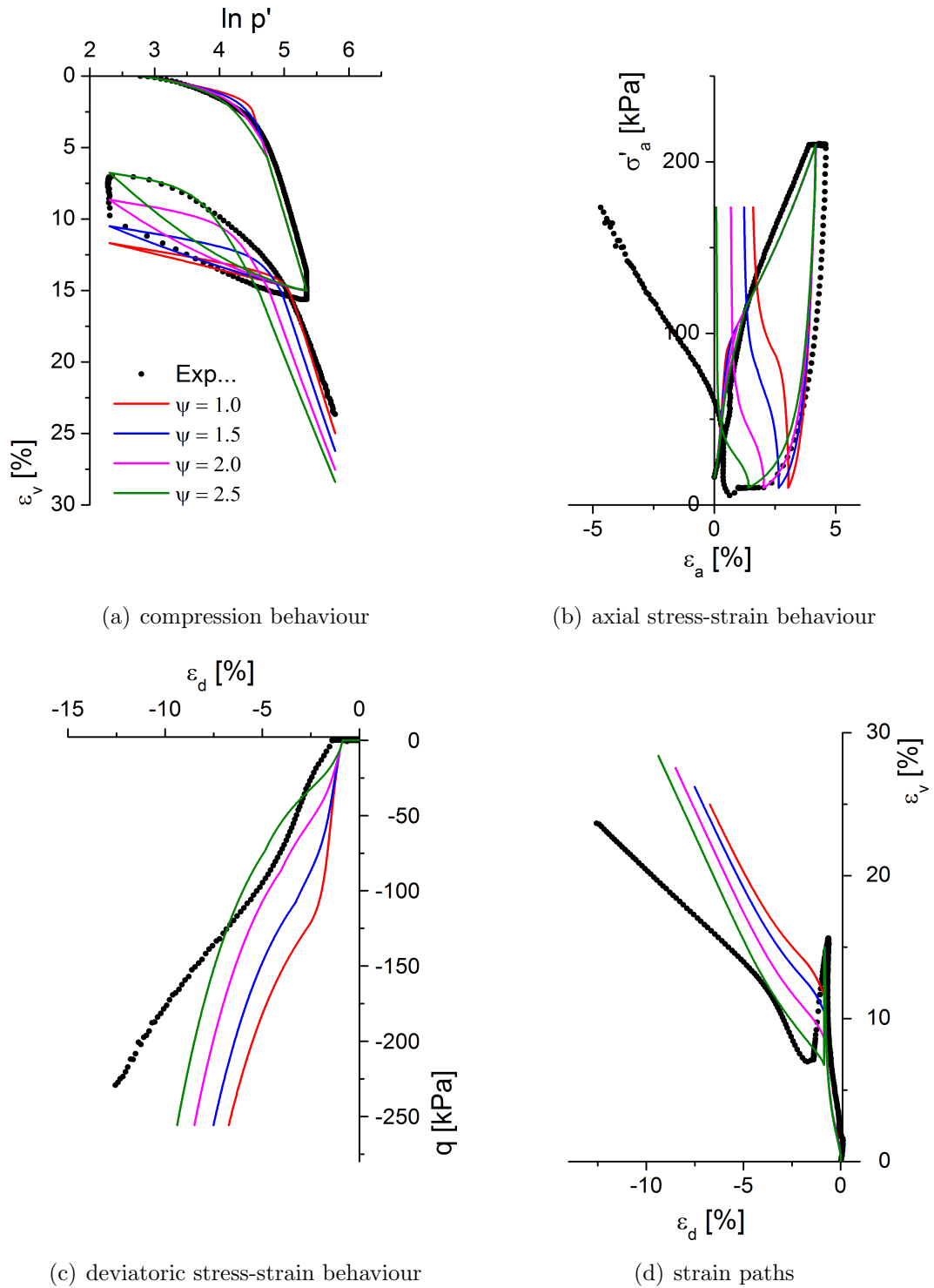


Figure 6.4: Influence of hardening parameter ψ of Test B6 (McGinty, 2006) simulation, where $\eta_1 = 0$ and $\eta_2 = -0.70$

6.4 Standard parameters

The parametric study carried out with the standard parameters of intrinsic compression index λ_i , swelling index κ and Poisson's ratio ν' . To investigate their significance, following ranges of parameter values were assumed $\lambda_i = 0.19, 0.20, 0.21$ and 0.22 , $\kappa = 0.01, 0.02, 0.03$ and 0.04 and $\nu' = 0.1, 0.2, 0.3$ and 0.4 . The simulations of varying λ_i value are shown in Figs. 6.5 and 6.6 for Test B2 and Test B6 respectively. Similarly, κ and ν' simulations are shown in Figs. 6.7, 6.8, Figs. 6.9 and 6.10, respectively. In each figure the stress strain behaviour presented in terms of volumetric strain ϵ_v versus logarithm of mean effective stress $\ln p'$, deviator stress q versus deviatoric strain ϵ_d , axial stress σ_a versus axial strain ϵ_a and deviatoric strain ϵ_d versus volumetric strain ϵ_v .

Figs. 6.5(a) to 6.10(a) show $\ln p'$ vs ϵ_v plots for λ_i , κ and ν' , respectively. Figs. 6.5(a) and 6.6(a) show that lower values of λ_i underestimate the volumetric strain and $\lambda_i = 0.21$ shows the best agreement against the experimental data. Simulation of varying κ value is shown in Figs. 6.7(a) and 6.8(a) for $\ln p'$ vs ϵ_v where κ has more influence during unloading-reloading. The κ value of 0.02 gives a good match to the experimental data. The Poisson's ratio has no influence in $\ln p'$ vs ϵ_v plot, see Figs. 6.9(a) and 6.10(a).

The axial stress-strain plots are shown in Figs. 6.5(b) to 6.10(b) for λ_i , κ and ν' respectively. Figs. 6.5(b) and 6.5(b) show good agreement with the higher values of λ_i (0.21 or 0.22) but in contrast the Test B6 shows lower value of λ_i predicts the experimental data better (see Fig. 6.6(b)). The influence of the κ is visible again during unloading stage (see Figs. 6.7(b) and 6.8(b)). Though Poisson's ratio ν' has no influence in isotropic loading and unloading-reloading, it has an influence in Test B2 and Test B6 in other plots. Higher values of Poisson's ratio ν' correspond more closely to the experimental data than lower values (see Figs. 6.9(b) and 6.10(b)).

Figs. 6.5(b) to 6.10(b) show the plot of deviatoric stress-strain behaviour for varying λ_i , κ and ν' values for Test B2 and Test B6 respectively. A small amount of negative shear strain (around 1%) is observed in the experimental data of Test B2 and this behaviour is well predicted by the model (see Figs. 6.5(c), 6.7(c) and 6.9(c)). Compared to the λ_i and κ values, the ν' values has more influence in the deviatoric stress-strain behaviour (see Figs. 6.9(c) and 6.10(c)) and higher values of ν' match best with the experimental data.

Strain paths plots are shown in Figs. 6.5(d) to 6.10(d) for λ_i , κ and ν' for Test B2 and B6 respectively. The model simulation of Test B2 and B6 show an influence of varying λ_i , κ and ν' in the behaviour of the deviatoric and volumetric strain, see Figs. 6.5(d), 6.6(d), 6.7(d), 6.8(d), 6.9(d) and 6.10(d). The lower values of λ_i underestimate the volumetric and deviatoric strains, see Figs. 6.5(d) and 6.6(d). In contrast to the λ_i , the higher values of κ underestimate the volumetric and deviatoric strains, see Figs. 6.7(d) and 6.8(d). A higher value of ν' predicts more closely to the experimental deviatoric strain than a lower value of ν' , see Figs. 6.9(d) and 6.10(d).

In general, parameter values of $\lambda_1 = 0.21$, $\kappa = 0.02$ and $\nu' = 0.2$ provide best match to the experimental data.

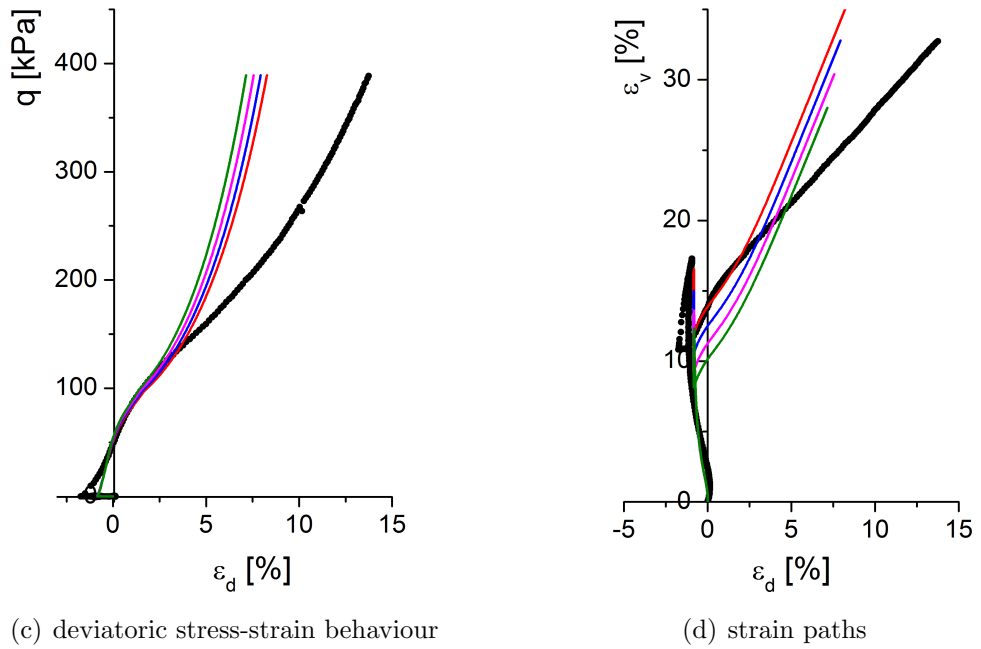
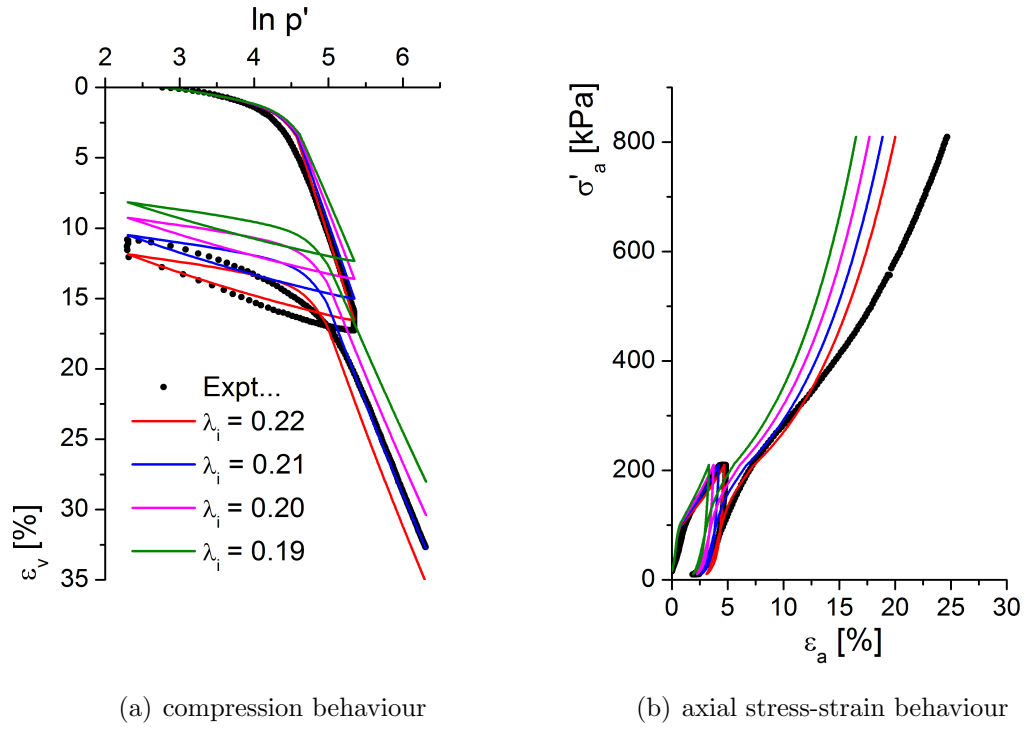


Figure 6.5: Influence of intrinsic compression index λ_i of Test B2 (McGinty, 2006) simulation, where $\eta_1 = 0$ and $\eta_2 = 0.70$

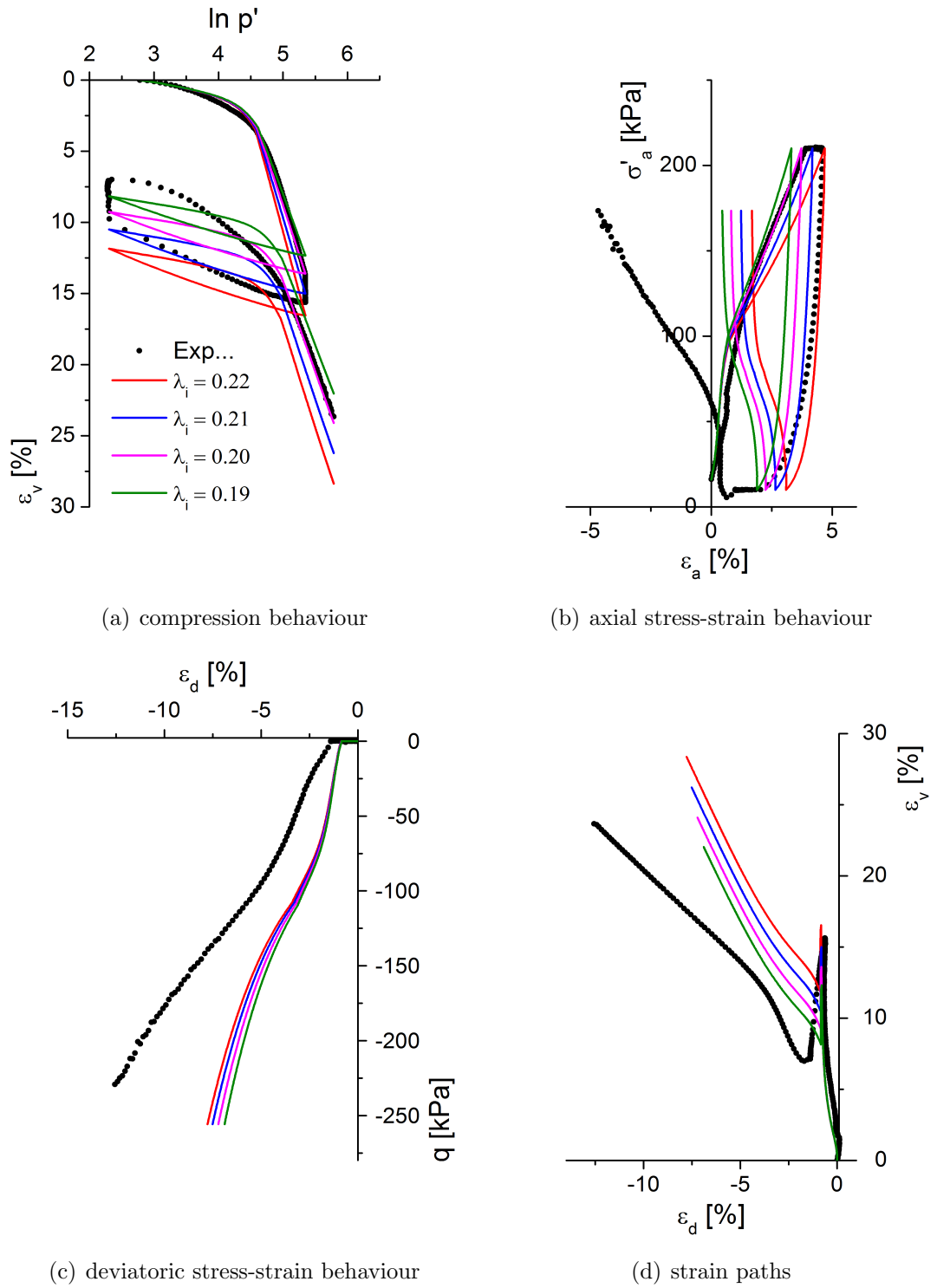
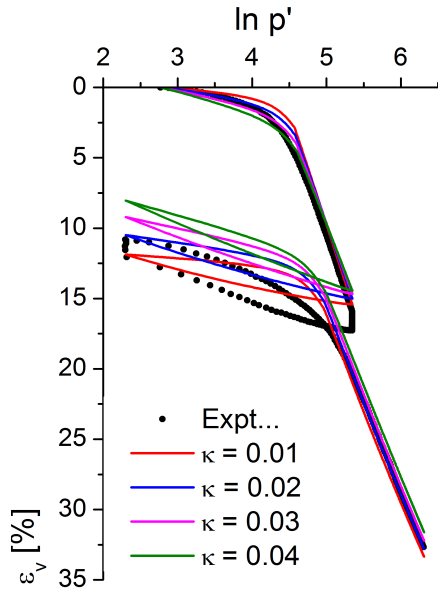
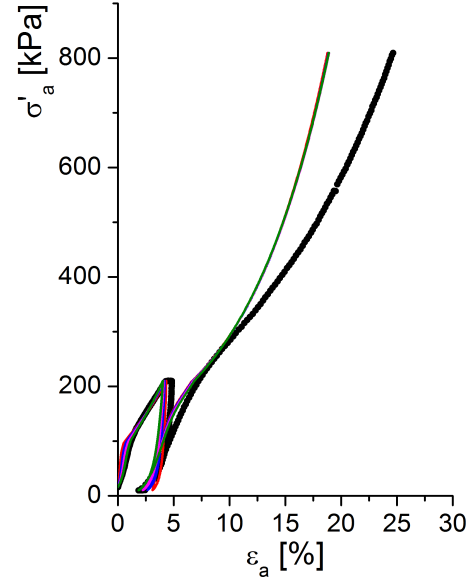


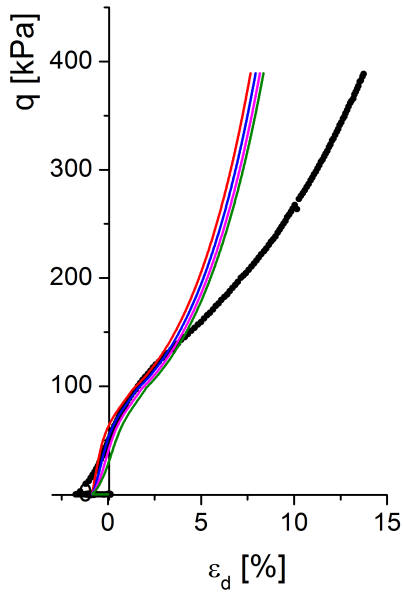
Figure 6.6: Influence of intrinsic compression index λ_i of Test B6 (McGinty, 2006) simulation, where $\eta_1 = 0$ and $\eta_2 = -0.70$



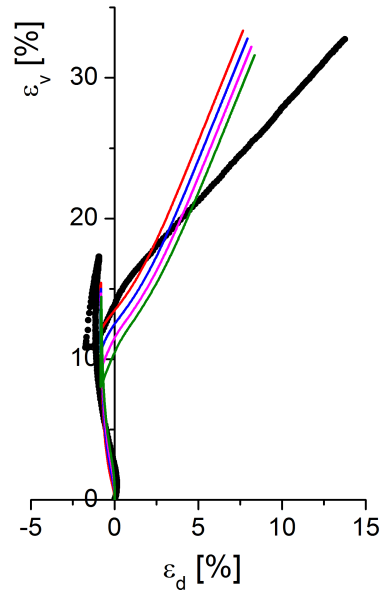
(a) compression behaviour



(b) axial stress-strain behaviour



(c) deviatoric stress-strain behaviour



(d) strain paths

Figure 6.7: Influence of swelling index κ of Test B2 (McGinty, 2006) simulation, where $\eta_1 = 0$ and $\eta_2 = 0.70$

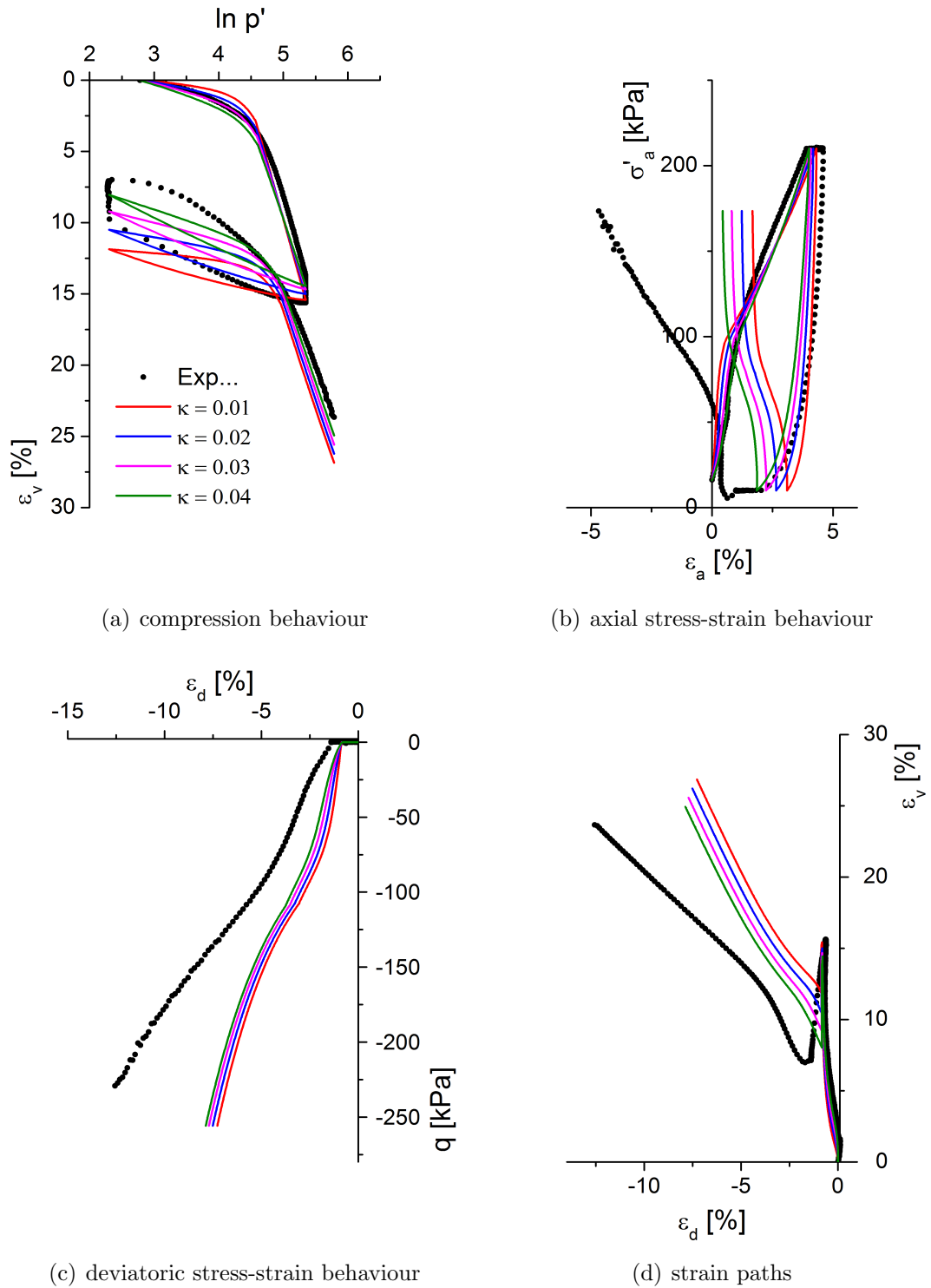
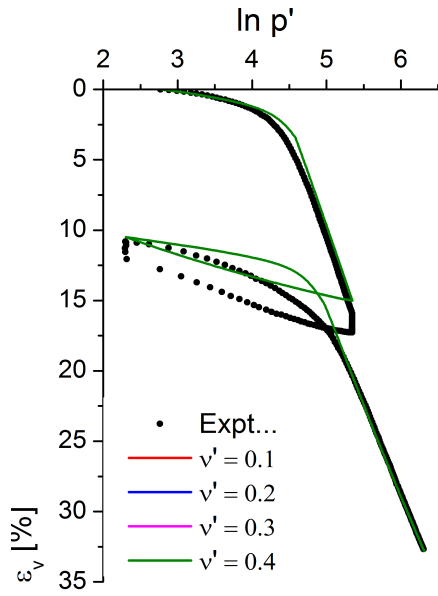
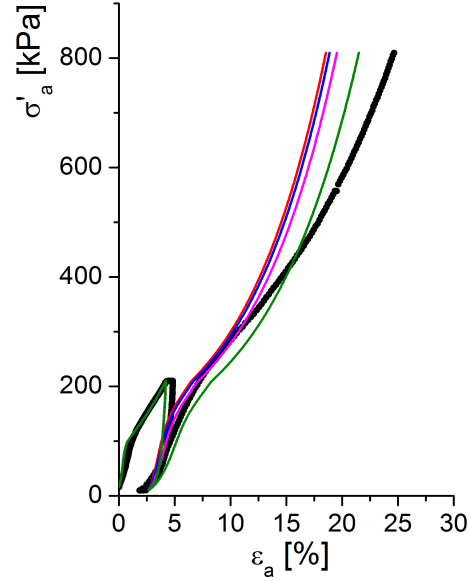


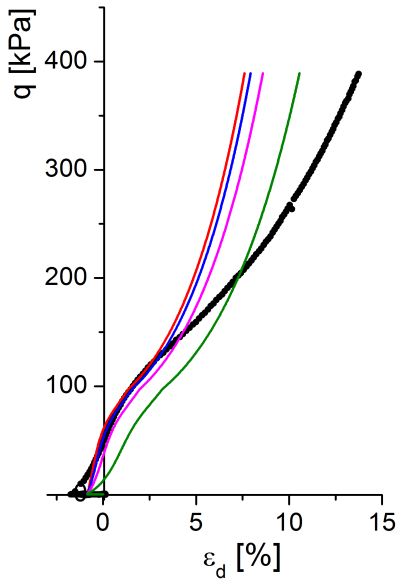
Figure 6.8: Influence of swelling index κ of Test B6 (McGinty, 2006) simulation, where $\eta_1 = 0$ and $\eta_2 = -0.70$



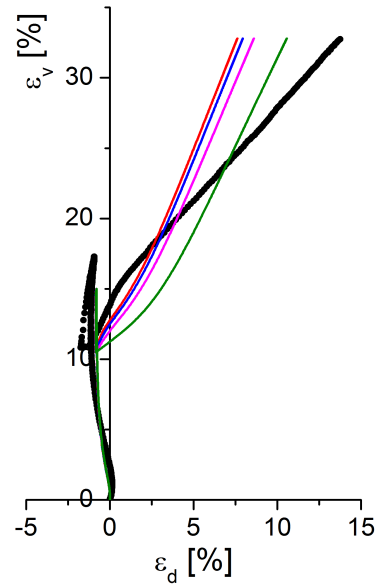
(a) compression behaviour



(b) axial stress-strain behaviour



(c) deviatoric stress-strain behaviour



(d) strain paths

Figure 6.9: Influence of Poisson's ratio ν' of Test B2 (McGinty, 2006) simulation, where $\eta_1 = 0$ and $\eta_2 = 0.70$

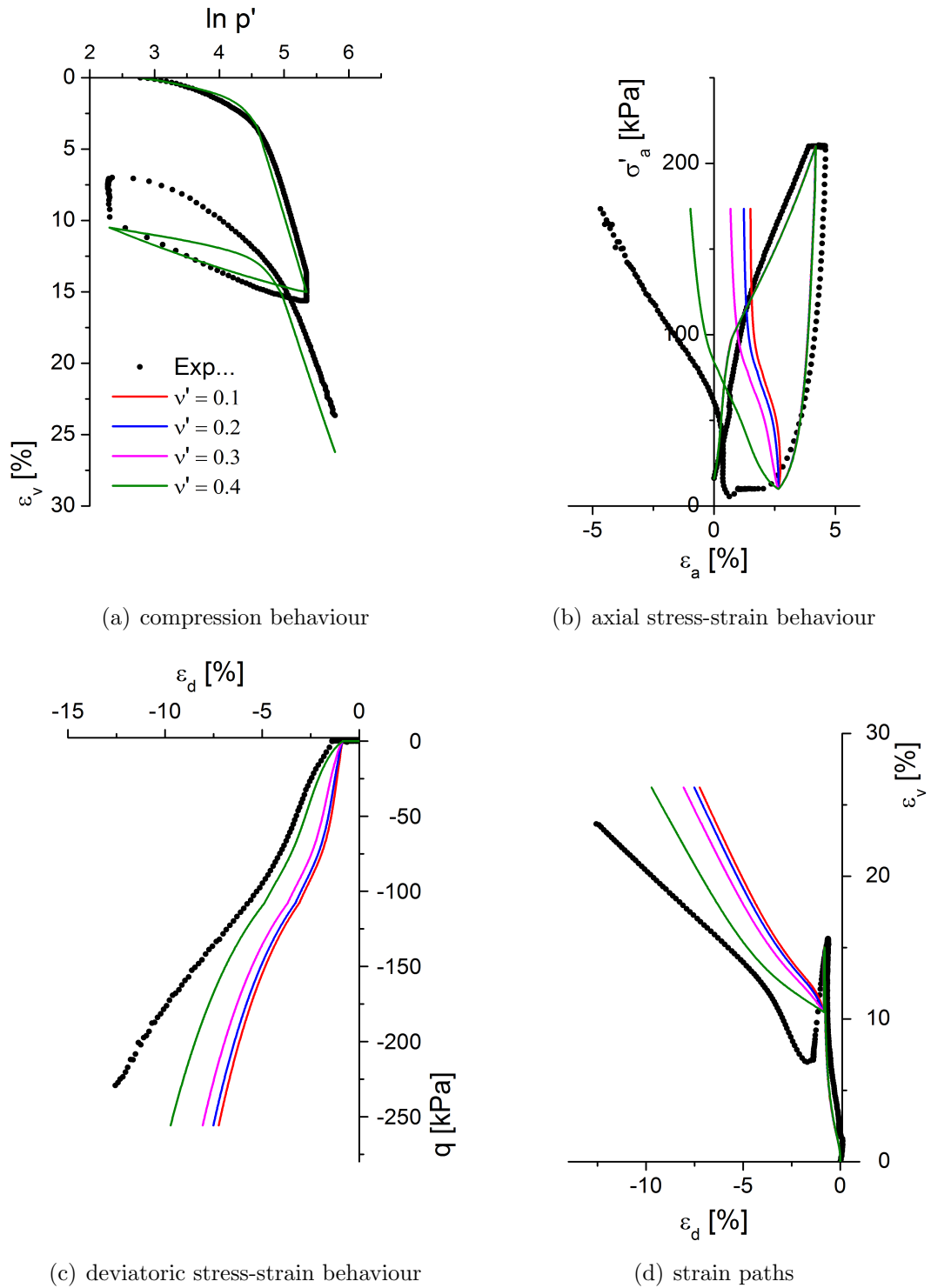


Figure 6.10: Influence of Poisson's ratio ν' of Test B6 (McGinty, 2006) simulation, where $\eta_1 = 0$ and $\eta_2 = -0.70$

6.5 Anisotropy parameters

Absolute effectiveness of rotational hardening μ and relative effectiveness of rotational hardening β were used for the parametric study of anisotropic parameters in the range of $\mu = 20, 30, 40$ and 50 and $\beta = 0.90, 0.94, 0.98$ and 1.02 . The simulations of varying μ and β values are shown in Figs. 6.11 and 6.12 and Figs. 6.13 and 6.14 respectively. In each figure the stress strain behaviour presented in terms of volumetric strain ϵ_v versus logarithm of mean effective stress $\ln p'$, deviator stress q versus deviatoric strain ϵ_d , axial stress σ_a versus axial strain ϵ_a and deviatoric strain ϵ_d versus volumetric strain ϵ_v .

Figs. 6.11(a) and 6.12(a) and Figs. 6.13(a) and 6.14(a) show $\ln p'$ vs ϵ_v plots for μ and β respectively. The μ has minimal influence in the generation volumetric strain (Figs. 6.11(a) and 6.12(a)) however, β has no influence in the generation volumetric strain (see Figs. 6.13(a) and 6.14(a)). Both μ and β show good agreement against the experimental data.

The axial stress-strain plots are shown in Figs. 6.11(b) and 6.12(b) and Figs. 6.13(b) and 6.14(b) for μ and β respectively. Though the influence of μ is minimal in Test B2 ($\eta_1 = 0$ and $\eta_2 = 0.70$), it shows a significant influence in Test B6 ($\eta_1 = 0$ and $\eta_2 = -0.70$). The lower values of μ match more closely with the experimental data than the higher values of μ (see Figs. 6.12(b)). The β value has again no influence in this plot (see Figs. 6.13(b) and 6.14(b)).

Figs. 6.11(b) and 6.14(b) plot the deviatoric stress-strain behaviour for varying μ and β values for Test B2 and Test B6, respectively. A small amount of negative shear strain (around 1%) is observed in the experimental data of Test B2 and this behaviour is predicted by the model (see Figs. 6.11(c) and 6.13(c)). Compared to the Test B2, μ has more influence in the Test B6 and lower values of μ give a better match with the experimental data (see Figs. 6.11(c) and 6.12(c)). Again β has no influence in deviatoric stress-strain prediction.

Strain paths plots are shown in Figs. 6.11(d) and 6.12(d) and Figs. 6.13(d) and 6.14(d) for μ and β values for Test B2 and Test B6, respectively. A lower value of μ predicts gives a marginal better match with the experimental deviatoric strain than a higher value of μ , see Fig. 6.11(d). Again β has no influence in deviatoric and volumetric strain simulation.

Simulation of B-SCLAY1S shows $\mu = 30$ and $\beta = 0.94$ give a good agreement to the experimental data.

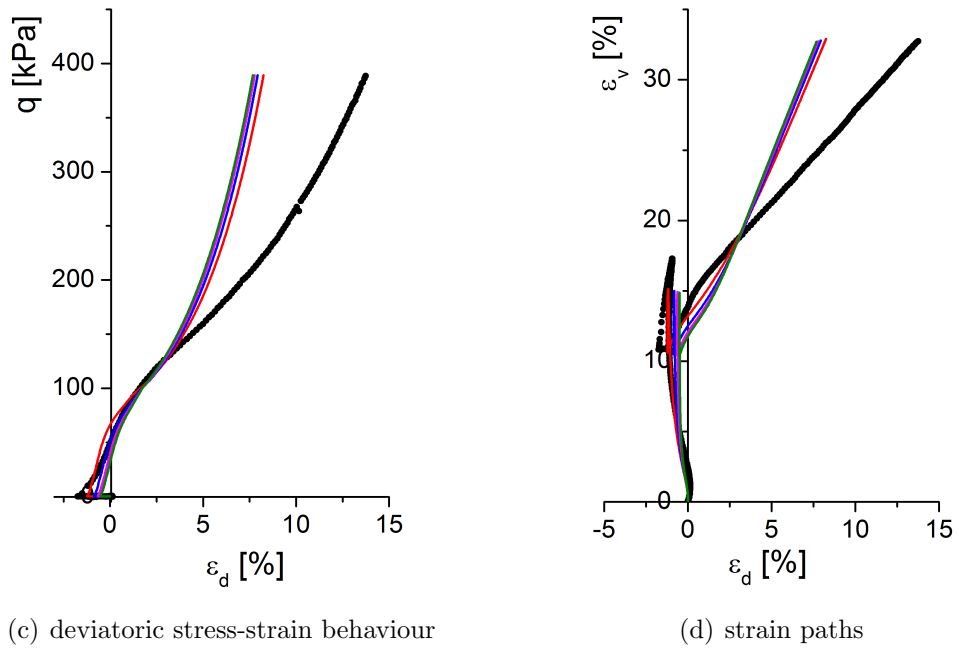
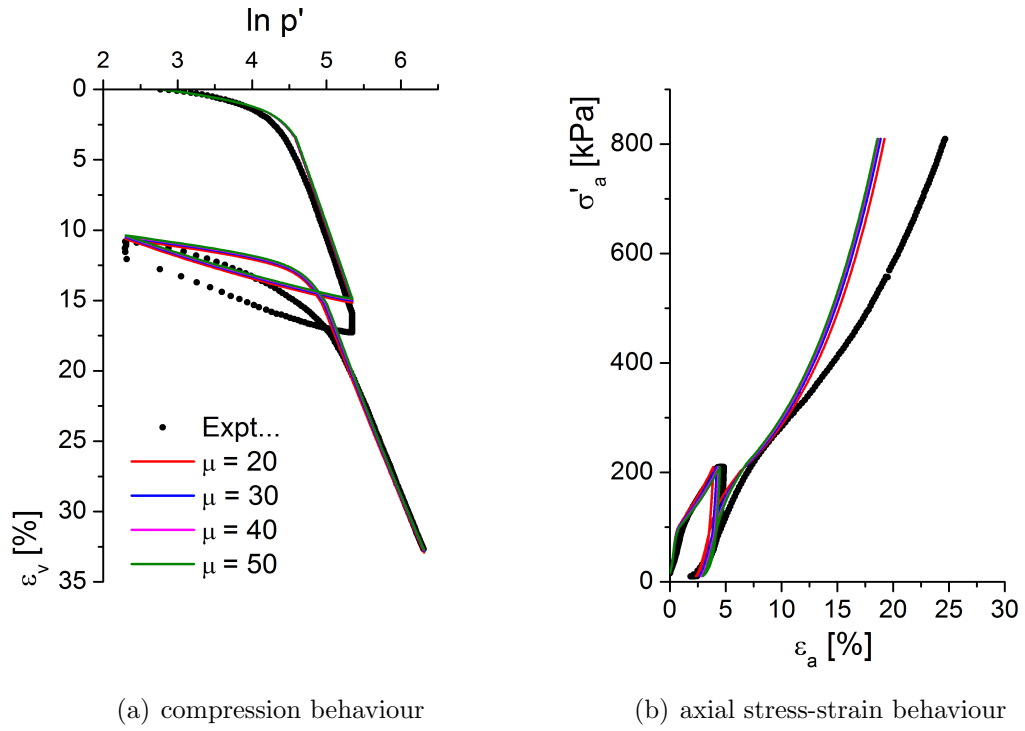


Figure 6.11: Influence of anisotropy parameter μ of Test B2 (McGinty, 2006) simulation, where $\eta_1 = 0$ and $\eta_2 = 0.70$

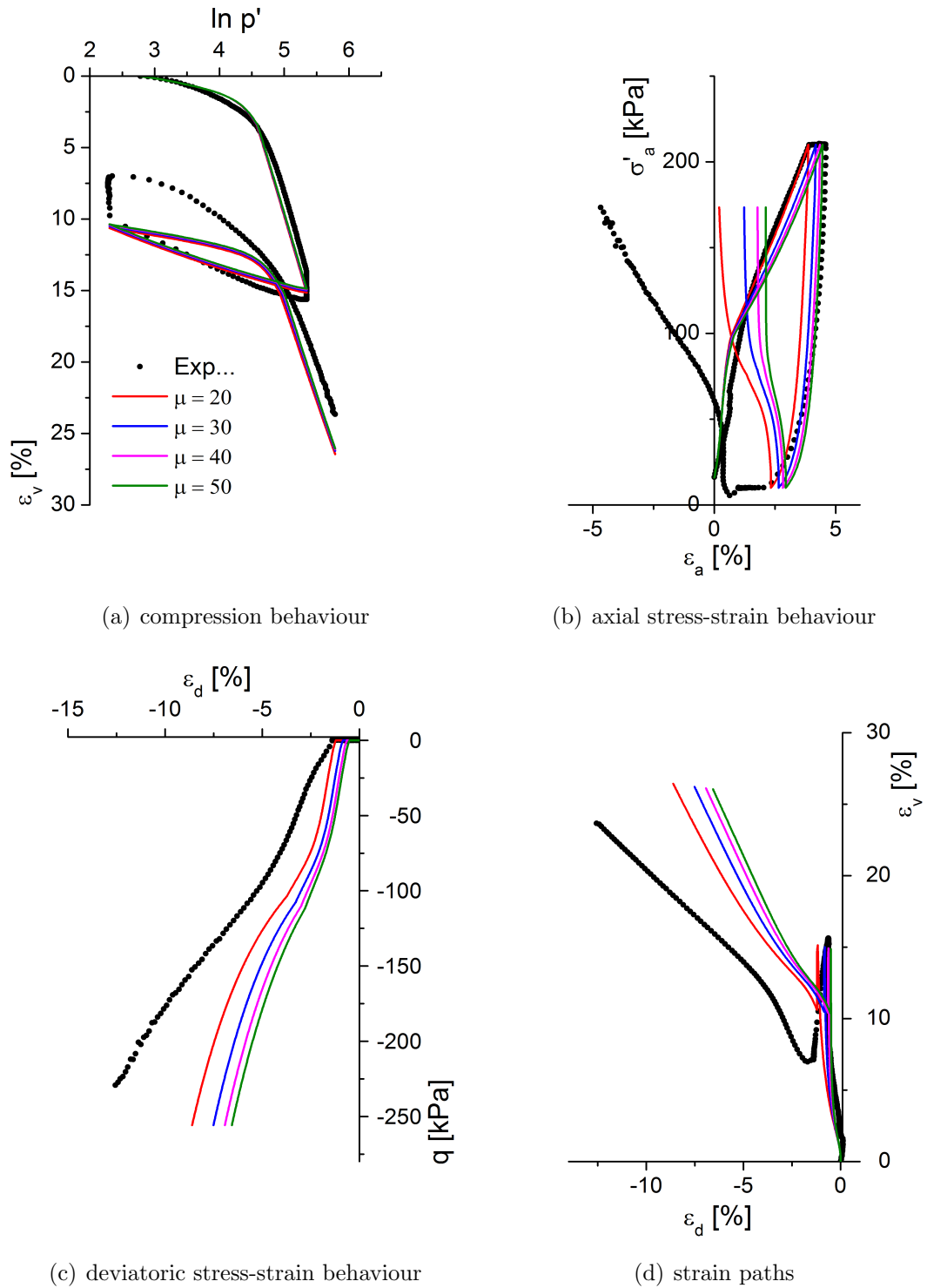


Figure 6.12: Influence of anisotropy parameter μ of Test B6 (McGinty, 2006) simulation, where $\eta_1 = 0$ and $\eta_2 = -0.70$

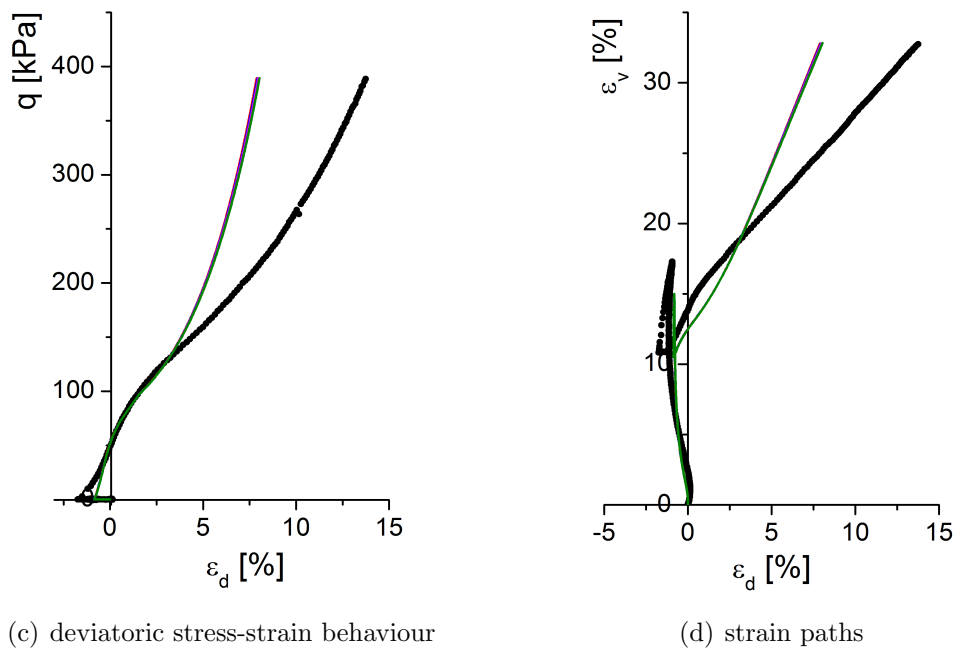
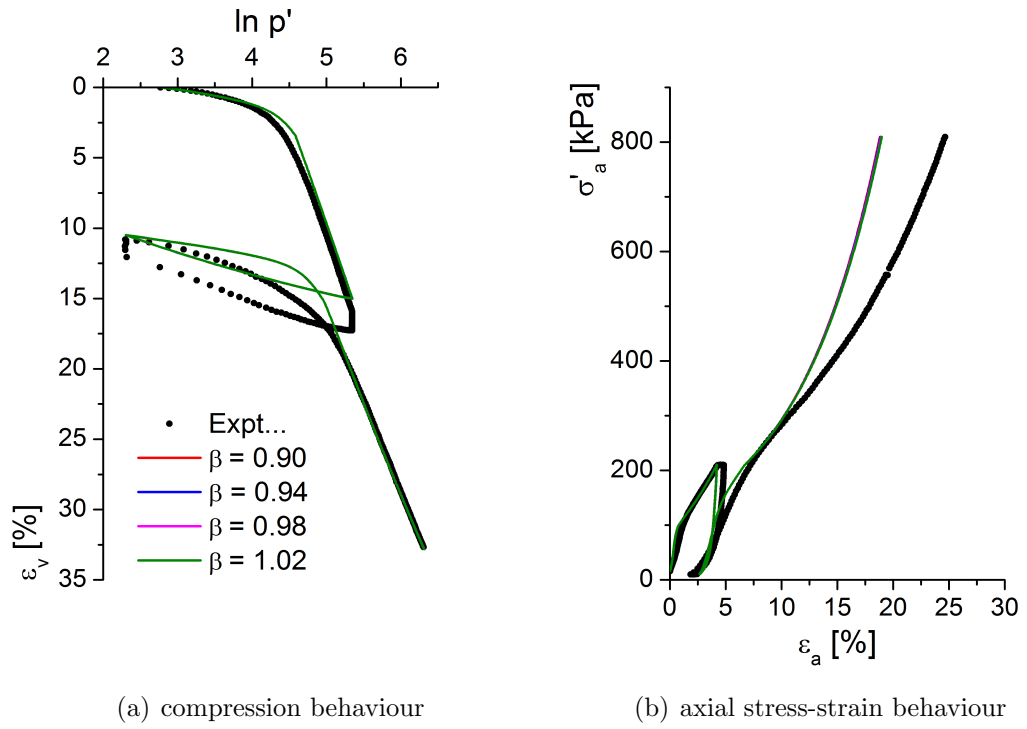


Figure 6.13: Influence of anisotropy parameter β of Test B2 (McGinty, 2006) simulation, where $\eta_1 = 0$ and $\eta_2 = 0.70$

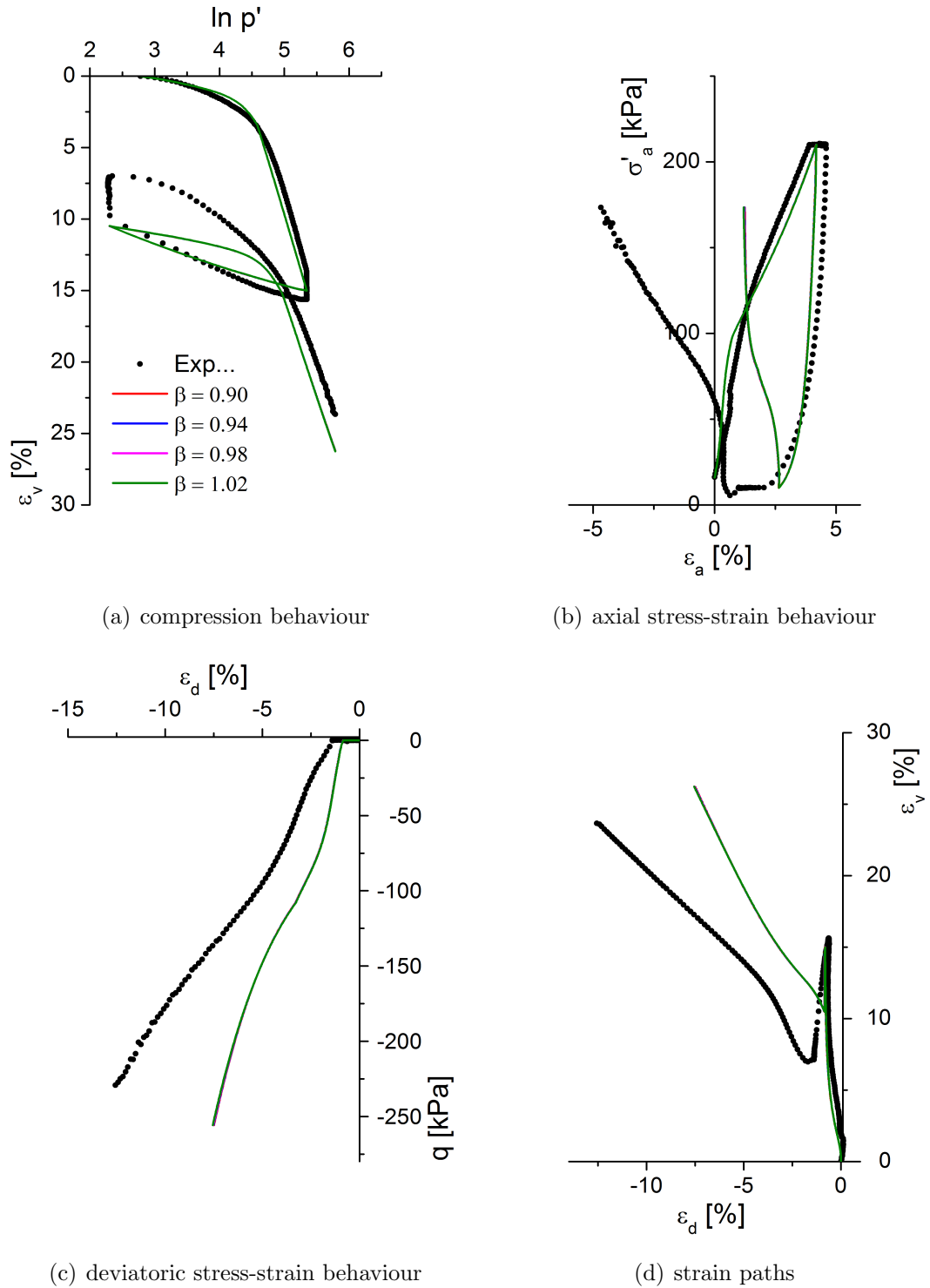


Figure 6.14: Influence of anisotropy parameter β of Test B6 (McGinty, 2006) simulation, where $\eta_1 = 0$ and $\eta_2 = -0.70$

6.6 Destructuration parameter

The initial bonding χ_0 and absolute and relative rate of destructuration a and b parameters were used in this parametric study in the range of $\chi_0 = 6, 8, 10, 12$ and $a = 9 \ \& \ b = 0.2, a = 9 \ \& \ b = 0.4, a = 10 \ \& \ b = 0.2$ and $a = 10 \ \& \ b = 0.4$. The simulations of varying χ_0 and $a \ \& \ b$ values are shown in Figs. 6.15 and 6.16 and Figs. 6.17 and 6.18, respectively.

Figs. 6.15(a) and 6.16(a) and Figs. 6.17(a) and 6.18(a) show $\ln p'$ vs ϵ_v plots for χ_0 and $a \ \& \ b$, respectively. Higher values of χ_0 predicts a better match with the experimental data, see Figs. 6.15(a) and 6.16(a). The absolute rate of destructuration parameter a has significant influence of the model predictions whereas the relative rate of destructuration parameter b has no significant influence in the model predictions, see Figs. 6.17(a) and 6.18(a).

The axial stress-strain plots are shown in Figs. 6.15(b) and 6.16(b) and Figs. 6.17(b) and 6.18(b) for χ_0 and $a \ \& \ b$, respectively. The parameters χ_0 and a have more influence than parameter b in the prediction of the model. An influence of $a \ \& \ b$ is marginal in Test B2 ($\eta_1 = 0$ and $\eta_2 = 0.70$) compared to the other tests, see Fig. 6.17(b).

Figs. 6.15(b), 6.16(b) and Figs. 6.17(b), 6.18(b) show the plot of deviatoric stress-strain behaviour for varying χ_0 and $a \ \& \ b$ values for Test B2 and Test B6, respectively. The highest value of χ_0 predicts the best match with the experimental results, see Figs. 6.15(b) and 6.16(b). In deviatoric stress-strain behaviour, the $a \ \& \ b$ have a minor influence see Figs. 6.17(b) and 6.18(b). A small amount of negative shear strain (around 1%) is observed in the experimental data of Test B2 and again this behaviour is predicted by the model (see Figs. 6.15(c) and 6.17(c)).

Strain paths plots are shown in Figs. 6.15(d) and 6.16(d) and Figs. 6.17(d) and 6.18(d) for χ_0 and $a \ \& \ b$ values for Test B2 and Test B6, respectively. The highest value of χ_0 gives the best match with the experimental volumetric strain than the lowest value of χ_0 , see Figs. 6.15(d) and 6.16(d). However the model predictions significantly underestimate the deviatoric strains. Compared to the influence of χ_0 , the $a \ \& \ b$ has a marginal influence in the model predictions, see Figs. 6.17(d) and 6.18(d).

The test data is well modelled by B-SCLAY1S of the destructuration parameters $\chi_0 = 10$ and $a = 9 \ \& \ b = 0.4$.

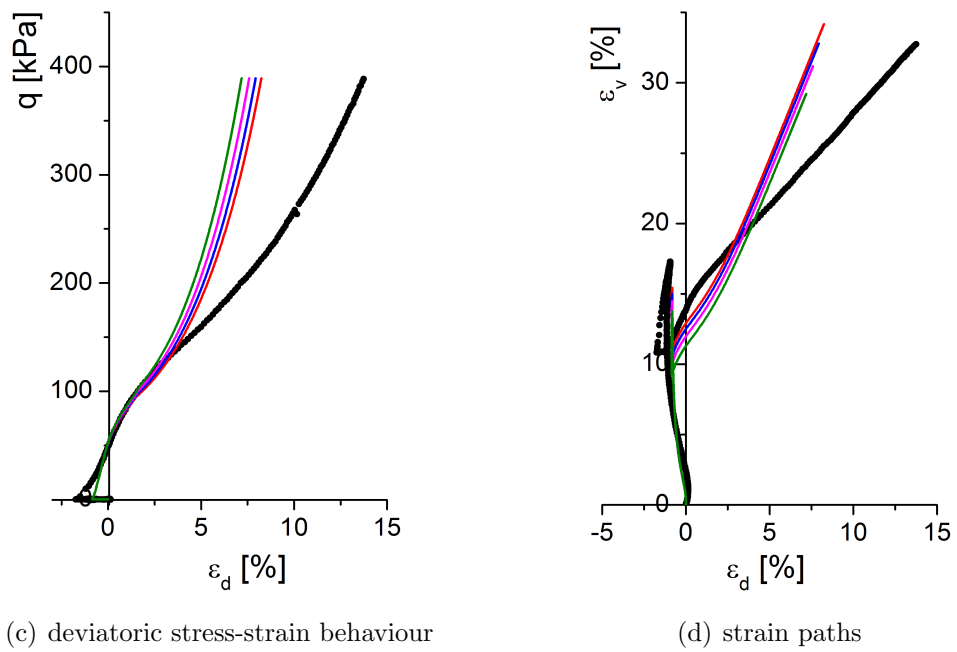
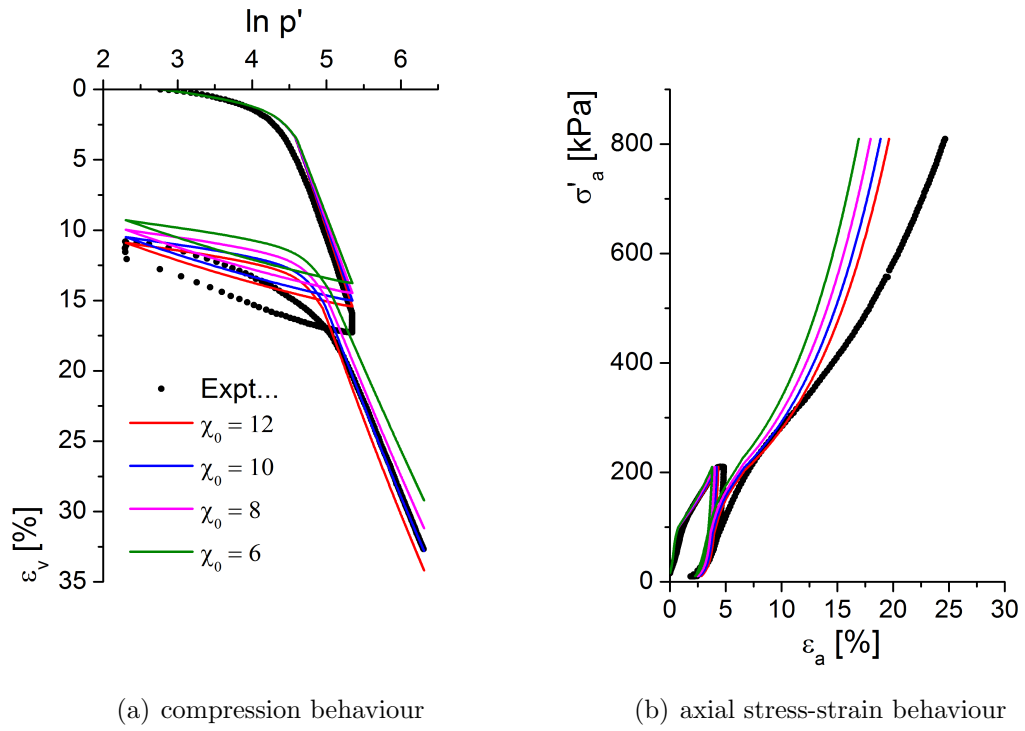


Figure 6.15: Influence of initial bonding χ_0 of Test B2 (McGinty, 2006) simulation, where $\eta_1 = 0$ and $\eta_2 = 0.70$

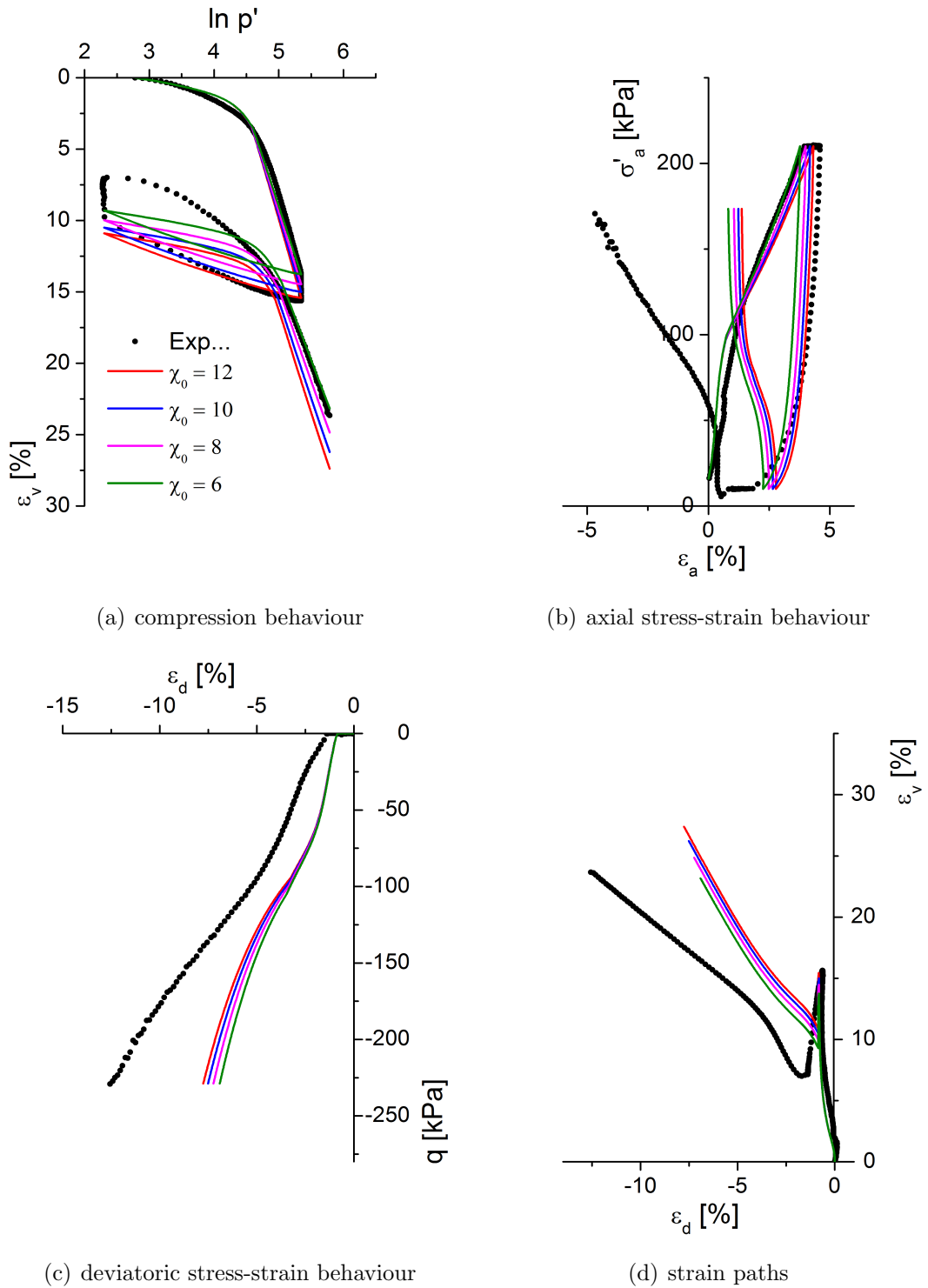
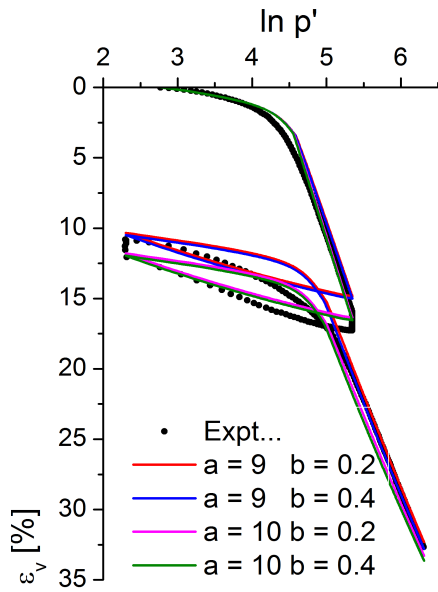
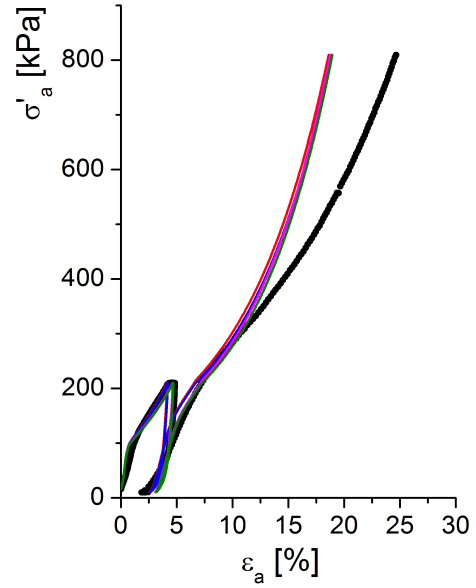


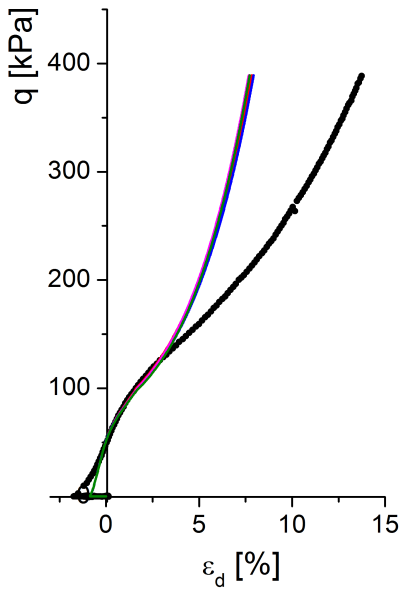
Figure 6.16: Influence of initial bonding χ_0 of Test B6 (McGinty, 2006) simulation, where $\eta_1 = 0$ and $\eta_2 = -0.70$



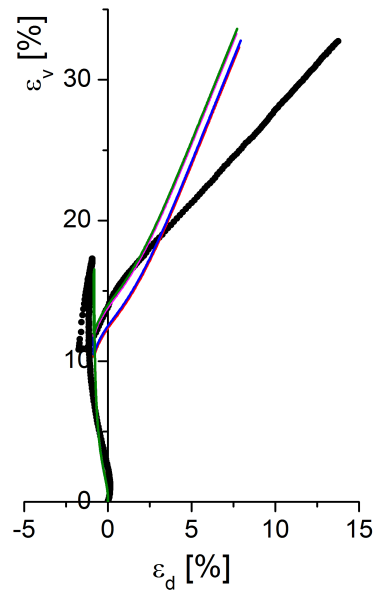
(a) compression behaviour



(b) axial stress-strain behaviour



(c) deviatoric stress-strain behaviour



(d) strain paths

Figure 6.17: Influence of destructurational parameter a and b of Test B2 (McGinty, 2006) simulation, where $\eta_1 = 0$ and $\eta_2 = 0.70$

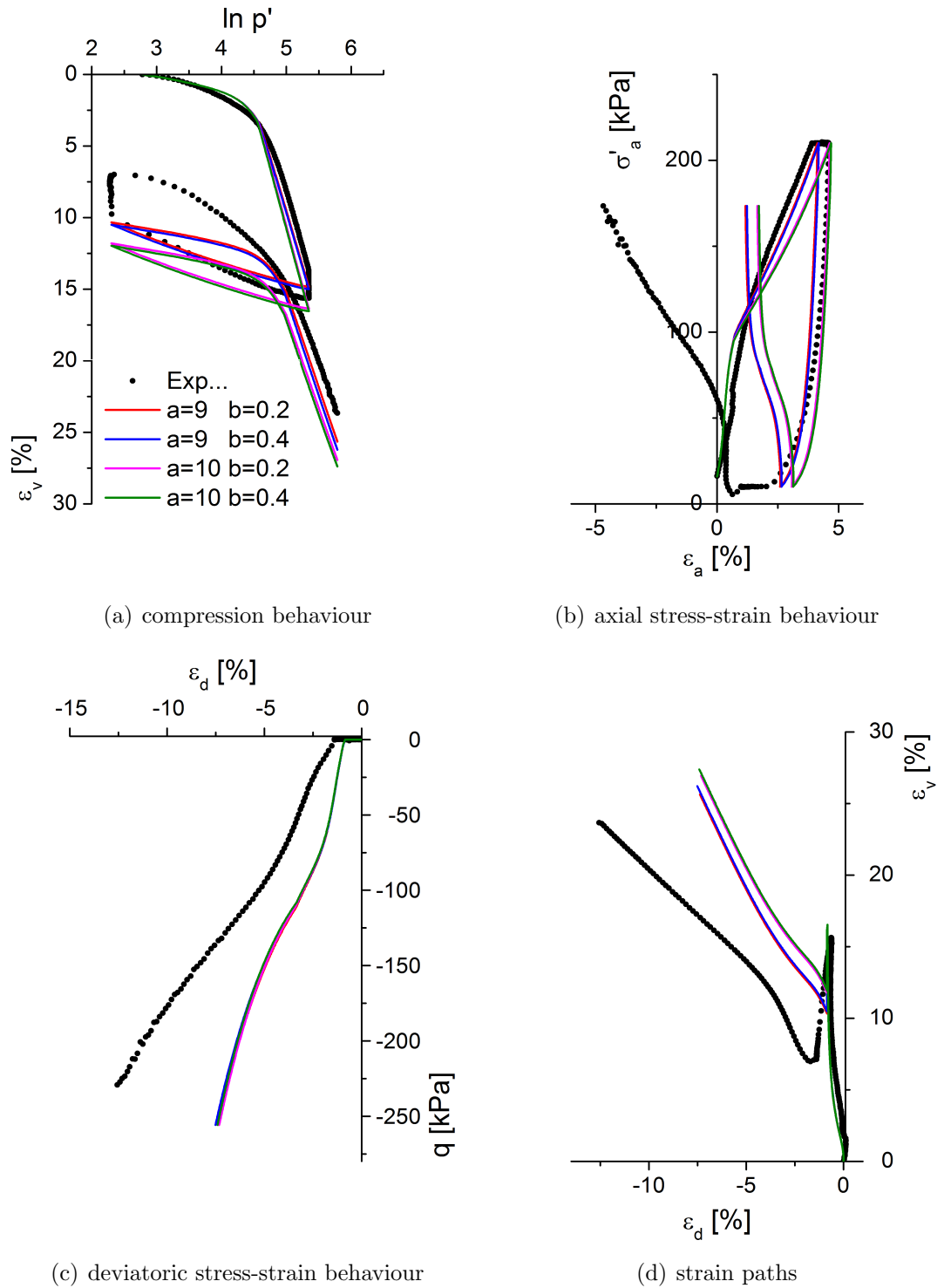


Figure 6.18: Influence of destructurational parameter a and b of Test B6 (McGinty, 2006) simulation, where $\eta_1 = 0$ and $\eta_2 = -0.70$

6.7 Small strain stiffness

The proposed B-SCLAY1S model predicts small strain behaviour during loading through an introduction of the bubble surface. The size of the bubble (i.e. elastic range) determines the non-linear behaviour. If the size of the bubble is very small ($R \leq 0.01$), the model shows a non-linear behaviour from the beginning of loading. Though a small value of R can produce a smooth transition in modulus, it may increase computational time significantly and errors in calculation. To avoid these problems, the R value should be larger ($R \geq 0.05$).

The undrained shear modulus (G_u) against shear strain behaviour is considered for this parametric study. Two parameters R and ψ are considered to be the most influential model parameters on the small-strain behaviour. The initial preconsolidation pressure of the bounding surface is assumed 400 kPa and accordingly, initial bubble is sized for $R = 0.05, 0.10, 0.15, 0.20$ and 0.25 with the bubble centre being at the isotropic line ($p' = 300 \text{ kPa}$) as shown in Fig. 6.19. The plastic modulus parameter ψ is assumed to have varying values of $1.0, 1.5, 2.0$ and 2.5 . Rest of the all parameters are the same as the reference data given in Section 6.1 for Bothkennar clay. For a comparison, simulation is done using $R = 1.0$ i.e. S-CLAY1S. Triaxial undrained simulation is done using 10% of vertical strain and a small strain increment of 0.001% per step is used.

The undrained shear modulus (G_u) normalized with respect to the mean stress at the start of the shearing (p'_0) is plotted against the shear strain (ϵ_s) in Figs. 6.20(a) and 6.20(b) for varying R and ψ values respectively. In undrained triaxial condition, shear strain (ϵ_s) is equal to axial strain (ϵ_a). The undrained shear modulus (G_u) is given by:

$$G_u = \frac{1}{3} \frac{\Delta q}{\Delta \epsilon_s} \quad (6.1)$$

Fig. 6.20(a) represents $G - \gamma$ curves for R equal to $0.05, 0.10, 0.15, 0.20, 0.25$ and 1.0 respectively with constant $\psi = 1.5$. It can be seen that shear modulus start to degrades faster with shear strain if R is smaller. At the beginning of the curves, there is a flat portion due to the presence of elastic region of the bubble. This flat portion of the curves increases when the size of the bubble increases. There is a sudden drop in stiffness when the stresses touch the bubble surface and a relatively small drop of stiffness with strain for smaller values of R . Because of this, a new hardening modulus is required in order to have smooth transition in stiffness.

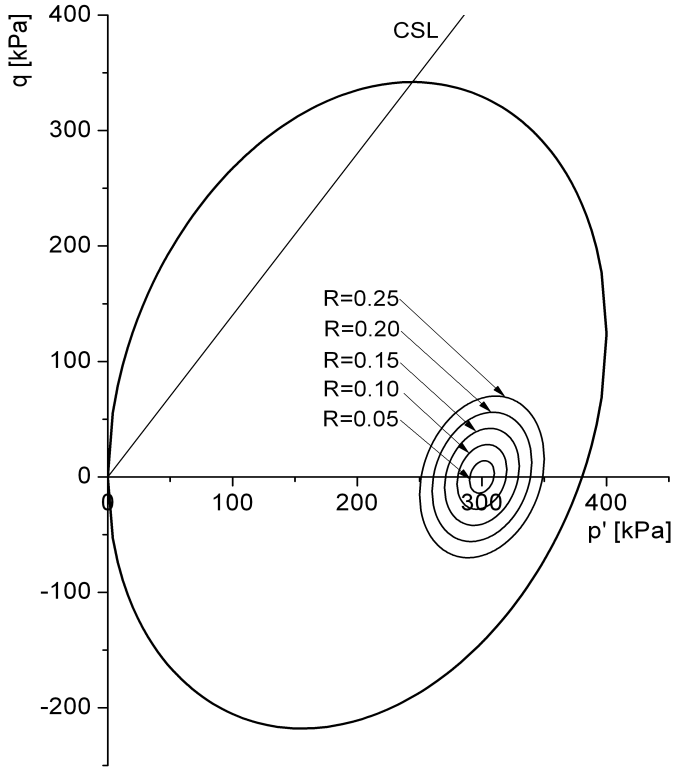


Figure 6.19: Initial location and size of the bubbles and bounding surfaces

Fig. 6.20(b) shows the influence of the plastic modulus parameter ψ for constant $R = 0.15$. The shear modulus start to degrade when stress passes the elastic region defined by the bubble, this is faster the lower the values of ψ .

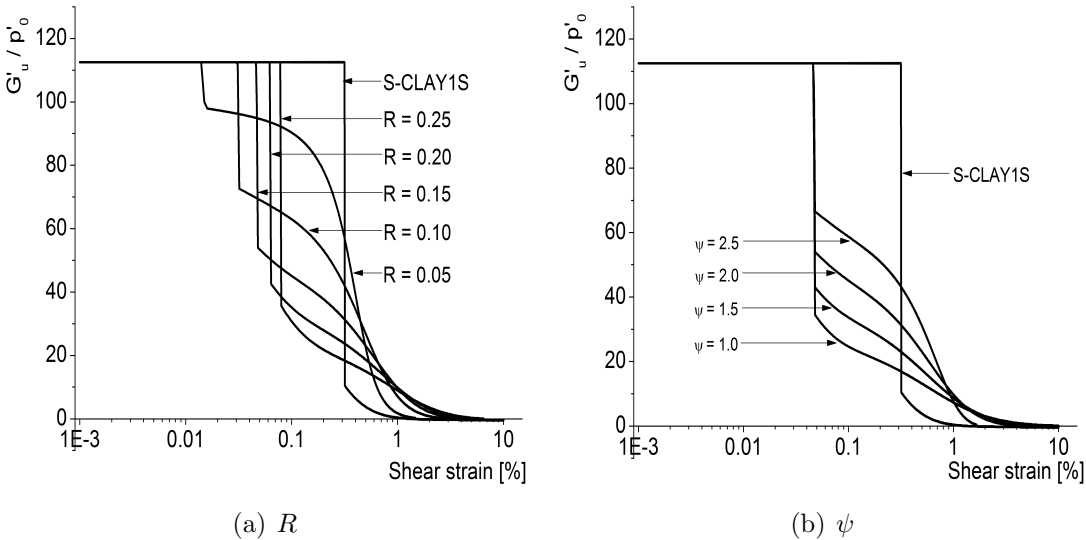


Figure 6.20: $G - \gamma$ curves

6.8 Constant q slow cyclic triaxial simulations

To investigate the effect of the two parameters (R and ψ) related to the bubble surface and the κ value on the performance of the B-SCLAY1S model, a simple constant q slow cyclic triaxial simulation was performed. The soil sample was assumed to be slightly over-consolidated ($\text{OCR}=1.1$) with an initial stress of $p'=66.7 \text{ kPa}$ and $q=50 \text{ kPa}$. The deviatoric stress was kept constant while cell pressure was increased and then decreased (one way cyclic loading). Ten load cycles were applied. First four cycles, p' varies from 91.6 kPa to 41.6 kPa ; second three cycles, p' varies from 111.6 kPa to 41.6 kPa and final three cycles, p' varies from 121.6 kPa to 41.6 kPa . The soil input parameters were used to represent the Bothkennar clay (Table. 6.1). Two out of three parameters were kept constant while third parameter was varied so that its effect on the model's performance could be seen.

Firstly, Figs. 6.21 - 6.23 show the effect of κ on the performance of the B-SCLAY1S model. The higher the value of κ , the more strain (both axial and volumetric) the model will recover upon unloading. In other words, the lower the value of κ , the more permanent strains the model will predict. This is because a larger value of κ leads to the soil being softer during unloading and hence, larger amounts of strains are recovered.

Secondly, the effect of the parameter R which relates to the size of the bubble surface is investigated. The permanent strains (both axial and volumetric) increases as the value of R decreases, see Figs. 6.24 - 6.26. This is because a smaller value of R causes the soil to be softer during loading/reloading stages and strains increase as a result.

Finally, the parameter ψ (exponent in the hardening function) is examined in cyclic behaviour of clay. Figs. 6.27 - 6.29 shows the results when $\psi = 1.0, 1.5$ and 2.0 , respectively. It can be seen that a bigger value of ψ will make the soil become softer during reloading, and as a result more permanent strains occur.

6.8 Constant q slow cyclic triaxial simulations

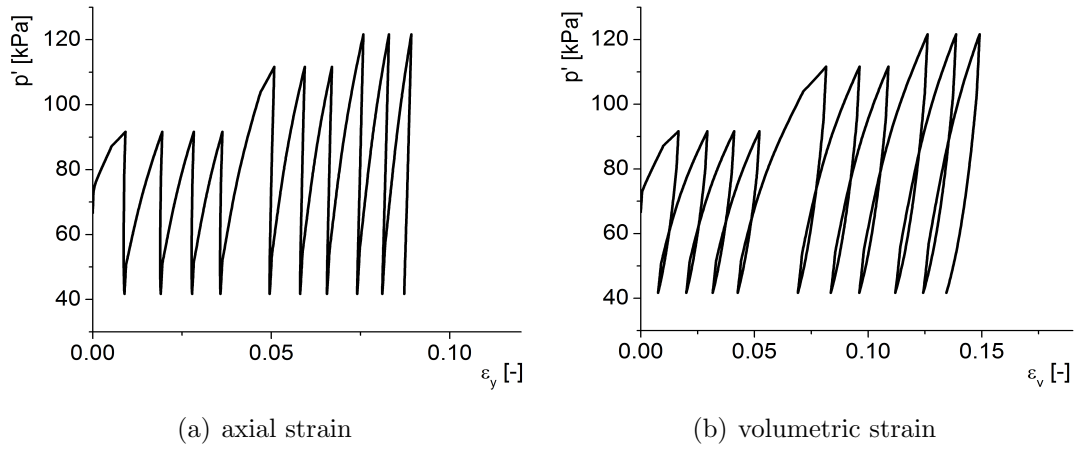


Figure 6.21: Influence of $\kappa = 0.02$

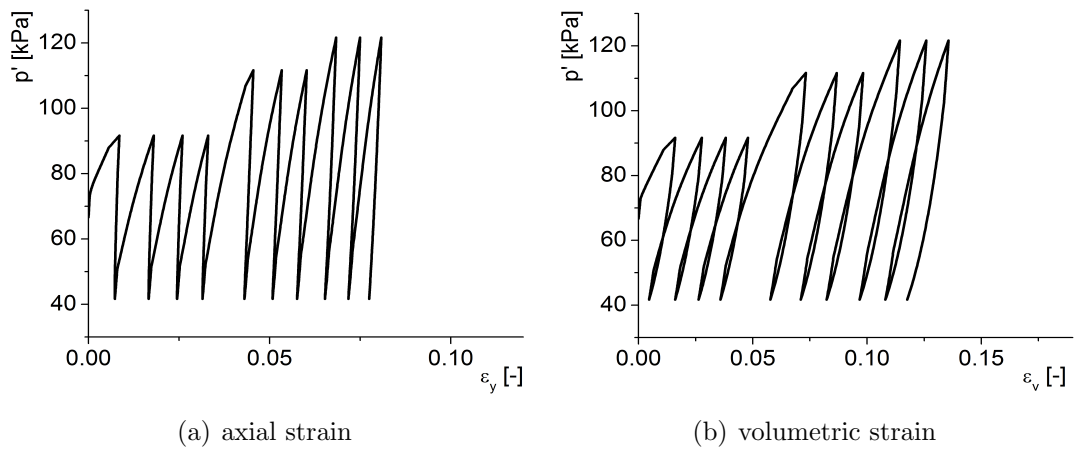


Figure 6.22: Influence of $\kappa = 0.03$

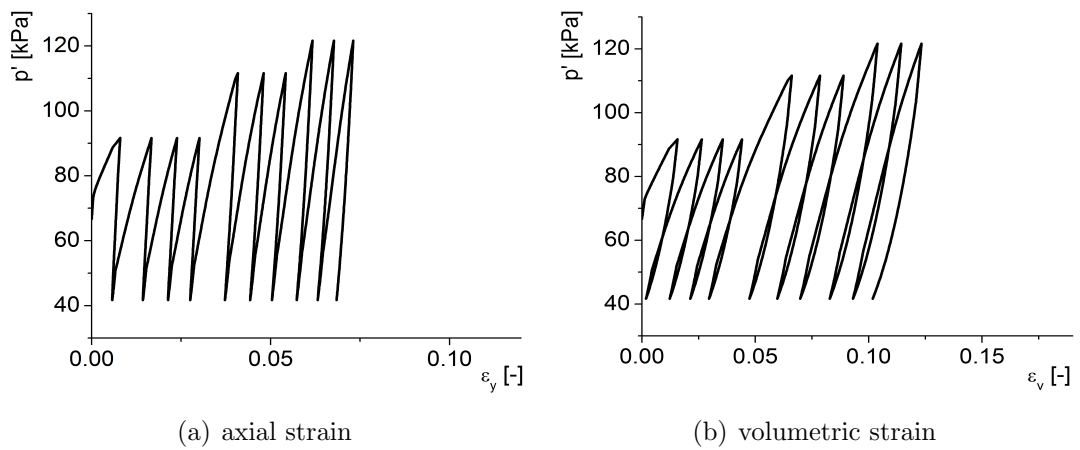


Figure 6.23: Influence of $\kappa = 0.04$

6.8 Constant q slow cyclic triaxial simulations

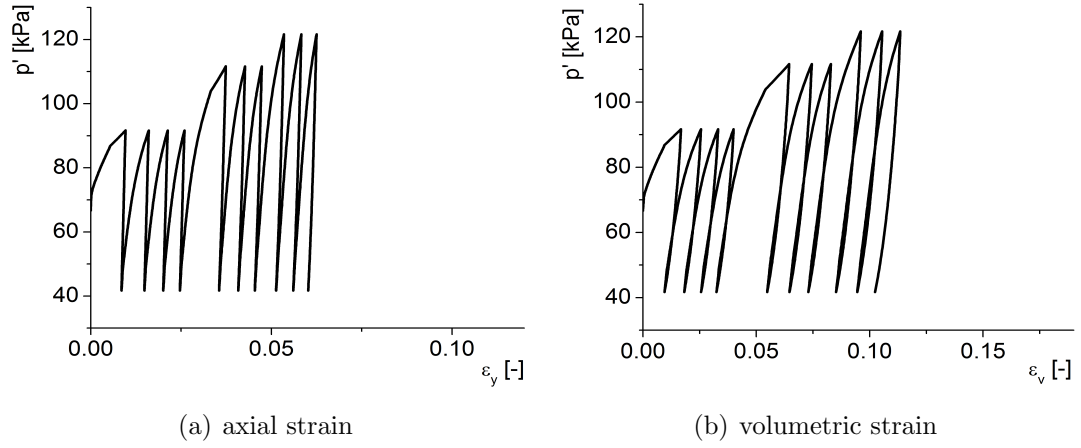


Figure 6.24: Influence of $R = 0.10$

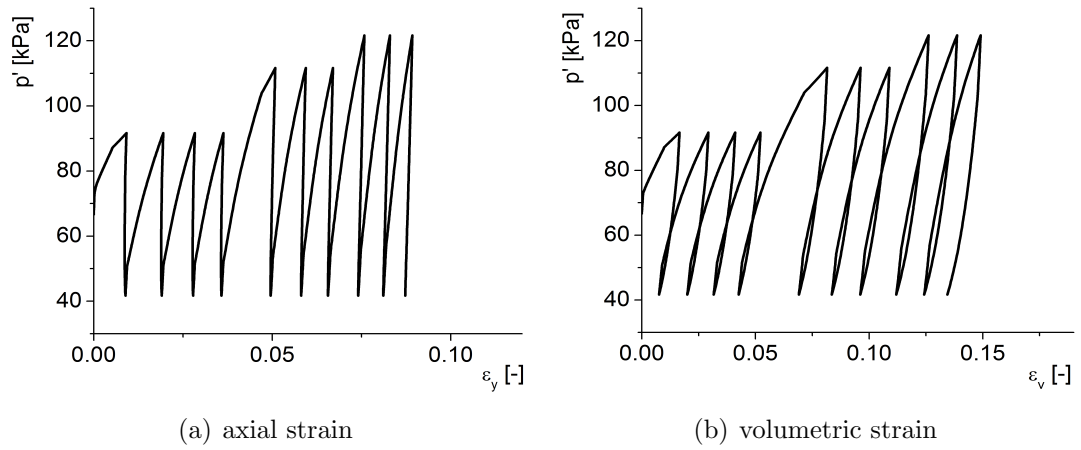


Figure 6.25: Influence of $R = 0.15$

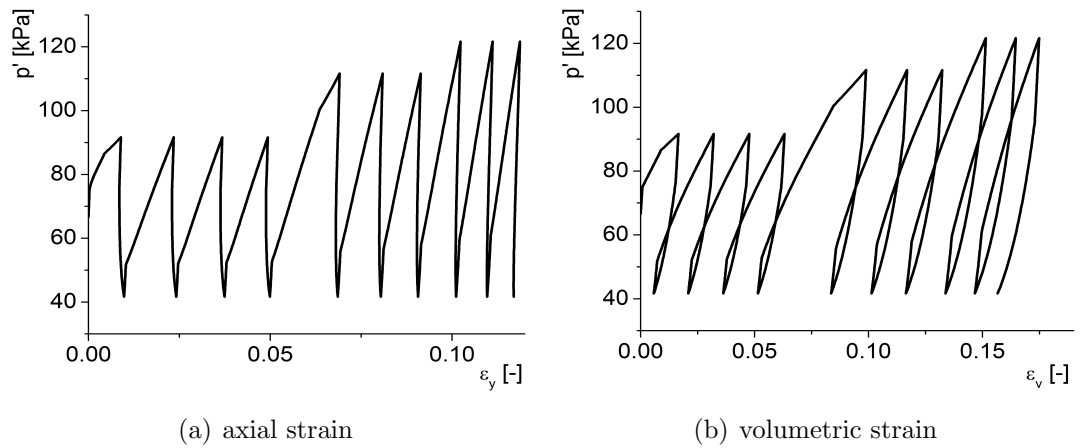


Figure 6.26: Influence of $R = 0.20$

6.8 Constant q slow cyclic triaxial simulations

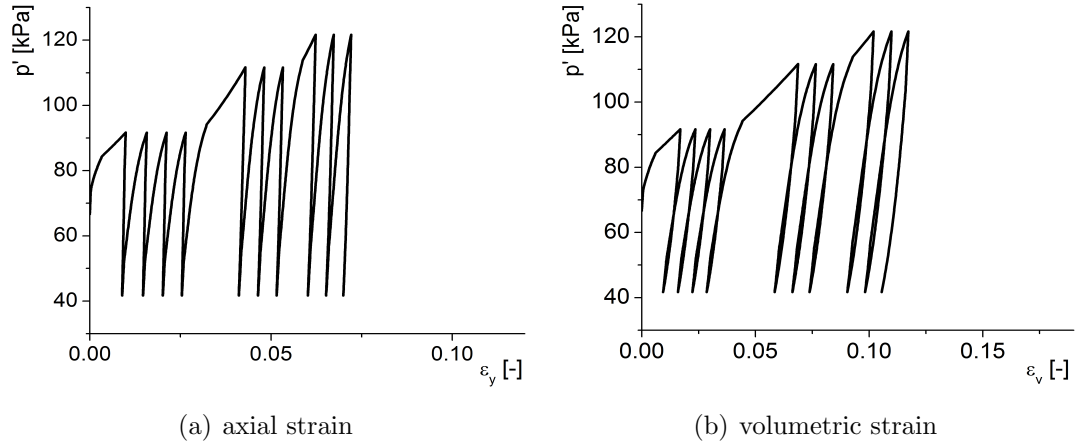


Figure 6.27: Influence of $\psi = 1.0$

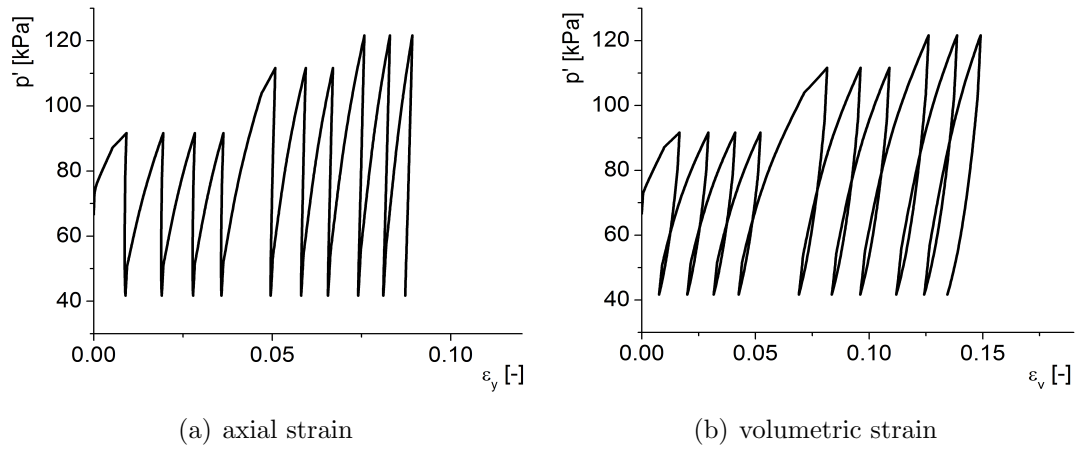


Figure 6.28: Influence of $\psi = 1.5$

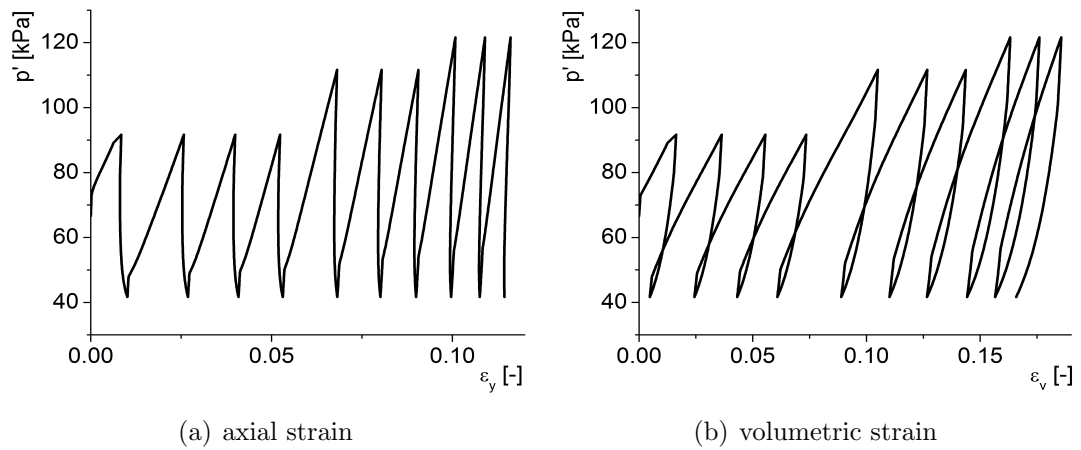


Figure 6.29: Influence of $\psi = 2.0$

6.9 Summary

In summary, a parametric study of the B-SCLAY1S model detailed in Chapter 5 has been carried out in this chapter. This study indicates that parameters related to the bubble (R and ψ) and to S-CLAY1S (λ_i and κ) have more influence on the bubble model simulations than the other soil constants. Poisson's ratio (ν'), anisotropy parameters (β and μ) and destructuration parameters (χ , a and b) generally have a less important role in the B-SCLAY1S model prediction. The test data for Bothkennar clay is well modelled by the B-SCLAY1S model in general for the R value of 0.15 and the plastic modulus parameter $\psi = 1.5$. In general, parameter values of $\lambda_1 = 0.21$, $\kappa = 0.02$ and $\nu' = 0.2$ provide best match to the experimental data. Simulation of B-SCLAY1S shows anisotropic parameter $\mu = 30$ and $\beta = 0.94$ the destructuration parameters $\chi_0 = 10$ and $a = 9$ & $b = 0.4$ good agreement with Bothkennar test data.

The size of bubble R and plastic modulus parameter ψ affects small strain stiffness and control the degradation of stiffness due to plastic straining. The value of R needs to decrease to smoothen the stiffness transition from elastic region to yielding. However, very small value of R may cause numerical errors.

Furthermore, three important parameters (R , ψ and κ) which are most relevant in cyclic behaviour of the B-SCLAY1S were used for a parametric study. It has been found that B-SCLAY1S was very flexible in predicting cyclic soil behaviour.

Chapter 7

Verification and application of the B-SCLAY1S model

This Chapter presents series of slow cyclic oedometer tests and triaxial tests for verification of the model implementation followed by application of the model to benchmark problems. First part of this chapter involves verification of the model implementation against a number of simulations presented by Al-Tabbaa (1987) which does not include anisotropy and destructuration. Secondly, triaxial test results of Swiss lacustrine clay presented by Messerklinger (2006) are compared with B-SCLAY1, S-CLAY1 and MCC simulations as explained in Table 5.1 in Chapter 5. Thirdly, the B-SCLAY1S model simulations are compared with the laboratory test results presented by McGinty (2006) for Bothkennar clay. Finally the B-SCLAY1S model is applied to benchmark problems for static and dynamic loading condition.

7.1 Verification against *Al-Tabbaa (1987)* simulations

The implementation of proposed model was first verified in a case of isotropic soil by comparing against the results of Al-Tabbaa (1987) model predictions for a slow cyclic triaxial test at constant deviatoric stress q and a number of undrained triaxial tests on speswhite kaolin. In order to repeat this simulation, the features of B-SCLAY1S model are switched off for anisotropy and destructuration by setting corresponding parameters to zero. The model parameters were derived by Al-Tabbaa (1987) from

7.1 Verification against *Al-Tabbaa (1987)* simulations

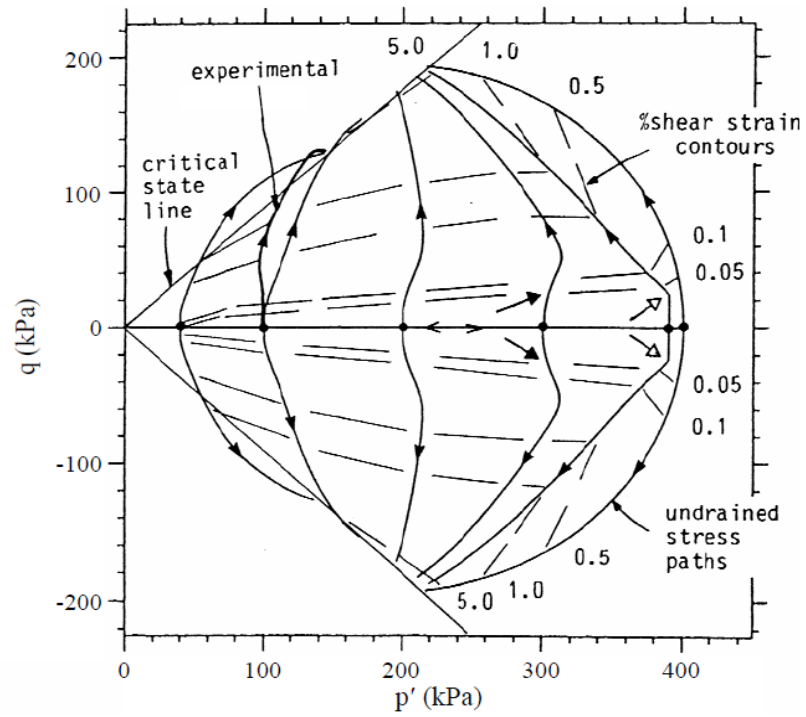
Table 7.1: Material parameters used by Al-Tabbaa (1987) for speswhite kaolin

Soil constants			
κ	ν'	λ	M
0.0172	0.3	0.187	0.90
State variables			
e_0	α_0		
1.2	0.0		
Additional parameters for anisotropy			
β	μ		
0.37	60		
Additional parameters for the bubble			
R	ψ		
0.2	1.5		

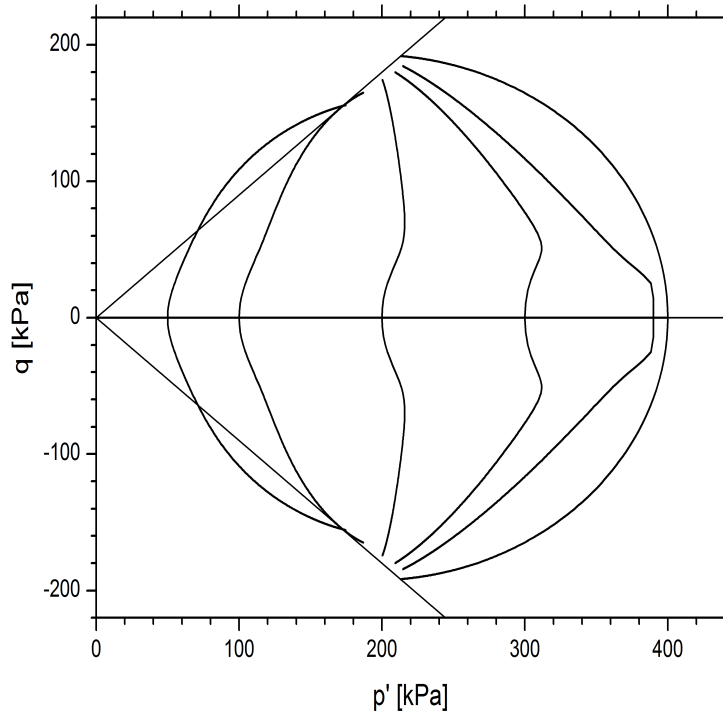
slow cyclic oedometer and triaxial test results, and are given in Table 7.1. Furthermore, the isotropic bubble model (B-MCC) is compared against the anisotropic bubble model (B-SCLAY1) for K_0 consolidation followed by shearing on speswhite kaolin. The additional soil constant and state variables related to anisotropy were determined based on the suggestions by Wheeler *et al.* (2003) for β and Karstunen & Koskinen (2008); Karstunen *et al.* (2005) for μ .

Figs. 7.1 and 7.2 show a number of simulations for undrained stress paths initiated from isotropically and one-dimensionally normally and overconsolidated states. Comparison of Figure 7.1(a) with Fig. 7.1(b) and Fig. 7.2(a) with Fig. 7.2(b) for Al-Tabbaa (1987) simulations and the B-MCC model respectively, shows that the implemented B-SCLAY1S model reproduces the same stress paths to the ones presented by Al-Tabbaa (1987).

7.1 Verification against *Al-Tabbaa (1987)* simulations



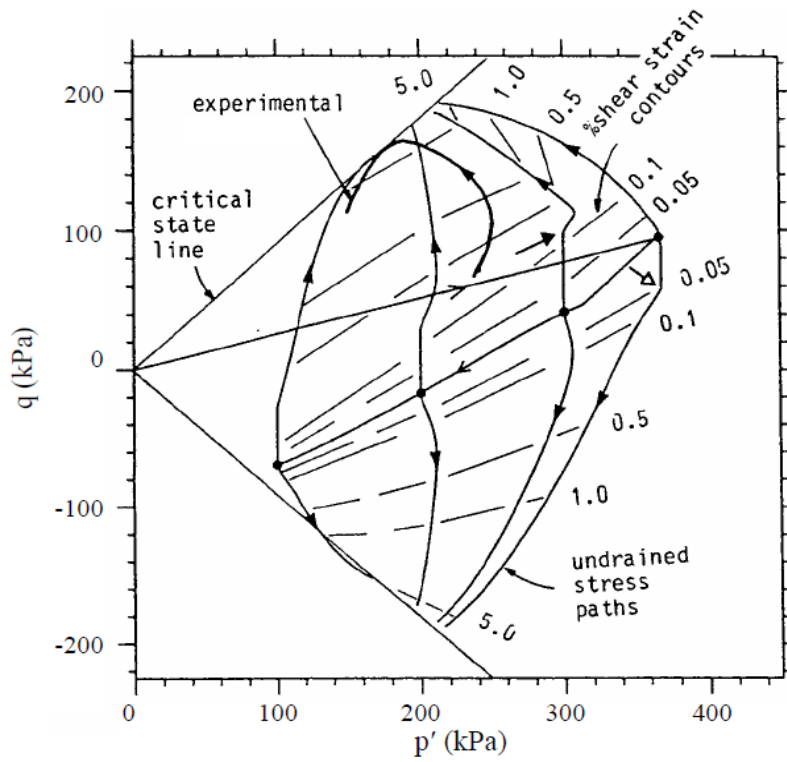
(a) Al-Tabbaa (1987) model predictions



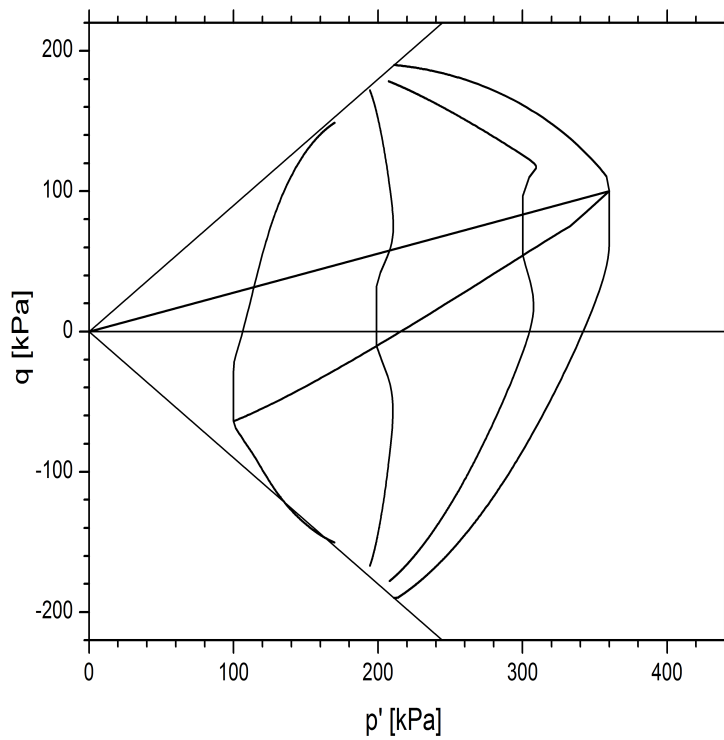
(b) B-MCC model predictions

Figure 7.1: Undrained stress paths after isotropic stress history

7.1 Verification against *Al-Tabbaa (1987)* simulations



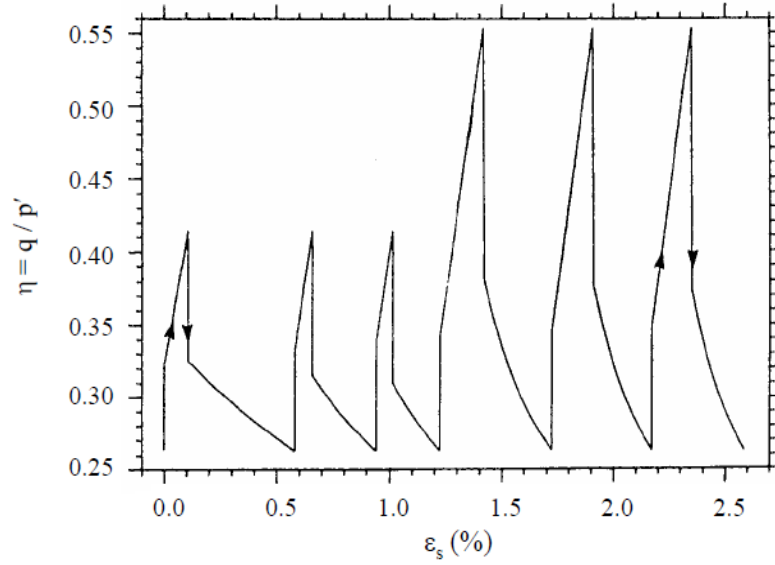
(a) Al-Tabbaa (1987) model predictions



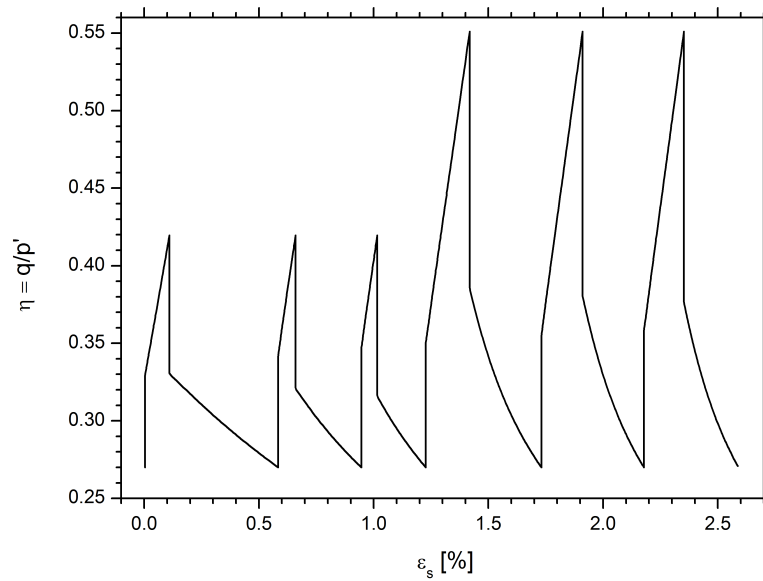
(b) B-MCC model predictions

Figure 7.2: Undrained stress paths after a one-dimensional stress history

7.1 Verification against *Al-Tabbaa (1987)* simulations



(a) Al-Tabbaa (1987) model predictions



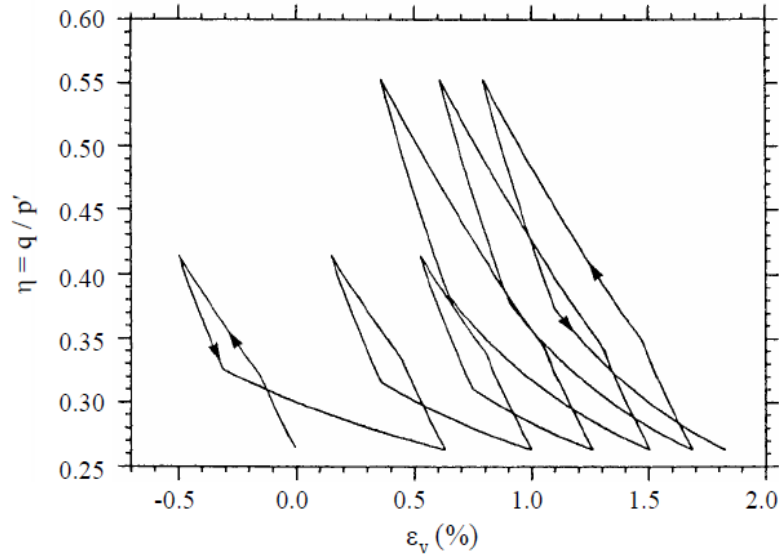
(b) B-MCC model predictions

Figure 7.3: Slow cyclic isotropic constant q triaxial simulation: η against ϵ_s

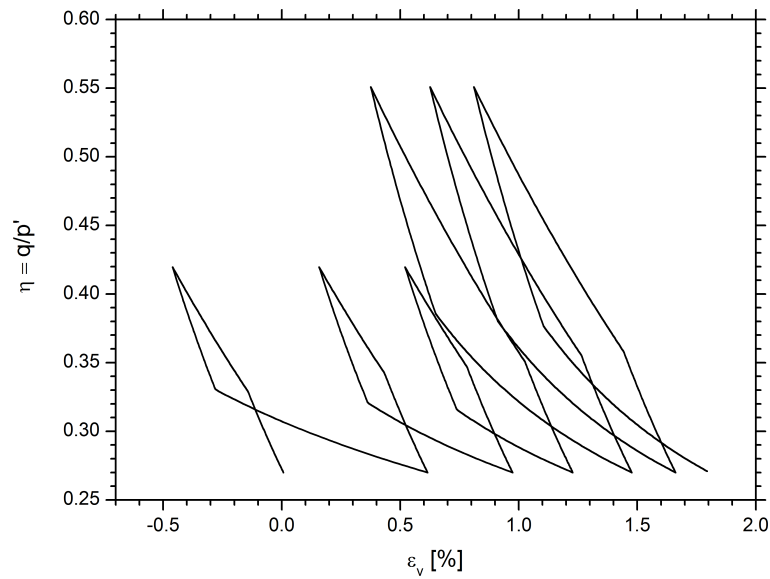
The cyclic triaxial simulation was initially started from normally consolidated state corresponding to one-dimensional loading, and the deviator stress q was kept constant when cyclic loading (unloading/reloading) were applied by changing p' .

Figs. 7.3 and 7.4 show slow cyclic triaxial test at constant deviator stress q simulation for $\eta = q/p'$ against ϵ_s and $\eta = q/p'$ against ϵ_v , respectively. The initial values of p' and q are 300 kPa and 80 kPa respectively, and q is kept constant while

7.1 Verification against *Al-Tabbaa (1987)* simulations



(a) Al-Tabbaa (1987) model predictions



(b) B-MCC model predictions

Figure 7.4: Slow cyclic isotropic constant q triaxial simulation: η against ϵ_v

cyclic changes of p' are applied. As mentioned above, initial anisotropy has been switched off ($\alpha_0 = 0$) and additionally, the evolution of anisotropy was switched off by setting μ equal to zero. Comparison of the B-SCLAY1S model prediction with Al-Tabbaa (1987) simulations shows good agreement. Although B-SCLAY1S is very similar to the Al-Tabbaa (1987) model, the modified compression and swelling indices were used by Al-Tabbaa (1987) instead of λ and κ , and hence small differences

would be expected.

In Fig. 7.5, thick solid lines represent the predictions of the anisotropic B-SCLAY1 model and the dashed lines represent the equivalent results by the isotropic B-MCC model. In this simulation, initial anisotropy has been switched off ($\alpha_0 = 0$) and the additional evolution of anisotropy parameters were given as in Table 7.1. In reality, anisotropy has been created through initial K_0 consolidation, resulting in a theoretical value of $\alpha_0 = 0.35$.

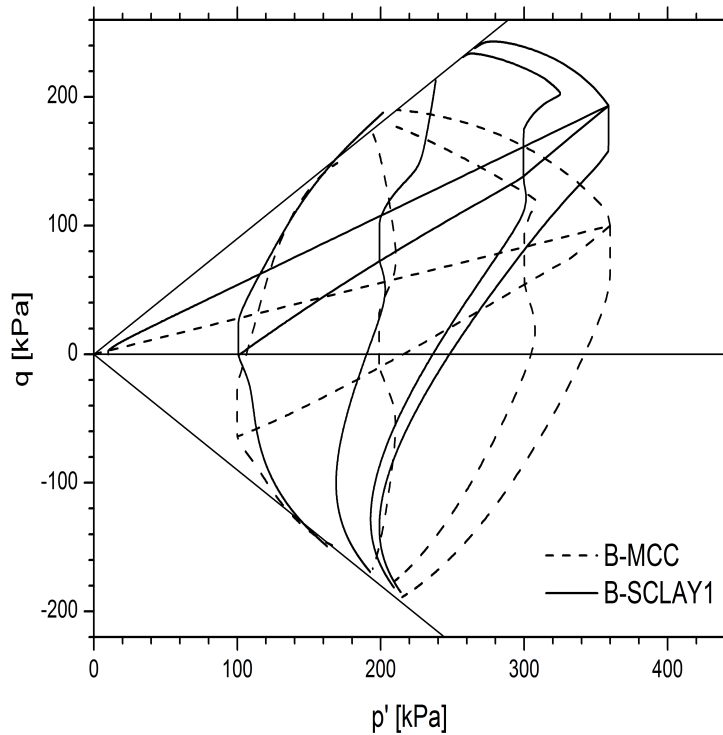


Figure 7.5: Undrained stress paths after a one-dimensional stress history

The differences between the two model predictions are very striking relating to the simulations of anisotropically consolidated undrained shearing in compression and extension. The soil is assumed initially isotropic, but during the initial K_0 consolidation anisotropy evolves in the case of B-SCLAY1 model, resulting in an value of 0.35 at the start of undrained shearing. Due to the associated flow rule, K_0 - loading results in different predicted stress paths, both for loading and unloading. B-MCC gives, like the MCC model, a very poor K_0 prediction. Overall, during compression the B-SCLAY1 model predicts higher undrained strength than B-MCC, and the predicted undrained strength in extension is notably lower than

7.2 Comparison with *Messerklinger (2006)* triaxial test results

in compression. In contrast the isotropic B-MCC model predicts almost the same value of undrained shear strength in compression and extension.

7.2 Comparison with *Messerklinger (2006)* triaxial test results

This section compares the simulated response of B-SCLAY1 (without destructuration) for Swiss lacustrine clay with triaxial test data provided by Messerklinger (2006). The triaxial tests consists of four major stress paths in triaxial stress space are compression (S2T4), one-dimensional (S2cT1), isotropic (S2T3) and extension (S2aT4).

The natural test samples were first reconsolidated in the triaxial apparatus to a stress state of $p' = 300 \text{ kPa}$ and $q = 225 \text{ kPa}$ beyond the in-situ preconsolidation stress along the stress ratio $\eta_{K0} = 0.75$, unloaded to a common stress state of $p' = 150 \text{ kPa}$ and $q = 112.5 \text{ kPa}$ using drained swelling along the stress ratio $\eta_{K0} = 0.75$ and finally reloaded along various probing stress paths of constant stress increment ratios to failure.

Table 7.2: Material parameters of lacustrine clay (data after Messerklinger, 2006)

Soil constants			
κ	ν'	λ	M
0.01	0.1	0.053	1.25
State variables			
e_0	α_0		
0.693	0.42		
Additional parameters for anisotropy			
β	μ		
1.31	5		
Additional parameters for the bubble			
R	ψ		
0.15	1.5		

7.2 Comparison with Messerklinger (2006) triaxial test results

Table 7.2 summarizes the model parameters which were obtained from Messerklinger (2006). In order to compare the performance of the B-SCLAY1 simulation, S-CLAY1 and MCC were also simulated for the lacustrine clay response. The yield surfaces (see Fig. 7.6) for S-CLAY1 bubble, S-CLAY1 bounding/yield and MCC yield surfaces were drawn and compared to the yield stress points from Messerklinger (2006). Comparing the S-CLAY1 bounding surface to the MCC yield surface, S-CLAY1 gives a much better agreement than the MCC yield surface.

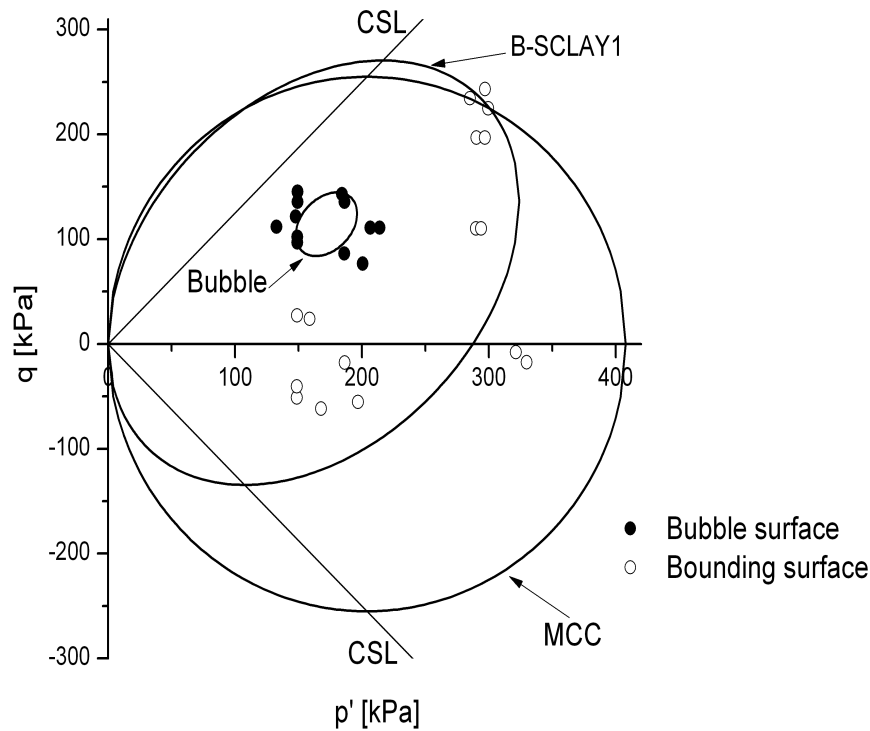
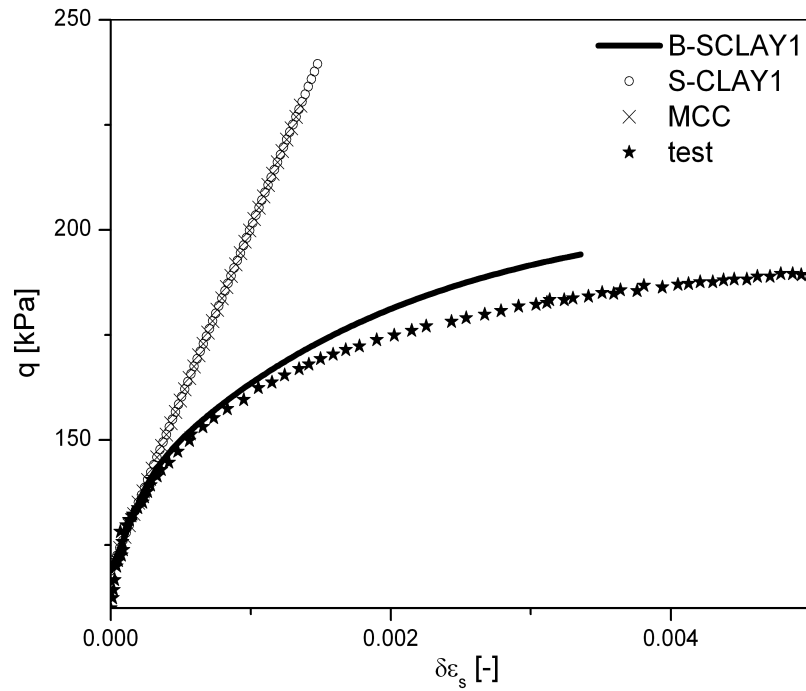


Figure 7.6: B-SCLAY1 and MCC yield surfaces compared with test data (data after Messerklinger, 2006)

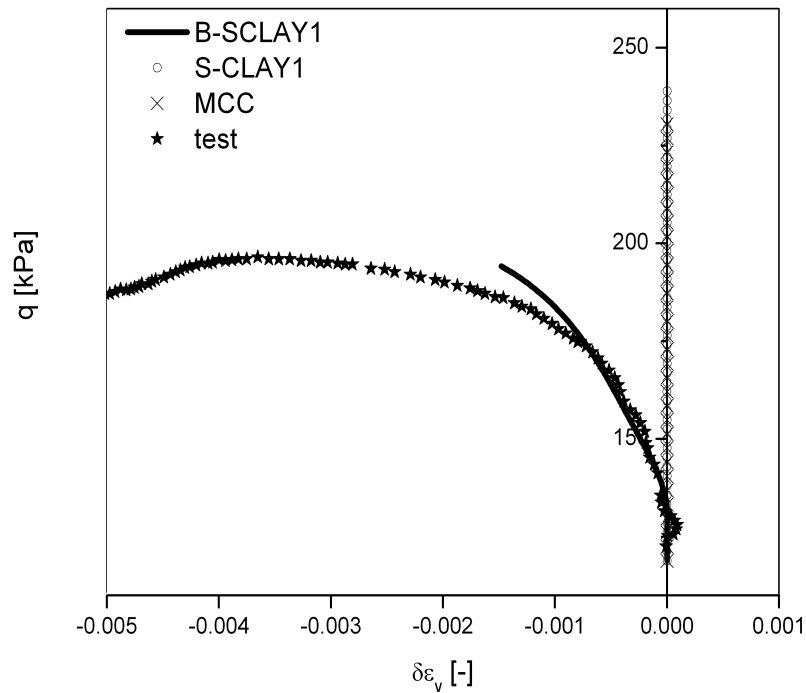
7.2.1 Compression test: S2T4 ($\Delta p' = \text{constant}$)

The probing compression stress path was simulated at the start point $p' = 150$ kPa and $q = 112.5$ kPa with a previous one-dimensional consolidation history to maximum values of stresses $p' = 300$ kPa and $q = 225$ kPa. Mean effective stress remained constant during probing stress path stress increment ratio $\eta = \infty$ and $\delta\sigma'_1/\delta\sigma'_3 = -2$.

7.2 Comparison with *Messerklinger (2006)* triaxial test results



(a) Deviator stress versus shear strain increment



(b) Deviator stress versus volumetric strain increment

Figure 7.7: Model simulation and test results for compression test: S2T4 (data after Messerklinger, 2006)

7.2 Comparison with *Messerklinger (2006)* triaxial test results

Fig. 7.7 shows the failure behaviour simulated by B-SCLAY1, S-CLAY1 and MCC in the corresponding stress-strain plots. The deviator stress versus shear strain increment curves are shown in Fig. 7.7(a). However, the comparison of simulations show the same linear elastic response for S-CLAY1 and MCC, and both models behave stiffly due to linear elastic response. The B-SCLAY1 model is the only model that follows the test data from small strains quite effectively. This is because B-SCLAY1 incorporate a bubble surface to simulate non-linearity in the elastic region.

The deviator stress versus volumetric strains simulation is shown in Fig. 7.7(b). The S-CLAY1 and MCC models are not able to simulate the observed behaviour in test data. This is because these models are based on critical state theory and couple the development of volumetric strains to the change in mean effective stress only. This drawback comes from the assumption of isotropic elastic behaviour. The B-SCLAY1 model captures the trend with test data in the shear stress versus volumetric strain increment plot.

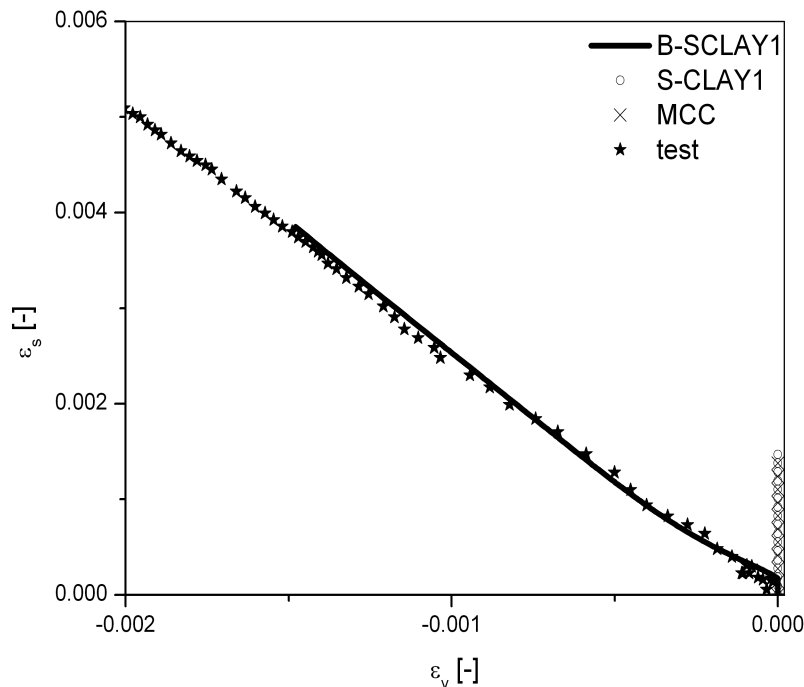


Figure 7.8: Model simulation and test results for compression test: S2T4. Shear versus volumetric strain increment (data after Messerklinger, 2006)

Fig. 7.8 shows the simulation of the shear strain versus the volumetric strain increments and the test data. The MCC and S-CLAY1 models are unable to capture

the behaviour again due to the poor volumetric strain predictions. However, B-SCLAY1 model follows the test data remarkably well.

7.2.2 Compression test: S2cT1 ($\eta = 0.9$)

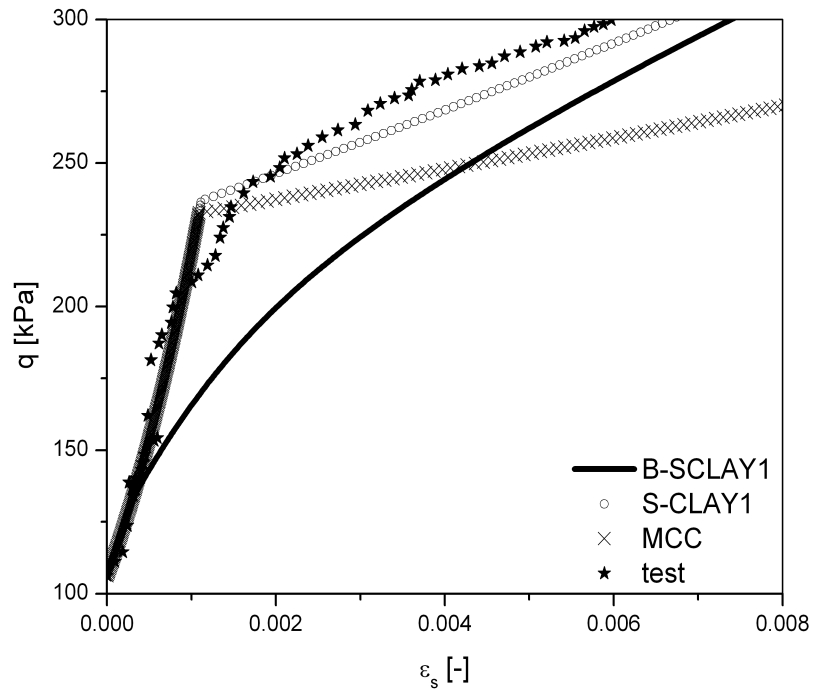
The probing stress path was simulated at the start point $p' = 150 \text{ kPa}$ and $q = 112.5 \text{ kPa}$ with a previous one-dimensional consolidation history to greatest stresses $p' = 300 \text{ kPa}$ and $q = 225 \text{ kPa}$. The stress was applied in stress increment ratio $\eta = 0.9$ and $\delta\sigma'_1/\delta\sigma'_3 = 2.3$. With the stress path simulated no failure occurs (recompressed) and stress path was applied beyond the previous one-dimensional consolidation.

Fig. 7.9 shows the deviator stress versus the shear strain and the volumetric strain increment plot. The S-CLAY1 model corresponds better to test data than the MCC and B-SCLAY1 model in the deviator stress versus shear strain increment plot, see Fig. 7.9(a). However, the B-SCLAY1 model simulation has more realistic curvature than the other models. The volumetric strain increment response is presented in Fig. 7.9(b). The B-SCLAY1 model simulation shows better agreement the test data than the S-CLAY1 and MCC models, but also these models follow the trend of the test data reasonably well.

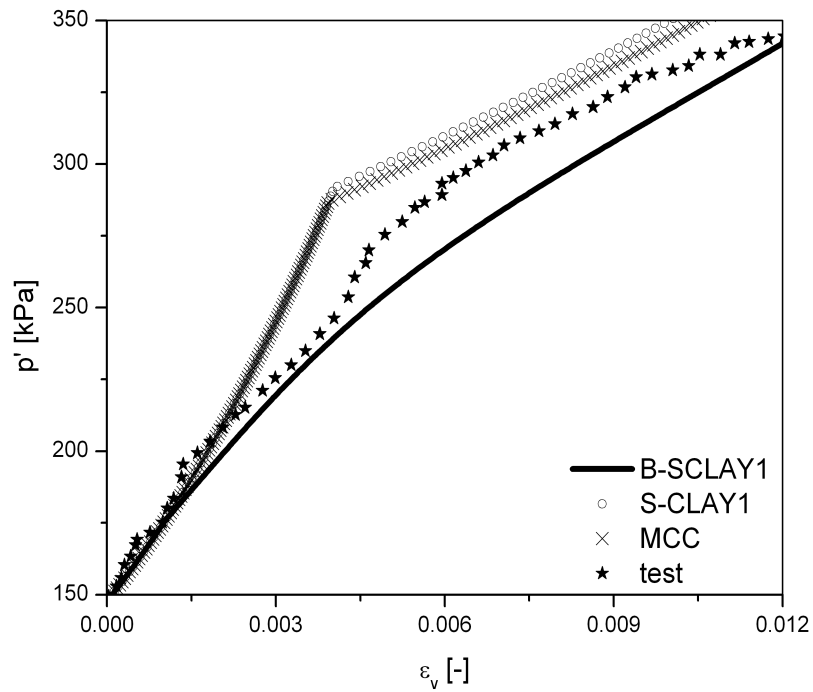
The shear versus volumetric strain increment is presented in Fig. 7.10. While the S-CLAY1 and MCC models overpredict the shear strain, the B-SCLAY1 model slightly underpredicts the shear strain.

The comparison demonstrates a reasonably good agreement between the simulation and test data for all models. It can be noted that for these results, non-linearity in the elasticity is not very dominant in the deformation behaviour due to the stress path in this simulation is applied well beyond the consolidation stress state reached in the laboratory.

7.2 Comparison with Messerklinger (2006) triaxial test results



(a) Deviator stress versus shear strain increment



(b) Deviator stress versus volumetric strain increment

Figure 7.9: Model simulation and test results for compression test: S2cT1 (data after Messerklinger, 2006)

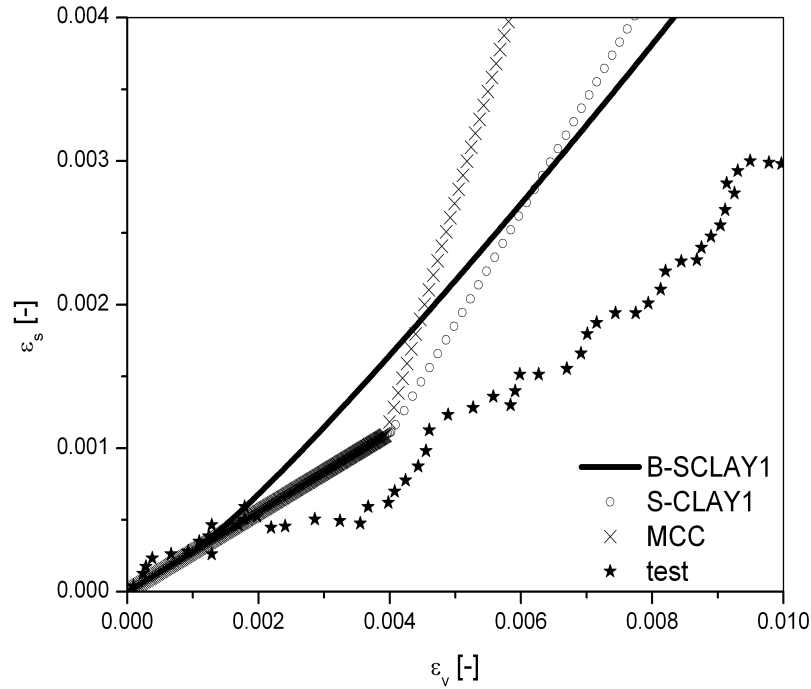


Figure 7.10: Model simulation and test results for isotropic compression test: S2cT1. Shear versus volumetric strain increment (data after Messerklinger, 2006)

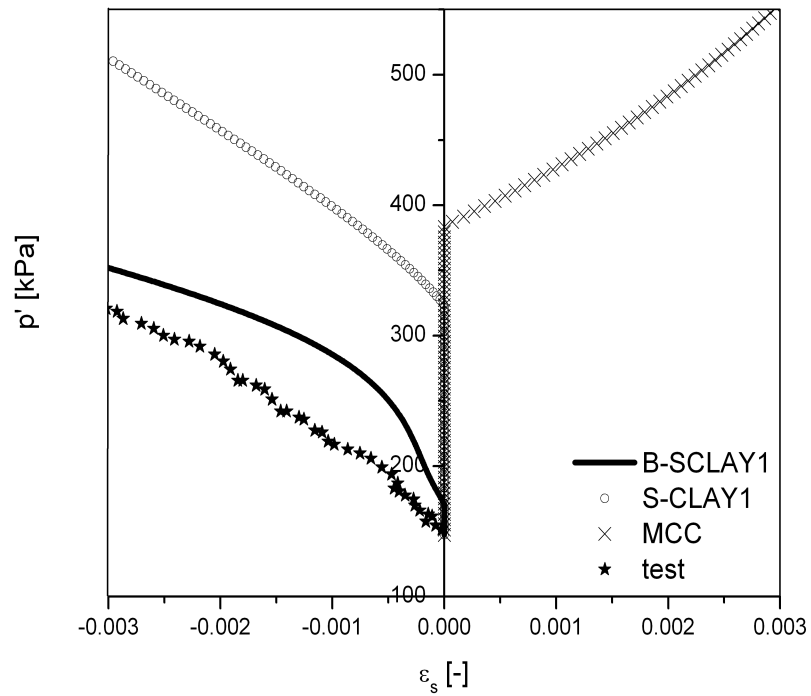
7.2.3 Isotropic compression test: S2T3 ($\Delta q = \text{constant}$)

The probing isotropic compression stress path was simulated at the start point $p' = 150 \text{ kPa}$ and $q = 112.5 \text{ kPa}$. The stress was applied in stress increment ratio $\eta = 0$ and $\delta\sigma'_1/\delta\sigma'_3 = 1$.

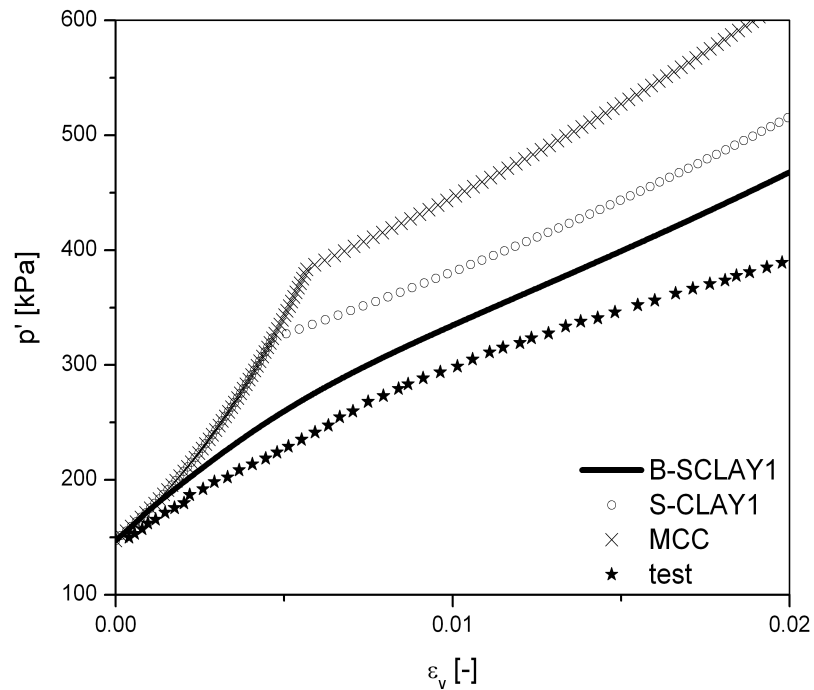
The deviatoric stress-strain plots are presented in Fig. 7.11 together with the shear strain versus volumetric strain plot in Fig. 7.12. The negative shear strain increment developed in test data (Fig. 7.11(a)) is predicted by the B-SCLAY1 and S-CLAY1 models only due to inclination of the yield surface (anisotropy). However, the MCC model predicts positive shear strain increment due to the isotropic behaviour of the model. The B-SCLAY1 model only responds to the test data corresponding to the negative shear strain increment developing immediately.

The S-CLAY1 model simulates isotropic elastic behaviour until it reaches the yield surface, which gives zero shear strain increment for isotropic compression. This can be improved by inclusion of an elastic anisotropic formulation.

7.2 Comparison with *Messerklinger (2006)* triaxial test results



(a) Mean effective stress versus shear strain increment



(b) Mean effective stress versus volumetric strain increment

Figure 7.11: Model simulation and test results for isotropic compression test: S2T3 (data after Messerklinger, 2006)

7.2 Comparison with *Messerklinger (2006)* triaxial test results

The B-SCLAY1 and S-CLAY1 models only predict similar trend of the shear strain versus volumetric strain increment test data in Fig. 7.12. The MCC model is not able predict the strain increment plot for isotropic load paths due to anisotropic nature of lacustrine clays. Lacustrine clays have an inherent anisotropy due to the deposition mode (Messerklinger, 2006).

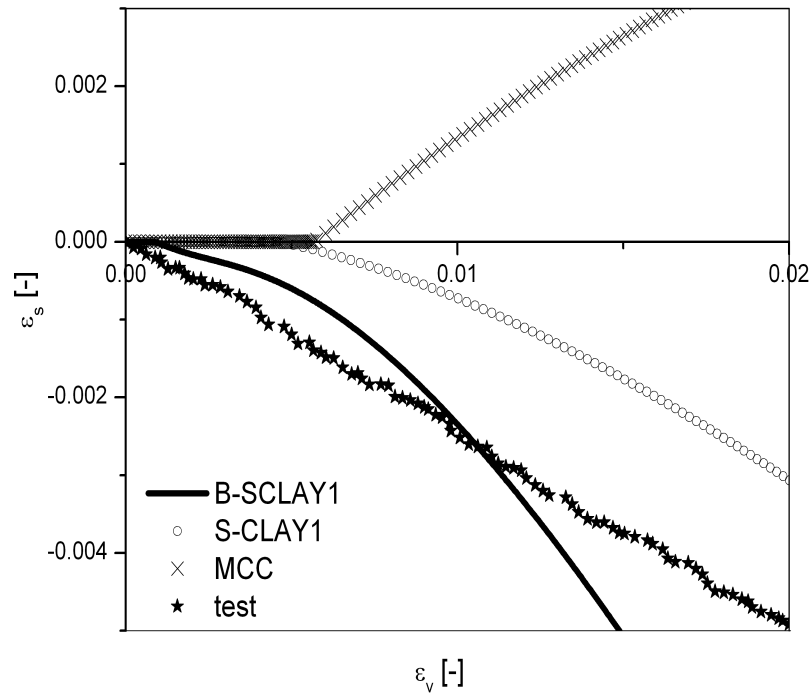


Figure 7.12: Model simulation and test results for isotropic compression test: S2T3. Shear versus volumetric strain increment (data after Messerklinger, 2006)

7.2.4 Extension test: S2aT4 ($\Delta p' = \text{constant}$)

The probing extension stress path was simulated at the start point $p' = 150 \text{ kPa}$ and $q = 112.5 \text{ kPa}$. The stress was applied in stress increment ratio $\eta = -7.1$ and $\delta\sigma'_1/\delta\sigma'_3 = -1.1$.

The deviator stress versus shear and volumetric strain increments are presented in Fig. 7.13. Fig. 7.13(a) shows comparison of model responses to test data for the shear strain development. The S-CLAY1 and MCC model simulations show

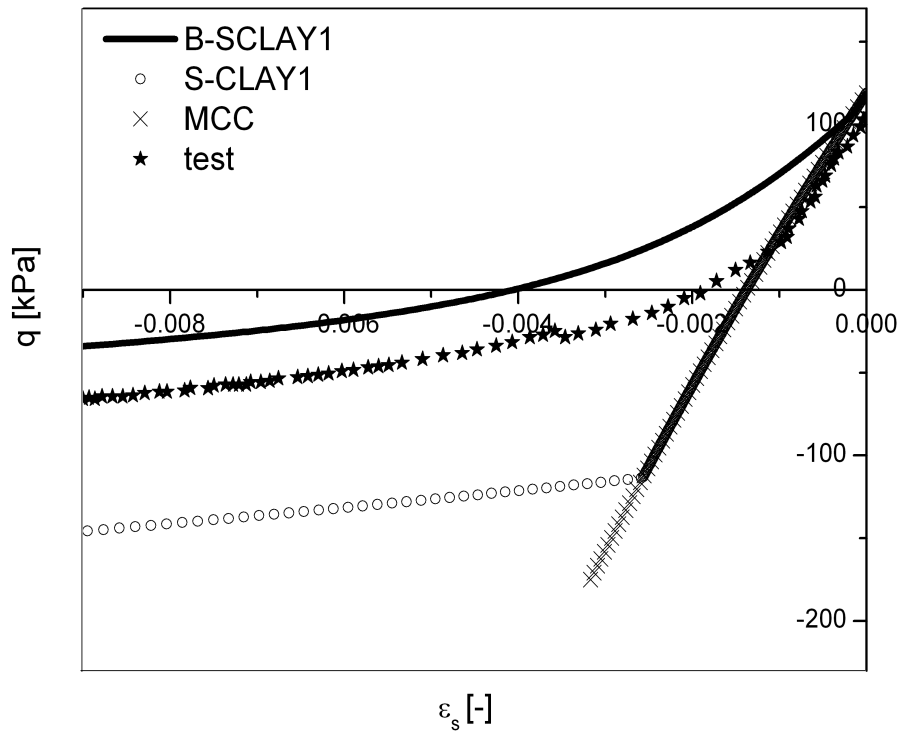
7.2 Comparison with *Messerklinger (2006)* triaxial test results

linear elastic response well within the first $\Delta q \approx 100 \text{ kPa}$ and after that MCC cannot simulate the stiffness decreases. Both the B-SCLAY1 and S-CLAY1 models capture the general trend of the shear strain behaviour but the S-CLAY1 model underpredicts shear strains whereas B-SCLAY1 overpredicts the shear strains. However, B-SCLAY1 predicts non-linear from small strain up to failure but lower stiffness throughout failure. The S-CLAY1 model simulation would improve by using Matsuoka-Nakai type failure criterion rather than the Drucker-Prager failure criterion.

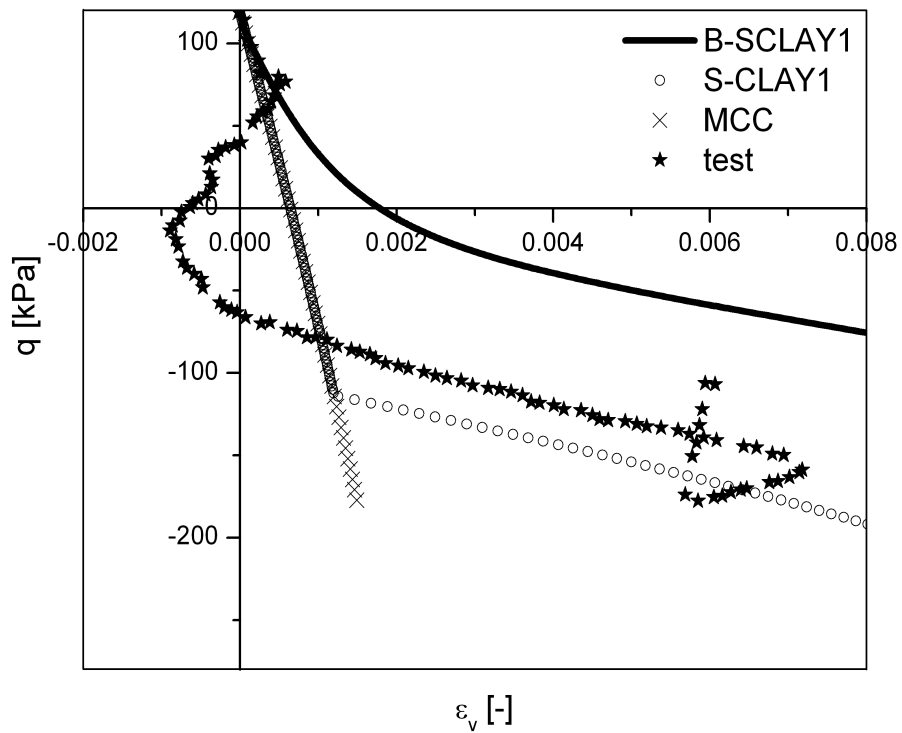
The deviator stress versus volumetric strain increment plot is presented in Fig. 7.13(b). The comparison of simulations and test data shows S-CLAY1 and B-SCLAY1 simulate plastic volumetric straining whereas MCC shows elastic volumetric straining. The S-CLAY1 model predicts volumetric strain increment with deviator stress very well to test data correspond to the B-SCLAY1 model. The B-SCLAY1 model underpredicts the deviator stress at failure whereas MCC underpredicts volumetric strains at failure.

Fig. 7.14 shows models simulation and test data for the shear versus the volumetric strain increment. The comparison shows that none of the models are able to predict the strain increment very well. While B-SCLAY1 and the S-CLAY1 models simulate elastic and plastic volumetric straining, the MCC model simulates elastic straining only.

7.2 Comparison with *Messerklinger (2006)* triaxial test results



(a) Deviator stress versus shear strain increment



(b) Deviator stress versus volumetric strain increment

Figure 7.13: Model simulation and test results for extension test: S2aT4 (data after Messerklinger, 2006)

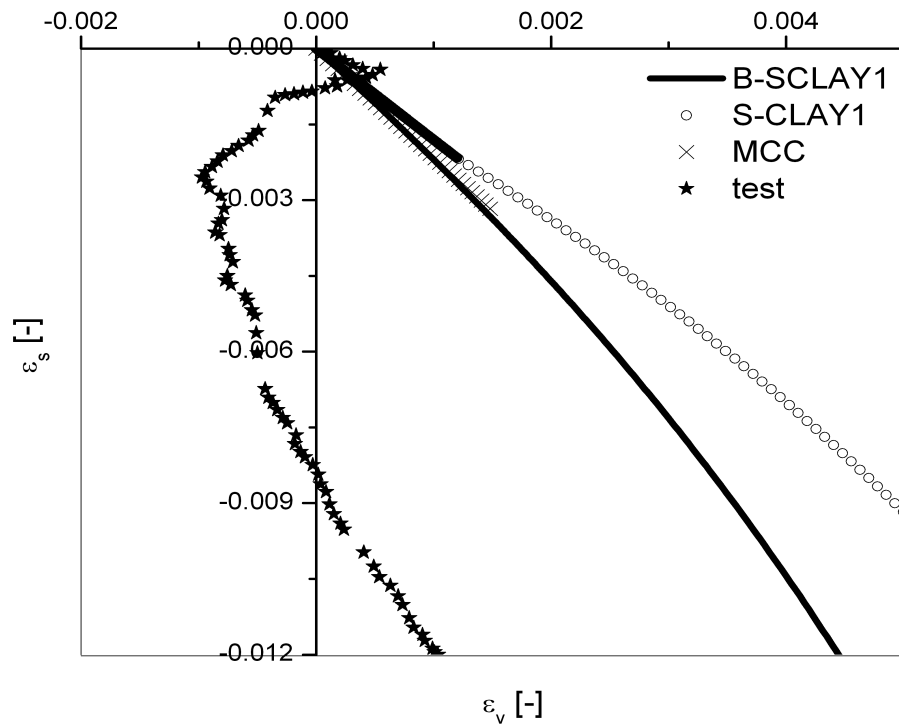


Figure 7.14: Model simulation and test results for extension test: S2T4. Shear versus volumetric strain increment (data after Messerklinger, 2006)

7.3 Comparison with *McGinty (2006)* triaxial results

This section compares the B-SCLAY1S and S-CLAY1S model simulations with experimental triaxial test data on vertical samples of Bothkennar clay by McGinty (2006). Applicability and limitations of the both models were assessed in predicting soft clay behaviour in particular the small strain stiffness (Bubble surface) during the loading. The S-CLAY1S model is included to provide a benchmark in order to assess whether B-SCLAY1S simulations produce more accuracy than the S-CLAY1S model.

Model parameters have been obtained from McGinty (2006) data and from the parametric study in Chapter 6 and are summarized in Table 6.1 in Chapter 6. The B-SCLAY1S model was used to generate the S-CLAY1S model simulation by setting

7.3 Comparison with *McGinty (2006)* triaxial results

the parameter R value to one. Stress increments were chosen to be sufficiently small ($\Delta p' = 0.5 \text{ kPa}$) so that there is no influence of stress increment size.

Chapter 6 contains parametric study simulations involving samples first loaded isotropically (Test series B) and hence this Section discuss samples first loaded anisotropically (Test series C). Details of the multi-stage stress paths in Test series C taken into simulations using B-SCLAY1S and S-CLAY1S are given in Table 7.3. The information includes the stress ratio for first and second loading stages (η_1 and η_2) and the maximum mean effective stresses in the first and second loading stages (p'_1 and p'_2).

Table 7.3: Summary of stress paths used in simulation from test series C

Test	η_1	$p'_1 \text{ (kPa)}$	η_2	$p'_2 \text{ (kPa)}$
C2	1.10	198	-0.50	587
C6	0.20	210	1.03	318
C7	0.42	210	-0.70	354

Test C2 was first loaded at relatively high stress ratio in triaxial compression followed by relatively low stress ratio in the second loading stage. Test C6 and C7 were first loaded at low stress ratio in triaxial compression followed by a much higher stress ratio in triaxial compression and a relatively higher stress ratio in triaxial extension for Test C6 and C7, respectively.

Compression behaviour of model simulations and test data is presented in terms of semi-logarithmic ($\epsilon_v : \ln p'$) plots in Figs. 7.15(a), 7.16(a) and 7.17(a) for Test C2, C6 and C7, respectively. In each case, the B-SCLAY1S and S-CLAY1S model predicts a good match to the experimental data for the magnitude of volumetric strain in the second loading stages. However, first loading, unloading and reloading stages, the B-SCLAY1S model predicts well due to the small strain stiffness nature of the model. During unloading and reloading after each of the first loading stage, the S-CLAY1S model shows differences between experimental data and simulations due to the assumption of purely elastic behaviour inside the yield surface. Furthermore, during first loading stage, the S-CLAY1S model predicts slightly higher mean effective stress, which generally provides a slightly poorer match to the experimental data than B-SCLAY1S. Before first loading stage yielding, S-CLAY1S predicts linear elastic behaviour in contrast to the experimental data (although the difference is minimal) whereas B-SCLAY1S predicts satisfactorily the experimental data which is non-linear.

7.3 Comparison with *McGinty (2006)* triaxial results

The deviatoric stress-strain ($\epsilon_s : q$) behaviour of test data and model simulations are plotted in Figs. 7.15(b), 7.16(b) and 7.17(b) for Test C2, C6 and C7, respectively. Inspection of the deviatoric stress-strain curves, the B-SCLAY1S model predicts reasonably well except test C2, but S-CLAY1S predicts less accurately to the test data. Post yield deviatoric strains in the first loading stage is well predicted by B-SCLAY1S model in Test C2. The B-SCLAY1S and S-CLAY1 models overpredict the amount of shear strain during first loading stage in Test C2 (see Fig. 7.15(b)) whereas both models underpredict the amount of shear strain during first loading stage in Test C7 (see Fig. 7.17(b)).

Axial stress-strain ($\epsilon_y : \sigma_y$) behaviour of test data and simulations are shown in Figs. 7.15(c), 7.16(c) and 7.17(c) for Test C2, C6 and C7, respectively. Axial stress-strain behaviour show similar predictions to the deviatoric stress-strain plots. Again, the B-SCLAY1S model shows considerable improvement over S-CLAY1S in the prediction of Test C6 and C7.

The strains paths observed in test data and model simulation are plotted in terms of deviatoric and volumetric strains ($\epsilon_s : \epsilon_v$) in Figs. 7.15(d), 7.16(d) and 7.17(d) for Test C2, C6 and C7, respectively. Strain paths for Test C6 (7.16(d)) and Test c7 (see 7.17(d)) are reasonably well predicted by B-SCLAY1S compared to the S-CLAY1S model. Fig. 7.16(d) shows the both models overpredict deviator strain for Test C2 because the deviatoric strain predicted by the first loading stage is so large. However, B-SCLAY1S model predicts correctly the trend of the experimental data during unloading and reloading stages in Test C2.

7.3 Comparison with *McGinty (2006)* triaxial results

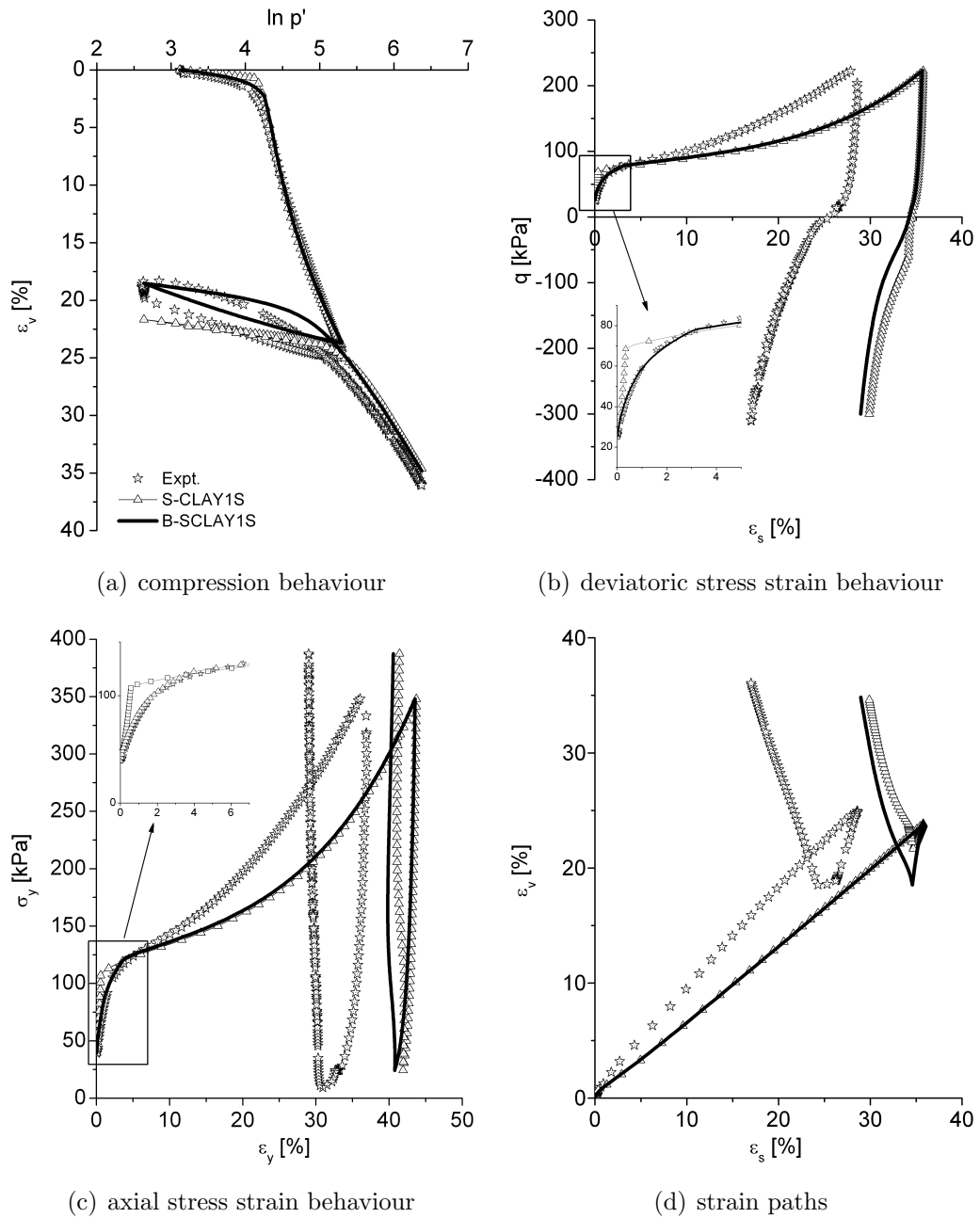


Figure 7.15: B-SCLAY1S and S-CLAY1S simulations of Test C2 where $\eta_1 = 1.10$ and $\eta_2 = -0.50$

7.3 Comparison with *McGinty (2006)* triaxial results

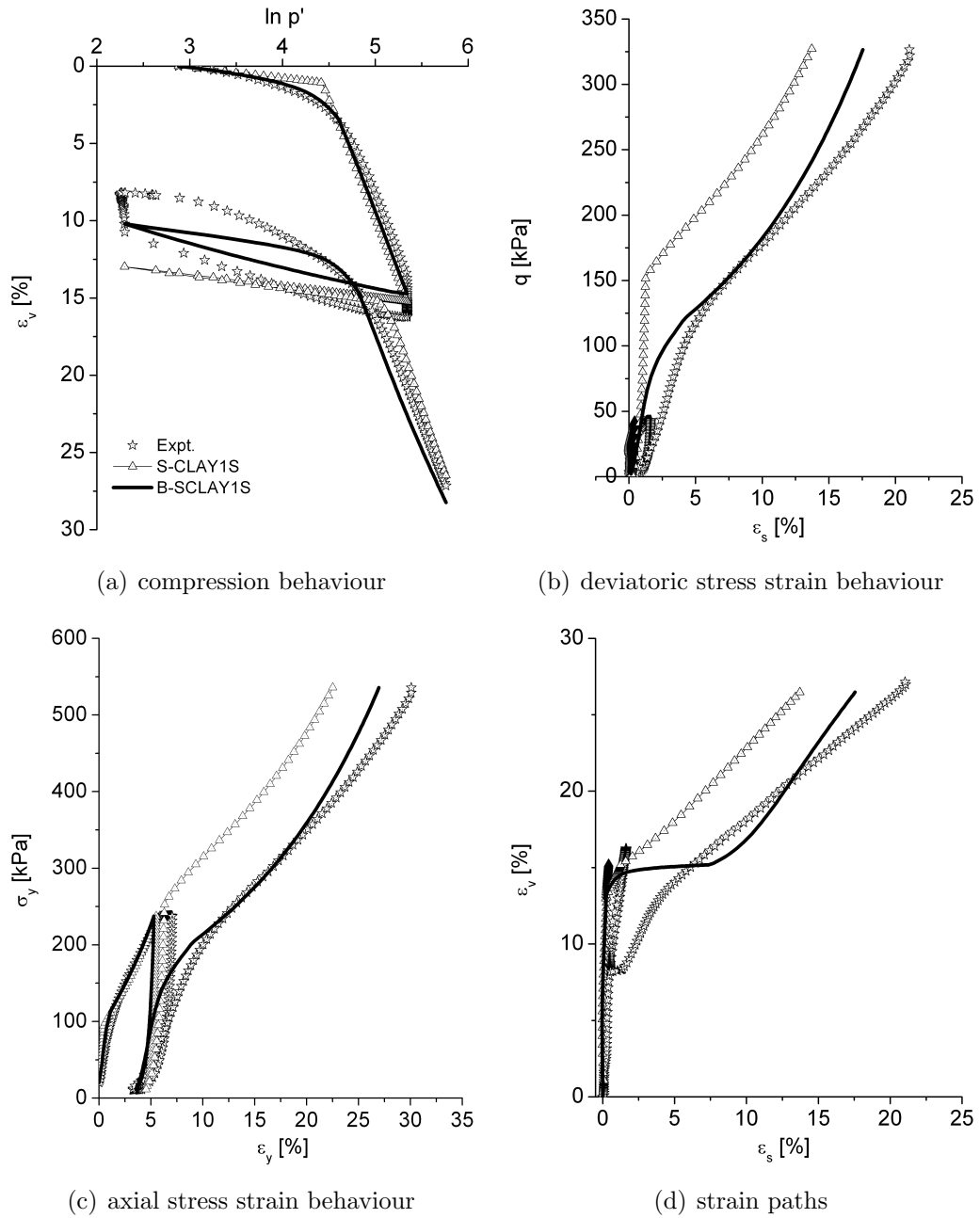


Figure 7.16: B-SCLAY1S and S-CLAY1S simulations of Test C6 where $\eta_1 = 0.20$ and $\eta_2 = 1.04$

7.3 Comparison with *McGinty (2006)* triaxial results

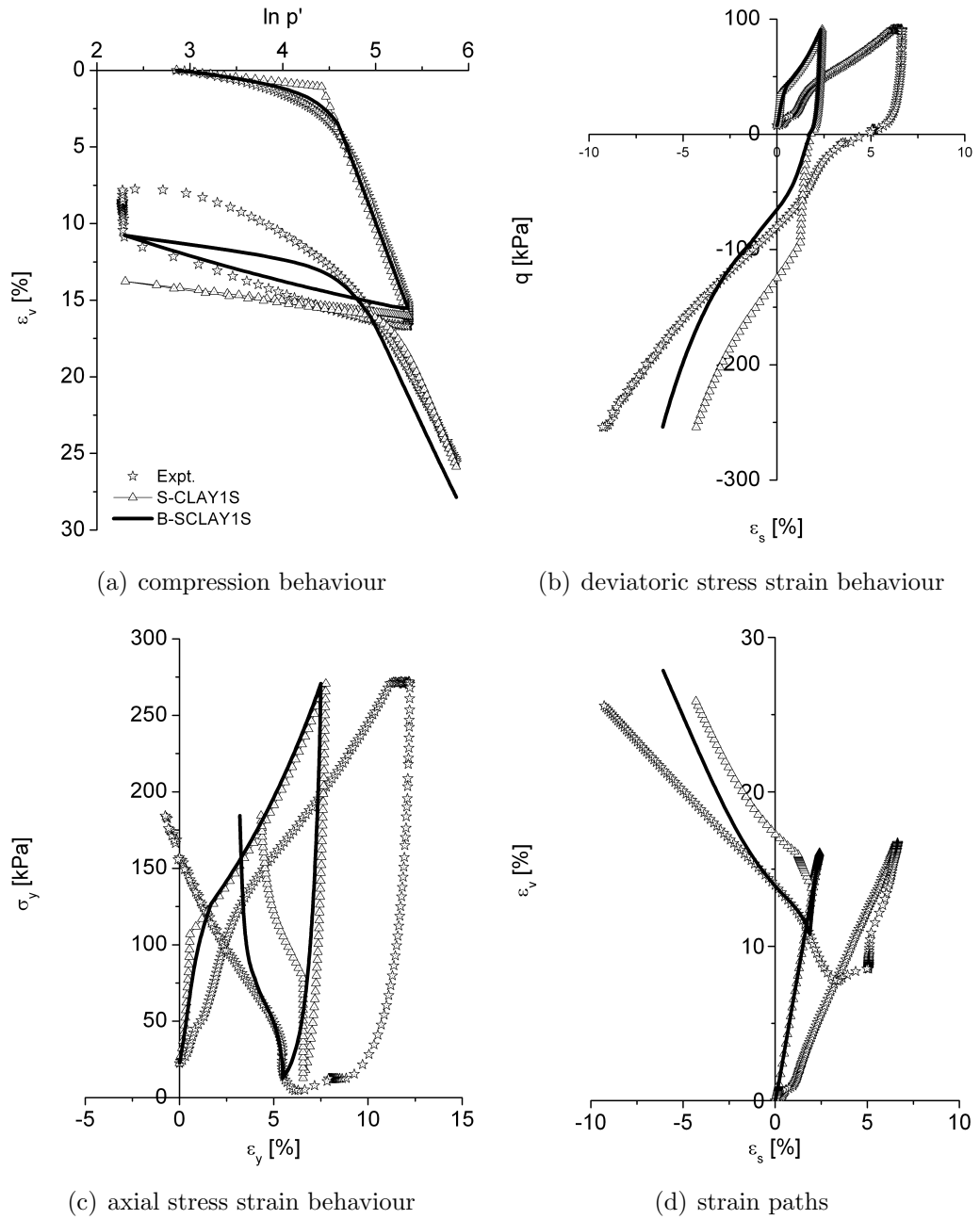


Figure 7.17: B-SCLAY1S and S-CLAY1S simulations of Test C7 where $\eta_1 = 0.42$ and $\eta_2 = -0.70$

7.4 Application to an embankment

The proposed B-SCLAY1S model performance is also evaluated using an embankment boundary value problem constructed on Bothkennar soft clay deposit. The purpose of this analysis to see any obvious numerical problems in the implementation of the B-SCLAY1S model into PLAXIS when subjected to static loading and consolidation analysis. For verification, the simulation was also compared with the S-CLAY1S model. Model parameter values for Bothkennar clay related to S-CLAY1S were obtained from McGinty (2006) and additional parameters required for B-SCLAY1S were obtained by parametric study and are summarized in Chapter 6, Table 6.1. Geometry of the embankment and construction details were given in Chapter 4, Section 4.4.

Results of finite element analysis using PLAXIS v9 are presented in terms of time-settlement curve, surface settlement, horizontal displacement and excess pore water pressures (PWP) generated during construction. The two constitutive models used for the subsoil differ only for the fact that B-SCLAY1S model includes small strain stiffness due to the inclusion of the bubble surface. Differences between results can therefore be uniquely attributed to the small strain stiffness behaviour of the subsoil.

In Fig. 7.18, results are presented in terms of vertical displacement versus time at the ground surface corresponding to the centreline of the embankment. The B-SCLAY1S model predicts a final settlement about 0.4 m, which is larger than the one predicted by the S-CLAY1S model of about 0.3 m. A general tendency of B-SCLAY1S to predict larger settlement than S-CLAY1S due to the assumption of small size of elastic region by incorporating the bubble surface, because of this plastic deformation is taking place from early stages of loading.

Fig. 7.19 shows horizontal displacement immediately after construction of 2nd layer of embankment and end of the analysis underneath of the toe of the embankment. The B-SCLAY1S model predicts considerably larger displacement than the S-CLAY1S model.

Surface settlement at end of the analyses is presented in Fig. 7.20. Both models give similar trend in surface settlement, but the B-SCLAY1S model predicts more than the S-CLAY1S model. After a distance of 10 m from the centreline, both models predicts the same quantitative response.

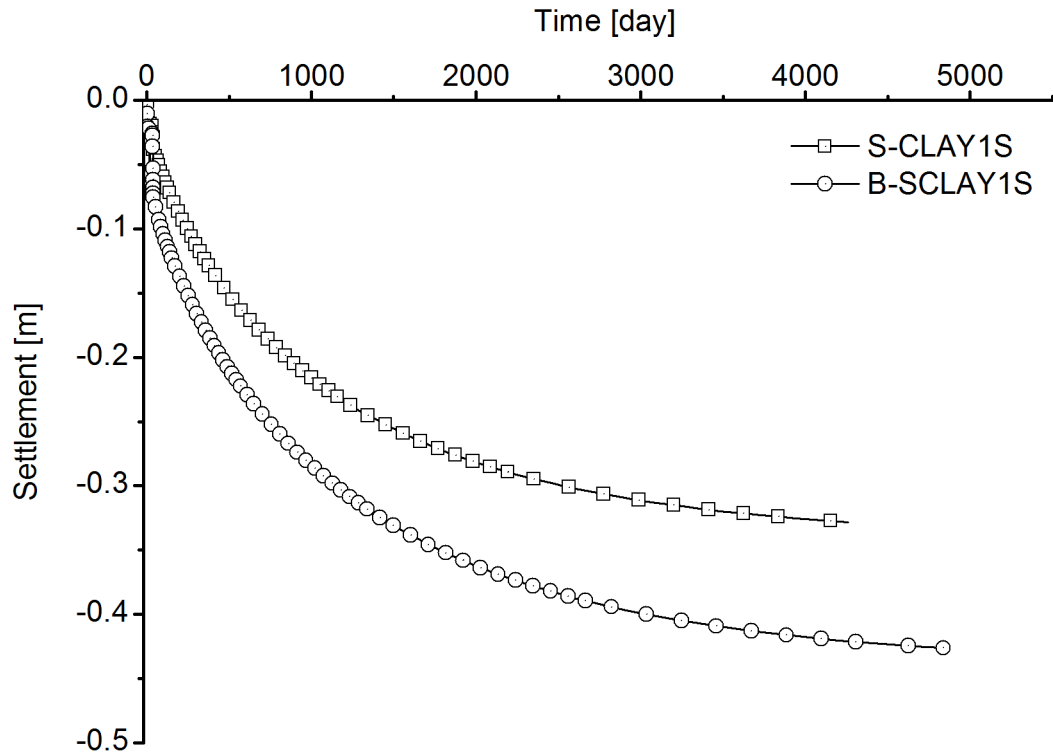


Figure 7.18: Comparison of time settlement curve at point A

Excess pore water pressure distribution immediately after construction of 1st and 2nd layer of embankment are presented in Figs. 7.21(a) and 7.21(b), respectively. Both models predict same qualitative distribution, which is also quantitatively correspondent to immediately after construction of 1st layer of embankment.

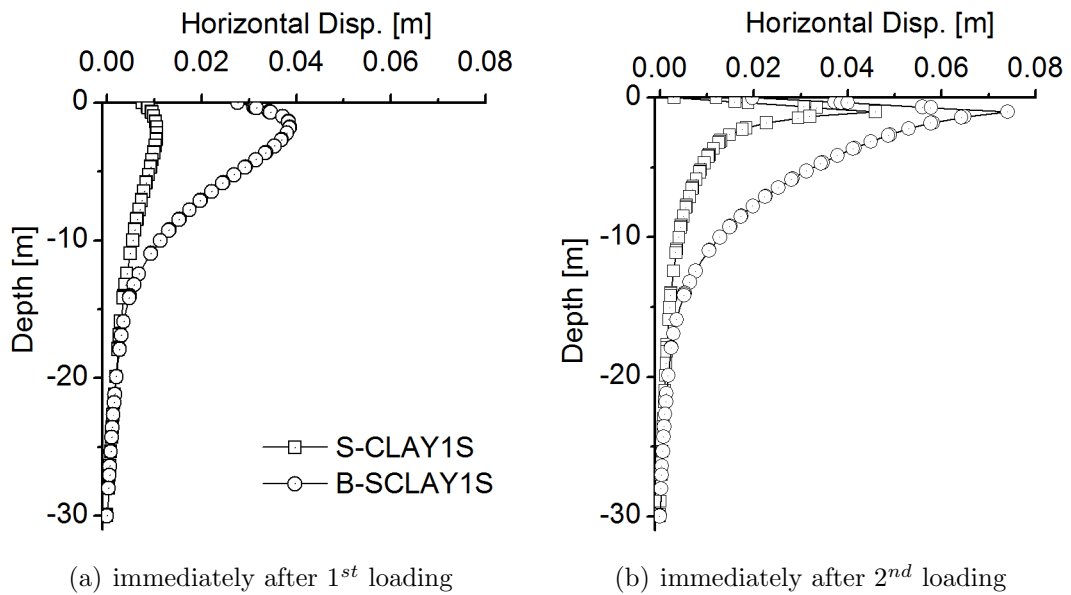


Figure 7.19: Comparison of horizontal displacement predictions at the embankment toe for B-SCLAY1S and S-CLAY1S

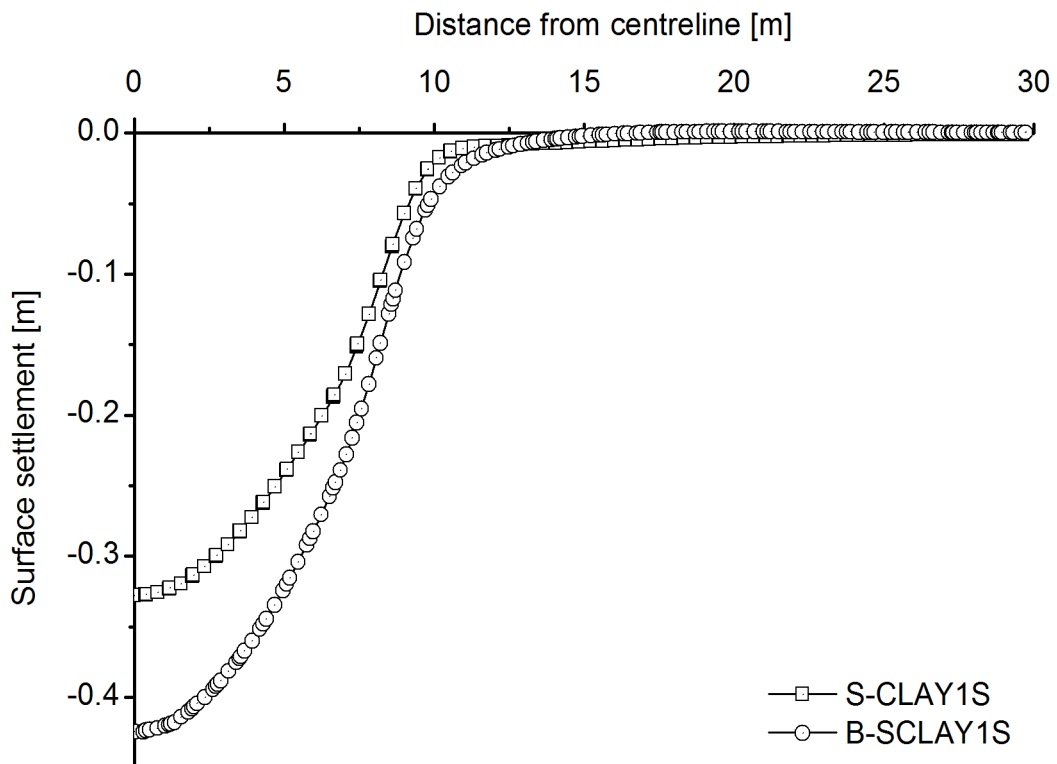


Figure 7.20: Comparison of surface settlement curves at the end of analyses

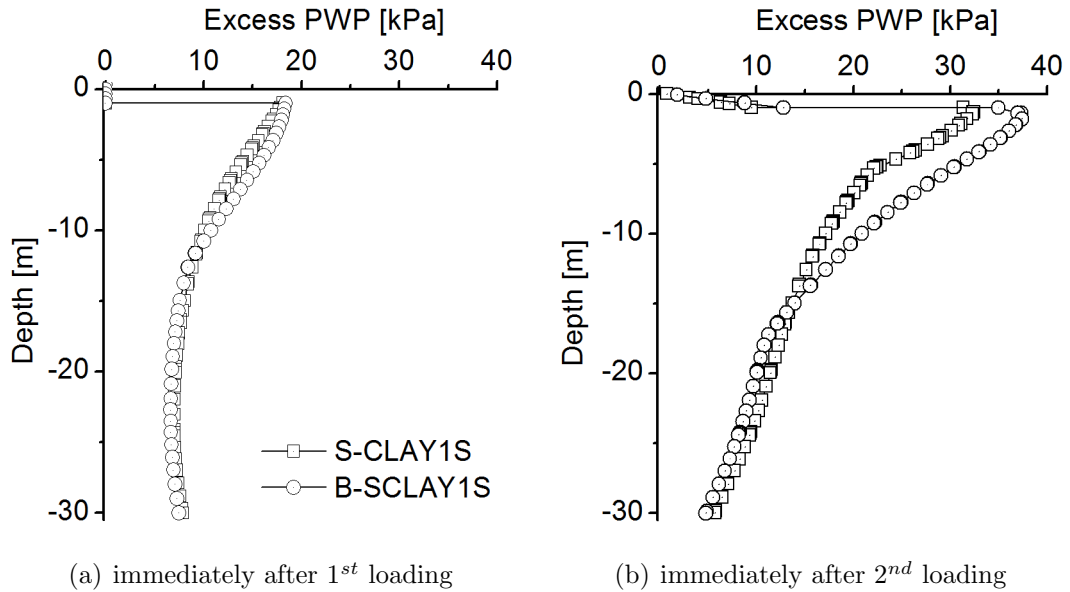


Figure 7.21: Comparison of excess PWP at the centreline of the embankment for B-SCLAY1S and S-CLAY1S

7.5 Application to a pile driving problem

This section involves penetration of a concrete pile into a Bothkennar clay layer using dynamic pulse loading. Bothkennar clay is modelled using the B-SCLAY1S and S-CLAY1S models. The main objective of this analyses is to investigate the difference in B-SCLAY1S and S-CLAY1S in the penetration of a pile and to visually check any numerical issues when dynamic loading is applied. Furthermore, excess pore pressures generated due to the rapid stress increases around the pile are also analysed. The pile driving problem used here is similar to that used in PLAXIS dynamics manual (Brinkgreve *et al.*, 2008).

An axisymmetric geometry model is used, where the pile is positioned along the axis of symmetry and the driving analysis for a pile already in place at a depth of 11 m is assumed, as shown in Fig. 7.23. In the beginning, the pile is not placed, so initially the Bothkennar clay properties are assigned to the pile cluster too. The pile has a diameter of 0.4m. The finite element mesh used in this analysis is shown in Fig. 7.24. A double blow is simulated using a periodic force function and the force time variation is illustrated in Fig. 7.22 for a single blow. A dynamic load is applied to 0.01s with peak value of 5000 kPa and for the rest of the 0.19s, dynamic analysis

7.5 Application to a pile driving problem

done with dynamic loading to zero. The blow (driving force) is a distributed unit load (system A) applied on top of the pile.

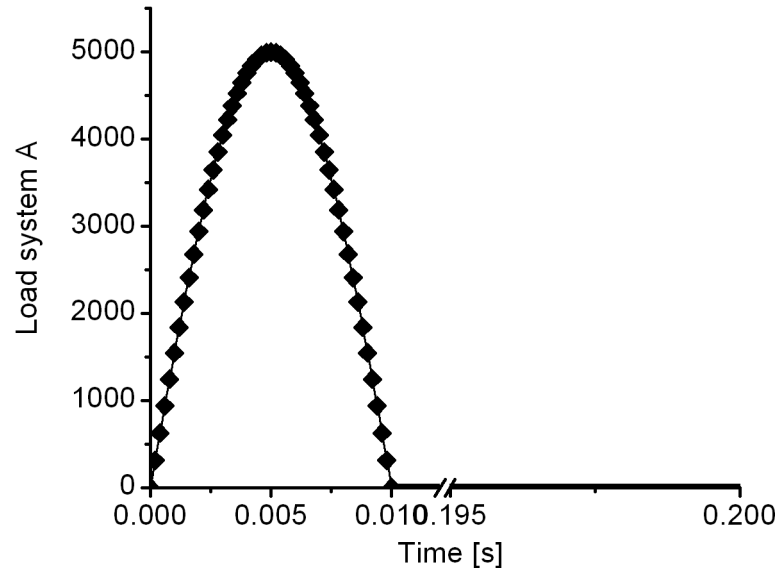


Figure 7.22: Pulse load time curve

The subsoil is assumed to be Bothkennar clay (undrained behaviour) and material properties are given in Table 6.1 in Chapter 6. Linear elastic behaviour is assumed for concrete pile considering non-porous behaviour and interface elements are used to allow the slip between the pile and soil. The pile properties are $E_{ref} = 3 \times 10^7$, $\nu = 0.1$ and $\gamma = 24 \text{ kN/m}^3$. Standard PLAXIS absorbent boundaries are applied at the bottom and at the right hand boundary to prevent wave reflection resulting from the driving process.

Fig. 7.25 shows pile tip penetration for B-SCLAY1S and S-CLAY1S versus dynamic time for a double blow. It can be seen that the pile penetration under the B-SCLAY1S model is more than that of the S-CLAY1S model. During first blow, maximum vertical settlement and the final settlement of the pile tip is about 18 mm & 19 mm and 10.5 mm & 11 mm for S-CLAY1S and B-SCLAY1S, respectively. In the second blow, the vertical settlement shows significant difference due to more plasticity mobilized by B-SCLAY1S model (the maximum settlement 31 mm and 28 mm and the final settlement 20 mm and 23 mm for S-CLAY1S and B-SCLAY1S, respectively).

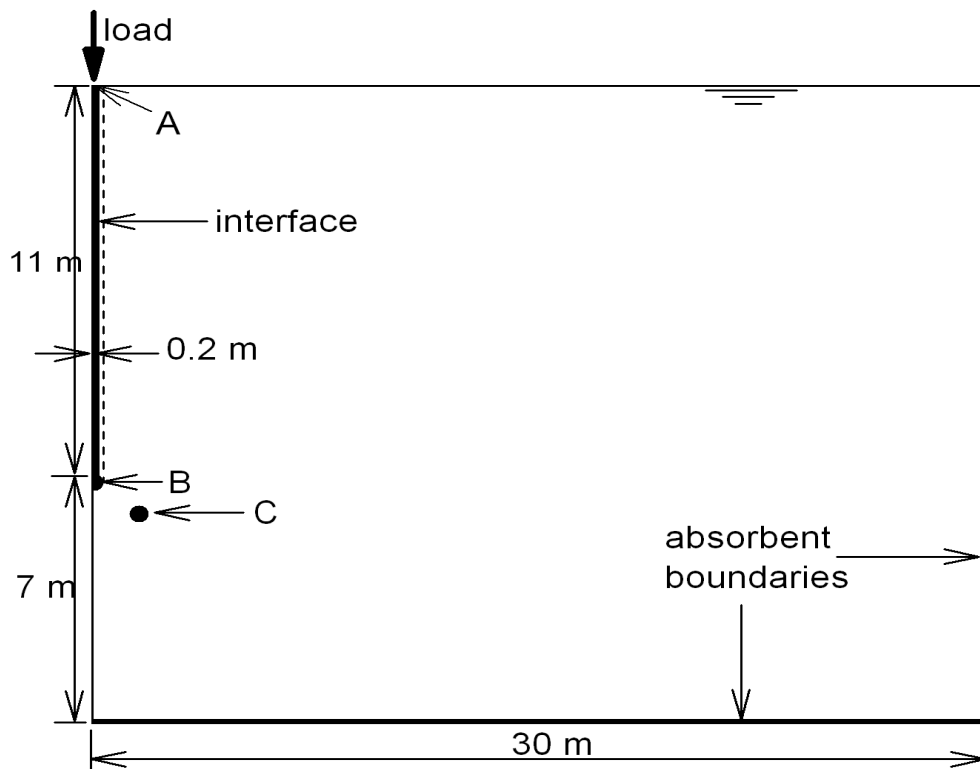


Figure 7.23: Geometry for pile driving problem

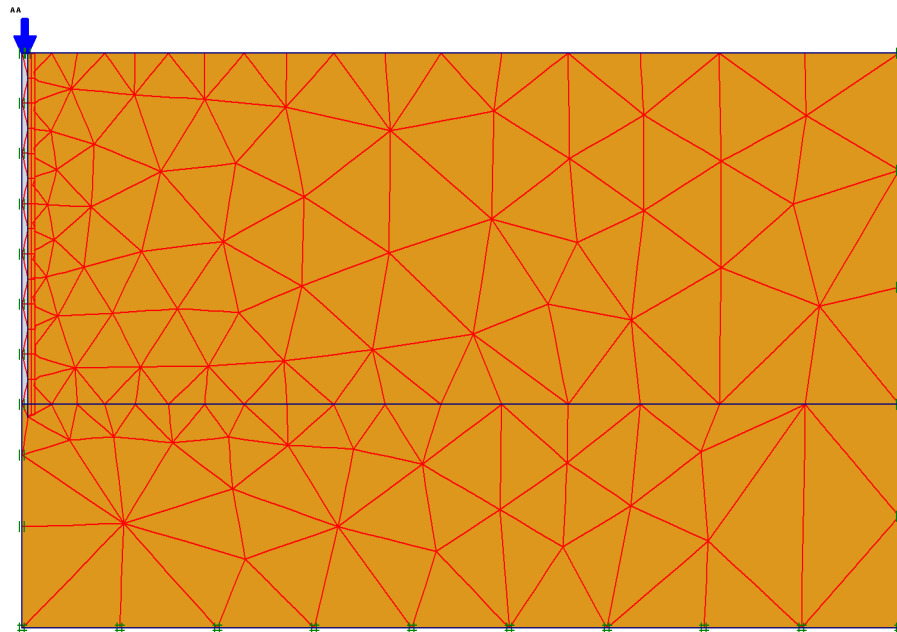


Figure 7.24: Mesh used for pile driving problem

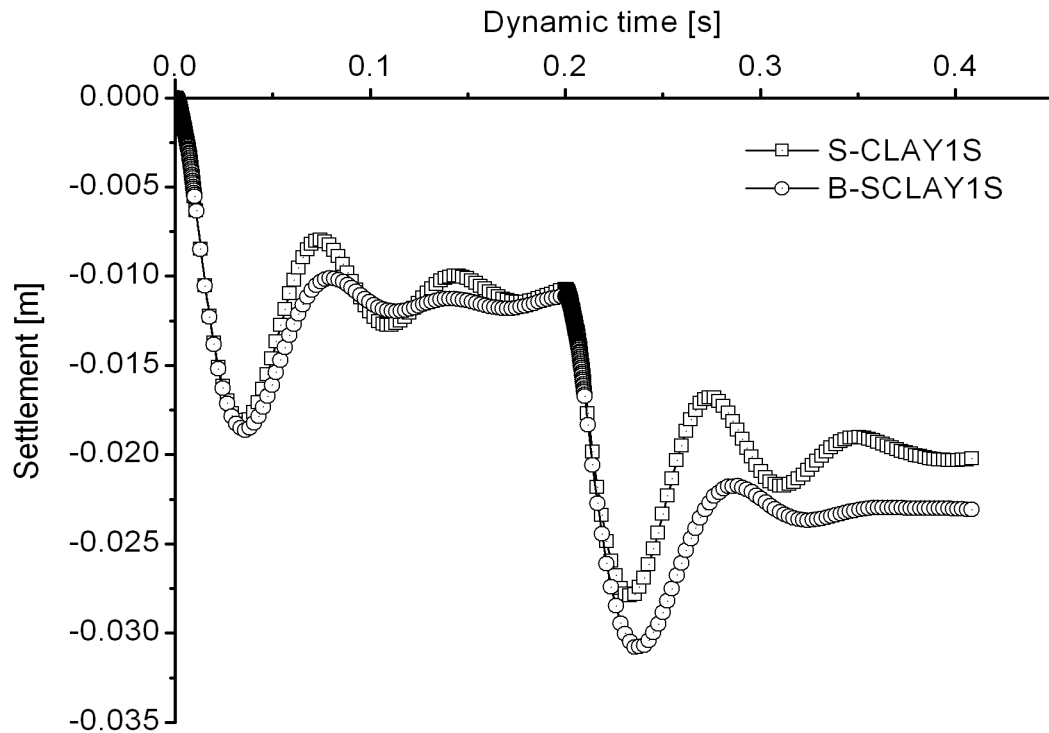
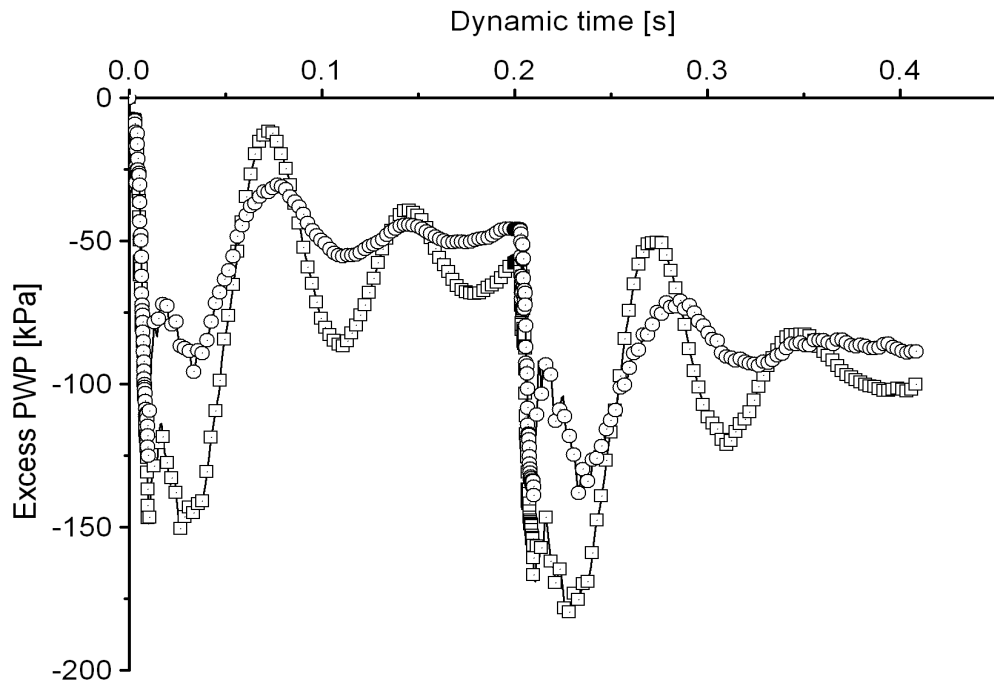


Figure 7.25: Pile settlement with time comparison for B-SCLAY1S and S-CLAY1S

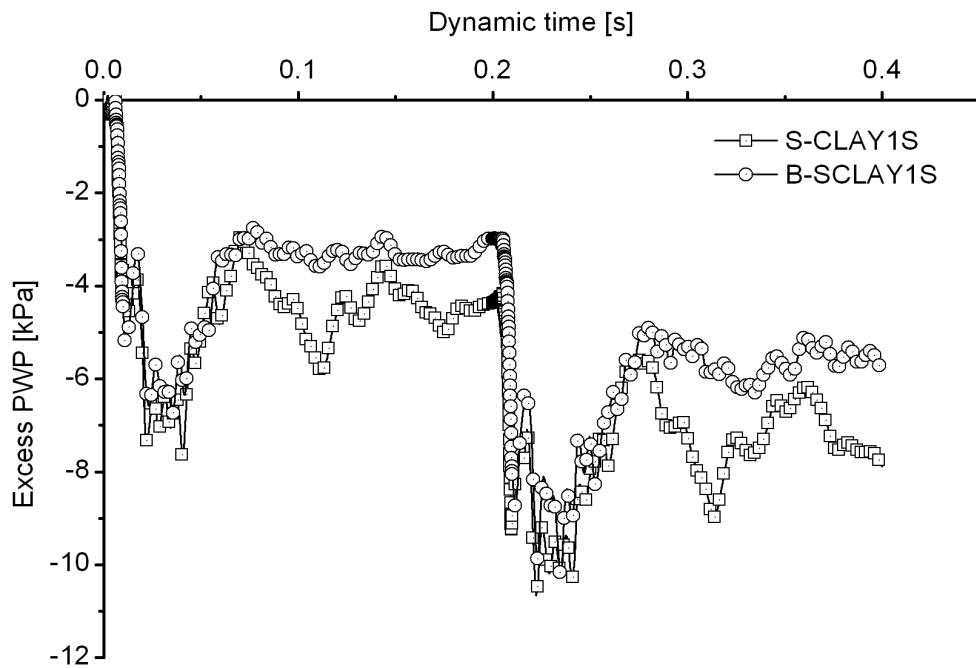
Most of the settlement occurs after the blow is ended (after 0.01s) because of the fact that compression wave is still propagating downwards in the pile and that causes additional pile penetrations. The pile is damped more for B-SCLAY1S than S-CLAY1S due to the mobilized soil plasticity.

It can be seen that large excess pore water pressures are generated very locally around the pile tip (see Fig. 7.26) and relatively low excess pore water pressures occurs away from pile tip (see Fig. 7.26(b)). Due to the large excess pore water pressure, the effective shear strength of the soil around the tip is reduced and hence contributes to the penetration of the pile into the clay layer. This excess pore water pressure remains in the analysis since consolidation is not considered and analysis time also very short (total analysis time is 0.4 s).

7.5 Application to a pile driving problem



(a) at point B (pile tip)



(b) at point C (subsoil)

Figure 7.26: Excess PWP with time comparison for B-SCLAY1S and S-CLAY1S

7.6 Summary

This chapter is divided into five parts. The first part of the chapter described the validation of the B-SCLAY1S model implemented into PLAXIS through a series of IPP simulations. A number of stress paths simulated by Al-Tabbaa (1987) were repeated and the results were compared with already published data for isotropic bubble model. Good agreement has been found.

Further, the anisotropic bubble model (B-SCLAY1) performance was compared to S-CLAY1 and MCC at IPP level. The comparison of simulations against to Messerklinger (2006) test results was presented in the second part of the chapter. The third part compared the structured anisotropic bubble model (B-SCLAY1S) simulations to McGinty (2006) test data for Bothkennar clay. Comparison of the B-SCLAY1S model simulation to published experimental data highlights the importance of the bubble surface in natural soil behaviour prediction.

In final two sections, the B-SCLAY1S model performance was evaluated using an embankment boundary value problem and a pile driving problem for static and dynamic loading condition respectively. In addition, the B-SCLAY1S model results were compared with the prediction by the S-CLAY1S model. Implementation of B-SCLAY1S into the FE code PLAXIS was verified through these benchmark tests.

Chapter 8

Conclusions and Recommendations

The research presented in this thesis includes a study on implementation of advanced non-linear constitutive models in the finite element code PLAXIS. The most significant contribution is the development and implementation of the bubble B-SCLAY1S model and its benchmark applications to static and dynamic loadings. Below, the main findings of this thesis as well as directions for future research are outlined.

8.1 Summary and Conclusions

The work described in this thesis had the following objectives:

- To explore numerical methodologies for implementing advanced constitutive models of soft soil in PLAXIS to minimize the numerical instability and improve the numerical efficiency.
- To study the existing S-CLAY1S model, which accounts for anisotropy and destructuration of soft soil, to further improve the model and to implement these improvements in PLAXIS using robust numerical algorithms.
- To develop a numerical algorithm to solve the singularity problem of the Sekiguchi-Ohta (SO) models in order to implement the models in PLAXIS.
- To develop a mathematical formulation for cyclic behaviour of soft soil and implement the model in PLAXIS. This model, developed by the author, is

known as B-SCLAY1S, and forms the major original part of this research project.

- To verify and validate the constitutive models implemented in PLAXIS, and to apply them to a number of benchmark problems representing typical geotechnical applications.

In the following sections, the conclusions that can be drawn from this research are summarized to demonstrate how these objectives were achieved.

8.1.1 Numerical algorithms to implement into FE code

An automatic substepping modified Newton-Raphson (MNR) implicit integration algorithm has been developed to implement the S-CLAY1S model within the finite element code PLAXIS. Elementary tests under monotonic loading conditions demonstrate the numerical performance and accuracy of the proposed MNR algorithm over the Euler-backward implicit and explicit algorithms. The simulation results indicate that the MNR algorithm is relatively insensitive to loading steps. Furthermore, the robustness of the MNR algorithm was also verified by the analysis of a benchmark test.

8.1.2 Lode angle dependency

The Lode angle dependency (Sheng *et al.*, 2000) has been implemented without adding too much complexity to the S-CLAY1S model. Simulations of extension triaxial tests against Hong Kong Marine clay data (Zhou *et al.*, 2006) showed improvement in the predictions of failure condition in extension. The importance of Lode angle dependency and verification of implementation were achieved using benchmark tests.

8.1.3 Hybrid algorithm to implement the SO models

A hybrid implicit algorithm, which consists of MNR algorithm and Stolle's algorithm has been developed to implement the inviscid/viscid Sekiguchi-Ohta (SO) models into the FE code PLAXIS. The hybrid algorithm has computational advantage to

overcome the vertex singularity of the SO models. The developed algorithm was verified through several triaxial simulations. The implementation and performance of inviscid/viscid models in the FE code was demonstrated at benchmark level to verify the robustness of the hybrid algorithm.

8.1.4 Bubble surface B-SCLAY1S model

A new bubble surface model, which incorporates natural clay phenomena such as anisotropy and destructuration, has been developed and implemented into the FE code PLAXIS. A parametric study using triaxial test data has been performed to determine the model parameters and their importance. The model prediction has been validated with experimental data on kaolin, Bothkennar clay and Swiss lacustrine clay. Despite the strong ratcheting feature of the model (Sivasithamparam *et al.*, 2010), the B-SCLAY1S model gives realistic predictions for loading and unloading response and cyclic loading response. The model implementation into the FE code PLAXIS is verified through static and cyclic benchmark tests.

8.2 Recommendations for future work

In line with the work presented in this thesis, the following topics are worthy of further investigation.

8.2.1 Modified S-CLAY1S model

Despite the advances in modelling the behaviour of natural clay for non-monotonic loading, a number of aspects of modelling behaviour should be further improved.

- Natural clay shows significant anisotropic pre-yield behaviour (McGinty, 2006). The modified S-CLAY1S model requires elastic cross-anisotropy.
- Further validation is required in 3D finite element applications.

8.2.2 Sekiguchi-Ohta models

The numerical instability in the dry side of the SO viscid model was treated in such a way that the model does not include the dry side. Numerical instability should be further investigated in order to find a way to include the dry side of the model in the implementation.

8.2.3 B-SCLAY1S model

Despite the advances in modelling the cyclic behaviour of natural clay, a number of aspects of modelling behaviour should be further improved.

- In order to improve the model prediction for cyclic loading, the parameter R could be made to be a function of number of cycles. This may eliminate the strong ratcheting behaviour of the model.
- A modification of the hardening modulus is required to eliminate the abrupt drop in stiffness once stress state becomes elasto-plastic.
- Before the model can be used in any real applications, extensive full scale tests should be performed to validate the model predictions.

References

- ABOIM, C. & ROTH, W. (1982). Bounding surface plasticity theory applied to cyclic loading of sand. *Int. Symp. on Numerical Models in Geomechanics*, 65 – 72.
- AL-TABBAA, A. (1987). *Permeability and stress-strain response of speswhite kaolin*. Ph.D. thesis, University of Cambridge.
- AL-TABBAA, A. & WOOD, D. (1989). An experimentally based bubble model for clay. *Proc. 3rd Int. Conf. on Numerical Models in Geomechanics*, 91 – 99.
- ATKINSON, J.H. & SALLFORS, G. (1991). Experimental determination of soil properties. general report to session 1. *Proc. of the 10th European Conference in Soil Mechanics*, **3**, 915 – 956.
- BARDET, J.F. (1986). Bounding surface plasticity model for sands. *Journal of Engineering Mechanics (ASCE)*, **112(11)**, 1198 – 1217.
- BRINKGREVE, R., BROERE, W. & WATERMAN, D. (2008). *PLAXIS Finite Element Code for Soil and Rock Analyses*. 2D-Version 9, The Netherlands.
- CARTER, J.R., BOOKER, J.R. & WROTH, C.P. (1982). A critical state soil model for cyclic loading. *Soil Mechanics - Transient and Cyclic Loads*, eds. G. N. Pande, & O. C. Zienkiewicz, 219–252.
- CARTER, J.R., DESAI, C.S., POTTS, D.M., SCHWEIGER, H.F. & SLOAN, S.W. (2000). Computing and computer modelling in geotechnical engineering. *Proc. GeoEng 2000*, **1: invited papers**, 1157–1252.
- CHAMBON, R. & DESRUES, J. (1985). Bifurcation par localization at non linéarité incrémentale, un exemple heuristique d'analysis complète. *Proc. Plastic Instability Press E.N.P.C.*, 101 – 103.

REFERENCES

- COLLINS, I. & HOULSBY, G. (1997). Application of thermomechanical principles to the modelling of geotechnical materials. *Proc. Royal Society of London (Series A)*, **453**, 1975–2001.
- DAFALIAS, Y.F. (1986a). An anisotropic critical state soil plasticity model. *Mechanics Research Communications*, **13(6)**, 341–347, (Pergamon Journals Ltd).
- DAFALIAS, Y.F. (1986b). Bounding surface plasticity i: Mathematical foundation and hypoplasticity. *Journal of Engineering Mechanics (ASCE)*, **112(9)**, 966–987.
- DAFALIAS, Y.F. & HERRMANN, L.R. (1982). Bounding surface formulation of plasticity. *Soil Mechanics - Transient and cyclic loads*, 253 – 282, (Editors: G. N. Pande and O. C. Zienkiewicz).
- DAFALIAS, Y.F. & POPOV, E.P. (1975). A model of nonlinearly hardening materials for complex loadings. *Acta. Mech.*, **21**, 173 – 192.
- DESAI, C.S. (1974). A consistent finite element technique for work softening behavior. *Proc., Int. Conf. on Computer Methods in Nonlinear Mechanics*, University of Texas, Austin, TX.
- DESAI, C.S. (2001). *Mechanics of Materials and Interfaces: The Disturbed State Concept*. CRC Press, Boca Raton, Florida.
- DESAI, C.S. & TOTH, J. (1996). Disturbed state constitutive modelling based on stress-strain and non-destructive behaviour. *International Journal of Solids and Structures*, **33(11)**, 1619–1650.
- DESAI, C.S. & ZHANG, W. (1998). Computational aspects of disturbed state constitutive models. *Int. J. of computer methods in Appl. Mech. And Eng.*, **151**, 361–376.
- DRUCKER, D.C. & PRAGER, W. (1952). Soil mechanics and plastic analysis for limit design. *Quart. Appl. Math.*, **10**, 157 – 165.
- GENS, A. & NOVA, R. (1993). Conceptual bases for a constitutive model for bonded soils and weak rocks. *Proc. of Int. Symp. on Hard Soils Soft Rocks*, 485–494, Athens.
- GÉOTECHNIQUE SYMPOSIUM IN PRINT (1992). *Géotechnique*, **42(2)**.

- GHABOUSSI, J. & MOMEN, H. (1982). Modelling and analysis of cyclic behaviour of sands. *Soil Mechanics - Transient and Cyclic Loads*, eds. G. N. Pande, & O. C. Zienkiewicz, 313–342.
- GRAMMATIKOPOULOU, A. (2004). *Development, implementation and application of kinematic hardening models for overconsolidated clays*. Ph.D. thesis, Imperial College, Univ. of London.
- GUDEHUS, G. (1996). A comprehensive constitutive equation for granular materials. *Soils and Foundations*, **36(1)**, 1–12.
- GUDEHUS, G. (2004). A visco-hypoplastic constitutive relation for soft soils. *Soils and Foundations*, **44(4)**, 11–25.
- HASHIGUCHI, K. (1980). Constitutive equations of elasto-plastic materials with elastic-plastic transition. *J. Appl. Mech. (ASME)*, **47**, 266 – 272.
- HASHIGUCHI, K. (1985). Two- and three-surface models of plasticity. *Proc. of 5th Int. Conf. on Numerical Methods in Geomechanics*, 285–292, nagoya.
- HASHIGUCHI, K. (1989). Subloading surface model in unconventional plasticity. *Int. J. Solids Struct*, **25**, 917 – 945.
- HERLE, I. & KOLYMBAS, D. (2004). Hypoplasticity for soils with low friction angles. *Computers and Geotechnics*, **31(5)**, 365–373.
- HIGHT, D.W., BOND, A.J. & LEGGE, J.D. (1992). Characterization of the bothkennar clay: an overview. *Geotechnique*, **42(2)**, 303–347.
- HOULSBY, G. (1981). *A study of plasticity theories and their applicability to soils*. Ph.D. thesis, University of Cambridge.
- HOULSBY, G. & PUZRIN, A. (1999). An approach to plasticity based on generalised thermodynamics. *Proc. of the International Symposium on Hypoplasticity*, 233–245.
- HOULSBY, G. & PUZRIN, A. (2002). Rate-dependent plasticity models derived from potential functions. *Journal of Rheology*, **46(1)**, 113–126.
- HOULSBY, G. & PUZRIN, A. (2006). *Principles of Hyperplasticity: An Approach to Plasticity Theory Based on Thermodynamic Principles*. Springer, Verlag London Limit.

- IIZUKA, A. & OHTA, A. (1987). A determination procedure of input parameters in elasto-viscoplastic finite element analysis. *Soils and Foundations*, **27,3**, 71–87.
- IIZUKA, A. & TACHIABNA, S. (2009). Theoretical and numerical implementation of sekiguchi-ohta model, personnel communication in PLAXIS, The Netherlands.
- ISHIHARA, K. (1996). *Soil Behaviour in Earthquake Geotechnics*. Oxford Engineering Science Series, Oxford University Press.
- IWAN, W.D. (1967). On a class of models for the yield behavior of continuous and composite systems. *Journal of Applied Mechanics (ASME)*, **34**, 612–617.
- KARSTUNEN, M. & KOSKINEN, M. (2008). Plastic anisotropy of soft reconstituted clays. *Canadian Geotechnical Journal*, **45**, 314 – 328.
- KARSTUNEN, M. & YIN, Z.Y. (2010). Modelling time-dependent behaviour of murro test embankment. *Geotechnique*, **29**, 1 – 34.
- KARSTUNEN, M., KRENN, H., WHEELER, S., KOSKINEN, M. & ZENTAR, R. (2005). The effect of anisotropy and destructuration on the behaviour of murro test embankment. *International Journal of Geomechanics (ASCE)*, **5(2)**, 87 – 97.
- KOITER, W. (1953). Stress-strain relations, uniqueness and variational theorems for elasto-plastic materials with a singular yield surface. *Quart. Appl. Math.*, **11**, 350–354.
- KOLYMBAS, D. (1987). A novel constitutive law for soils. *Proc. 2nd Int. Conf. on Constitutive laws for Engineering Materials*, Elsevier **1**, 319 – 326.
- KOLYMBAS, D. (1988). Generalized hypoplastic constitutive equation. *Constitutive Equations for Granular Soils*, 349 – 366.
- KONDNER, R. (1963). Hyperbolic stress-strain response: cohesive soils. *Journal of the Soil Mechanics and Foundations Division (ASCE)*, **89(SM1)**, 115 – 143.
- KORHONEN, M., K.-H. & LOJANDER, M. (1987). Yielding of perno clay. *In Proc. of the 2nd Int. Conf. on Constitutive Laws for Engineering Materials*, **2**, 1249 – 1255.
- KOSKINEN, M., KARSTUNEN, M. & S.J., W. (2002a). Modeling destructuration and anisotropy of a natural soft clay. *Proc. of the 5th European Conf. Numerical Methods in Geotechnical Engineering*, 11 – 20.

- KOSKINEN, M., ZENTAR, R. & KARSTUNEN, M. (2002b). Anisotropy of reconstituted poko clay. *Proc. 8th International Symp. Numerical Models in Geomechanics (NUMOG)*, 99 – 105.
- KRENN, H. (2008). *Numerical modelling of embankments on soft soils*. Ph.D. thesis, University of Strathclyde, Scotland.
- KRIEG, R.D. (1975). A practical two-surface plasticity theory. *J. Appl. Mech.*, **34**, 641 – 646.
- LADE, P.V. & DUNCAN, J.M. (1975). Elasto-plastic stress strain theory for cohesionless soil. *J. Geotech. Eng. Div.*, **101**, 1037 – 1053, aSCE.
- LEONI, M., KARSTUNEN, M. & VERMEER, P. (2008). Anisotropic creep model for soft soils. *Geotechnique*, **58 (3)**, 215–226.
- LUCCIONI, L.X., PESTANA, J. & TAYLOR, R. (2001). Finite element implementation of non-linear elasto-plastic constitutive laws using local and global explicit algorithms with automatic error control. *Int. J. for Numerical Methods in Engineering*, **50 (5)**, 1191–1212.
- MAIR, R. (1993). Developments in geotechnical engineering research: applications to tunnels and deep excavations. *Unwin Memorial Lecture 1992, Proceedings of the Institute of Civil Engineers*, **97(1)**, 27–41.
- MAȘIN, D. (2005). A hypoplastic constitutive model for clays. *Int. J. Numer. Anal. Methods Geomech.*, **29(4)**, 311–336.
- MAȘIN, D. (2007). A hypoplastic constitutive model for clays with meta-stable structure. *Canadian Geotechnical Journal*, **44(3)**, 363–375.
- MATSUOKA, H. & NAKAI, T. (1974). Stress deformation and strength characteristics of soil under three different principal stresses. *Proc. Japan Soc. Civil Engineers*, **232**, 59.
- MATSUOKA, H. & NAKAI, T. (1982). A new failure criterion for soils in three dimensional stresses. *Proc. IUTAM Symp. on deformation and failure of granular materials*, 253 – 263, (editors: P. A. Vermeer and H. J. Luger).
- MCGINTY, K. (2006). *The stress-strain behaviour of Bothkennar clay*. Ph.D. thesis, Department of Civil Engineering, University of Glasgow, UK.

REFERENCES

- MCGINTY, K., KARSTUNEN, M. & WHEELER, S.J. (2008). Modelling destructure and anisotropy of bothkennar clay. *Proc. 2nd Int. Workshop on Geotechnics of Soft Soils - Focus on Ground Improvement*, 263–268, (Eds. Karstunen & Leoni).
- MCVAY, M. & TAESIRI, Y. (1985). Cyclic behaviour of pavement base materials. *Journal of Geotechnical Engineering (ASCE)*, **111**(1), 1 – 17.
- MESRI, G. & GODLEWSKI, P.M. (1977). Time and stress-compressibility interrelationship. *Proc. ASCE*, **103**, 417 – 430.
- MESSERKLINGER, S. (2006). *Non-linearity and small strain behaviour in lacustrine clay*. Ph.D. thesis, Swiss Federal Institute of Technology, Zurich.
- MRÓZ, Z. (1967). On the description of anisotropic workhardening. *Journal of the Mechanics and Physics of Solids*, **15**, 163–175.
- MRÓZ, Z., NORRIS, V. & ZIENKIEWICZ, O.C. (1979). Application of an anisotropic hardening model in the analysis of elasto-plastic deformation of soils. *Geotechnique*, **29**, 1 – 34.
- MUIR WOOD, D. (1990). *Soil behaviour and critical state soil mechanics*. Cambridge University Press.
- MUIR WOOD, D. (1995). Kinematic hardening model for structured soil. *Mechanics of Cohesive-Frictional Materials*, 83 – 88, pande and Pietruszczak (eds).
- MUIR WOOD, D. (2004). *Geotechnical modelling*. Taylor & Francis.
- MUIR WOOD, D. & ROUAINIA, M. (2000). A kinematic hardening constitutive model for natural clays with loss of structure. *Geotechnique*, **50**,2, 153–164.
- NASH, D.F.T., POWELL, J.J.M. & LLOYD, I.M. (1992a). Initial investigations of the soft clay test site at bothkennar. *Geotechnique*, **42**(2), 163–181.
- NASH, D.F.T., SILLS, G.C. & DAVISON, L.R. (1992b). One-dimensional consolidation testing of soft clay from bothkennar. *Geotechnique*, **42**(2), 241–256.
- NAYLOR, D., PANDE, G., SIMPSON, B. & TABB, R. (1981). *Finite Elements in Geotechnical Engineering*. Pineridge Press, Swansea.

- NOVA, R. (1982). A constitutive model for soil under monotonic and cyclic loading. *Soil Mechanics - Transient and Cyclic Loads*, eds. G. N. Pande, & O. C. Zienkiewicz, 343–373.
- PANDE, G. & SHARMA, K. (1983). Multilaminate model of clays - a numerical evaluation of the influence of rotation of principal stress axes. *International Journal for Numerical and Analytical Methods in Geomechanics*, **7**, 397–418.
- PENDER, M.J. (1982). A model for the cyclic loading of overconsolidated soil. *Soil Mechanics - Transient and Cyclic Loads*, eds. G. N. Pande, & O. C. Zienkiewicz, 283–311.
- PERZYNA, P. (1966a). Fundamental problems in viscoplasticity. *Adv. Appl. Mech.*, **9**, No.3, 244 – 377.
- PERZYNA, P. (1966b). Fundamental problems in viscoplasticity. *Adv. Appl. Mech.*, **9**, 244377.
- PIETRUSZCZAK, S. & PANDE, G. (1987). Multi-laminate framework of soil models- plasticity formulation. *International Journal for Numerical and Analytical Methods in Geomechanics*, **11(6)**, 651–658.
- PIPATPONGSA, T. & OHTA, H. (2000). Return-mapping algorithm for sekiguchi-ohta model. *2nd Inter. Summer Sym., JSCE*, 229–232.
- PIPATPONGSA, T. & OHTA, H. (2008). How can we describe strain changes due to isotropic consolidation by using the original cam clay model? *The 13th National Convention on Civil Engineering of Thailand*, **GTE**, 96–101.
- PIPATPONGSA, T. & TACHIBANA, S. (2005). Corner mode in the sekiguchi-ohta model. *2005 Workshop and Meeting on Safety & Stability of Infrastructures Against Environmental Impacts, organized by JSPS Core University Program on Environmental Engineering, De La Salle University, Manila, Philippines*, 147–159.
- PIPATPONGSA, T., KOBAYASHI, I., OHTA, H. & IIZUKA, A. (2001). The vertex singularity in the sekiguchi-ohta model. *56th JSCE Annual Meeting*, **CD III-B341**.

- PIPATPONGSA, T., IIZUKA, A., KOBAYASHI, I. & OHTA, H. (2002a). Fem formulation for analysis of soil constitutive model with a corner on the yield surface. *Journal of Structural Engineering*, **48**, 185 – 194.
- PIPATPONGSA, T., KOBAYASHI, I., IIZUKA, A. & OHTA, H. (2002b). Implicit finite element implementation of an anisotropic soil model. *Proc. of 51th Jap. Nat. Conf. on Theo. Appl. Mech.*, 211–212.
- PIPATPONGSA, T., KHOSRAVI, M. & OHTA, H. (2009a). Backward-euler stress update algorithm for the original cam-clay model with vertex singularity. *International Symposium on Predication and Simulation Methods for Geohazard Mitigation*, 179–184, (IS-Kyoto 2009).
- PIPATPONGSA, T., TAKEYAMA, T., OHTA, H. & IIZUKA, A. (2009b). On the vertex singularity of the sekiguchi-ohta model. *Theoretical and Applied Mechanics Japan*, **57**, 89–94.
- POTTS, D. & GENS, A. (1985). A critical assessment of methods of correcting for drift from the yield surface in elasto-plastic finite element analysis. *Int. J. for Numerical and Analytical Methods in Geomechanics*, **9**, 149–59.
- POTTS, D. & ZDRAVKOVIC, L. (1999). *Finite element analysis in geotechnical engineering. Theory*. Thomas Telford Publishing, London.
- POTTS, D., AXELSSON, K., GRANDE, L., SCHWEIGER, H. & LONG, M. (2002). *Guidelines for the use of advanced numerical analysis*. Thomas Telford Ltd, London.
- PRÉVOST, J.H. (1977). Mathematical modelling of monotonic and cyclic undrained clay behaviour. *International Journal for Numerical and Analytical Methods in Geomechanics*, **1**, 195–216.
- PRÉVOST, J.H. (1978). Anisotropic undrained stress-strain behaviour of clays. *Journal of the Geotechnical Engineering Division (ASCE)*, **104**, 1075–1090.
- ROSCOE, K. & BURLAND, J. (1968). On the generalised stress-strain behaviour of wet clay. *Engineering Plasticity*, 535 – 609.
- ROSCOE, K. & SCHOFIELD, A. (1963). Mechanical behaviour of an idealised wet clay. *Proc. 2nd European Conf. on Soil Mechanics and Foundation Engineering*, **1**, 47 – 54, wiesbaden.

- ROSCOE, K.H. & POOROOSHASB, H. (1963). A fundamental principle of similarity in model test for earth pressure problems. *Proceedings of the 2nd Asian Regional Conference on Soil Mechanics*, **1**, 134 – 140, bangkok.
- ROSCOE, K.H., SCHOFIELD, A.N. & WROTH, C.P. (1958). On the yielding of soils. *Geotechnique*, **8**, 22 – 53.
- ROSCOE, K.H., SCHOFIELD, A.N. & THURAIRAJAH, A. (1963a). Yielding of clays in state wetter than critical. *Geotechnique*, **13-3**, 211–240.
- ROSCOE, K.H., SCHOFIELD, A.N. & THURAIRAJAH, A.H. (1963b). Yielding of soils in states wetter than critical. *Geotechnique*, **13**, 211 – 240.
- SCHOFIELD, A. & WROTH, C. (1968). *Critical State Soil Mechanics*. McGraw-Hill, London.
- SCHULLER, H. (2000). *A multilaminate model for soils and its application to numerical analysis of tunnel excavation*. Ph.D. thesis, Graz University of Technology, Austria.
- SCHULLER, H. & SCHWEIGER, H. (2002). Application of a multilaminate model to simulation of shear band formation in natm-tunneling. *Computers and Geotechnics*, **7**, 501–524.
- SCHWEIGER, H., WILTAFSKY, C., SCHARINGER, F. & GALAVI, V. (2009). A multilaminate framework for modelling induced and inherent anisotropy of soils. *Geotechnique*, **59(2)**, 87–101.
- SEKIGUCHI, H. (1984). Theory of undrained creep rupture of normally consolidated clay based on elasto-viscoplasticity. *Soils and Foundations*, **24 (1)**, 129 – 147.
- SEKIGUCHI, H. & OHTA, H. (1977). Induced anisotropy and time dependency in clays. *9th ICSMFE, Tokyo, Constitutive equations of Soils*, **17**, 229 – 238.
- SHENG, D., SLOAN, S. & YU, H. (2000). Aspects of finite element implementation of critical state models. *Computational Mechanics*, **26**, 185–196.
- SHIBATA, T. (1963). On the volume changes of normally-consolidated clays. *Annual disaster prevention research institute*, **6**, 128 – 134, in Japanese.

REFERENCES

- SIMO, J., KENNEDY, J. & GOVINDJEE, S. (1988). Non-smooth multisurface plasticity and viscoplasticity loading/unloading conditions and numerical algorithms. *Int. J. Numer. Methods Engrg*, **26**, 2161–2185.
- SIVASITHAMPARAM, N., KAMRAT-PIETRASZEWSKA, D. & KARSTUNEN, M. (2010). An anisotropic bubble model for soft clays. *Proc. 7th European Conference on Numerical Methods in Geotechnical Engineering*, 21 – 26, trondheim, Norway.
- SLOAN, S. (1987). Substepping schemes for the numerical integration of elastoplastic stress-strain relations. *Int. J. Numerical Methods in Engineering*, **24**, 893–911.
- SLOAN, S., ABBO, A.J. & SHENG, D. (2001). Refined explicit integration of elastoplastic models with automatic error control. *Engineering Computations*, **18(1/2)**, 121–54.
- STALLEBRASS, S.E. (1990). *Modelling the effects of recent stress history on the behaviour of overconsolidated soils*. Ph.D. thesis, City University, London.
- STOLLE, D.F.E. (1991). An interpretation of initial stress and strain methods, and numerical stability. *Int. J. for Numerical and Analytical Methods in Geomechanics*, **15**, 399–416.
- STOLLE, D.F.E., BONNIER, P.G. & VERMEER, P.A. (1997). A soft soil model and experiences with two integration schemes. *Numerical Models on Geomechanics*, **NUMOG VI**, 123–128, pietruszczak and Pande (eds).
- TAKEYAMA, T., OHNO, S., PIPATPONGSA, T., IIZUKA, A. & OHTA, H. (2005). The stress update using implicit integration for the viscid version of sekiguchi-ohta model. *Technical report*, in Japanese.
- TAKEYAMA, T., PIPATPONGSA, T., IIZUKA, A., MIZUTA, T., OHNO, S. & OHTA, H. (2007). Soil/water coupled f.e. simulation of field performance of 5 embankments placed on homogeneous clay. *First Sri Lankan Geotechnical Society International Conference on Soil and Rock Engineering*, 1–10, (Sri Lanka).
- TRESCA, H. (1864). Sur l'écoulement des corps solides soumis a de fortes pressions. *C.R. Acas. Sci. (Paris)*, **59**, 754.
- VON MISES, R. (1913). Mechanik der fasten korper im plastisch deformation. *Zustand. Nachr. Ges. Wiss. Gottingen*, 582.

- VON WOLFFERSDORFF, P.A. (1996). A hypoplastic relation for granular materials with a predefined limit state surface. *Mechanics of Cohesive-Frictional Materials*, **1**, 251–271.
- WHEELER, S. (1997). A rotational hardening elasto-plastic model for clays. *In Proc. 14th Int. Conf. on Soil Mechanics and Foundation Engineering*, **1**, 431 – 434.
- WHEELER, S., KARSTUNEN, M. & NÄÄTÄNEN, A. (1999). Anisotropic hardening model for normally consolidated soft clay. *Proc. 7th Int. Symp. on Numerical Models in Geomechanics (NUMOG VII)*, 33 – 40.
- WHEELER, S., NÄÄTÄNEN, A., KARSTUNEN, M. & LOJANDER, M. (2003). An anisotropic elasto-plastic model for soft clays. *Canadian Geotechnical Journal*, **40**, 403 – 418.
- WHITE, D., TAKE, M., BOLTON, M. & MUNACHEN, S. (2001). A deformation measurement system for geotechnical testing based digital image, close-range photogrammetry, and piv image analysis. *15th Int. Conf. of Soil Mechanics and Foundation Engineering*, 539–542.
- WHITTLE, A. (1993a). Evaluation of a constitutive model for overconsolidated clays. *Geotechnique*, **43 (2)**, 289 – 313.
- WHITTLE, A. & KAVVADAS, M. (1994). Formulation of mit-e3 constitutive model for overconsolidated clays. *Journal of Geotechnical Engineering (ASCE)*, **120(1)**, 173 – 198.
- WHITTLE, A.J. (1993b). Evaluation of constitutive model for overconsolidated clays. *Geotechnique*, **43**, 289 – 313.
- WILTAFSKY, C. (2003). S-clay1s, user defined soil model documentation, documentation, University of Glasgow, UK.
- WROTH, C.P. & HOULSBY, G.T. (1985). Soil mechanics property characterization and analysis procedures. *Proceedings of the 11th International Conference on Soil Mechanics and Foundation Engineering*, **1**, 1 – 55.
- YU, H.S. (2006). *Plasticity and geotechnics*. Springer.
- YU, H.S. & KHONG, C.D. (1993). Bounding surface formulation of a unified critical state models for clay and sand. *Proc. 3rd Int. Conf. Deformation Characteristics of Geomaterials*, 1111 – 1118.

REFERENCES

- YUTTAPONGTADA, Y., PIPATPONGSA, A., T. AND IIZUKA & OHTA, H. (2003). Fem for the sekiguchi-ohta model considering non-smooth yield surface. *Proc. of 38th Japanese Nat. Conf. on Geotech. Engrg*, 285–286.
- ZENTAR, R., KARSTUNEN, M., WILTAFAFSKY, C., SCHWEIGER, H.F. & KOSKINEN, M. (2002). Comparison of two approaches for modelling anisotropy of soft clays. *Proc. 8th Int. Symp. on Numerical Models in Geomechanics (NUMOG VIII)*, 115–121, in G. N. Pande & S. Pietruszczak (eds.), Rome.
- ZHAO, J.D., SHENG, D.C., ROUAINIA, M. & SLOAN, S.W. (2005). Explicit stress integration of complex soil models. *Int. J. for Numerical and Analytical Methods in Geomechanics*, **29** (12), 1209–1229.
- ZHOU, C., YIN, J.H., ZHU, J.G. & CHENG, C.M. (2006). Elastic anisotropic viscoplastic modeling of the strain-rate dependent stress-strain behaviour of k₀-consolidated natural marine clays in triaxial shear test. *Int. J. Geomech*, **5**(3), 218–232.
- ZIEGLER, H. (1983). *An introduction to thermomechanics*. North Holland, Amsterdam.
- ZIENKIEWICZ, O. & PANDE, G. (1977). Time-dependent multilaminate model of rocks - a numerical study of deformation and failure of rock masses. *International Journal for Numerical and Analytical Methods in Geomechanics*, **1**(3), 219–247.

Appendix A

Definitions in general stress space

The generalization of the constitutive models used in this thesis can be performed in general stress space by using the following definitions.

Stress vector $\underline{\sigma}'$ is defined as:

$$\underline{\sigma}' = \left\{ \begin{array}{c} \sigma'_{xx} \\ \sigma'_{yy} \\ \sigma'_{zz} \\ \sigma'_{xy} \\ \sigma'_{yz} \\ \sigma'_{zx} \end{array} \right\} \quad (\text{A.1})$$

Mean effective stress p' is defined as:

$$p' = \frac{1}{3} (\sigma'_{xx} + \sigma'_{yy} + \sigma'_{zz}) \quad (\text{A.2})$$

Deviator stress vector $\underline{\sigma}'_d$ is defined as:

$$\underline{\sigma}'_d = \left\{ \begin{array}{c} \sigma'_{xx} - p' \\ \sigma'_{yy} - p' \\ \sigma'_{zz} - p' \\ \sqrt{2}\sigma'_{xy} \\ \sqrt{2}\sigma'_{yz} \\ \sqrt{2}\sigma'_{zx} \end{array} \right\} \quad (\text{A.3})$$

strain increment vector $\Delta\underline{\epsilon}$ is defined as:

$$\Delta\underline{\epsilon} = \begin{Bmatrix} \Delta\epsilon_{xx} \\ \Delta\epsilon_{yy} \\ \Delta\epsilon_{zz} \\ \Delta\epsilon_{xy} \\ \Delta\epsilon_{yz} \\ \Delta\epsilon_{zx} \end{Bmatrix} \quad (\text{A.4})$$

Deviatoric strain increment vector $\Delta\bar{\epsilon}_d$ is defined as:

$$\Delta\underline{\epsilon}_d = \begin{Bmatrix} \frac{1}{3}(2\Delta\epsilon_{xx} - \Delta\epsilon_{yy} - \Delta\epsilon_{zz}) \\ \frac{1}{3}(2\Delta\epsilon_{yy} - \Delta\epsilon_{xx} - \Delta\epsilon_{zz}) \\ \frac{1}{3}(2\Delta\epsilon_{zz} - \Delta\epsilon_{yy} - \Delta\epsilon_{xx}) \\ \frac{1}{\sqrt{2}}\Delta\epsilon_{xy} \\ \frac{1}{\sqrt{2}}\Delta\epsilon_{yz} \\ \frac{1}{\sqrt{2}}\Delta\epsilon_{zx} \end{Bmatrix} \quad (\text{A.5})$$

Volumetric strain increment $\Delta\epsilon_v$ is defined as:

$$\Delta\epsilon_v = \Delta\epsilon_{xx} + \Delta\epsilon_{yy} + \Delta\epsilon_{zz} \quad (\text{A.6})$$

Deviatoric fabric tensor $\bar{\alpha}_d$ is defined as:

$$\underline{\alpha}_d = \begin{Bmatrix} \alpha_{xx} - 1 \\ \alpha_{yy} - 1 \\ \alpha_{zz} - 1 \\ \sqrt{2}\alpha_{xy} \\ \sqrt{2}\alpha_{yz} \\ \sqrt{2}\alpha_{zx} \end{Bmatrix} \quad (\text{A.7})$$

where components of fabric tensor have the property:

$$\frac{1}{3}(\alpha_{xx} + \alpha_{yy} + \alpha_{zz}) = 1 \quad (\text{A.8})$$

The scalar value of fabric tensor, α , which defines the orientation of the yield surface in the triaxial space can be defined as:

$$\alpha^2 = \frac{3}{2}\{\bar{\alpha}_d\}^T\{\bar{\alpha}_d\} \quad (\text{A.9})$$

The scalar value of $\Delta\epsilon_d^p$ is defined as:

$$\Delta\epsilon_d^p = \sqrt{\frac{3}{2} \{\Delta\epsilon_d^p\}^T \{\Delta\epsilon_d^p\}} \quad (\text{A.10})$$

where the superscript p refers to plastic component.

The second $(J_2)_\alpha$ and third $(J_3)_\alpha$ invariants of the modified stress deviator $\underline{\sigma}'_d - \underline{\alpha}_d p'$ are defined as follows:

$$\begin{aligned} (J_2)_\alpha = \frac{1}{2} & \left[(\sigma'_{xx} - (1 + \alpha_{xx}^d)p')^2 + (\sigma'_{yy} - (1 + \alpha_{yy}^d)p')^2 + \right. \\ & (\sigma'_{zz} - (1 + \alpha_{zz}^d)p')^2 \\ & \left. + (\sigma'_{xy} - \alpha_{xy}^d p')^2 + (\sigma'_{yz} - \alpha_{yz}^d p')^2 + (\sigma'_{zx} - \alpha_{zx}^d p')^2 \right] \end{aligned} \quad (\text{A.11})$$

$$\begin{aligned} (J_3)_\alpha = & (\sigma'_{xx} - (1 + \alpha_{xx}^d)p')(\sigma'_{yy} - (1 + \alpha_{yy}^d)p')(\sigma'_{zz} - (1 + \alpha_{zz}^d)p') - \\ & (\sigma'_{xx} - (1 + \alpha_{xx}^d)p')(\sigma'_{zx} - \alpha_{zx}^d p')^2 - \\ & (\sigma'_{yy} - (1 + \alpha_{yy}^d)p')(\sigma'_{yz} - \alpha_{yz}^d p')^2 - \\ & (\sigma'_{zz} - (1 + \alpha_{zz}^d)p')(\sigma'_{xy} - \alpha_{xy}^d p')^2 + \\ & 2(\sigma'_{zx} - \alpha_{zx}^d p')(\sigma'_{yz} - \alpha_{yz}^d p')(\sigma'_{xy} - \alpha_{xy}^d p') \end{aligned} \quad (\text{A.12})$$

Appendix B

Derivatives of S-CLAY1S

The yield function of S-CLAY1S model in general space can be written as:

$$f_y = \frac{3}{2} \frac{\bar{q}}{(M^2(\theta)_\alpha - \alpha^2)} + (p' - \frac{p'_m}{2})^2 - \left(\frac{p'_m}{2}\right)^2 = 0 \quad (\text{B.1})$$

$$\bar{q} = \bar{s}_{ij} : \bar{s}_{ij} = \bar{s}_{xx}^2 + \bar{s}_{yy}^2 + \bar{s}_{zz}^2 + \bar{s}_{xy}^2 + \bar{s}_{yz}^2 + \bar{s}_{zx}^2 \quad (\text{B.2})$$

$$\bar{s}_{ij} = \underline{\sigma}'_d - \underline{\alpha}_d p' \quad (\text{B.3})$$

$$\frac{\partial f_y}{\partial \sigma_{ij}} = \frac{\partial f_y}{\partial p'} \frac{\partial p'}{\partial \sigma'_{ij}} + \frac{\partial f_y}{\partial \bar{q}} \frac{\partial \bar{q}}{\partial \sigma'_{ij}} + \frac{\partial f_y}{\partial \alpha} \frac{\partial \alpha}{\partial \alpha_d} \frac{\partial \alpha_d}{\partial \sigma'_{ij}} + \frac{\partial f_y}{\partial M(\theta)_\alpha} \frac{\partial M(\theta)_\alpha}{\partial \sigma'_{ij}} \quad (\text{B.4})$$

$$\frac{\partial f_y}{\partial p'} = \frac{3}{2} \frac{1}{(M^2(\theta)_\alpha - \alpha^2)} \frac{\partial \bar{q}}{\partial p'} + 2(p' - \frac{p'_m}{2}) \quad (\text{B.5})$$

$$\begin{aligned} \frac{\partial \bar{q}}{\partial p'} = -2 \left(\bar{s}_{xx}(1 + \alpha_{xx}) + \bar{s}_{yy}(1 + \alpha_{yy}) + \bar{s}_{zz}(1 + \alpha_{zz}) + \right. \\ \left. \sqrt{2} \bar{s}_{xy} \alpha_{xy} + \sqrt{2} \bar{s}_{yz} \alpha_{yz} + \sqrt{2} \bar{s}_{zx} \alpha_{zx} \right) \end{aligned} \quad (\text{B.6})$$

$$\frac{\partial p'}{\partial \sigma_{ij}} = \frac{1}{3} [1 \quad 1 \quad 1 \quad 0 \quad 0 \quad 0] \quad (\text{B.7})$$

$$\frac{\partial f_y}{\partial \bar{q}} = \frac{3}{2} \frac{1}{(M^2(\theta)_\alpha - \alpha^2)} \quad (\text{B.8})$$

$$\frac{\partial \bar{q}}{\partial \sigma'_{xx}} = \frac{2}{3} \left(3\bar{s}_{xx} - \bar{s}_{xx}(1 + \alpha_{xx}) - \bar{s}_{yy}(1 + \alpha_{yy}) - \bar{s}_{zz}(1 + \alpha_{zz}) - \sqrt{2}\bar{s}_{xy}\alpha_{xy} - \sqrt{2}\bar{s}_{yz}\alpha_{yz} - \sqrt{2}\bar{s}_{zx}\alpha_{zx} \right) \quad (\text{B.9})$$

$$\frac{\partial \bar{q}}{\partial \sigma'_{yy}} = \frac{2}{3} \left(3\bar{s}_{yy} - \bar{s}_{xx}(1 + \alpha_{xx}) - \bar{s}_{yy}(1 + \alpha_{yy}) - \bar{s}_{zz}(1 + \alpha_{zz}) - \sqrt{2}\bar{s}_{xy}\alpha_{xy} - \sqrt{2}\bar{s}_{yz}\alpha_{yz} - \sqrt{2}\bar{s}_{zx}\alpha_{zx} \right) \quad (\text{B.10})$$

$$\frac{\partial \bar{q}}{\partial \sigma'_{zz}} = \frac{2}{3} \left(3\bar{s}_{zz} - \bar{s}_{xx}(1 + \alpha_{xx}) - \bar{s}_{yy}(1 + \alpha_{yy}) - \bar{s}_{zz}(1 + \alpha_{zz}) - \sqrt{2}\bar{s}_{xy}\alpha_{xy} - \sqrt{2}\bar{s}_{yz}\alpha_{yz} - \sqrt{2}\bar{s}_{zx}\alpha_{zx} \right) \quad (\text{B.11})$$

$$\frac{\partial \bar{q}}{\partial \sigma'_{xy}} = 2\sqrt{2}\bar{s}_{xy} \quad (\text{B.12})$$

$$\frac{\partial \bar{q}}{\partial \sigma'_{yz}} = 2\sqrt{2}\bar{s}_{yz} \quad (\text{B.13})$$

$$\frac{\partial \bar{q}}{\partial \sigma'_{zx}} = 2\sqrt{2}\bar{s}_{zx} \quad (\text{B.14})$$

$$\frac{\partial \alpha_d}{\partial \sigma'_{ij}} = 0 \quad (\text{B.15})$$

So,

$$\frac{\partial f_y}{\partial \alpha} \frac{\partial \alpha}{\partial \alpha_d} \frac{\partial \alpha_d}{\partial \sigma'_{ij}} = 0 \quad (\text{B.16})$$

$$\frac{\partial f_y}{\partial M(\theta)_\alpha} = -3 \frac{\bar{q}}{(M^2(\theta)_\alpha - \alpha^2)^2} M(\theta)_\alpha \quad (\text{B.17})$$

$$\frac{\partial M(\theta)_\alpha}{\partial \sigma'_{ij}} = \frac{\sqrt{27}}{8} M_c (1 - m^4) \frac{(2m^4)^{\frac{1}{4}}}{\left(1 + m^4 - (1 - m^4) \left[\frac{\sqrt{27}}{2} \frac{(J_3)_\alpha}{(J_2)_\alpha} \right] \right)^{\frac{5}{4}}} \frac{\partial \left[\frac{(J_3)_\alpha}{(J_2)_\alpha} \right]}{\partial \sigma'_{ij}} \quad (\text{B.18})$$

$$\frac{\partial \left[\frac{(J_3)_\alpha}{(J_2)_\alpha} \right]}{\partial \sigma'_{ij}} = \frac{(J_2)_\alpha^{\frac{3}{2}} \frac{\partial (J_3)_\alpha}{\partial \sigma'_{ij}} - \frac{3}{2} (J_2)_\alpha^{\frac{1}{2}} (J_3)_\alpha \frac{\partial (J_2)_\alpha}{\partial \sigma'_{ij}}}{(J_2)_\alpha^3} \quad (\text{B.19})$$

$$\frac{\partial(J_2)_\alpha}{\partial\sigma'_{xx}} = \bar{s}_{xx} - \frac{1}{3} \left[\bar{s}_{xx}(1 + \alpha_{xx}^d) + \bar{s}_{yy}(1 + \alpha_{yy}^d) + \bar{s}_{zz}(1 + \alpha_{zz}^d) + \bar{s}_{xy}\alpha_{xy}^d + \bar{s}_{yz}\alpha_{yz}^d + \bar{s}_{zx}\alpha_{zx}^d \right] \quad (\text{B.20})$$

$$\begin{aligned} \frac{\partial(J_3)_\alpha}{\partial\sigma'_{xx}} = \bar{s}_{yy}\bar{s}_{zz} - \frac{1}{3} \left[\bar{s}_{yy}\bar{s}_{zz}(1 + \alpha_{xx}^d) + \bar{s}_{xx}\bar{s}_{zz}(1 + \alpha_{yy}^d) + \bar{s}_{xx}\bar{s}_{yy}(1 + \alpha_{zz}^d) \right] \\ - \bar{s}_{zx}^2 + \frac{1}{3} \left[\bar{s}_{zx}^2(1 + \alpha_{xx}^d) + \bar{s}_{yz}^2(1 + \alpha_{yy}^d) + \bar{s}_{xy}^2(1 + \alpha_{zz}^d) \right] \\ + \frac{2}{3} \left[\bar{s}_{xx}\bar{s}_{zx}\alpha_{zx}^d + \bar{s}_{yy}\bar{s}_{yz}\alpha_{yz}^d + \bar{s}_{zz}\bar{s}_{xy}\alpha_{xy}^d \right] \\ - \frac{2}{3} \left[\bar{s}_{yz}\bar{s}_{zx}\alpha_{xy}^d + \bar{s}_{xy}\bar{s}_{zx}\alpha_{yz}^d + \bar{s}_{yz}\bar{s}_{xy}\alpha_{zx}^d \right] \end{aligned} \quad (\text{B.21})$$

Similarly other derivative components can be derived.

$$\frac{\partial f_y}{\partial\bar{s}_{ij}} = \frac{\partial f_y}{\partial\bar{q}} \frac{\partial\bar{q}}{\partial\bar{s}_{ij}} + \frac{\partial f_y}{\partial M(\theta)_\alpha} \frac{\partial M(\theta)_\alpha}{\partial\bar{s}_{ij}} \quad (\text{B.22})$$

$$\frac{\partial f_y}{\partial\bar{q}} = \frac{\bar{3}}{2(M^2(\theta)_\alpha - \alpha^2)} \quad (\text{B.23})$$

$$\frac{\partial\bar{q}}{\partial\bar{s}_{ij}} = 2\bar{s}_{ij} \quad (\text{B.24})$$

$$\frac{\partial M(\theta)_\alpha}{\partial\bar{s}_{ij}} = \frac{\sqrt{27}}{8} M_c(1 - m^4) \frac{(2m^4)^{\frac{1}{4}}}{\left(1 + m^4 - (1 - m^4) \left[\frac{\sqrt{27}}{2} \frac{(J_3)_\alpha}{(J_2)_\alpha^{\frac{3}{2}}} \right] \right)^{\frac{5}{4}}} \frac{\partial \left[\frac{(J_3)_\alpha}{(J_2)_\alpha^{\frac{3}{2}}} \right]}{\partial\bar{s}_{ij}} \quad (\text{B.25})$$

$$\frac{\partial \left[\frac{(J_3)_\alpha}{(J_2)_\alpha^{\frac{3}{2}}} \right]}{\partial\bar{s}_{ij}} = \frac{(J_2)_\alpha^{\frac{3}{2}} \frac{\partial(J_3)_\alpha}{\partial\bar{s}_{ij}} - \frac{3}{2} (J_2)_\alpha^{\frac{1}{2}} (J_3)_\alpha \frac{\partial(J_2)_\alpha}{\partial\bar{s}_{ij}}}{(J_2)_\alpha^3} \quad (\text{B.26})$$

$$\frac{\partial(J_2)_\alpha}{\partial\bar{s}_{xx}} = \bar{s}_{xx} \quad (\text{B.27})$$

$$\frac{\partial(J_3)_\alpha}{\partial\bar{s}_{xx}} = \bar{s}_{yy}\bar{s}_{zz} - \bar{s}_{zx}^2 \quad (\text{B.28})$$

Similarly other derivatives components can be derived.

$$\frac{\partial f_y}{\partial \alpha_{ij}^d} = \frac{\partial f_y}{\partial \bar{q}} \frac{\partial \bar{q}}{\partial \alpha_{ij}^d} + \frac{\partial f_y}{\partial M(\theta)_\alpha} \frac{\partial M(\theta)_\alpha}{\partial \alpha_{ij}^d} \quad (\text{B.29})$$

$$\frac{\partial \bar{q}}{\partial \alpha_{ij}^d} = -2\bar{s}_{ij}p' \quad (\text{B.30})$$

$$\frac{\partial M(\theta)_\alpha}{\partial \alpha_{ij}^d} = \frac{\sqrt{27}}{8} M_c (1 - m^4) \frac{(2m^4)^{\frac{1}{4}}}{\left(1 + m^4 - (1 - m^4) \left[\frac{\sqrt{27}}{2} \frac{(J_3)_\alpha}{(J_2)_\alpha} \right] \right)^{\frac{5}{4}}} \frac{\partial \left[\frac{(J_3)_\alpha}{(J_2)_\alpha} \right]}{\partial \alpha_{ij}^d} \quad (\text{B.31})$$

$$\frac{\partial \left[\frac{(J_3)_\alpha}{(J_2)_\alpha} \right]}{\partial \alpha_{ij}^d} = \frac{(J_2)_\alpha^{\frac{3}{2}} \frac{\partial (J_3)_\alpha}{\partial \alpha_{ij}^d} - \frac{3}{2} (J_2)_\alpha^{\frac{1}{2}} (J_3)_\alpha \frac{\partial (J_2)_\alpha}{\partial \alpha_{ij}^d}}{(J_2)_\alpha^3} \quad (\text{B.32})$$

$$\frac{\partial (J_2)_\alpha}{\partial \alpha_{xx}^d} = -\bar{s}_{xx}p' \quad (\text{B.33})$$

$$\frac{\partial (J_3)_\alpha}{\partial \alpha_{xx}^d} = -\bar{s}_{yy}\bar{s}_{zz}p' + \bar{s}_{zx}^2 p' \quad (\text{B.34})$$

Similarly other derivatives components can be derived.

$$\frac{\partial f_y}{\partial \chi} = \frac{\partial f_y}{\partial p'_m} \frac{\partial p'_m}{\partial \chi} \quad (\text{B.35})$$

$$\frac{\partial f_y}{\partial p'_m} = -p' \quad (\text{B.36})$$

$$\frac{\partial p'_m}{\partial \chi} = p'_{mi} \quad (\text{B.37})$$

$$\frac{\partial \alpha_d}{\partial \epsilon_v^p} = \mu \left(\frac{3\sigma'_d}{4p'} - \alpha_d \right) \quad (\text{B.38})$$

$$\frac{\partial \alpha_{ij}^d}{\partial \epsilon_d^p} = \beta \mu \left(\frac{3\sigma'_d}{4p'} - \alpha_d \right) \quad (\text{B.39})$$

$$\frac{\partial \chi}{\partial \epsilon_v^p} = -a\chi \tag{B.40}$$

$$\frac{\partial \chi}{\partial \epsilon_d^p} = -ab\chi \tag{B.41}$$

$$\frac{\partial p'_{mi}}{\partial \epsilon_v^p} = \frac{(1+e)p'_{mi}}{\lambda - \kappa} \tag{B.42}$$

Appendix C

The SO model

$$\eta_{ij}^T = \begin{pmatrix} -\frac{1 - K_0^{nc}}{2 + 2K_0^{nc}} & 2\frac{1 - K_0^{nc}}{2 + 2K_0^{nc}} & -\frac{1 - K_0^{nc}}{2 + 2K_0^{nc}} & 0 & 0 & 0 \end{pmatrix} \quad (\text{C.1})$$

$$\bar{s} = \begin{bmatrix} \sigma'_{xx} - p' - p'\eta_{xx} \\ \sigma'_{yy} - p' - p'\eta_{yy} \\ \sigma'_{zz} - p' - p'\eta_{zz} \\ \sigma'_{xy} - p'\eta_{xy} \\ \sigma'_{yz} - p'\eta_{yz} \\ \sigma'_{zx} - p'\eta_{zx} \end{bmatrix} \quad (\text{C.2})$$

$$\bar{J}_2 = \frac{1}{2} \left(\bar{s}_{xx}^2 + \bar{s}_{yy}^2 + \bar{s}_{zz}^2 \right) + \bar{s}_{xy}^2 + \bar{s}_{yz}^2 + \bar{s}_{zx}^2 \quad (\text{C.3})$$

$$\bar{q} = \sqrt{3\bar{J}_2} \quad (\text{C.4})$$

$$\frac{\partial \bar{q}}{\partial \sigma'} = \frac{3}{2\bar{q}} \frac{\partial \bar{J}_2}{\partial \sigma'} \quad (\text{C.5})$$

$$\begin{aligned} \frac{\partial \bar{J}_2}{\partial \sigma'_{xx}} = & (\sigma'_{xx} - p' - p'\eta_{xx}) \frac{(2 - \eta_{xx})}{3} + (\sigma'_{yy} - p' - p'\eta_{yy}) \frac{(-1 - \eta_{yy})}{3} + \\ & (\sigma'_{zz} - p' - p'\eta_{zz}) \frac{(-1 - \eta_{zz})}{3} + 2(\sigma'_{xy} - p'\eta_{xy}) \frac{(-\eta_{xy})}{3} + \\ & 2(\sigma'_{yz} - p'\eta_{yz}) \frac{(-\eta_{yz})}{3} + 2(\sigma'_{zx} - p'\eta_{zx}) \frac{(-\eta_{zx})}{3} \end{aligned} \quad (\text{C.6})$$

$$\begin{aligned} \frac{\partial \bar{J}_2}{\partial \sigma'_{yy}} = & (\sigma'_{xx} - p' - p'\eta_{xx}) \frac{(-1 - \eta_{xx})}{3} + (\sigma'_{yy} - p' - p'\eta_{yy}) \frac{(2 - \eta_{yy})}{3} + \\ & (\sigma'_{zz} - p' - p'\eta_{zz}) \frac{(-1 - \eta_{zz})}{3} + 2(\sigma'_{xy} - p'\eta_{xy}) \frac{(-\eta_{xy})}{3} + \\ & 2(\sigma'_{yz} - p'\eta_{yz}) \frac{(-\eta_{yz})}{3} + 2(\sigma'_{zx} - p'\eta_{zx}) \frac{(-\eta_{zx})}{3} \end{aligned} \quad (\text{C.7})$$

$$\begin{aligned} \frac{\partial \bar{J}_2}{\partial \sigma'_{zz}} = & (\sigma'_{xx} - p' - p'\eta_{xx}) \frac{(-1 - \eta_{xx})}{3} + (\sigma'_{yy} - p' - p'\eta_{yy}) \frac{(-1 - \eta_{yy})}{3} + \\ & (\sigma'_{zz} - p' - p'\eta_{zz}) \frac{(2 - \eta_{zz})}{3} + 2(\sigma'_{xy} - p'\eta_{xy}) \frac{(-\eta_{xy})}{3} + \\ & 2(\sigma'_{yz} - p'\eta_{yz}) \frac{(-\eta_{yz})}{3} + 2(\sigma'_{zx} - p'\eta_{zx}) \frac{(-\eta_{zx})}{3} \end{aligned} \quad (\text{C.8})$$

$$\frac{\partial \bar{J}_2}{\partial \sigma'_{xy}} = 2(\sigma'_{xy} - p'\eta_{xy}) \quad (\text{C.9})$$

$$\frac{\partial \bar{J}_2}{\partial \sigma'_{yz}} = 2(\sigma'_{yz} - p'\eta_{yz}) \quad (\text{C.10})$$

$$\frac{\partial \bar{J}_2}{\partial \sigma'_{zx}} = 2(\sigma'_{zx} - p'\eta_{zx}) \quad (\text{C.11})$$

Appendix D

Determination of SO models parameters

A determination procedure for input parameters to the SO models is detailed by Iizuka & Ohta (1987). In this section, the determination procedure of input parameters to be used in SO models is summarized.

D.0.4 SO inviscid model parameters

The SO inviscid model requires a total of seven parameters. These parameters with their standard units are listed below:

Modified compression index and modified swelling index

These parameters can be obtained from an isotropic compression test including isotropic unloading. When plotting the logarithm of the mean stress as a function of the volumetric strain for clay type materials, the plot can be approximated by two straight lines. The slope of the primary loading line gives the modified compression index, and the slope of the unloading (or swelling) line gives the modified swelling index.

parameter		description	unit
λ^*	:	Modified compression index	[-]
κ^*	:	Modified swelling index	[-]
ν'	:	Poisson's ratio	[-]
K_0^{NC}	:	Earth pressure coefficient at rest	[-]
M	:	Slope of critical state line	[-]
OCR_0	:	Initial overconsolidation ratio	[-]
POP_0	:	Initial pre-overburden pressure	[kN/m^2]

Poisson's ratio

The Poisson's ratio (ν') is a real elastic parameter and not a pseudo-elasticity constant as used in the Mohr-Coulomb model. Its value will usually be in the range between 0.1 and 0.2.

K_0^{nc} -parameter

K_0^{nc} is defined as a stress ratio in a state of normal consolidation.

$$K_0^{nc} = \frac{\sigma'_{xx}}{\sigma'_{yy}} \quad (D.1)$$

Slope of the critical state line

In order to obtain the correct shear strength, the parameter M should be based on the friction angle ϕ . The critical state line is comparable with Drucker-Prager failure line, and represents a (circular) cone in principal stress space. Hence, the value of M can be obtained from ϕ in a similar way as the Drucker-Prager friction constant α is obtained from ϕ .

Initial overconsolidation ratio

The initial overconsolidation ratio OCR_0 is defined as the highest stress experienced divided by the current stress. A soil which is currently experiencing its highest stress is said to be normally consolidated and to have an OCR of one.

Initial pre-overburden pressure

The initial pre-overburden pressure POP_0 is defined as:

$$POP_0 = \sigma'_p - \sigma'_{yy}$$

where σ'_p is the pre-consolidation stress (the greatest vertical stress reached previously) and σ'_{yy} is the in situ effective vertical stress.

D.0.5 SO viscid model parameters

Compared to the SO inviscid model, the SO viscid model requires two additional parameters as input: C_α and \dot{v}_0 . All other parameters remain the same as in the SO inviscid model. The input two additional parameters of viscid model are listed below:

parameter		description	unit
C_α	:	Coefficient of secondary compression	[-]
\dot{v}_0	:	Initial volumetric strain rate	[day^{-1}]

Coefficient of secondary compression

The coefficient of secondary compression C_α is expressed as:

$$C_\alpha = \frac{d\epsilon_v}{d(\ln t)}$$

at time t_c . Mesri & Godlewski (1977) proposed a correlation to find $C_{\alpha,e}$ for clay and peat as:

$$C_{\alpha,e}/\lambda = 0.05 \pm 0.02 \quad (\text{clay}) \qquad C_{\alpha,e}/\lambda = 0.07 \pm 0.02 \quad (\text{peat})$$

where C_α and $C_{\alpha,e}$ are correlated by Sekiguchi & Ohta (1977) as follows:

$$C_\alpha = \frac{C_{\alpha,e}}{1 + e_0}$$

Initial volumetric strain rate

The physical meaning of initial volumetric strain rate is obvious (Sekiguchi, 1984), but it is rather difficult to estimate from the laboratory test data. The initial volumetric strain rate at reference state is expressed as:

$$\dot{v}_0 = \frac{C_\alpha}{t_c}$$

where t_c is the time at the end of primary consolidation. t_c can be derived (Sekiguchi & Ohta, 1977) as:

$$t_c \approx t_{90} = \frac{H^2 T_v(90\%)}{c_v}$$

where C_v is coefficient of consolidation has dimensions $L^2 T^{-1}$. H is the drainage distance and $T_v(90\%)$ is the nondimensional time factor. Time factor $T_v(90\%)$ is constant using

The following equations are summarized from Iizuka & Ohta (1987) to determine the coefficient of consolidation C_v .

$$m_v = \frac{3\lambda}{(1 + e_0)(1 + 2K_0)\sigma'_{v0}}$$

$$C_v = \frac{k}{m_v \gamma_w}$$

$$\log C_v (cm^2/min) = -0.025PI - 0.25 \pm 1$$

Appendix E

Derivatives of B-SCLAY1S

The derivatives related to the bubble surface is detailed in this section.

if we set $\bar{Q} = (\bar{s} - \bar{s}_b) : (\bar{s} - \bar{s}_b)$, then bubble surface of B-SCLAY1S model become:

$$f_b = \frac{3}{2} \frac{\bar{Q}}{M^2 - \alpha^2} + (p' - p'_b)^2 - R^2 \left(\frac{p'_m}{2} \right)^2 = 0 \quad (\text{E.1})$$

$$\begin{aligned} \bar{Q} = & (\bar{s}_{xx} - \bar{s}_{bxx})^2 + (\bar{s}_{yy} - \bar{s}_{byy})^2 + (\bar{s}_{zz} - \bar{s}_{bzz})^2 + (\bar{s}_{xy} - \bar{s}_{bxy})^2 + \\ & (\bar{s}_{yz} - \bar{s}_{byz})^2 + (\bar{s}_{zx} - \bar{s}_{bzx})^2 \end{aligned} \quad (\text{E.2})$$

$$\frac{\partial f_b}{\partial \sigma_{ij}} = \frac{\partial f_b}{\partial p'} \frac{\partial p'}{\partial \sigma_{ij}} + \frac{\partial f_b}{\partial \bar{Q}} \frac{\partial \bar{Q}}{\partial \sigma_{ij}} \quad (\text{E.3})$$

$$\frac{\partial f_b}{\partial p'} = \frac{3}{2} \frac{1}{M^2 - \alpha^2} \frac{\partial \bar{Q}}{\partial p'} + 2(p' - \frac{p'_b}{2}) \quad (\text{E.4})$$

$$\begin{aligned} \frac{\partial \bar{Q}}{\partial p'} = & -2 \left[(\bar{s}_{xx} - \bar{s}_{bxx})(1 + \alpha_{xx}) + (\bar{s}_{yy} - \bar{s}_{byy})(1 + \alpha_{yy}) + \right. \\ & (\bar{s}_{zz} - \bar{s}_{bzz})(1 + \alpha_{zz}) + \sqrt{2}(\bar{s}_{xy} - \bar{s}_{bxy})\alpha_{xy} + \\ & \left. \sqrt{2}(\bar{s}_{yz} - \bar{s}_{byz})\alpha_{yz} + \sqrt{2}(\bar{s}_{zx} - \bar{s}_{bzx})\alpha_{zx} \right] \end{aligned} \quad (\text{E.5})$$

$$\frac{\partial f_b}{\partial \bar{Q}} = \frac{3}{2} \frac{1}{M^2 - \alpha^2} \quad (\text{E.6})$$

$$\begin{aligned} \frac{\partial \bar{Q}}{\partial \sigma'_{xx}} = & 2 \left[(\bar{s}_{xx} - \bar{s}_{bxx}) - \frac{1}{3}(\bar{s}_{xx} - \bar{s}_{bxx})(1 + \alpha_{xx}) - \frac{1}{3}(\bar{s}_{yy} - \bar{s}_{byy})(1 + \alpha_{yy}) - \right. \\ & \left. \frac{1}{3}(\bar{s}_{zz} - \bar{s}_{bzz})(1 + \alpha_{zz}) - \frac{\sqrt{2}}{3}(\bar{s}_{xy} - \bar{s}_{bxy})\alpha_{xy} - \frac{\sqrt{2}}{3}(\bar{s}_{yz} - \bar{s}_{byz})\alpha_{yz} - \right. \\ & \left. \frac{\sqrt{2}}{3}(\bar{s}_{zx} - \bar{s}_{bzx})\alpha_{zx} \right] \end{aligned} \quad (\text{E.7})$$

$$\begin{aligned} \frac{\partial \bar{Q}}{\partial \sigma'_{yy}} = & 2 \left[(\bar{s}_{yy} - \bar{s}_{byy}) - \frac{1}{3}(\bar{s}_{xx} - \bar{s}_{bxx})(1 + \alpha_{xx}) - \frac{1}{3}(\bar{s}_{yy} - \bar{s}_{byy})(1 + \alpha_{yy}) - \right. \\ & \left. \frac{1}{3}(\bar{s}_{zz} - \bar{s}_{bzz})(1 + \alpha_{zz}) - \frac{\sqrt{2}}{3}(\bar{s}_{xy} - \bar{s}_{bxy})\alpha_{xy} - \frac{\sqrt{2}}{3}(\bar{s}_{yz} - \bar{s}_{byz})\alpha_{yz} - \right. \\ & \left. \frac{\sqrt{2}}{3}(\bar{s}_{zx} - \bar{s}_{bzx})\alpha_{zx} \right] \end{aligned} \quad (\text{E.8})$$

$$\begin{aligned} \frac{\partial \bar{Q}}{\partial \sigma'_{zz}} = & 2 \left[(\bar{s}_{zz} - \bar{s}_{bzz}) - \frac{1}{3}(\bar{s}_{xx} - \bar{s}_{bxx})(1 + \alpha_{xx}) - \frac{1}{3}(\bar{s}_{yy} - \bar{s}_{byy})(1 + \alpha_{yy}) - \right. \\ & \left. \frac{1}{3}(\bar{s}_{zz} - \bar{s}_{bzz})(1 + \alpha_{zz}) - \frac{\sqrt{2}}{3}(\bar{s}_{xy} - \bar{s}_{bxy})\alpha_{xy} - \frac{\sqrt{2}}{3}(\bar{s}_{yz} - \bar{s}_{byz})\alpha_{yz} - \right. \\ & \left. \frac{\sqrt{2}}{3}(\bar{s}_{zx} - \bar{s}_{bzx})\alpha_{zx} \right] \end{aligned} \quad (\text{E.9})$$

$$\frac{\partial \bar{Q}}{\partial \sigma'_{xy}} = 2\sqrt{2}(\bar{s}_{xy} - \bar{s}_{bxy}) \quad (\text{E.10})$$

$$\frac{\partial \bar{Q}}{\partial \sigma'_{yz}} = 2\sqrt{2}(\bar{s}_{yz} - \bar{s}_{byz}) \quad (\text{E.11})$$

$$\frac{\partial \bar{Q}}{\partial \sigma'_{zx}} = 2\sqrt{2}(\bar{s}_{zx} - \bar{s}_{bzx}) \quad (\text{E.12})$$

$$\frac{\partial F_b}{\partial \bar{s}} = 3 \frac{\bar{s} - \bar{s}_b}{M^2 - \alpha^2} \quad (\text{E.13})$$

Appendix F

Determination of B-SCLAY1S model parameters

Table F.1 shows the required parameters for B-SCLAY1S and their meanings.

Compression index λ & λ_i

These parameter can be obtained from an isotropic compression test. When plotting the logarithm of the mean stress as a function of the void ratio for clay type materials, the plot can be approximated by lines . The initial slope of the primary loading loading line gives the compression index as shown in Fig. F.1.

Poisson's ratio ν'

The Poisson's ratio (ν') is a real elastic parameter and not a pseudo-elasticity constant as used in the Mohr-Coulomb model. Its value will usually be in the range between 0.1 and 0.3.

Table F.1: Parameters required for the B-SCLAY1S model

λ	:	Compression index (B-SCLAY1)	[-]
λ_i	:	Intrinsic compression index (B-SCLAY1S)	[-]
κ	:	Swelling index	[-]
ν'	:	Poisson's ratio	[-]
M	:	Slope of critical state line	[-]
e_0	:	Initial void ratio	[-]
α_0	:	Initial inclination of yield surface	[-]
μ	:	Absolute effectiveness of rotational hardening	[-]
β	:	Relative effectiveness of rotational hardening	[-]
χ_0	:	Initial bonding	[-]
a	:	Absolute rate of destructuration	[-]
b	:	Relative rate of destructuration	[-]
R	:	Ratio of the size of the bubble surface to that of bounding surface	[-]
ψ	:	Exponent in the hardening function \mathcal{H}_b	[-]
OCR_0	:	Initial overconsolidation ratio	[-]
POP_0	:	Initial pre-overburden pressure	$[kN/m^2]$

K_0^{nc} -parameter

K_0^{nc} is defined as stress ratio in a state of normal consolidation.

$$K_0^{nc} = \frac{\sigma'_{xx}}{\sigma'_{yy}} \quad (F.1)$$

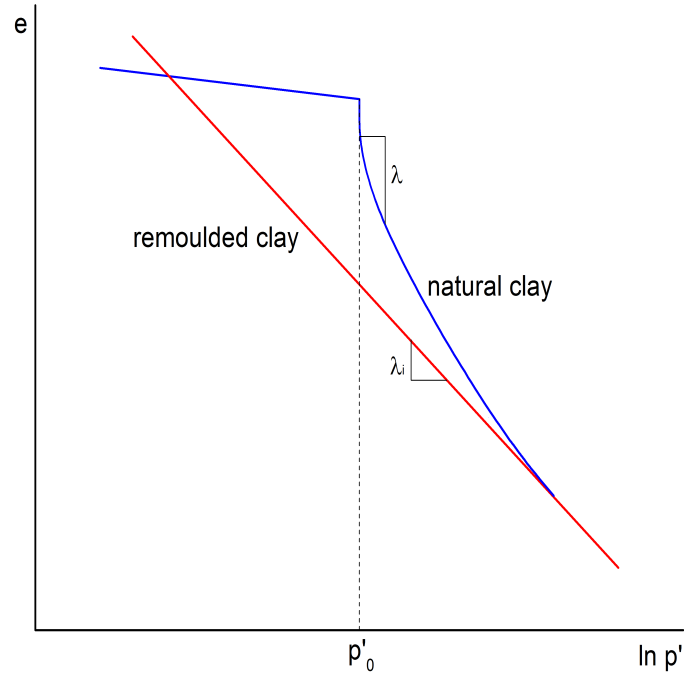


Figure F.1: The compression index of remoulded and natural soil

Initial void ratio e_0

Initial void ratio e_0 is a physical characteristic of soil sample. The e_0 is defined as follows:

$$e_0 = \frac{\text{volume of voids}}{\text{volume of solids}} \quad (\text{F.2})$$

Slope of the critical state line M

In order to obtain the correct shear strength, the parameter M should be based on the friction angle φ' . The critical state line is comparable with Drucker-Prager failure line, and represents a (circular) cone in principal stress space. Hence, the value of M can be obtained from φ' in a similar way as the Drucker-Prager friction constant α is obtained from φ' . Hence, the parameter M can be determined from the critical state soil friction angle φ' by the following expression:

$$M = \frac{6 \sin \varphi'}{3 - \sin \varphi'} \quad (\text{F.3})$$

Initial overconsolidation ratio OCR_0

The initial overconsolidation ratio OCR_0 is defined as the highest stress experienced divided by the current stress, see Eq. F.4. A soil which is currently experiencing its highest stress is said to be normally consolidated and to have an OCR of one.

$$OCR_0 = \frac{\sigma'_p}{\sigma'_{yy}} \quad (F.4)$$

Initial pre-overburden pressure

The initial pre-overburden pressure POP_0 is defined as:

$$POP_0 = \sigma'_p - \sigma'_{yy} \quad (F.5)$$

where σ'_p is the pre-consolidation stress (the greatest vertical stress reached previously) and σ'_{yy} is the in situ effective vertical stress.

Initial inclination α_0

Wheeler *et al.* (2003) described a procedure to estimate the initial inclination α_0 for normal or slightly overconsolidated soils. The initial inclination of the yield surface can be derived by following expression:

$$\alpha_0 = \frac{\eta_{K0}^2 + 3\eta_{K0} - M^2}{3} \quad (F.6)$$

M is the slope of the critical state line and η_{K0} is normally consolidated stress ratio. η_{K0} can be estimated using Jaky's empirical formula ($K_0 = 1 - \sin \varphi'$; φ' is the critical state friction angle) as following expression:

$$\eta_{K0} = \frac{\sin \varphi'}{1 - \frac{2}{3} \sin \varphi'} \quad (F.7)$$

Hence, the initial inclination of yield surface α_0 can be determined using critical state friction angle φ' of the soil.

Relative effectiveness of rotational hardening β

Model parameter β defines the relative effectiveness of plastic shear strains and plastic volumetric strains in the rotational hardening. Wheeler *et al.* (2003) suggest that the soil parameter β corresponding to the α_0 , can be calculated from the following expression:

$$\beta = \frac{3(4M^2 - 4\eta_{K0}^2 - 3\eta_{K0})}{8(\eta_{K0}^2 - M^2 - 2\eta_{K0})} \quad (\text{F.8})$$

Absolute effectiveness of rotational hardening μ

The parameter μ can not be derived through a direct method. Therefore, it can be determined through several model simulations with different values of μ compare the predicted behaviour with observed behaviour. Alternatively, it can be found from a empirical formula suggested by Zentar *et al.* (2002) as follows:

$$\mu = \frac{10 \dots 20}{\lambda} \quad (\text{F.9})$$

Initial bonding χ_0

Koskinen *et al.* (2002a) suggested a procedure for determining the initial value of χ_0 . The value of χ_0 can be best derived from the sensitivity S_t measured from a fall cone test. S_t provides an estimate for the bonding parameter χ_0 .

$$\chi_0 \approx S_t - 1 \quad (\text{F.10})$$

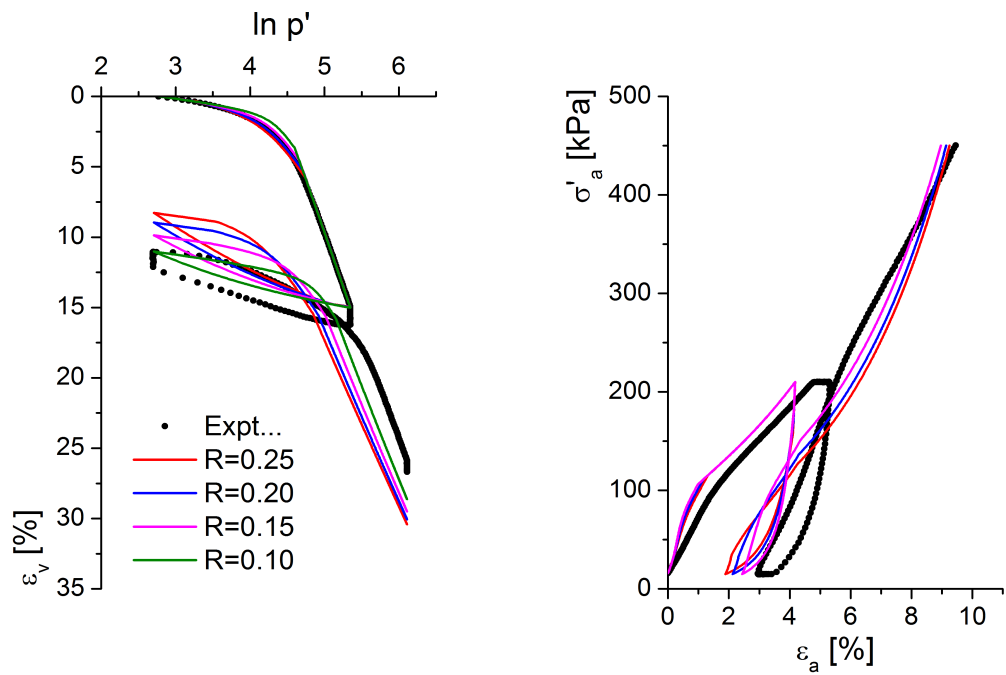
Absolute and relative rate of destructuration a, b

Koskinen *et al.* (2002a) suggested an optimization procedure using model simulations of laboratory test to derive parameters a and b . First, simulating a drained triaxial test involving a low value of η , the best value for parameter a is achieved. For example, a stress path close to isotropic compression can be chosen, where the shear strains are small and hence influence of parameter b is negligible (Krenn, 2008). The parameter b is selected through modelling test involving a high value of η where the contribution from shear strains is dominant (Krenn, 2008).

Appendix G

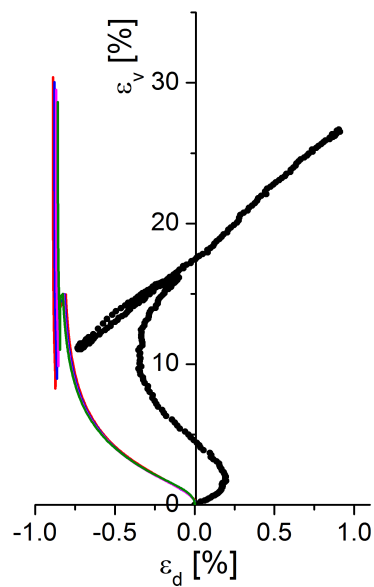
Parametric study of B-SCLAY1S

The B-SCLAY1S model simulations of triaxial tests on vertical samples (McGinty, 2006) of Bothkennar clay was used in test Series B named Test B7. The values of stress ratio η in the first and second loading stages were $\eta_1 = 0$ & $\eta_2 = 0$. Sample was first loaded isotropically from mean effective stress of $p' = 16 \text{ kPa}$ to $p' = 210 \text{ kPa}$ and then isotropically unloaded to mean effective stress of $p' = 14.8 \text{ kPa}$ and again isotropically reloaded to mean effective stress of $p' = 450 \text{ kPa}$.



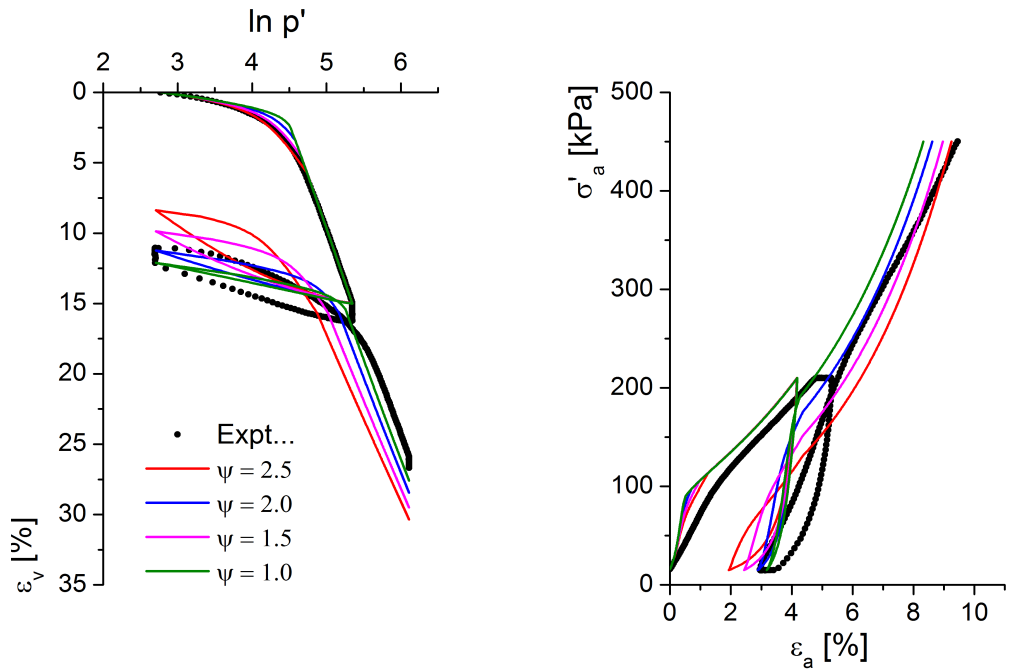
(a) compression behaviour

(b) axial stress-strain behaviour



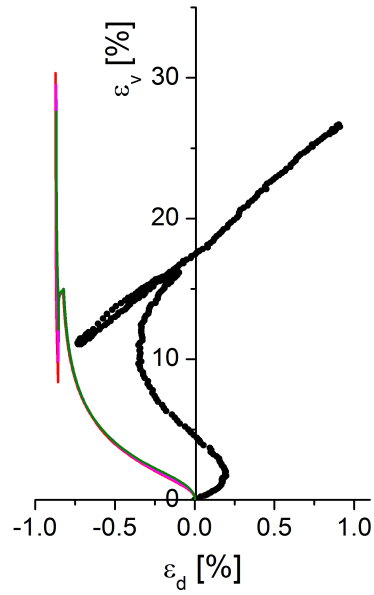
(c) strain paths

Figure G.1: Influence of bubble size R of Test B7 (McGinty, 2006) simulation, where $\eta_1 = 0$ and $\eta_2 = 0$



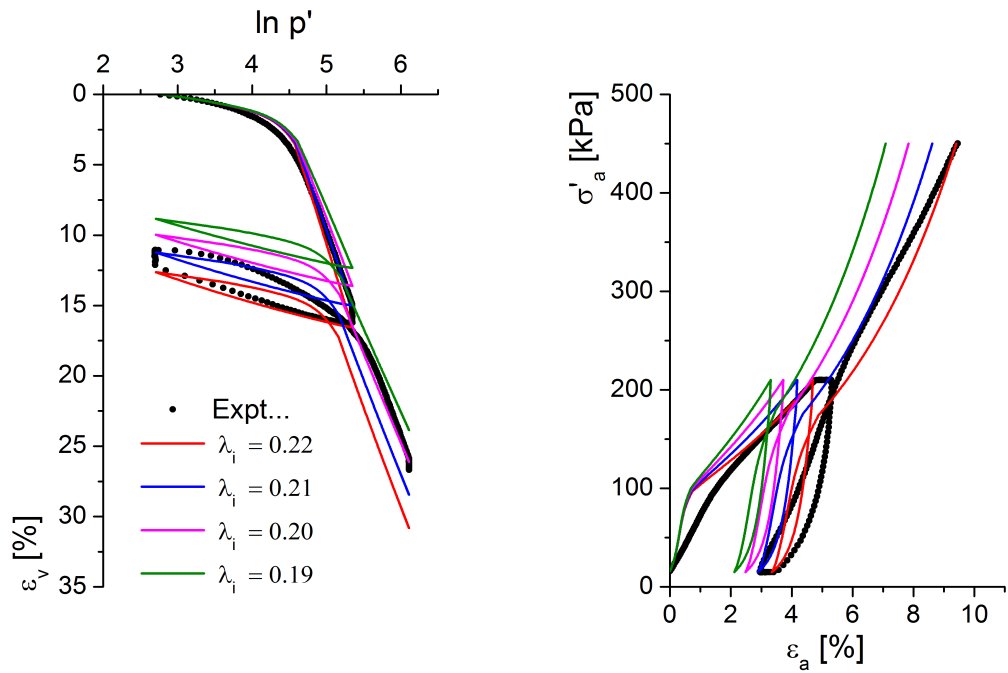
(a) compression behaviour

(b) axial stress-strain behaviour



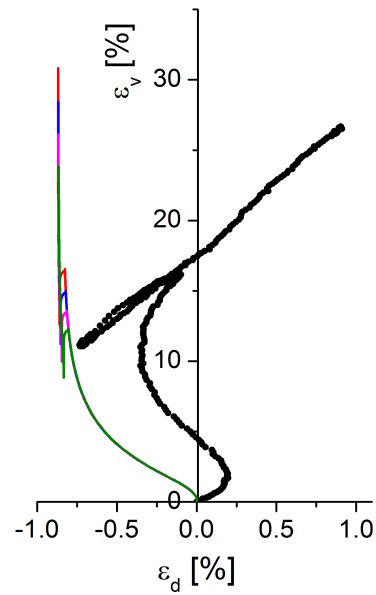
(c) strain paths

Figure G.2: Influence of hardening parameter ψ of Test B7 (McGinty, 2006) simulation, where $\eta_1 = 0$ and $\eta_2 = 0$



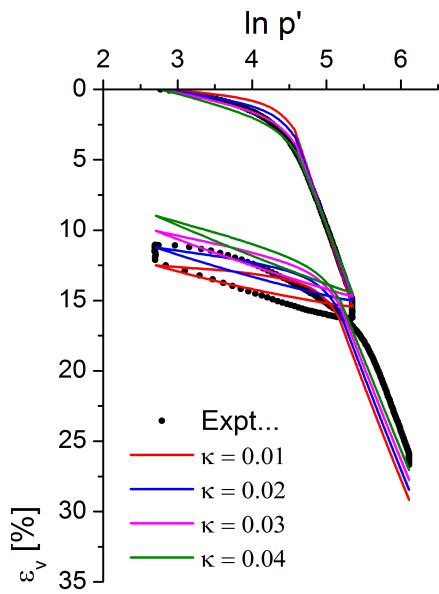
(a) compression behaviour

(b) axial stress-strain behaviour

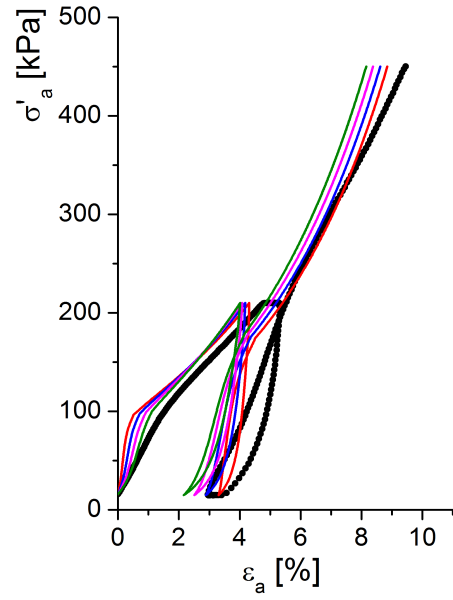


(c) strain paths

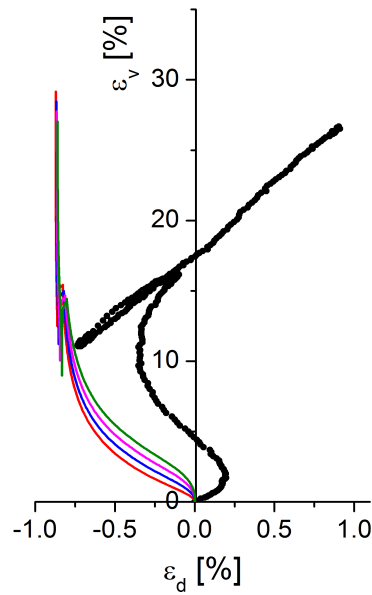
Figure G.3: Influence of intrinsic compression index λ_i of Test B7 (McGinty, 2006) simulation, where $\eta_1 = 0$ and $\eta_2 = 0$



(a) compression behaviour

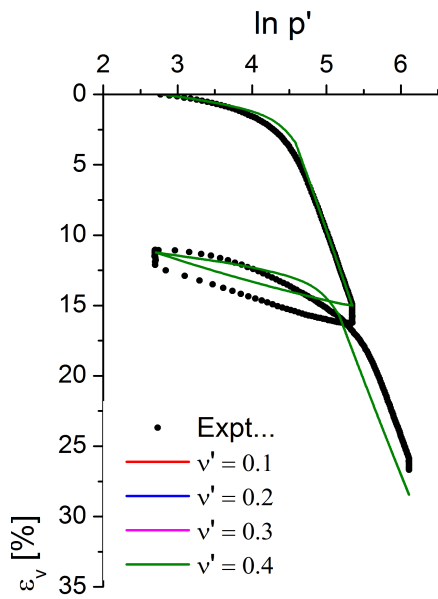


(b) axial stress-strain behaviour

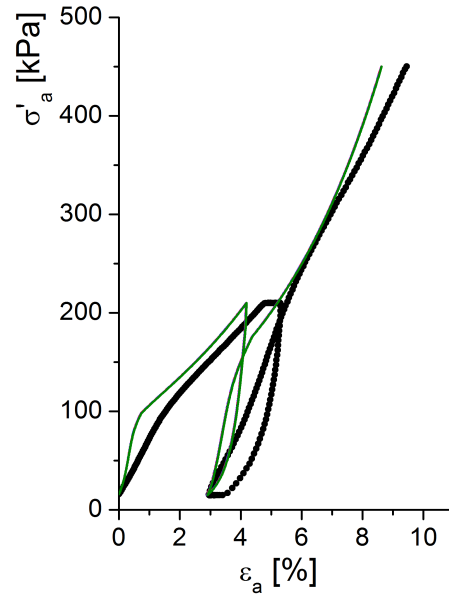


(c) strain paths

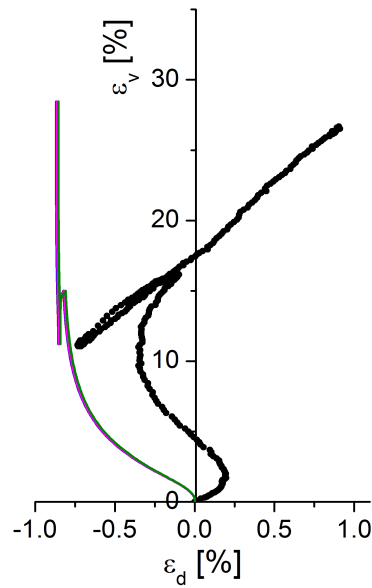
Figure G.4: Influence of swelling index κ of Test B7 (McGinty, 2006) simulation, where $\eta_1 = 0$ and $\eta_2 = 0$



(a) compression behaviour

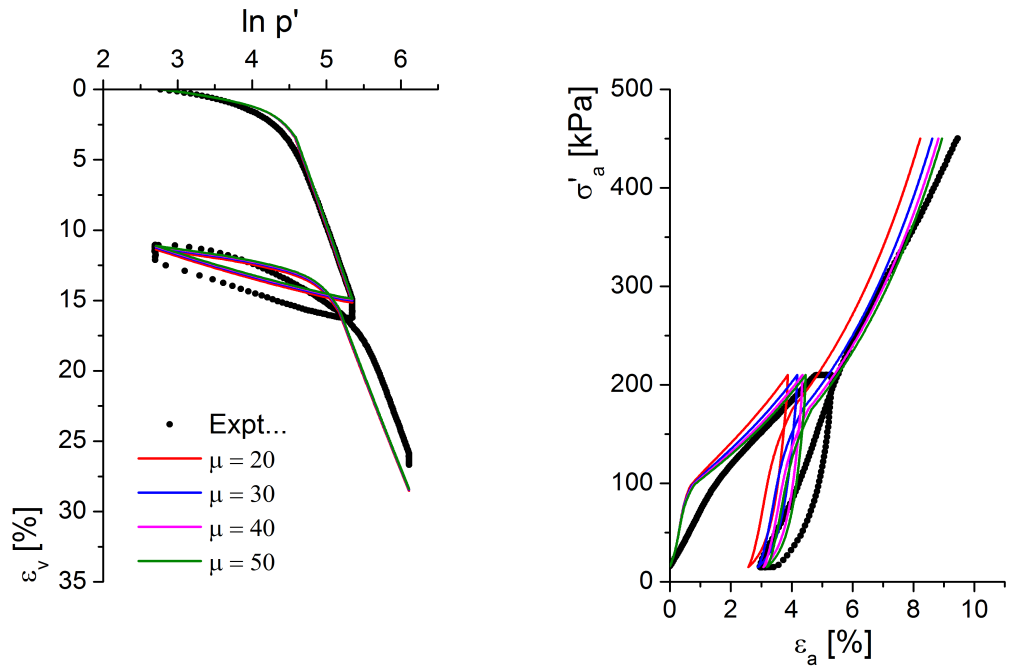


(b) axial stress-strain behaviour



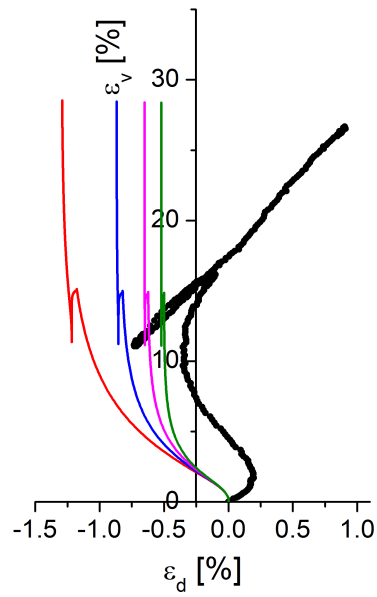
(c) strain paths

Figure G.5: Influence of Poisson's ratio ν' of Test B7 (McGinty, 2006) simulation, where $\eta_1 = 0$ and $\eta_2 = 0$



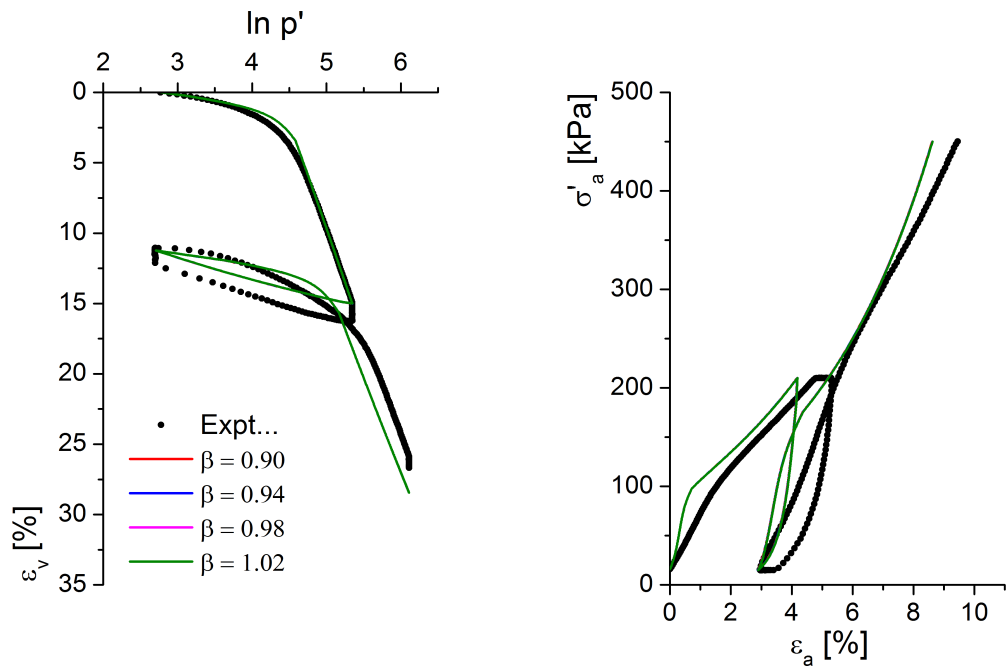
(a) compression behaviour

(b) axial stress-strain behaviour



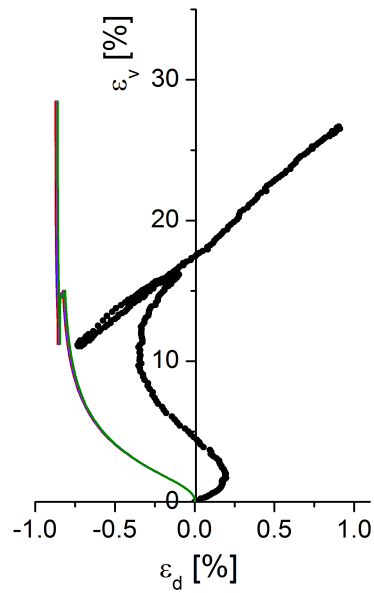
(c) strain paths

Figure G.6: Influence of anisotropy parameter μ of Test B7 (McGinty, 2006) simulation, where $\eta_1 = 0$ and $\eta_2 = 0$



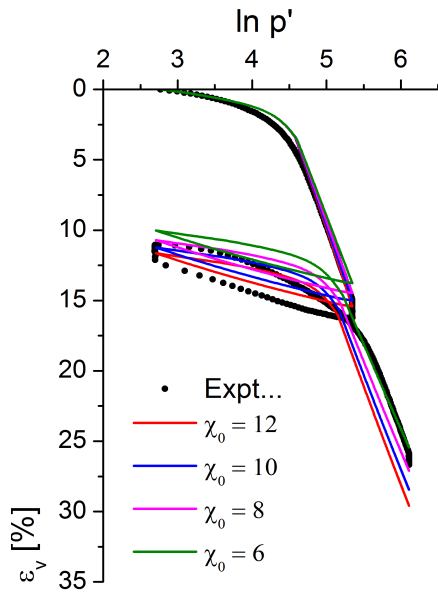
(a) compression behaviour

(b) axial stress-strain behaviour

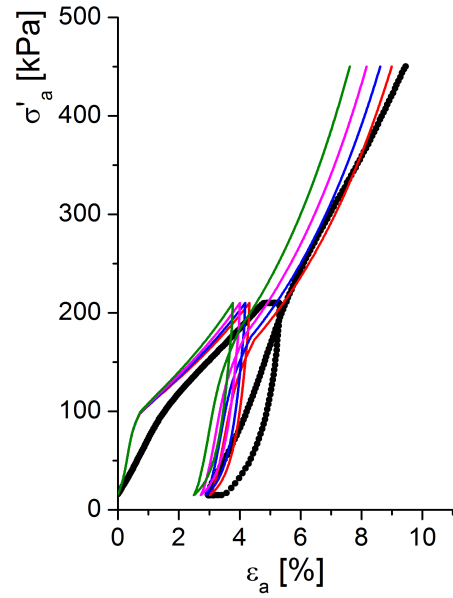


(c) strain paths

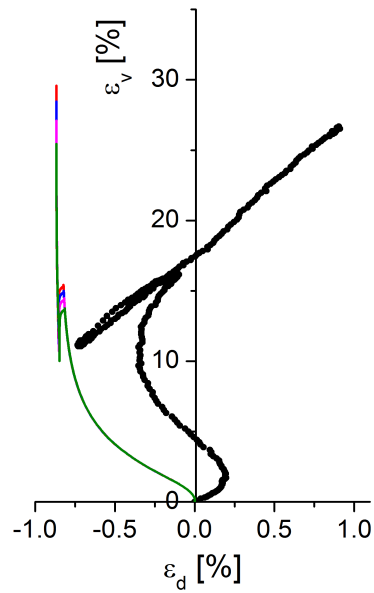
Figure G.7: Influence of anisotropy parameter β of Test B7 (McGinty, 2006) simulation, where $\eta_1 = 0$ and $\eta_2 = 0$



(a) compression behaviour

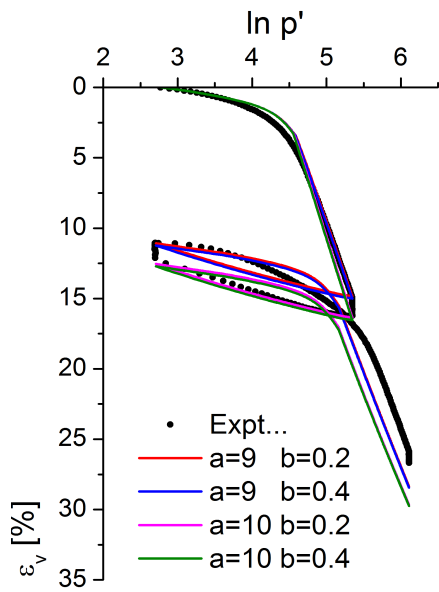


(b) axial stress-strain behaviour

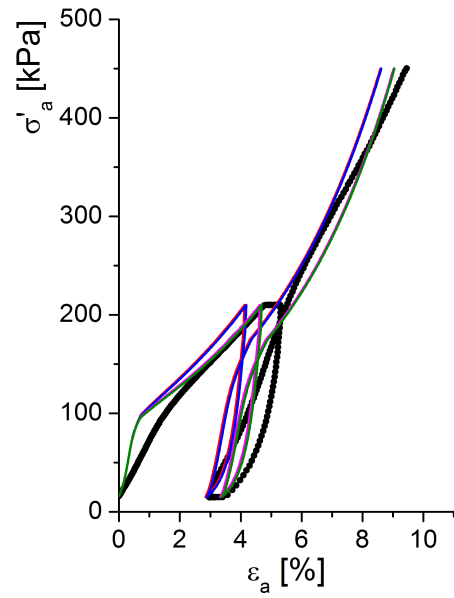


(c) strain paths

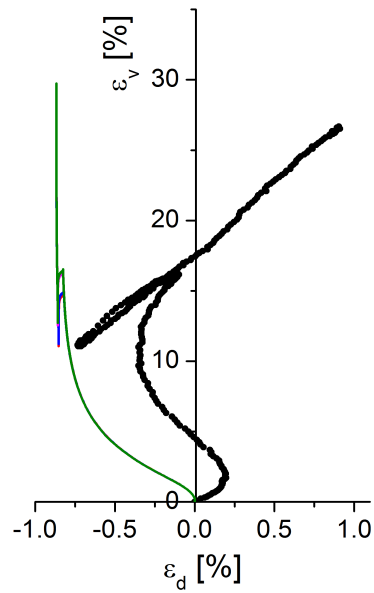
Figure G.8: Influence of initial bonding χ_0 of Test B7 (McGinty, 2006) simulation, where $\eta_1 = 0$ and $\eta_2 = 0$



(a) compression behaviour



(b) axial stress-strain behaviour



(c) strain paths

Figure G.9: Influence of destructurational parameter a and b of Test B7 (McGinty, 2006) simulation, where $\eta_1 = 0$ and $\eta_2 = 0$